An Energy- and Enstrophy-Constrained Parameterization of Mesoscale Ocean Eddies Over Topography

Rosie Eaves

University College

University of Oxford

A thesis submitted for the degree of

Doctor of Philosophy

2024

For my cat, Ida, who didn't care about any of this.

Acknowledgements

First and foremost, thank you to my supervisors David Marshall, James Maddison, and Stephanie Waterman. David, your unshakeable faith in me has encouraged me to attempt things even when I was convinced I wouldn't be able to do them. I hope I can carry that faith with me as I move forward in my career. James, I felt a huge weight lift off my shoulders when you wrote $\forall x \in \mathbb{R}$ while we were writing equations together on the board. The mathematical notation made me feel at home. Stephanie (and her red pen!), your attention to detail has improved my writing abilities to no end. Spending thanksgiving with you in Canada is a memory I will cherish. I feel extremely lucky to have worked with each of you.

Thank you to Elizabeth Yankovsky for constructive and helpful comments during the peer review process. The lessons I learned from these comments have been extremely useful in writing my thesis.

Thank you to my therapists: Polly, the work we did together early on in my PhD has been invaluable in maintaining mental stability these past four years; and Emily, for getting me through the last few arduous months.

Huge thanks to anyone who engaged in out of hours entertainment with me, including (but not limited to) Pete, Diya, Sol, Rhid, Jingxuan, Joe, Timmy, Jacob, Léa and Chun. Without the mental reset and physical recalibration that comes from dancing into the early hours of the morning with some lovely people, I don't think I would have been anywhere near as productive in my PhD.

Thanks to Charlie, Debs, Sol and Jingxuan for afternoon walks in the park, and to Fraser for answering endless questions when I first started.

I am eternally grateful for my cat, Ida, who sadly passed away during my PhD. Ida taught me how to care and be cared for, and the importance of doing nothing. Ironically, I learned so much about how to be a human from a cat. This knowledge has helped me to look after myself throughout my PhD. Special thanks also to Ida's sister Jiji who holds our little family together in Ida's absence.

Finally, thanks to my partner, Pete, without whom I probably would have eaten nothing but cereal in the six months prior to submitting my thesis, and who brings joy and silliness to my life every day. I am so happy that I get to have you by my side in all of my endeavours.

Abstract

Mesoscale ocean eddies have a profound influence on the large-scale oceanic flow, yet the effect of these eddies in driving rectified topography-following flows is often ignored in climate models. In this thesis, a new parameterization of barotropic eddy potential vorticity (PV) fluxes which is both energetically and enstrophetically constrained is developed for use in non-eddying models. The parameterization employs down-gradient PV mixing and incorporates a subgrid eddy kinetic energy and eddy potential enstrophy budget to constrain the parameterized PV mixing. The parameterization includes a mechanism through which kinetic energy can be exchanged bidirectionally between the resolved flow and the parameterized eddies, and a mechanism through which potential enstrophy can be converted from the resolved flow to the parameterized eddies.

The parameterization is tested in highly idealised simulations of barotropic freely decaying turbulence in a doubly periodic domain on an f-plane over variable topography. An emergent topography-following flow is produced by the parameterization. The constraints imposed in the parameterization are successful in constraining the resolved kinetic energy and potential enstrophy such that they are realistic when compared with an eddy-resolving model. The kinetic energy and potential enstrophy pathways associated with the parameterized and eddy-resolving models are quantified and compared. The parameterized transfer rates initially resemble those of the eddy-resolving simulation, but diverge from the eddy-resolving simulation when biharmonic diffusion dominates the flow.

The kinetic energy supercharger mechanism is introduced as a method of compensating for the erroneous kinetic energy and potential enstrophy transfers when biharmonic diffusion dominates the flow. The parameterization with the additional kinetic energy supercharger mechanism is tested in the setup described above, and produces kinetic energy and potential enstrophy transfers which more closely resemble those of the eddy-resolving simulation.

A method of implementing the parameterization of barotropic eddy PV fluxes in a baroclinic setup is outlined and referred to as GM+PV. The Gent and McWilliams (1990) parameterization is employed alongside the barotropic parameterization, and

the two are integrated by the APE-to-EKE conversion mechanism which mimics the process of barotropization. GM+PV is implemented in the Massachusetts Institute of Technology general circulation model.

GM+PV is tested in semi-realistic simulations of the Arctic Ocean. An emergent cyclonic flow around the Arctic Basin at depth, broadly resembling the Arctic Circumpolar Boundary Current and not present in simulations without GM+PV, is produced. The kinetic energy pathways associated with GM+PV simulations are quantified and utilised to explain the maintenance of the quasi-steady state as well as the functioning of GM+PV in a baroclinic setup.

Contents

Chapter 1

Introduction

Mesoscale ocean eddies occur on a scale of roughly 1 km - 100 km and are known to affect the large scale flow through a number of processes. They modulate the strength of the Antarctic Circumpolar Current through eddy saturation (Munday et al., 2013) and the residual overturning in the Southern Ocean through eddy compensation (Abernathey et al., 2011), and act to stabilise unstable jets (Waterman and Lilly, 2015) among many other processes. As such, they play a crucial role in modulating large scale ocean circulation (Hallberg and Gnanadesikan, 2006) and determining the global ocean stratification (Karsten et al., 2003) and are therefore a key component in the accurate prediction of global and localized climates. However, climate models typically have too coarse a resolution to explicitly simulate mesoscale eddies, particularly in high latitude regions. As a result, eddies are parameterized in almost all CMIP6-class models with an ocean component (Eyring et al., 2016; Gregory et al., 2016; Griffies et al., 2009, 2016; Jones et al., 2016). One eddy-driven process which is typically neglected in eddy parameterizations commonly employed in CMIP6-class models is the interaction of the eddies with the seafloor, specifically in producing rectified topography-following flows. In this thesis, we develop a parameterization of barotropic eddy potential vorticity (PV) fluxes for use in non-eddying models which specifically aims to produce an emergent topography-following flow of a realistic strength as determined by an eddy-resolving simulation. This is achieved by incorporating physically motivated constraints in the parameterization which aim to mimic the characteristics of the barotropic mode of quasigeostrophic turbulence.

Let us begin by exploring the behaviour of quasigeostrophic turbulence which is the

dominant regime in the ocean interior. Quasigeostrophic turbulence consists of both a barotropic mode and baroclinic modes. For the purposes of this thesis, we define the barotropic mode to be the depth-independent component of the turbulence. Energy in the ocean can exist in the baroclinic modes as either available potential energy (APE) and kinetic energy, or in the barotropic mode as kinetic energy. Potential enstrophy exists in both the baroclinic modes and the barotropic mode, and is defined as $q^2/2$ where q is the PV. Potential enstrophy can be thought of as a measurement of the variance of PV. Thus a decrease in potential enstrophy, corresponding to a decrease in the variance of PV, occurs during PV homogenization (Rhines and Young, 1982).

The cascades and conversions of energy and potential enstrophy, illustrated schematically in Figure 1.1 in the style of Salmon (1998), are key to describing the behaviour of quasigeostrophic turbulence in the ocean. In the description that follows, we distinguish between the large-scale flow and the small-scale eddies by the Rossby radius of deformation, which approximates the typical length scale of mesoscale eddy motion. Large-scale forcing of the ocean provides a source of energy and potential enstrophy in the baroclinic modes. This energy can be input as either kinetic energy or potential energy and may subsequently be converted between these two types. In the baroclinic modes, both energy and potential enstrophy cascade preferentially to smaller scales. At scales close to the Rossby radius of deformation, baroclinic eddies form and convert large-scale APE in the baroclinic modes to eddy energy. This eddy energy exists as either eddy APE in the baroclinic modes, or eddy kinetic energy (EKE) in either the barotropic or baroclinic modes. The baroclinic eddies also convert large-scale potential enstrophy in the baroclinic modes to eddy potential enstrophy (EPEnstr) in both the barotropic and baroclinic modes. This process of energy and potential enstrophy conversion from the baroclinic modes to the barotropic mode by the baroclinic eddies is known as barotropization. In the barotropic mode, barotropic eddies cascade kinetic energy preferentially to large scales, and potential enstrophy to small scales. Finally, small-scale processes dissipate both potential enstrophy and kinetic energy at small scales, and bottom drag dissipates kinetic energy at large scales. The overall effect of this process is an inverse cascade of kinetic energy (small scale to large scale), and a direct cascade of potential enstrophy (large scale to small scale).

The parameterization of mesoscale eddies in CMIP6-class models is typically accomplished through the parameterization of Gent and McWilliams (1990) (hereafter

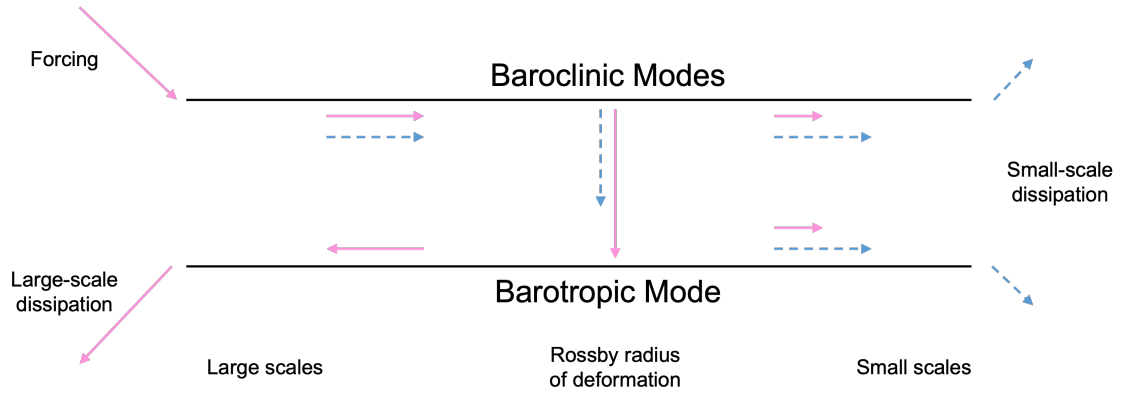

Figure 1.1: Schematic in the style of Salmon (1998) illustrating pathways of energy (pink arrows) and potential enstrophy (blue dashed arrows) in quasigeostrophic turbulence.

referred to as GM90). GM90 parameterizes the eddy-induced transport arising from eddy buoyancy fluxes as a prescribed advection of tracers (Gent et al., 1995), combined with diffusion along isopycnals (Redi, 1982), resulting in an adiabatic flattening of isopycnals. A key feature of GM90, and one its successes, is ensuring the conservation of fluid volume between isopycnals. This led to a number of improvements in ocean models by eliminating the spurious diapycnal mixing that resulted from previous eddy parameterization methods (Danabasoglu et al., 1994). Originally, GM90 was implemented with a constant GM-diffusivity, κ_{GM}, although it was recognised that varying κ_{GM} in space was important. Other studies have sought to incorporate such variability, for example, based on linear instability theory (e.g. Visbeck et al., 1997) or through numerical experiments (e.g. Ferreira et al., 2005).

GM90 specifically parameterizes the baroclinic eddies, aiming to mimic the conversion of APE to eddy energy described above. The flattening of isopycnals which occurs through the use of GM90 acts as an extraction of large-scale[1] APE. However, GM90 does not attempt to parameterize the barotropic mode of quasigeostrophic turbulence, and this extracted APE is left unaccounted for. Thus, GM90 introduces a sink of energy into the system and, without further parameterization methods, the effect of the barotropic mode of turbulence is neglected. The parameterization of the barotropic mode forms the focus of this thesis.

More recent work in the design of eddy parameterizations has incorporated additional

[1]In the context of eddy parameterizations, the terms large-scale and eddy are used to signify the resolved and unresolved dynamics respectively.

conservation properties, leading to the development of energetically constrained parameterizations via the integration of a subgrid energy budget. The subgrid energy is then used to inform the eddy parameterization employed, for example, with variants of GM90 (e.g. Cessi, 2008; Eden and Greatbatch, 2008; Mak et al., 2017, 2018) or a down-gradient PV mixing parameterization (Marshall and Adcroft, 2010). Incorporating an energetic constraint has been shown to improve the energetics of the large-scale flow (Marshall and Adcroft, 2010), as well as produce emergent features, such as eddy saturation in idealised models of the Southern Ocean circulation, consistent with the dynamics of eddy-resolving simulations (Mak et al., 2017, 2018).

Some eddy parameterization formulations also incorporate mechanisms to parameterize specific energy pathways. For example, it is a known problem that explicit diffusion, required in numerical models for stability, extracts energy at the grid scale (Jansen and Held, 2014). Additionally, as described above, the extraction of APE from the large-scale flow by GM90 represents a loss of energy in the system (Bachman, 2019). Backscatter[2] has been proposed as a method of compensating for these artificial energy sinks in eddy-permitting models, and involves accounting for the lost energy and reinjecting it to the resolved flow, typically via a negative Laplacian of the resolved velocity in the governing equation (Jansen and Held, 2014; Jansen et al., 2015; Bachman, 2019; Jansen et al., 2019; Juricke et al., 2019, 2020; Yankovsky et al., 2024). The resolved eddies may subsequently cascade this reinjected kinetic energy to larger scales. Incorporating a mechanism of backscatter has been shown to improve the kinetic energy spectra of the large-scale flow when compared to eddy-resolving simulations (Jansen and Held, 2014; Jansen et al., 2015; Bachman, 2019; Juricke et al., 2019; Yankovsky et al., 2024).

Jansen et al. (2019) extended the mechanism described above for use in non-eddying as well as eddy-permitting models by combining a backscatter mechanism with an energetically constrained implementation of GM90. In this parameterization formulation, APE extracted from the system by GM90 can re-energise the resolved flow, through the backscatter mechanism described above, or the parameterized eddies

[2]The term backscatter is often used to refer to two processes in the literature: the reinjection of extracted energy into the resolved flow; and the inverse cascade of kinetic energy present in quasigeostrophic turbulence. In fact, in the former process the energy reinjection typically occurs at scales larger than scales at which the energy is extracted and the resolved eddies may then cascade this reinjected energy to large scales. Thus, the former process facilitates the explicit simulation of the inverse kinetic energy cascade.

through the energetically informed value of κ_{GM}. Yankovsky et al. (2024) added vertical structure to the backscatter mechanism of Jansen et al. (2019), given by the equivalent barotropic mode, which produced more realistic energetics in eddy-permitting simulations than the combination of depth-independent backscatter with GM90 tested by Jansen et al. (2019).

Alternatively, parameterizing the eddies using a down-gradient PV mixing parameterization permits bidirectional conversion of kinetic energy between the resolved flow and the parameterized eddies (Marshall and Adcroft, 2010), with the direction of the energy transfer linked to Arnold's first stability theory (Arnold, 1965). Marshall and Adcroft (2010) demonstrated that this can lead to an emergent transfer of kinetic energy from small (unresolved) to large (resolved) scales in freely decaying turbulence experiments, consistent with the indirect cascade of kinetic energy in quasigeostrophic turbulence. In practice, this can lead to the forcing of large-scale flows, compatible with the inverse cascade of kinetic energy, demonstrated for example in Waterman and Jayne (2012) and Tamarin et al. (2016).

Whilst there are many instances in the literature of eddy parameterization formulations designed to respect energy dynamics, the same focus has not been applied as thoroughly to the dynamics of potential enstrophy. We have seen that quasigeostrophic theory predicts a direct cascade of potential enstrophy in both the barotropic and baroclinic modes, which is ultimately dissipated at small scales. Potential enstrophy dissipation is guaranteed by design in down-gradient PV mixing parameterizations through the mixing of PV, and is ensured in some backscatter parameterizations by reinjecting the energy at scales larger than it is extracted (Jansen and Held, 2014; Jansen et al., 2015; Bachman, 2019). However, to our knowledge, no parameterizations exist that explicitly consider a dynamical potential enstrophy budget and use this to constrain the parameterization.

Energy and enstrophy dynamics play a crucial role in the development of eddy-driven topography-following flows. Bretherton and Haidvogel (1976) hypothesised that the turbulent cascades of kinetic energy and potential enstrophy in barotropic freely decaying turbulence drive the flow towards a minimum enstrophy state for a given initial energy, resulting in an eddy-driven topography-following flow. This is known as the minimum enstrophy hypothesis. Recent evidence suggests that this hypothesis holds true for low-initial-energy states, in which the initial domain-integrated energy is less

than that of a PV-homogenized state, but does not hold for high-initial-energy states (Siegelman and Young, 2023; Gallet, 2024). Nonetheless, the minimum enstrophy hypothesis provides a starting point from which to build on. Indeed, numerical experiments have demonstrated that, over topography, eddies mix PV (Adcock and Marshall, 2000) and dissipate EPEnstr (Siegelman and Young, 2023; Gallet, 2024) by an amount determined by the energy of the initial state, supporting the hypothesis of Bretherton and Haidvogel (1976) for low-initial-energy states. Recent evidence also suggests that the initial enstrophy is important in determining the state of barotropic freely decaying turbulence over topography (He and Wang, 2024).

The importance of energy and enstrophy dynamics in the development of eddy-driven topography-following flows is further evidenced by the inability of energetically unconstrained parameterizations (i.e. formulations in which there is no feedback of the subgrid energetics on the parameterized eddy effects) to produce realistic eddy-driven topography-following flows. Crucially, they fail due to energetic inconsistencies in the underlying mechanisms of the parameterizations. For example, in freely decaying turbulence over topography, GM90 leads to an unrealistic state of rest (Adcock and Marshall, 2000) due to the fact that it introduces a sink of energy in the system as described above. In the same setup, down-gradient PV mixing with a constant eddy PV diffusivity can introduce a spurious source of energy into the system (Adcock and Marshall, 2000), leading to unrealistically energetic flow fields.

Related to the minimum enstrophy hypothesis is the idea that mesoscale eddies drive the flow towards a state of maximum entropy, which leads to topography-following flows. Holloway (1992) exploited this idea to develop the Neptune parameterization by using the cascades of energy and potential enstrophy inherent to the flow to derive a solution for the flow field with maximised entropy. The Neptune parameterization relaxes the resolved flow towards a simplified estimate of this maximum entropy flow field, which follows topographic contours resulting in an eddy-driven topography-following flow. Neptune has been implemented and tested in both global (Eby and Holloway, 1994) and Arctic regional (Nazarenko et al., 1998; Golubeva and Platov, 2007; Holloway and Wang, 2009) models. In these studies, it was found that inclusion of Neptune led to flow fields which were more in agreement with observations than simulations without Neptune. Although implementation of Neptune in climate models is rare, these studies show that incorporating eddy parameterizations which are capable of producing emergent eddy-driven topography-following flows may improve

the accuracy of ocean models.

In this thesis, we develop a parameterization of barotropic eddy PV fluxes which aims to produce realistic emergent eddy-driven topography-following flows. This parameterization specifically aims to parameterize the barotropic mode of quasigeostrophic turbulence, illustrated in Figure 1.1, in which kinetic energy is preferentially cascaded to large scales and potential enstrophy is cascaded to small scales. The parameterization is formulated by incorporating physically motivated constraints into a down-gradient PV mixing parameterization. We build on the success of previous energetically constrained parameterizations by implementing an energy constraint as well as an additional potential enstrophy constraint, implemented in a method analogous to that employed in energetically constrained parameterizations. The resulting parameterization:

- employs a subgrid EKE budget and a subgrid EPEnstr budget to constrain the parameterized eddy PV fluxes;
- includes a mechanism through which kinetic energy can be exchanged bidirectionally between the parameterized eddies and the large-scale flow;
- includes a mechanism through which potential enstrophy can be converted from the large-scale flow to the parameterized eddies.

We develop the parameterization for use in non-eddying models, in which the smallest resolved scale is larger than the Rossby radius of deformation. We do not attempt to parameterize the effects of the baroclinic modes of turbulence within this parameterization. Instead, we propose implementing the parameterization of barotropic eddy PV fluxes alongside a parameterization of baroclinic eddies.

In Chapter 2 we outline the formulation of the parameterization of barotropic eddy PV fluxes. We exploit a mathematical bound on the magnitude of the eddy PV fluxes to incorporate the kinetic energy and potential enstrophy constraints. We then construct parameterized budgets for the subgrid EKE and the subgrid EPEnstr which we use to constrain the parameterization. We focus on the underlying physics, comparing the methods proposed here with those of other eddy parameterization formulations.

In Chapter 3, we perform the first tests of the parameterization described in Chapter 2. We employ highly idealised simulations designed to isolate the effect of the

explicit or parameterized eddies, thus allowing us to determine the functionality of the parameterization. These simulations are of barotropic, freely decaying turbulence on an f-plane in a doubly periodic domain over variable bottom topography. We demonstrate that the parameterization results in a net conversion of kinetic energy from the parameterized eddies to the large-scale flow, as well as a conversion of potential enstrophy from the large-scale flow to the parameterized eddies. Thus, there is an emergent indirect cascade of kinetic energy and an emergent direct cascade of potential enstrophy in the simulations employing the energy- and enstrophy-constrained parameterization, consistent with the cascades in the barotropic mode of quasigeostrophic turbulence. Further, we show that the energetic and enstrophetic constraints imposed in the parameterization are successful in constraining the large-scale, eddy-driven, topography-following flow such that it has realistic kinetic energy and potential enstrophy when compared to the flow in an eddy-resolving simulation. We quantify the transfers of kinetic energy and potential enstrophy associated with the simulations, finding that the parameterized transfers initially resemble those of the eddy-resolving simulation, but become less accurate later in the simulation. The formulation of the parameterization in Chapter 2 and much of the results discussed in Chapter 3 are currently under review for publishing.

In Chapter 4, we implement a kinetic energy supercharger mechanism in the parameterization, motivated by the results of Chapter 3. This supercharger mechanism reinjects the kinetic energy extracted from the large-scale flow by biharmonic diffusion into the parameterized EKE budget. This kinetic energy may subsequently be transferred to the large-scale flow through the pre-existing kinetic energy conversion mechanism within the parameterization. We test this iteration of the parameterization in the same idealised setups employed in Chapter 3. We find that employing the parameterization with the additional supercharger mechanism leads to kinetic energy and potential enstrophy transfers which more closely resemble those of an eddy-resolving simulation when compared to the parameterized simulation without the supercharger mechanism (analysed in Chapter 3), leading to a quasi-steady state which more closely resembles that of the eddy-resolving simulation.

In Chapter 5, we outline one method of implementing the parameterization of barotropic eddy PV fluxes in a baroclinic setup. We choose to implement the barotropic parameterization alongside, and integrated with, the GM90 parameterization of baroclinic instability. That is, we parameterize the barotropic and baroclinic eddies separately,

incorporating a mechanism in the barotropic parameterization through which these parameterizations are integrated. Through this mechanism, APE extracted from the resolved flow by GM90 is reinjected into the parameterized barotropic EKE budget, thus mimicking the process of barotropization described above. We refer to this additional mechanism as the APE-to-EKE conversion mechanism. By employing the barotropic parameterization with the additional APE-to-EKE conversion mechanism alongside GM90, the conversion of mean APE to barotropic EKE by the baroclinic eddies, and the subsequent behaviour in the barotropic mode of quasigeostrophic turbulence, is parameterized. We outline the implementation of the barotropic parameterization with the additional APE-to-EKE conversion mechanism in the Massachusetts Institute of Technology general circulation model (MITgcm, Marshall et al., 1997b,a).

In Chapter 6, we test the implementation of the parameterization in a baroclinic setup described in Chapter 5. We choose to test the the parameterization in an idealised setup of the Arctic Ocean since topography-following flows are prevalent in this region (Orvik and Niiler, 2002). We provide an introduction to the dynamics of the Arctic Ocean in Chapter 6, choosing to separate it from the introduction above for narrative purposes. We run coarse-resolution simulations in MITgcm using an idealised Arctic Ocean setup with no eddy parameterization; with GM90 only; and with the barotropic parameterization with the additional APE-to-EKE conversion mechanism alongside GM90. We find that including the energy- and enstrophy-constrained parameterization of barotropic eddy PV fluxes leads to a cyclonic flow around the boundary of the Arctic Ocean, largely resembling the Arctic Circumpolar Boundary Current, which is not present in the other simulations. We analyse the behaviour of the parameterized EKE and the parameterized EPEnstr, finding that the flow reaches a quasi-steady state in which the APE-to-EKE conversion largely balances the eddy-to-mean kinetic energy conversion, and the mean-to-eddy potential enstrophy conversion balances the parameterized EPEnstr dissipation.

We conclude in Chapter 7 by summarising and discussing the work presented in this thesis.

I have conducted all of the work contained in this thesis, supervised by David Marshall (University of Oxford), James Maddison (University of Edinburgh) and Stephanie Waterman (University of British Columbia).

Chapter 2

An energy- and enstrophy-constrained parameterization of barotropic eddy potential vorticity fluxes

In this chapter we describe the parameterization formulation which forms the focus of this thesis. The formulation is an energetically and enstrophetically constrained down-gradient PV mixing parameterization of barotropic eddy PV fluxes. In Section 2.1 we describe the general form of a down-gradient PV mixing parameterization. In Section 2.2 we introduce the energetic and enstrophetic constraint. In Sections 2.3 and 2.4 we outline the EKE and EPEnstr budgets, respectively, which are employed to constrain the eddy PV fluxes. We summarise and discuss the parameterization formulation in Section 2.5.

2.1 Down-Gradient PV Mixing Parameterizations

For a barotropic fluid, the PV, q, is defined as

$$q = \frac{f + \xi}{\mathrm{H}} \tag{2.1}$$

where f is planetary vorticity; ξ is the vertical component of relative vorticity, defined as $\xi = \partial v/\partial x - \partial u/\partial y$ where u and v are the zonal (x) and meridional (y) components of the horizontal velocity, $\mathbf{u}$, respectively; and H is layer thickness[1]. We begin by performing a Reynolds average of the PV and the horizontal velocity to obtain

$$q = \overline{q} + q', \tag{2.2}$$

$$\mathbf{u} = \overline{\mathbf{u}} + \mathbf{u}', \tag{2.3}$$

where overbars denote a time-mean, used to represent the large-scale, slowly evolving component of the flow, which we refer to as the mean component; and primes denote a deviation from this time-mean, used to represent the small-scale, fast-evolving component of the flow, which we refer to as the eddy component. When discussing parameterized non-eddying models, overbars denote the resolved flow which is expected to consist only of a large-scale flow, and primes denote the unresolved eddy component of the flow[2]. Down-gradient PV mixing parameterizations parameterize the eddy PV fluxes as the mixing of PV down the mean PV gradient at a specified rate controlled by an eddy diffusivity. This takes the form

$$\overline{q'\mathbf{u}'} = -\kappa_{\mathrm{PV}} \nabla \overline{q}, \tag{2.4}$$

where κ_{PV} is the eddy PV diffusivity.

An unconstrained PV mixing parameterization, i.e. a down-gradient PV mixing parameterization in which κ_{PV} is constant in time and space, will continue to act on a flow until there are no PV gradients. That is, it will always drive the flow towards PV homogenization. However, Siegelman and Young (2023) demonstrate that for freely decaying, two-dimensional turbulence over topography, numerical simulations with an initial energy below that of a PV-homogenized state do not reach a state of PV homogenization. This can be understood from an energy conservation perspective: if the initial energy is below that of a PV-homogenized state, an energy input would be required to reach PV homogenization. Thus, by indiscriminately driving the flow to a PV-homogenized state, an unconstrained PV mixing parameterization can introduce

[1] Note that H must be invariant with time in order for Equation 2.4 to be true. In the experiments discussed and analysed in this paper, we consider one vertical layer with a rigid lid and a bottom topography that is invariant with time. Hence, this requirement is satisfied.

[2] We typically use the words resolved, large-scale and mean interchangeably; and unresolved, sub-grid and eddy interchangably in the context of parameterized eddy simulations.

a spurious source of energy into the system. We will demonstrate this phenomenon in Chapter 3. We aim to eliminate this spurious source of energy such that the large-scale flow resembles that of an eddy-resolving simulation by implementing physically motivated constraints on the value of κ_{PV}.

2.2 Constraining the Eddy PV Diffusivity

To constrain the time-mean eddy PV fluxes, $\overline{q'\mathbf{u}'}$, we exploit the following bound:

$$|\overline{q'\mathbf{u}'}|^2 \leq \overline{|q'|^2}\ \overline{|\mathbf{u}'|^2} = 4\Lambda K, \tag{2.5}$$

where we have used the Cauchy-Schwarz inequality, and where Λ is the EPEnstr and K is the EKE, defined as

$$\Lambda = \frac{\overline{q'^2}}{2}, \tag{2.6}$$

and

$$K = \frac{\overline{u'^2} + \overline{v'^2}}{2}, \tag{2.7}$$

respectively. This bound holds, for example, for eddy-mean decomposition via time-averaging as used in this study.

We now employ a similar approach to Marshall et al. (2012) to construct a down-gradient PV mixing parameterization from Equation 2.5. A dimensionless efficiency parameter, γ_q, can be defined from the bound in Equation 2.5, such that

$$|\overline{q'\mathbf{u}'}| = 2\gamma_q\sqrt{\Lambda K}, \tag{2.8}$$

where $0 \leq \gamma_q \leq 1$. When $\gamma_q = 0$, the eddy PV flux is zero on average. In this case, the eddies do not have a net effect on the large-scale flow. When $\gamma_q = 1$, the eddy PV flux magnitude is at its maximum value and the effect of the eddies on the large-scale flow is maximised. Hence, γ_q describes how efficient the eddies are at fluxing PV and we refer to it as the PV flux efficiency parameter.

Equation 2.5 leads to the following down-gradient PV mixing parameterization:

$$\overline{q'\mathbf{u}'} = -2\gamma_q\sqrt{\Lambda K}\,\widehat{\nabla\overline{q}}, \tag{2.9}$$

where $\widehat{\ }$ denotes a unit vector. Note that Equation 2.9 satisfies the bound in Equation 2.5 due to the constraint on the magnitude of γ_q.

Equation 2.9 describes a down-gradient PV mixing parameterization in which the magnitude of the eddy PV fluxes is determined by the EKE (K), the EPEnstr (Λ), and the PV flux efficiency parameter (γ_q) which is strongly bounded. Physically, Equation 2.9 implies that both EPEnstr, i.e. PV anomalies, and EKE, i.e. eddies, are required for an eddy PV flux to be present. In other words, if there are no eddies, or if the PV is uniform, there will be no eddy PV flux.

When written in the form described by Equation 2.4 (i.e. without the unit vector), the eddy PV diffusivity is given by

$$\kappa_{\mathrm{PV}} = \frac{2\gamma_q\sqrt{\Lambda K}}{|\nabla\overline{q}|}. \tag{2.10}$$

The factor $1/|\nabla\overline{q}|$ in Equation 2.10 implies that the eddy PV diffusivity is suppressed in regions of large background PV gradient. Marshall et al. (2006) estimated the eddy diffusivity from satellite altimetry data in the Southern Ocean and found that regions of large/small diffusivities were collocated with regions of weak/strong PV gradients, respectively, providing evidence for the suppressive effect of PV gradients on the eddy diffusivity. This behaviour is consistent with the idea that the eddy diffusivity is suppressed across jets (Ferrari and Nikurashin, 2010), which has been observed in the Southern Ocean (Naveira Garabato et al., 2011; Abernathey and Marshall, 2013). In the context of a barotropic fluid on an f-plane (explored in Chapters 3 and 4), Equation 2.10 implies that the eddy PV diffusivity is suppressed in regions of large topographic slope. Sterl et al. (2024) derived an analytical expression for the eddy diffusivity, finding that strong topographic slopes do indeed have a suppressive effect on the eddy diffusivity, and verified this suppressive effect through numerical experiments. Equation 2.10 therefore suggests that the parameterization may be capable of reproducing the suppressive effects outlined above. We note from Equation 2.9 that the strength of the background PV gradient, and therefore the topographic slope, does not directly[3] affect the magnitude of the parameterized eddy PV fluxes which

[3]The magnitude of the eddy PV fluxes may be indirectly affected by the topographic slope through the values of the parameterized EKE and EPEnstr.

quantifies the amount of eddy PV mixing. Thus, suppressed eddy PV diffusivity and large eddy PV mixing can co-exist over regions of large topographic slope[4].

The choice to include a factor of -1 in Equation 2.9 imposes down-gradient PV mixing by design. One caveat to this approach is that, whilst it is true that the eddies flux PV down the mean PV gradient on average (Marshall et al., 1999), this is not necessarily the case locally (e.g. Waterman and Jayne, 2012). However, imposing down-gradient PV mixing is a common tactic in eddy parameterization design (e.g. Treguier et al., 1997; Marshall and Adcroft, 2010; Eden, 2009) and we deem it an appropriate assumption for this first demonstration-of-concept exercise.

It remains to determine the EKE and EPEnstr for use in informing the parameterization. One strategy for determining these parameters used widely in the literature (e.g. Eden and Greatbatch, 2008; Cessi, 2008; Marshall and Adcroft, 2010; Marshall et al., 2012; Mak et al., 2017, 2018; Jansen et al., 2019; Yankovsky et al., 2024) is to employ prognostic equations, i.e. budgets for unresolved, subgrid-scale quantities. We adopt this strategy here, stepping forward budgets for the depth-averaged values of EKE and EPEnstr at each time step and using the time-evolving values of EKE and EPEnstr to inform the parameterization. The intention of this formulation is that the parameterization's dependence on time-evolving budgets of EKE and EPEnstr will act to realistically constrain the kinetic energy and potential enstrophy of the resolved flow.

2.3 The EKE Budget

We now specify the parameterized EKE budget which will be used to constrain the eddy PV fluxes through Equation 2.9. The depth-integrated EKE equation (derived in Appendix A) is

$$\mathrm{H}\frac{\partial}{\partial t}\left(\frac{\overline{\mathbf{u}'\cdot\mathbf{u}'}}{2}\right) = \mathrm{H}\overline{q'\mathbf{u}'}\cdot\nabla\overline{\psi} - \nabla\cdot\mathrm{H}\overline{\mathbf{u}'B'} + \mathbf{F}_{\mathrm{EKE}}, \tag{2.11}$$

[4]We note that the terms eddy diffusivity and eddy mixing are sometimes used interchangeably in the literature with the conclusion that both eddy diffusivities *and* eddy mixing are suppressed in the presence of large background PV gradients. Here we define the eddy PV mixing as the eddy PV fluxes.

where ψ is the transport stream function, B is the Bernoulli potential defined as $B = \mathbf{u} \cdot \mathbf{u}/2 + p/\rho_0$ where p is the pressure and ρ_0 a reference density, and $\mathbf{F}_{\text{EKE}}$ represents sources and sinks of EKE.

We construct a parameterized EKE budget from Equation 2.11. The first term on the right hand side of Equation 2.11 represents kinetic energy conversion between the large-scale flow and the eddies, discussed in more detail below. The second term on the right hand side integrates to zero over the domain and therefore acts only to redistribute the energy. Following the literature (e.g. Eden and Greatbatch (2008), Marshall and Adcroft (2010), Jansen et al. (2019), Yankovsky et al. (2024)), we represent this redistribution of depth-integrated EKE as advection by the large-scale flow and Laplacian diffusion with coefficient μ. Finally, we include only a sink of EKE through bottom friction in $\mathbf{F}_{\text{EKE}}$ which we parameterize as linear drag with coefficient r_K. Thus our depth-averaged parameterized EKE budget is

$$\frac{\partial K}{\partial t} = \overline{q'\mathbf{u}'} \cdot \nabla\overline{\psi} - \frac{1}{\mathrm{H}}\nabla \cdot (K\mathrm{H}\overline{\mathbf{u}}) + \frac{\mu}{\mathrm{H}}\nabla^2\mathrm{H}K - r_K K, \tag{2.12}$$

where K is now the the parameterized EKE, overbars represent resolved values (which represent mean components in parameterized simulations), and the eddy parameterization (Equation 2.9) is used to evaluate $\overline{q'\mathbf{u}'}$.

The first term on the right hand side of Equation 2.12 represents kinetic energy conversion between the large-scale flow and the parameterized eddies (Marshall and Adcroft, 2010) with a positive value signifying conversion from the large-scale flow to the eddies. This term also appears in the budget of Marshall and Adcroft (2010) where it is shown to represent a parameterized analogue of Arnold's first stability theorem (Arnold, 1965). This term is capable of converting kinetic energy from the parameterized eddies to the large-scale flow, mimicking the inverse cascade typical of quasigeostrophic turbulence, however the magnitude and direction of the conversion will depend on the values of the parameterized EKE and EPEnstr due to the formulation of the parameterized eddy PV fluxes (Equation 2.9). This term differs from the energy backscatter term in, for example, Jansen and Held (2014), Jansen et al. (2015), Bachman (2019), Jansen et al. (2019), Yankovsky et al. (2024) in several ways: 1. it represents a distinct energy pathway, i.e., it represents the conversion of kinetic energy between the large-scale flow and the eddies as opposed to the compensation of extracted energy; 2. it allows for bidirectional kinetic energy conversion, i.e., the

parameterized eddies can accelerate the large-scale flow and/or the large-scale flow can accelerate the parameterized eddies; 3. it is analytically derived as opposed to inserted in the budget as a forcing term; and 4. it does not require the use of a negative Laplacian in the governing equation to re-energise the large-scale flow, which leads to a backscattering of energy whenever and wherever there is a resolved flow. Note that the magnitude of this kinetic energy conversion term ($|\overline{q'\mathbf{u}'}||\nabla\overline{\psi}|$) does not depend on the background PV gradient. Thus, in the context of a barotropic fluid on an f-plane (explored in Chapters 3 and 4) the topographic slope does not directly affect the magnitude of this parameterized kinetic energy conversion.

2.4 The EPEnstr Budget

Having specified the parameterized EKE budget, it remains to specify the parameterized EPEnstr budget. The depth-integrated EPEnstr equation (derived in Appendix B) is

$$\mathrm{H}\frac{\partial}{\partial t}\left(\frac{\overline{q'^2}}{2}\right) = -\mathrm{H}\overline{q'\mathbf{u}'}\cdot\nabla\overline{q} - \nabla\cdot\left(\frac{\overline{q'^2}}{2}\mathrm{H}\overline{\mathbf{u}}\right) - \nabla\cdot\left(\mathrm{H}\overline{\frac{q'^2}{2}\mathbf{u}'}\right) + \mathbf{F}_{\mathrm{EPEnstr}}, \tag{2.13}$$

where $\mathbf{F}_{\mathrm{EPEnstr}}$ represents sources and sinks of EPEnstr.

We construct a parameterized EPEnstr budget from Equation 2.13. The first term on the right hand side of Equation 2.13 represents the conversion of potential enstrophy between the large-scale flow and the eddies, discussed in more detail below. The second and third terms represent the advection of depth-integrated EPEnstr by the large-scale and eddy components of the flow, respectively. We neglect the third term since it is a product of three eddy terms, although numerical simulations indicate that this term is important in the redistribution of EPEnstr (Wilson and Williams, 2004). We include both damping of depth-integrated EPEnstr and viscous diffusion in $\mathbf{F}_{\mathrm{EPEnstr}}$, which we represent as linear and Laplacian damping with coefficients r_Λ and μ respectively. Thus our depth-averaged parameterized EPEnstr budget is

$$\frac{\partial\Lambda}{\partial t} = -\overline{q'\mathbf{u}'}\cdot\nabla\overline{q} - \frac{1}{\mathrm{H}}\nabla\cdot(\Lambda\mathrm{H}\overline{\mathbf{u}}) + \frac{\mu}{\mathrm{H}}\nabla^2\mathrm{H}\Lambda - r_\Lambda\Lambda, \tag{2.14}$$

where Λ is now the parameterized EPEnstr, overbars represent resolved values (which represent mean components in parameterized simulations), and the eddy parameterization (Equation 2.9) is used to evaluate $\overline{q'\mathbf{u}'}$.

Analogous to the first term on the right hand side of the parameterized EKE budget, the first term on the right hand side of Equation 2.14 represents potential enstrophy conversion between the large-scale flow and the parameterized eddies. Let us first consider this term in the context of Equation 2.13, that is, in the EPEnstr budget of a fluid. When $-\overline{q'\mathbf{u}'} \cdot \nabla\overline{q}$ is positive, the eddy PV flux is, on average, down the mean PV-gradient, that is, the eddies act to mix PV. This mixing of PV by the eddies results in a conversion of potential enstrophy from the large-scale component of the flow to the eddy component, i.e. a direct potential enstrophy cascade. When $-\overline{q'\mathbf{u}'} \cdot \nabla\overline{q}$ is negative, the eddy PV flux is, on average, up the mean PV gradient, i.e. the eddies act to unmix PV, resulting in a conversion of potential enstrophy from the eddy component to the large-scale component. Quasigeostrophic theory predicts that this term is positive on average, producing a direct cascade of potential enstrophy, but we note it can be negative locally. Now, let us consider this term in the context of the parameterized EPEnstr budget (Equation 2.14). Due to the formulation of the parameterization, which imposes down-gradient mixing of PV by construction (Equation 2.9), this term will always be positive in simulations that employ the parameterization to model the eddy effects. Thus, the parameterization acts only to mix PV, and converts potential enstrophy from the large-scale flow to the parameterized eddy component only.

In Section 2.2, we showed that large background PV gradients can suppress the eddy PV diffusivity, κ_{PV}, but do not directly affect the strength of the eddy PV mixing, given by the magnitude of the parameterized eddy PV fluxes. Let us consider how the background PV gradient affects the parameterized mean-to-eddy potential enstrophy conversion term. The magnitude of this term is $|\overline{q'\mathbf{u}'}||\nabla\overline{q}|$. Thus, both strong parameterized eddy PV mixing *and* large background PV gradients can enhance parameterized mean-to-eddy potential enstrophy conversion. In the context of a barotropic fluid on an f-plane (explored in Chapters 3 and 4), both strong parameterized eddy PV mixing and large topographic slope can enhance the parameterized mean-to-eddy potential enstrophy conversion, and the strength of the parameterized eddy PV mixing is not directly affected by the topographic slope. Thus, strong conversion can be exhibited over regions of small topographic slope if the parameterized

eddy PV fluxes are large. Similarly, weak conversion can be exhibited over regions of large topographic slope if the parameterized eddy PV fluxes are sufficiently small.

2.5 Summary and Discussion

We have formulated an energetically and enstrophetically constrained down-gradient PV mixing parameterization of barotropic eddy PV fluxes. The energetically and enstrophetically constrained specification of down-gradient eddy PV fluxes (Equation 2.9), the parameterized EKE budget (Equation 2.12) and the parameterized EPEnstr budget (Equation 2.14) describe the parameterization fully. There are four input parameters to the parameterization: the eddy PV flux efficiency parameter, γ_q; the EKE and EPEnstr diffusivity, μ; the EKE dissipation coefficient, r_K; and the EPEnstr dissipation coefficient, r_Λ. The initial distributions of parameterized EKE, K_0, and parameterized EPEnstr, Λ_0, must also be specified. The parameterized EKE and EPEnstr evolve with time through the time integration of their respective budgets and the time-evolving values are then used to determine the magnitude of the parameterized down-gradient eddy PV fluxes at each time-step. Through these budgets, the parameterization accounts for the conversion of kinetic energy bidirectionally between the large-scale flow and the parameterized eddies, and the conversion of potential enstrophy from the large-scale flow to the parameterized eddies, as well as the redistribution and dissipation of EKE and EPEnstr.

There are some significant limitations to the parameterization as it is in its current form. Firstly, it is a known problem that, in a multiply-connected domain employing a down-gradient PV mixing parameterization, integral constraints on the eddy PV fluxes must be satisfied in order for angular momentum conservation to hold (Marshall, 1981; Marshall et al., 2012). The current form of the parameterization does not satisfy this constraint. Solutions to this problem have been proposed in previous studies, for example, Eden (2009) introduced a gauge term in the PV closure which acts as a rotational eddy PV flux and hence does not contribute to the eddy PV flux divergence. Angular momentum is then satisfied through this gauge term. Alternatively, Marshall (1981) and Wardle and Marshall (2000) introduced constraints on κ_{PV} to ensure angular momentum conservation. Further work would be required to implement such a solution into the parameterization and hence, without this effort, the current form of the parameterization could not be employed successfully in

multiply-connected domains, e.g. in a circumpolar Southern Ocean.

Additionally, we have specified that the eddy PV fluxes are directed down the mean PV gradient, which is true on average but may not hold locally. For example, up-gradient eddy PV fluxes are important in driving time-mean recirculation gyres in western boundary current jets (Waterman et al., 2011). Hence, there are important instances where the parameterization in its current form is not able to capture the full effect of the eddies on the mean flow. Up-gradient fluxes may also be important in the development of topographically trapped vortices which have been demonstrated through numerical experiments (Solodoch et al., 2021; Siegelman and Young, 2023) and observed in the Lofoten Basin (Søiland and Rossby, 2013). These topographically trapped vortices are opposite in sign to that predicted by minimum enstrophy theory (Bretherton and Haidvogel, 1976), that is, coherent anticyclones are trapped above topographic troughs, surrounded by cyclonic flow. The formation of topographically trapped anticyclones involves anticyclones propagating into the trough and subsequent vortex merging which strengthens the coherent anticyclonic vortex (Köhl, 2007; Solodoch et al., 2021), equivalent to an unmixing of PV. Without up-gradient PV fluxes, it is unlikely that these topographically trapped coherent vortices would be produced by the parameterization. Thus, incorporating up-gradient eddy PV fluxes could be an important avenue for future work to broaden the applicability of the parameterization.

Chapter 3

Freely Decaying Turbulence Simulations

3.1 Introduction

Having outlined the parameterization of barotropic eddy PV fluxes in Chapter 2, we now run a set of idealised simulations to test the functionality of the parameterization. We aim to answer the following key questions:

1. Does the parameterization result in a net conversion of kinetic energy from the eddy field to the large-scale flow resulting in a topography-following flow?
2. Do the parameterized energetics and enstrophetics exhibit similar behaviour to their explicit counterparts in an eddy-resolving simulation?
3. What are the parameterized kinetic energy and potential enstrophy pathways associated with the parameterization?
4. How do the input parameters to the parameterization affect the energetics and enstrophetics of the simulated flow?

To answer these questions, we run a set of numerical simulations in which we simulate barotropic, freely-decaying turbulence over variable bottom topography on an f-plane in a doubly periodic domain. The large-scale flow produced by this setup in an eddy-resolving simulation is an eddy-driven topography-following flow (Section 3.3). We use the following four configurations:

(a) an eddy-resolving (5 km horizontal resolution) simulation with explicit eddies only (5km_{EXP});

(b) a coarse-resolution (50 km horizontal resolution) simulation without employing any eddy parameterization ($50\text{km}_{\text{NOPAR}}$);

(c) a coarse-resolution simulation with parameterized eddies where we employ an unconstrained down-gradient PV mixing parameterization, i.e. Equation 2.4 with constant eddy PV diffusivity, κ_{PV} ($50\text{km}_{\text{UNCON}}$);

(d) a coarse-resolution simulation with parameterized eddies as described in Chapter 2, i.e. with an energetically and enstrophetically constrained down-gradient PV mixing parameterization ($50\text{km}_{\text{EECON}}$).

For simulations which do not employ any eddy parameterization (5km_{EXP} and $50\text{km}_{\text{NOPAR}}$) we perform a Reynolds average of the variables (as described in Equations 2.2 and 2.3) to separate the flow into mean/large-scale and eddy components, representing the large-scale slowly-evolving component of the flow and the small-scale fast-evolving component of the flow respectively. In $50\text{km}_{\text{EECON}}$, the mean/large-scale and eddy components are defined as the resolved field and the unresolved parameterized field respectively. The aim is that, in $50\text{km}_{\text{EECON}}$, the effect of the unresolved parameterized eddies on the resolved flow resembles the effect of the explicit eddies on the mean flow in the eddy-resolving simulation 5km_{EXP}, thus leading to a resolved flow in $50\text{km}_{\text{EECON}}$ which resembles the mean flow in 5km_{EXP}.

We compare $50\text{km}_{\text{EECON}}$ with $50\text{km}_{\text{UNCON}}$ to assess if the energetic and enstrophetic constraints imposed are successful in constraining the resolved flow. We use 5km_{EXP} as a reference to inform on realistic values for the resolved flow, thus allowing us to determine if the resolved flow in $50\text{km}_{\text{EECON}}$ is well-constrained by the parameterization. The details of these simulations are outlined in Table 3.1. In Section 4.3.3, we run many variations of $50\text{km}_{\text{EECON}}$ in which we systematically vary the input parameters to the parameterization.

3.2 Barotropic Model

In this section, we outline the model of barotropic, freely decaying turbulence in a doubly periodic domain which we employ to test the parameterization, as well as the

Configuration	Resolution	Eddies	μ_ξ (m^4s^{-1})	γ_q	r_Λ (s^{-1})	r_K (s^{-1})	μ (m^2s^{-1})	κ_{PV} (m^2s^{-1})
$5km_{EXP}$	5 km	Explicit	10^8	-	-	-	-	-
$50km_{NOPAR}$	50 km	Explicit	10^{11}	-	-	-	-	-
$50km_{UNCON}$	50 km	Parameterized	10^{11}	-	-	-	-	60
$50km_{EECON}$	50 km	Parameterized	10^{11}	0.1	$5. \times 10^{-8}$	0	500	-

Table 3.1: Parameters used in the simulations analysed in Sections 3.3 and 3.4.

parameterization implementation in the model. We begin with the model equations in Section 3.2.1, followed by the numerical implementation in Section 3.2.2. We then describe the kinetic energy and potential enstrophy pathways associated with the model and parameterization setup in Section 3.4.3. Finally, we specify the model setup for the configurations described above in Section 3.2.4.

3.2.1 Model Equations

We begin with the equations for barotropic (i.e. one vertical layer) freely decaying turbulence with a rigid lid over variable bottom topography. We restrict our attention to an f-plane, so that only the topography affects the background PV. The equations of motion are the depth-integrated PV equation, which, for simulations without any eddy parameterization is

$$\frac{\partial \xi}{\partial t} = -\nabla \cdot \zeta \mathbf{u} - \mu_\xi \nabla^4 \xi, \tag{3.1}$$

and for parameterized eddy simulations is

$$\frac{\partial \xi}{\partial t} = -\nabla \cdot \zeta \mathbf{u} - \nabla \cdot \overline{\zeta' \mathbf{u}'} - \mu_\xi \nabla^4 \xi, \tag{3.2}$$

and the continuity equation,

$$\nabla \cdot \mathrm{H}\mathbf{u} = 0, \tag{3.3}$$

where $\zeta = f + \xi$ is the absolute vorticity, and μ_ξ is the biharmonic diffusion coefficient. We employ biharmonic diffusion in Equations (3.1) and (3.2) for numerical stability.

In the eddy-resolving simulation, employing Equation 3.1, it is assumed that the resolved flow contains both a large-scale and an eddy component, and can be decomposed into these components by performing a Reynolds average. In simulations with

parameterized eddies, employing Equation 3.2, it is assumed that the resolved flow contains only a large-scale component, and that the effect of eddies on the large-scale flow must be parameterized by including the divergence of the eddy vorticity fluxes, $\nabla \cdot \overline{\zeta' \mathbf{u}'}$, in the governing vorticity equation. The eddy vorticity flux is replaced with the appropriate parameterization.

Defining a transport streamfunction from Equation 3.3 produces the following relationship

$$\xi = \nabla \cdot \left(\frac{\nabla \psi}{\mathrm{H}} \right). \tag{3.4}$$

Equation 3.4 allows us to solve for the flow field at each time-step.

3.2.2 Numerical Implementation

We now describe the numerical implementation of the governing equations (Equations 3.1 and 3.2) as well as the parameterized EKE and EPEnstr budgets.

3.2.2.1 Vorticity Equation

The variables are arranged according to an Arakawa C-grid as shown in Figure 3.1, with vorticities (f, ξ and q), stream function (ψ) and layer depth (H) defined at the cell vertices[1]. The zonal and meridional components of the velocity are calculated using a centred second-order differencing scheme. Advection of relative vorticity is calculated using an energy- and enstrophy-conserving scheme defined by Arakawa (1966). Biharmonic diffusion of vorticity is calculated using a centred differencing scheme. Time-stepping of Equations (3.1) and (3.2) is computed using the third order Adams-Bashforth method (Durran, 1991), with the first two time steps calculated using a first-order forward approximation.

[1] Styles et al. (2022) identified a number of spurious forces associated with the bathymetry which can dominate the vorticity budget when using an Arakawa C-grid with a z-coordinate representation of the sea floor. The majority of these spurious forces will not occur in the model setup described here, however, we note that spurious forces due to changes in cell thickness may be present.

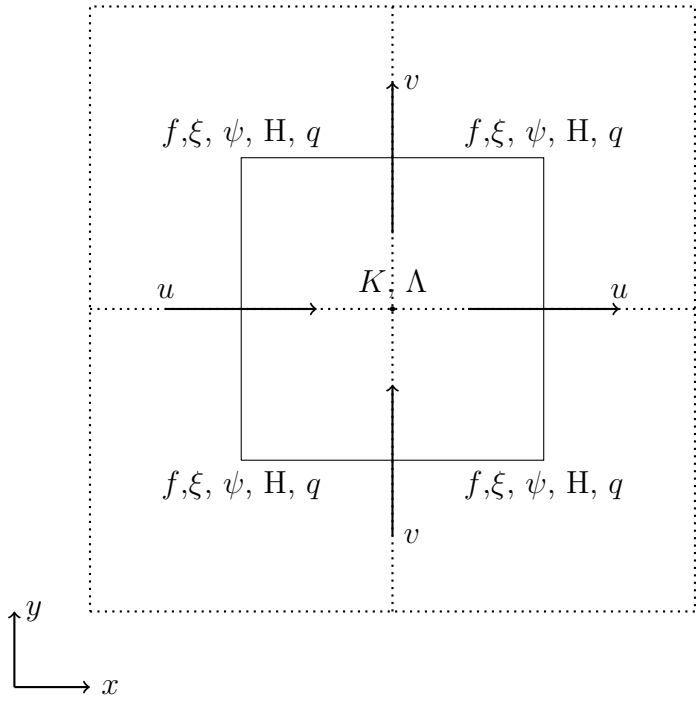

Figure 3.1: A single model grid box (solid line) and the discretization of variables in the model. Dotted lines indicate the area over which the eddy PV flux in the governing equation for parameterized simulations (Equations 3.2) are calculated, having vorticity at their centre.

3.2.2.2 EKE and EPEnstr Budgets

For simulations employing the parameterization described in Chapter 2, the parameterized EKE (K) and EPEnstr (Λ) are defined at the cell centre points (Figure 3.1). Time-stepping of the parameterized EKE and EPEnstr budgets (Equations 2.12 and 2.14) is computed using the third order Adams-Bashforth method (Durran, 1991), with the first two time steps calculated using a first-order forward approximation. Advective and diffusive terms are calculated in flux form over each model grid box (solid line in Figure 3.1). We set a minimum value of zero for K and Λ to ensure negative values are not generated. The divergence of the eddy vorticity fluxes is calculated in flux form over a grid box centred around the vorticity (dashed lines in Figure 3.1). The x and y components of the kinetic energy and potential enstrophy conversion terms are calculated at v and u points respectively (these points enable the computation of the divergence of the eddy vorticity in flux form described above). That is, $\overline{q'u'}(\partial\overline{\psi}/\partial x)$ and $\overline{q'u'}(\partial\overline{q}/\partial x)$ are calculate at v points and $\overline{q'v'}(\partial\overline{\psi}/\partial y)$ and $\overline{q'v'}(\partial\overline{q}/\partial y)$ are calculated at u points. These values are linearly interpolated to cell

centre points to calculate the kinetic energy conversion, $\overline{q'\mathbf{u}'} \cdot \nabla\overline{\psi}$, and the potential enstrophy conversion, $\overline{q'\mathbf{u}'} \cdot \nabla\overline{q}$. In the calculation of $\widehat{\nabla\overline{q}} = \nabla\overline{q}/|\nabla\overline{q}|$, a minimum value for $|\nabla\overline{q}|$ is specified to prevent division by a very small number, which we set at 10^{-16} $\mathrm{m^{-1}s^{-1}}$.

3.2.3 Kinetic Energy and Potential Enstrophy Pathways

In the analysis that follows, it is helpful to consider the kinetic energy and potential enstrophy pathways associated with the model described above, specifically for the eddy-resolving configuration ($5\mathrm{km_{EXP}}$) and for the energy- and enstrophy-constrained parameterized simulations ($50\mathrm{km_{EECON}}$). To describe these pathways, we consider the components of the volume-integrated mean kinetic energy (MKE), EKE, mean potential enstrophy (MPEnstr) and EPEnstr budgets for both $5\mathrm{km_{EXP}}$ and $50\mathrm{km_{EECON}}$. We now outline these budgets and provide a summary of the components and their associated kinetic energy and potential enstrophy pathways.

3.2.3.1 Kinetic Energy Budgets

Here, we derive the volume-integrated MKE budget, relevant to both $5\mathrm{km_{EXP}}$ and $50\mathrm{km_{EECON}}$, the EKE budget for $5\mathrm{km_{EXP}}$, and the parameterized EKE budget for $50\mathrm{km_{EECON}}$.

The volume-integrated MKE budget for both $5\mathrm{km_{EXP}}$ and $50\mathrm{km_{EECON}}$ (derived in Appendix C) is

$$\underbrace{\frac{d}{dt}\int\int_A \mathrm{H}\frac{\overline{\mathbf{u}}\cdot\overline{\mathbf{u}}}{2}\,dA}_{\substack{\text{rate of change}\\ \text{of MKE}}} = \underbrace{-\int\int_A \mathrm{H}\overline{q'\mathbf{u}'}\cdot\nabla\overline{\psi}\,dA}_{\substack{\text{kinetic energy}\\ \text{conversion}}} + \underbrace{\int\int_A \mu_\xi\overline{\psi}\nabla^4\mathrm{H}\overline{q}\,dA}_{\substack{\text{MKE extracted}\\ \text{via biharmonic}\\ \text{diffusion}}}, \tag{3.5}$$

where A is the domain area. The first term on the right hand side of Equation 3.5 represents kinetic energy conversion between the mean and eddy fields[2]. The second

[2]For $50\mathrm{km_{EECON}}$, this term is evaluated using the parameterized eddy PV fluxes (Equation 2.9). This is also true for the subsequent equations in this section relevant to $50\mathrm{km_{EECON}}$, specifically, the kinetic energy conversion term in the parameterized EKE budget (Equation 3.7), and the potential enstrophy conversion term in the MPEnstr budget (Equation 3.8) and the parameterized EPEnstr budget (Equation 3.10). We retain the eddy PV flux notation for clarity when comparing $5\mathrm{km_{EXP}}$ and $50\mathrm{km_{EECON}}$.

term represents MKE extracted by biharmonic diffusion. It should be noted that this term is not a guaranteed sink of MKE. In fact, locally this term can extract or inject MKE. However, we find that, in the domain integral, this term is a sink of MKE and thus we refer to it as an extraction of MKE.

To obtain the volume-integrated EKE budget for 5km_{EXP}, we integrate the depth-integrated EKE equation (Equation 2.11) over the domain area, noting that integrals of divergent terms are zero since we are in a doubly periodic domain. This yields

$$\underbrace{\frac{d}{dt}\int\int_A \mathrm{H}\frac{\overline{\mathbf{u}'\cdot\mathbf{u}'}}{2}\,dA}_{\substack{\text{rate of change}\\ \text{of EKE}}} = \underbrace{\int\int_A \mathrm{H}\overline{q'\mathbf{u}'}\cdot\nabla\overline{\psi}\,dA}_{\substack{\text{kinetic energy}\\ \text{conversion}}} + \underbrace{\int\int_A \mathrm{H}\mathbf{F}_{\text{EKE}}\,dA}_{\substack{\text{effect of any}\\ \text{EKE forcing}}}. \tag{3.6}$$

The first term on the right hand side of equation 3.6 represents kinetic energy conversion between the mean and eddy components. The second term represents the effect of any forcing terms on the EKE budget. This includes only the effect of biharmonic diffusion on the EKE, which, in the domain integral, acts to extract EKE.

To obtain the volume-integrated EKE budget for $50\text{km}_{\text{EECON}}$, we integrate the parameterized EKE budget (Equation 2.12) over the domain volume, noting that divergence terms integrate to zero since we are in a doubly periodic domain. This yields

$$\underbrace{\frac{d}{dt}\int\int_A \mathrm{H}K\,dA}_{\substack{\text{rate of change of}\\ \text{parameterized EKE}}} = \underbrace{\int\int_A \mathrm{H}\overline{q'\mathbf{u}'}\cdot\nabla\overline{\psi}\,dA}_{\substack{\text{kinetic energy}\\ \text{conversion}}} - \underbrace{\int\int_A \mathrm{H}r_K K\,dA}_{\substack{\text{parameterized}\\ \text{EKE damping}}}. \tag{3.7}$$

The first term on the right hand side of Equation 3.7 represents parameterized kinetic energy conversion between the mean and parameterized eddy components. The second term represents dissipation of parameterized EKE.

The kinetic energy pathways associated with the components of the kinetic energy budgets for 5km_{EXP} and $50\text{km}_{\text{EECON}}$ are summarised schematically (in the style of Chen et al. (2014)) in Figures 3.2 and 3.3 respectively. In 5km_{EXP}, kinetic energy is converted bidirectionally between the mean and eddy components by the explicit barotropic eddies, and both MKE and EKE are extracted by biharmonic diffusion. In

$50\text{km}_{\text{EECON}}$, kinetic energy is converted bidirectionally between the mean and parameterized eddy components by the parameterized barotropic eddies, MKE is extracted by biharmonic diffusion, and parameterized EKE is extracted by the linear damping term in the parameterized EKE budget.

3.2.3.2 Potential Enstrophy Budgets

Here, we derive the volume-integrated MPEnstr budget, relevant to both 5km_{EXP} and $50\text{km}_{\text{EECON}}$, the EPEnstr budget for 5km_{EXP}, and the parameterized EPEnstr budget for $50\text{km}_{\text{EECON}}$.

The volume-integrated MPEnstr budget for both 5km_{EXP} and $50\text{km}_{\text{EECON}}$ (derived in Appendix D) is

$$\underbrace{\frac{d}{dt}\int\int_A \mathrm{H}\frac{\overline{q}\,\overline{q}}{2}\,dA}_{\substack{\text{rate of change}\\ \text{of MPEnstr}}} = \underbrace{\int\int_A \mathrm{H}\overline{q'\mathbf{u}'}\cdot\nabla\overline{q}\,dA}_{\substack{\text{potential enstrophy}\\ \text{conversion}}} - \underbrace{\int\int_A \overline{q}\mu_\xi\nabla^4\mathrm{H}\overline{q}\,dA}_{\substack{\text{MPEnstr input}\\ \text{via biharmonic}\\ \text{diffusion}}}. \tag{3.8}$$

The first term on the right hand side of Equation 3.8 represents potential enstrophy conversion between the mean and eddy components. The second term represents an input of MPEnstr by biharmonic diffusion. It should be noted that locally this term can input or extract MPEnstr. However, in the domain integral, this term represents an input of MPEnstr[3] and thus we refer to it as an input.

To obtain the volume-integrated EPEnstr budget for 5km_{EXP}, we integrate the depth-integrated EPEnstr equation (Equation 2.13) over the domain area, noting that integrals of divergent terms are zero since we are in a doubly periodic domain. This yields

$$\underbrace{\frac{d}{dt}\int\int_A \mathrm{H}\frac{\overline{q'^2}}{2}\,dA}_{\substack{\text{rate of change}\\ \text{of EPEnstr}}} = \underbrace{-\int\int_A \mathrm{H}\overline{q'\mathbf{u}'}\cdot\nabla\overline{q}\,dA}_{\substack{\text{potential enstrophy}\\ \text{conversion}}} + \underbrace{\int\int_A \mathrm{H}\mathbf{F}_\Lambda\,dA}_{\substack{\text{effect of any}\\ \text{EPEnstr forcing}}}. \tag{3.9}$$

The first term on the right hand side of Equation 3.9 represents potential enstrophy conversion between the mean and eddy components. The second term represents the effect of any forcing terms on the EPEnstr budget. For 5km_{EXP}, this term includes

[3] It may seem counter intuitive that biharmonic diffusion acts as a source of MPEnstr. We will demonstrate that this is the case in Section 3.4.

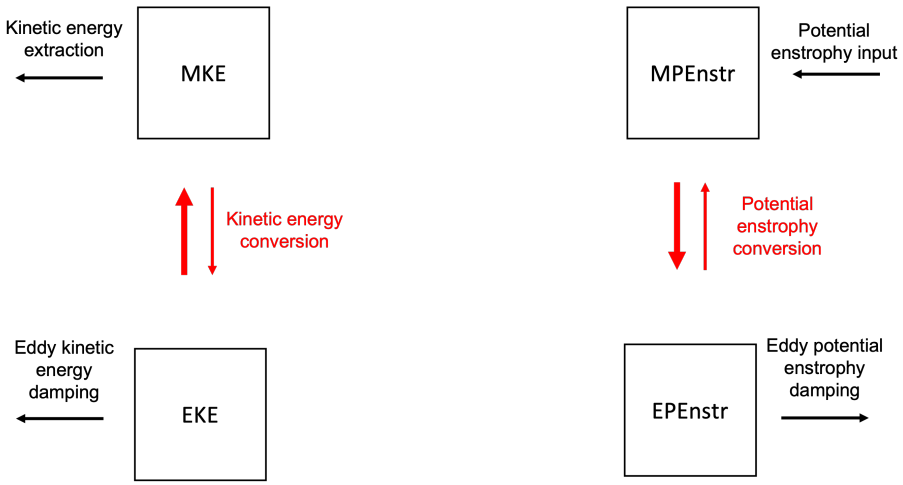

Figure 3.2: Kinetic energy (left) and potential enstrophy (right) pathways associated with the eddy-resolving simulation, 5km_{EXP}. Black arrows and labels indicate pathways associated with biharmonic diffusion. Red arrows and labels indicate pathways associated with the explicit barotropic eddies. In the case where there are two arrows, the dominant direction of transfer, as predicted by quasigeostrophic theory, is indicated by the bold arrow.

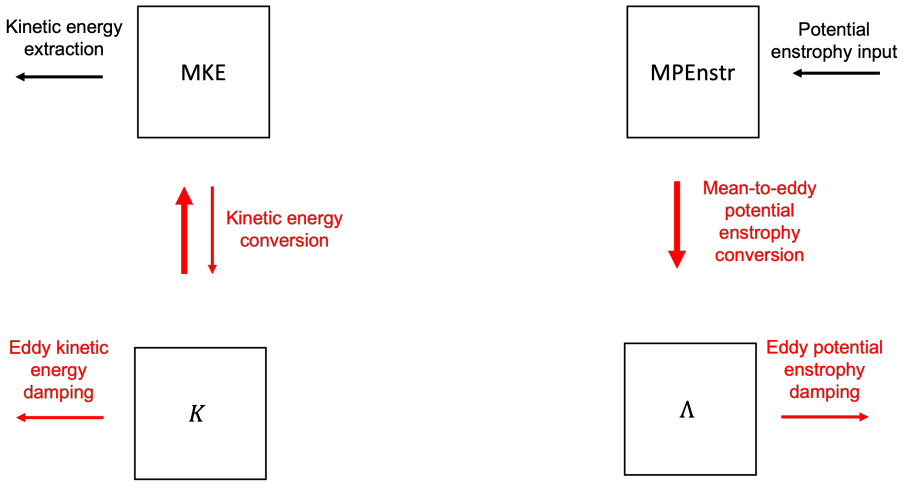

Figure 3.3: Kinetic energy (left) and potential enstrophy (right) pathways associated with the simulation employing the energetically and enstrophetically constrained parameterization, $50\text{km}_{\text{EECON}}$. Black arrows and labels indicate pathways associated with biharmonic diffusion. Red arrows and labels indicate pathways associated with the parameterized barotropic eddies. In the case where there are two arrows, the dominant direction of transfer, as predicted by quasigeostrophic theory, is indicated by the bold arrow.

only the effect of biharmonic diffusion, which acts to extract EPEnstr from the eddy field in the domain integral.

To obtain the volume-integrated EPEnstr budget for $50\text{km}_{\text{EECON}}$, we integrate the parameterized EPEnstr budget (Equation 2.14) over the domain volume, noting that divergence terms integrate to zero since we are in a doubly periodic domain. This yields

$$\underbrace{\frac{d}{dt}\int\int_A \Lambda \, dA}_{\substack{\text{rate of change} \\ \text{of parameterized} \\ \text{EPEnstr}}} = \underbrace{-\int\int_A \mathrm{H}\overline{q'\mathbf{u}'} \cdot \nabla\overline{q} \, dA}_{\substack{\text{mean-to-eddy} \\ \text{potential enstrophy} \\ \text{conversion}}} - \underbrace{\int\int_A \mathrm{H} r_\Lambda \Lambda \, dA}_{\substack{\text{parameterized} \\ \text{EPEnstr damping}}}. \tag{3.10}$$

The first term on the right hand side of Equation 3.10 represents parameterized potential enstrophy conversion between the mean and parameterized eddy components, which, due to the formulation of the parameterization, acts only to convert potential enstrophy from the mean component to the parameterized eddy component. The second term represents dissipation of parameterized EPEnstr.

The potential enstrophy pathways associated with the components of the potential enstrophy budgets for 5km_{EXP} and $50\text{km}_{\text{EECON}}$ are summarised schematically in Figures 3.2 and 3.3 respectively. In 5km_{EXP}, MPEnstr is input by biharmonic diffusion, potential enstrophy is converted bidirectionally between the mean and eddy components by the explicit barotropic eddies, and EPEnstr is extracted by biharmonic diffusion. In $50\text{km}_{\text{EECON}}$, MPEnstr is input by biharmonic diffusion, potential enstrophy is converted from the mean component to the parameterized eddy component by the parameterized barotropic eddies, and EPEnstr is extracted by the linear damping term in the parameterized EPEnstr budget.

3.2.4 Specification of Model Setup

Having described the numerics of the model, we now outline the model configuration used for the analysis in Sections 3.3 and 3.4.

3.2.4.1 Domain Geometry

All simulations are run in a periodic square domain of side length $L = 1000$ km with non-flat topography. The topography is created by using a seeded pseudorandom

number generator (NumPy `random.default_rng`) to generate independent Fourier modes at 5 km horizontal resolution. This is achieved by generating complex Fourier coefficients, A_k, for all wavenumbers k, where $k = \sqrt{k_x^2 + k_y^2}$ with k_x and k_y the wavenumbers in the x and y direction, respectively, such that

$$A_{k_x,k_y} = k_{\#}(Z_0 + iZ_1), \tag{3.11}$$

with $A_{0,k_y} = A_{k_x,0} = 0$ and where Z_0 and Z_1 are realisations of independent standard Gaussian random variables, i is the imaginary unit, and $k_{\#}$ is calculated using

$$k_{\#} = \left(k^{-1} + \left(1 + \frac{k}{k_{\text{peak}}} \right)^4 \right)^{-\frac{1}{2}}, \tag{3.12}$$

and k_{peak} is specified to set the scale of the variations[4]. For the generation of large-scale topography, we set $k_{\text{peak}} = 1$. The field generated by the Fourier modes is then multiplied by a constant and translated in depth in order to produce a topography with average depth of 5 km and depth variations of around 10%. The topography is regridded using spatial averaging to 50 km resolution for the coarse-resolution simulations. The topographic structures used are shown in Figure 3.4.

3.2.4.2 Model Parameters

The Coriolis parameter is taken as a constant with value $f = 0.7 \times 10^{-4}$ s^{-1} in all simulations. The biharmonic diffusion coefficient, μ_ξ, is set to 10^8 m^4 s^{-1} for simulations at 5 km resolution and 10^{11} m^4 s^{-1} for simulations at 50 km resolution. These values are chosen to be as small as possible such that grid scale noise is no longer generated and give an eddy diffusive timescale on the order of months. All simulations are run for a total of 3000 days in order to reach a point at which the eddy-to-mean kinetic energy conversion has plateaued. The value of parameters to be used in the parameterized simulations is diagnosed from the eddy-resolving simulation in Section 3.3.

[4]The code for generating pseudorandom fields was provided by, and used with permission from, Dr. Martin Brolly.

3.2.4.3 Initial Conditions

Simulations which do not employ any eddy parameterization (5km_{EXP} and $50\text{km}_{\text{NOPAR}}$) are initialised with a stream function which is generated at 5 km resolution using the same method as the topography with $k_{\text{peak}} = 5$ (using a different seed) and multiplied by a constant to produce velocities on the order of $1 - 10$ cm s^{-1}. This is regridded using volume averaging to 50 km resolution for coarse-resolution simulations which do not employ any eddy parameterization, i.e. $50\text{km}_{\text{NOPAR}}$. The initial stream functions are plotted in Figure 3.5. In 5km_{EXP} and $50\text{km}_{\text{NOPAR}}$, it is assumed that the turbulent cascades of kinetic energy and potential enstrophy, and hence the explicit eddies, are driving the large-scale flow. This effect is expected to be small in $50\text{km}_{\text{NOPAR}}$ due to the coarse resolution and we use the results of this simulation to identify the unresolved eddy effects. Simulations with parameterized eddies ($50\text{km}_{\text{EECON}}$ and $50\text{km}_{\text{UNCON}}$) are run with no initial stream function and, instead, the parameterized eddies drive the flow.

The initial streamfunction employed here corresponds to a low-initial-energy state in the classification defined in Siegelman and Young (2023), in which low-initial-energy and high-initial-energy states are defined as being below or above the energy of a PV-homogenized state respectively. The flow field for a PV homogenized state in the setup employed here has values of ψ in the range -575 Sv to 314 Sv. This is significantly stronger than the Antarctic Circumpolar Current, the world's strongest ocean current, which recent measurements estimate to be 173 Sv in the Drake Passage (Donohue et al., 2016). Thus, we deem high-initial-energy states to be unnecessarily unrealistic for the testing purposes presented here, and restrict our attention to low-initial-energy states.

3.3 Explicit Eddy Simulations

Thus far, we have outlined the methods employed in the numerical simulations. Here, we analyse the results of the simulations which do not employ any eddy parameterization (5km_{EXP} and $50\text{km}_{\text{NOPAR}}$) in order to specify the unresolved eddy effects in $50\text{km}_{\text{NOPAR}}$ and hence identify what is required of the parameterization in this setup. We also diagnose the input parameters for the parameterized simulation ($50\text{km}_{\text{EECON}}$) from the results of the eddy-resolving simulation (5km_{EXP}).

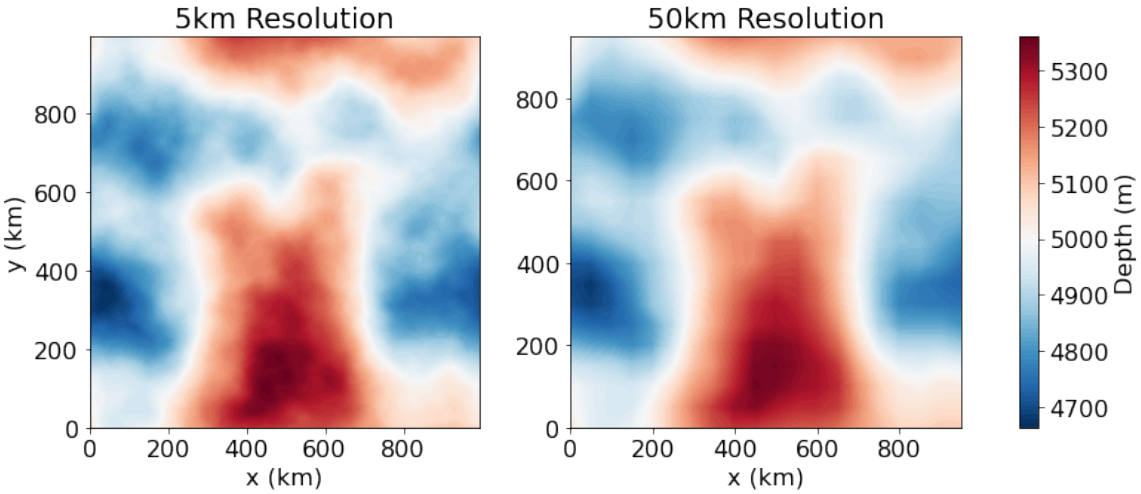

Figure 3.4: Topography used in simulations at 5 km horizontal resolution (left, namely $5km_{EXP}$) and at 50 km horizontal resolution (right, namely $50km_{NOPAR}$, $50km_{EECON}$ and $50km_{UNCON}$).

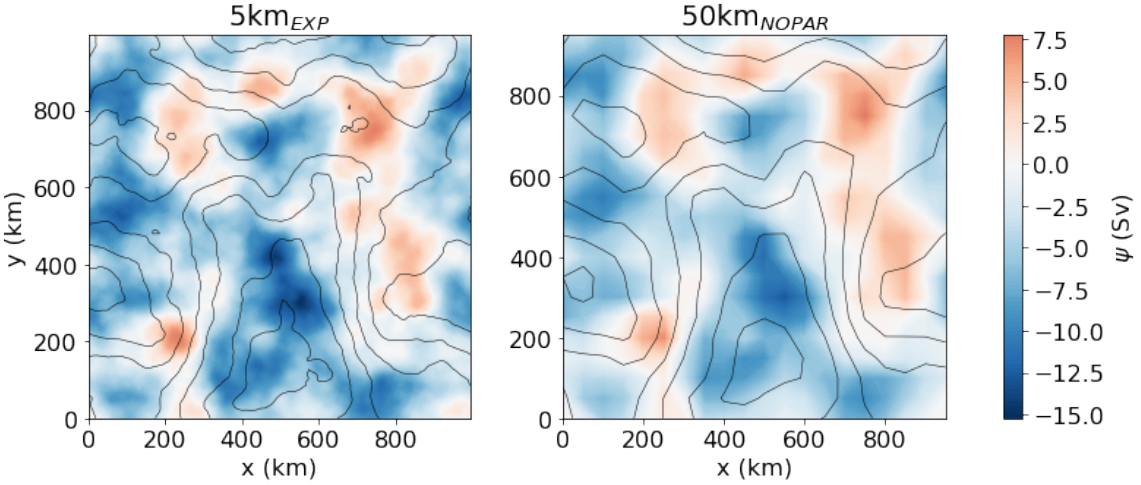

Figure 3.5: Initial stream function (filled contours) used in simulations which do not employ any eddy parameterization at 5 km resolution (left, namely $5km_{EXP}$) and 50 km resolution (right, namely $50km_{NOPAR}$). Black lines indicate topography contours.

3.3.1 Identifying the Unresolved Eddy Effects

We compare properties of the large-scale and eddy components of the flow in the eddy-resolving and coarse-resolution simulations, 5km_{EXP} and $50\text{km}_{\text{NOPAR}}$ respectively, to identify the unresolved eddy-driven effects on the large-scale flow in the coarse resolution simulation. Throughout the rest of this thesis, for simulations which do not employ any eddy parameterization (i.e. 5km_{EXP} and $50\text{km}_{\text{NOPAR}}$), the MKE is defined as $\overline{\mathbf{u}} \cdot \overline{\mathbf{u}}/2$, and MPEnstr is defined as $\overline{q}\ \overline{q}/2$ where overbars represent a time mean. The EKE is defined as $\overline{\mathbf{u}' \cdot \mathbf{u}'}/2$ and the EPEnstr is defined as $\overline{q'q'}/2$. Volume-averaged quantities are analysed and moving-window time means are taken every 50 days over a 500 day period.

We first identify the effects of the eddies on the energetics which are unresolved in the coarse-resolution simulation and hence need to be parameterized. In 5km_{EXP}, energy is converted from eddy to mean as the simulation progresses, indicated by the simultaneous decrease in EKE and increase in MKE (Figures 3.6b and 3.6a, respectively). In contrast, for $50\text{km}_{\text{NOPAR}}$, the EKE decreases throughout the simulation but the MKE does not increase. This is further illustrated by the eddy-to-mean kinetic energy conversion rate which is large and positive throughout the majority of the simulation in 5km_{EXP} and near-zero throughout the majority of the simulation in $50\text{km}_{\text{NOPAR}}$ (Figure 3.6e). Hence, there is no significant conversion of kinetic energy from eddy to mean in $50\text{km}_{\text{NOPAR}}$. The decrease in EKE in this case is due to damping from the biharmonic dissipation term. We aim to parameterize the effects of this unresolved conversion on the large-scale flow i.e. to parameterize a source of large-scale kinetic energy that mimics the effects of the eddy-to-mean kinetic energy conversion present in the eddy-resolving configuration.

We next identify the effects of the eddies on the enstrophetics which are unresolved in the coarse-resolution simulation and hence need to be parameterized. In 5km_{EXP} the mean-to-eddy potential enstrophy conversion rate is positive throughout the simulation (Figure 3.6f). That is, the eddy PV fluxes are, on average, fluxing PV down the mean PV gradient, thus producing a conversion of potential enstrophy from mean to eddy and a direct potential enstrophy cascade. As a result, the MPEnstr decays for the duration of the simulation (Figure 3.6c). The EPEnstr also decays throughout the simulation due to dissipation of potential enstrophy at small scales (Figure 3.6d). In $50\text{km}_{\text{NOPAR}}$, both the potential enstrophy conversion term and the EPEnstr are small in comparison to 5km_{EXP} (Figures 3.6f and 3.6d, respectively). Additionally,

the MPEnstr increases throughout the simulation as a result of biharmonic diffusion (Figure 3.6c). Thus, we require the parameterization to increase the magnitude of the mean-to-eddy potential enstrophy conversion, so as to decrease the MPEnstr.

3.3.2 Diagnosing the Input Parameters for the Parameterization

Having identified the effect of the unresolved eddies which must be parameterized, we now seek to determine appropriate values for the input parameters of the parameterization, namely: γ_q, the PV flux efficiency parameter; r_Λ, the EPEnstr damping parameter; r_K, the EKE damping parameter; and μ, the EKE and EPEnstr diffusion coefficient. We must also specify K_0 and Λ_0, the initial values for parameterized EKE and EPEnstr, respectively.

3.3.2.1 The PV Flux Efficiency Parameter, γ_q

Figure 3.7a shows a scatter of the magnitude of the eddy PV fluxes, $|\overline{q'\mathbf{u}'}|$, against their upper bound value, $2\sqrt{\Lambda K}$ for all grid points in 5km_{EXP}. This analysis shows that the bound in Equation 2.5 is indeed satisfied by all points in the domain. The line of best fit for the points, the gradient of which represents the average value of γ_q, has value 0.17 (blue line). Although there is some spatial pattern in γ_q in 5km_{EXP} (Figure 3.7b), as a first attempt we specify a constant value for γ_q which we set to 0.1.

3.3.2.2 The EPEnstr Damping Parameter, r_Λ

To calculate the volume-averaged value of the EPEnstr damping parameter, we take the volume-integrated EPEnstr budget for 5km_{EXP} (Equation 3.9) and assume that the term representing extraction of EPEnstr has a linear relationship with the EPEnstr. That is, we assume

$$\frac{\partial \Lambda}{\partial t} = -\overline{q'\mathbf{u}'} \cdot \nabla \overline{q} - r_\Lambda \Lambda, \tag{3.13}$$

where all terms are now the volume-averaged terms. Now, integrating with time we find that

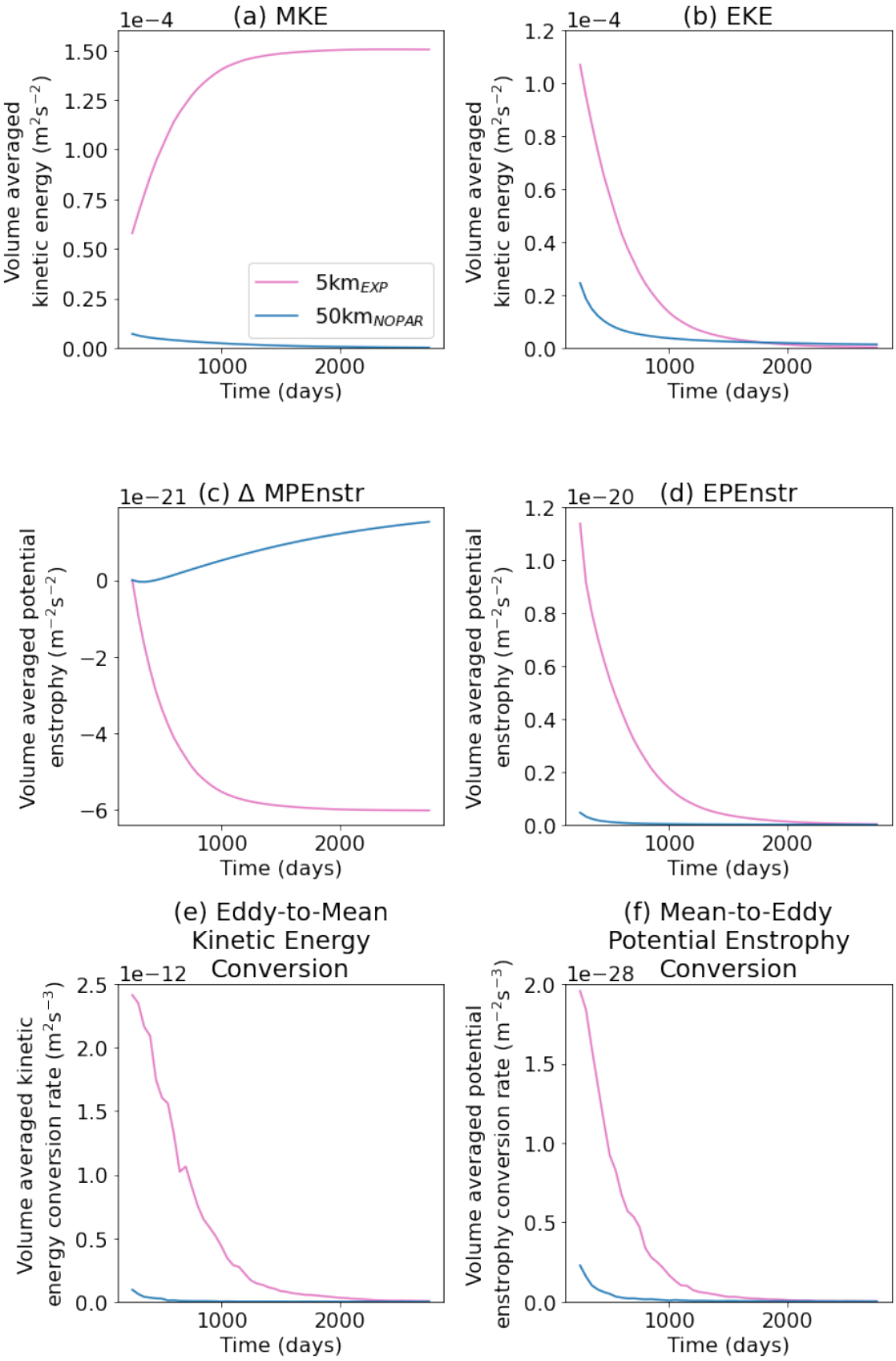

Figure 3.6: Volume-averaged (a) MKE; (b) EKE; (c) change in MPEnstr from initial value; (d) EPEnstr; (e) eddy-to-mean kinetic energy conversion, $-\overline{q'\mathbf{u}'} \cdot \nabla\psi$; and (f) mean-to-eddy potential enstrophy conversion, $-\overline{q'\mathbf{u}'} \cdot \nabla\overline{q}$, for 5km_{EXP} (pink) and $50\text{km}_{\text{NOPAR}}$ (blue). Moving-window time-means are calculated every 50 days over a 500-day period.

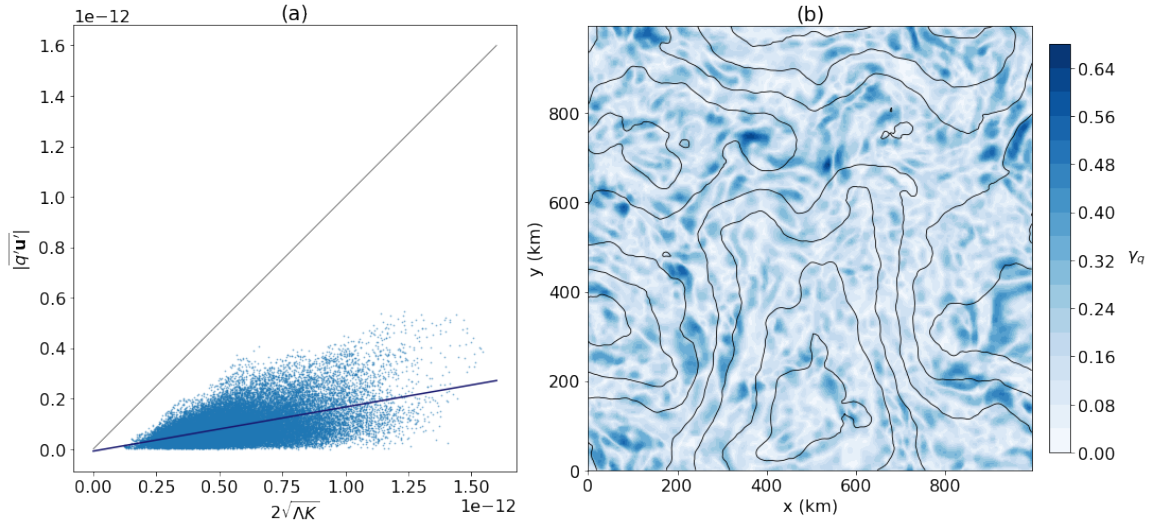

Figure 3.7: (a) Scatter plot of the magnitude of the time-mean eddy PV fluxes, $|\overline{q'\mathbf{u}'}|$, against their upper bound value, $2\sqrt{\Lambda K}$ for all grid points in 5km_{EXP}. The black line indicates values where $|\overline{q'\mathbf{u}'}| = 2\sqrt{\Lambda K}$ and hence the region to the right of the black line indicates values where $|\overline{q'\mathbf{u}'}| \leq 2\sqrt{\Lambda K}$. The blue line indicates the line of best for the points and has slope 0.17. Means are taken over the entire 3000 day simulation period and each point represents a grid-point in the simulation. (b) Spatial plot of the PV flux efficiency, γ_q, for 5km_{EXP} (filled contours) calculated using time-mean values over the entire 3000 day simulation period. Black lines indicate topography contours.

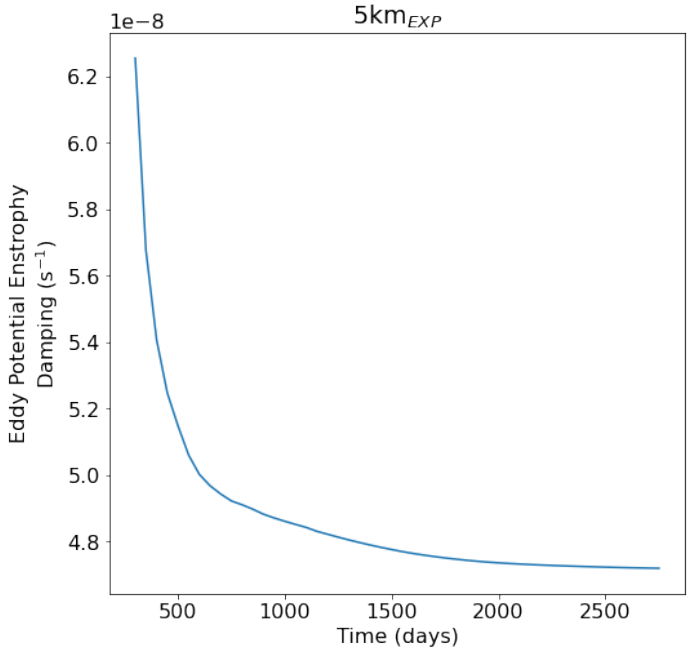

Figure 3.8: The estimated linear EPEnstr damping parameter, r_Λ, for 5km$_{\text{EXP}}$, calculated from time-means taken every 50 days over a 500 day period.

$$\Lambda(T) - \Lambda(0) = -\int_0^T \overline{q'\mathbf{u}'} \cdot \nabla\overline{q}\ dt - \int_0^T r_\Lambda \Lambda\ dt. \tag{3.14}$$

Assuming r_Λ is constant, we find that

$$r_\Lambda \sum_{t=0}^{t=T} \Lambda(t)\Delta t = \Lambda(0) - \Lambda(T) - \int_0^T \overline{q'\mathbf{u}'} \cdot \nabla\overline{q}\ dt. \tag{3.15}$$

Equation 3.15 is used to estimate the volume-averaged EPEnstr linear damping parameter for 5km$_{\text{EXP}}$ and the results are plotted in Figure 3.8. Initially, r_Λ is larger and decays as the simulation progresses. For simplicity in our setup, we choose to use a constant value for r_Λ, which we set as the mean value of that of 5km$_{\text{EXP}}$, i.e. $5. \times 10^8$ s^{-1}.

3.3.2.3 The EKE Damping Parameter, r_K

To replicate the conditions of freely decaying turbulence in 5km$_{\text{EXP}}$, we set $r_K = 0$ s^{-1}.

3.3.2.4 The EKE and EPEnstr Diffusivity, μ

We set the EKE and EPEnstr diffusivity, μ, to 500 $\mathrm{m^2 s^{-1}}$ to give a diffusive timescale on the order of months, consistent with that used for the biharmonic dissipation operator.

3.3.2.5 Initial Parameterized EKE and EPEnstr

The initial distributions of the parameterize EKE, K, and the parameterized EPEnstr, Λ, must be specified. For simplicity, we use constant values K_0 and Λ_0 respectively. We specify K_0 such that the volume-integrated initial parameterized EKE in $50\mathrm{km}_{\mathrm{EECON}}$ is the same as the volume-integrated initial kinetic energy of $5\mathrm{km}_{\mathrm{EXP}}$, resulting in $K_0 = 1.8 \times 10^{-4}$ $\mathrm{m^2 s^{-2}}$. Λ_0 is set to a similar value to the first time-mean volume-averaged value of Λ in $5\mathrm{km}_{\mathrm{EXP}}$, resulting in $\Lambda_0 = 10^{-20}$ $\mathrm{m^{-2} s^{-2}}$.

3.3.2.6 PV Diffusivity, κ_{PV}, for the Unconstrained Parameterized Simulation, $50\mathrm{km}_{\mathrm{UNCON}}$

For the coarse resolution simulation with unconstrained eddy PV fluxes, $50\mathrm{km}_{\mathrm{UNCON}}$, a constant value of κ_{PV} must be specified. We set this to the average of the non-zero values of κ_{PV} in simulation $50\mathrm{km}_{\mathrm{EECON}}$ which is 60 $\mathrm{m^2 s^{-1}}$.

3.4 Parameterized Eddy Simulations

Having determined the input parameters and initial conditions for the parameterized simulations ($50\mathrm{km}_{\mathrm{EECON}}$ and $50\mathrm{km}_{\mathrm{UNCON}}$) we now analyse the results of these simulations, focusing on the four key questions outlined in Section 3.2. In these simulations, the MKE is defined as the instantaneous resolved kinetic energy, i.e. $\mathbf{u} \cdot \mathbf{u}/2$; and the MPEnstr is defined as the instantaneous resolved potential enstrophy, i.e. $q\ q/2$. For $50\mathrm{km}_{\mathrm{EECON}}$, the EKE and EPEnstr are the parameterized values, i.e. K and Λ respectively. We compare the instantaneous values in the parameterized simulations with the time-mean values in the eddy-resolving simulation since we want to determine how well the parameterization simulates the large-scale flow.

3.4.1 Topography-Following Flow

The parameterization produces a net eddy-to-mean kinetic energy conversion (Figure 3.9e) resulting in a decrease in parameterized EKE (Figure 3.9b) and an increase in MKE (Figure 3.9a) in $50\text{km}_{\text{EECON}}$. Thus, an emergent inverse cascade of kinetic energy is produced. As a result of this parameterized eddy-to-mean kinetic energy conversion, a large-scale topography-following flow is produced (Figure 3.10).

3.4.2 Time Series of Kinetic Energy and Potential Enstrophy

We now consider the effects of the parameterization on the energetics and enstrophetics. The peak magnitude of MKE is 1.5×10^{-4} m^{2}s^{-2} in both 5km_{EXP} and $50\text{km}_{\text{EECON}}$. In contrast, the MKE in $50\text{km}_{\text{UNCON}}$ increases throughout the simulation, reaching a peak magnitude of 9.9×10^{-3} m^{2}s^{-2}, over 60 times greater than the maximum MKE of 5km_{EXP}. This suggests that the kinetic energy of the resolved flow in $50\text{km}_{\text{EECON}}$ is indeed well-constrained by the energetic and enstrophetic constraints imposed in the parameterization. This is further illustrated by the magnitude of the transport streamfunction (Figures 3.10 and 3.11) which peaks at a value of 24.9 Sv, 18.9 Sv and 202.2 Sv in 5km_{EXP}, $50\text{km}_{\text{EECON}}$ and $50\text{km}_{\text{UNCON}}$, respectively. Thus, the peak magnitude of the transport stream function in $50\text{km}_{\text{UNCON}}$ is over 700% larger than that of 5km_{EXP}, while in $50\text{km}_{\text{EECON}}$ it is 76% of that of 5km_{EXP}.

The behaviour of the MPEnstr is also improved by introducing the energetic and enstrophetic constraints. The mean-to-eddy potential enstrophy conversion in $50\text{km}_{\text{EECON}}$ is positive and non-zero initially (Figure 3.9f), resulting in a decrease in the MPEnstr (Figure 3.9c) and an increase in the parameterized EPEnstr as required (Figure 3.9d). The maximum absolute change in MPEnstr for 5km_{EXP}, $50\text{km}_{\text{EECON}}$ and $50\text{km}_{\text{UNCON}}$ is $6.\times10^{-21}$ m^{-2}s^{-2}, 1.2×10^{-20} m^{-2}s^{-2} and 6.7×10^{-20} m^{-2}s^{-2}, respectively. Thus, the maximum absolute change in MPEnstr in $50\text{km}_{\text{UNCON}}$ is more than 11 times that of 5km_{EXP}, while in $50\text{km}_{\text{EECON}}$ it is twice that of 5km_{EXP}. Physically, the MPEnstr in $50\text{km}_{\text{EECON}}$ decreases initially as the eddies mix PV (resulting in a positive mean-to-eddy potential enstrophy conversion) and increases when the parameterized eddies stop mixing PV and biharmonic diffusion dominates[5]. In contrast, the MPEnstr in

[5]Here, we can see why biharmonic diffusion inputs MPEnstr. If we consider barotropic freely decaying turbulence in which there is no mean flow initially, the eddies will act to mix PV on average, converting potential enstrophy from the mean component to the eddy component in the process, thus reducing the MPEnstr. If biharmonic diffusion acts to bring the system to a state of no flow (i.e. the mean flow has returned to it's original state) the MPEnstr must be returned to its initial

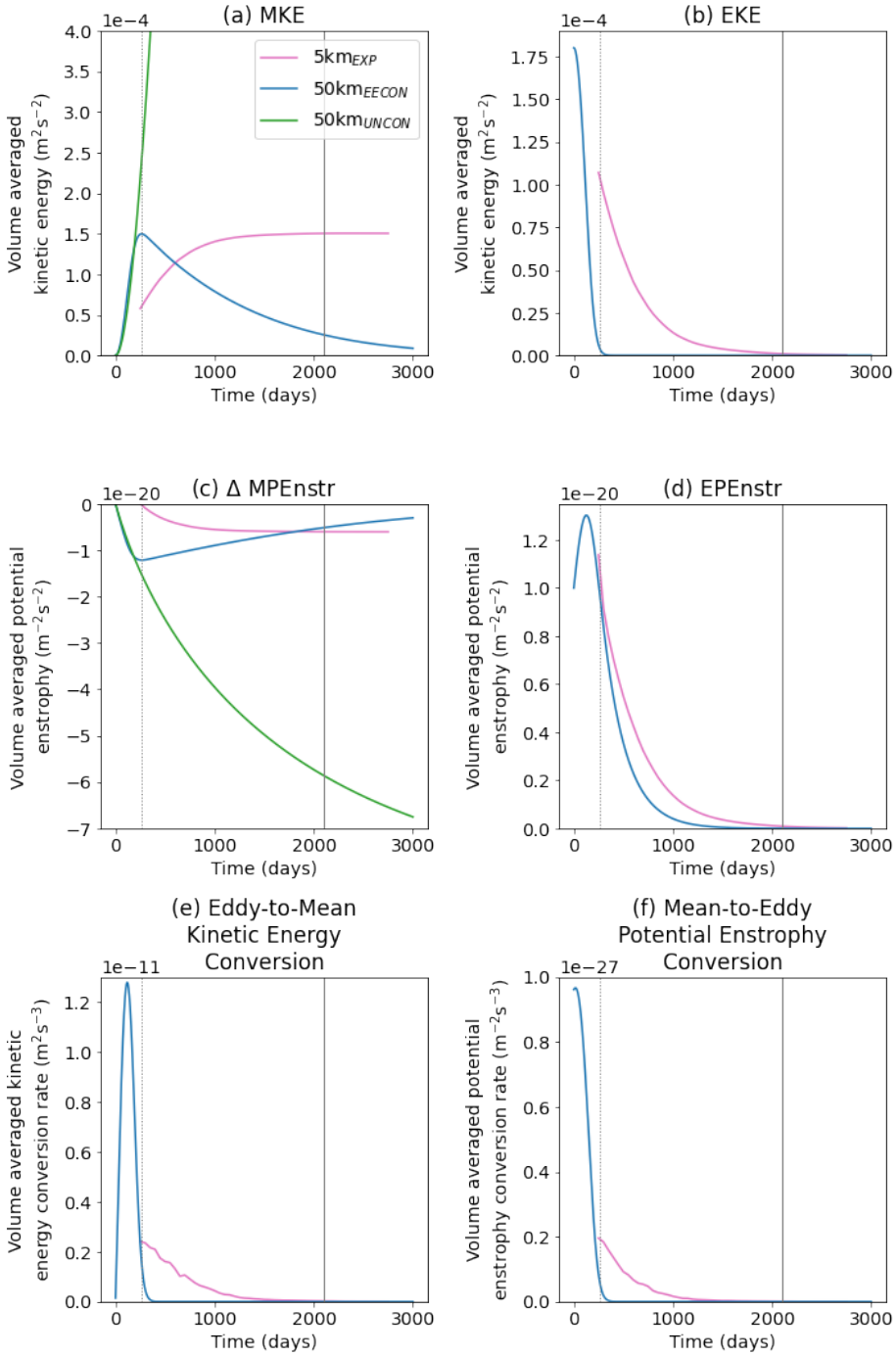

Figure 3.9: Volume-averaged (a) MKE; (b) EKE; (c) change in MPEnstr from initial value; (d) EPEnstr; (e) eddy-to-mean kinetic energy conversion, $-\overline{q'\mathbf{u}'} \cdot \nabla\psi$; and (f) mean-to-eddy potential enstrophy conversion, $-\overline{q'\mathbf{u}'} \cdot \nabla\overline{q}$, for 5km$_{\text{EXP}}$ (pink), 50km$_{\text{EECON}}$ (blue) and 50km$_{\text{UNCON}}$ (green). For 5km$_{\text{EXP}}$, values shown are moving-window time-means calculated every 50 days over a 500-day period. For 50km$_{\text{EECON}}$ and 50km$_{\text{UNCON}}$, values shown are instantaneous values. Note that data for 50km$_{\text{UNCON}}$ is not plotted in panels (b), (d), (e) and (f) since there is no parameterized EKE or EPEnstr budget in this simulation and these terms are therefore not well-defined. Vertical lines represent the time of maximum MKE for 5km$_{\text{EXP}}$ (solid) and 50km$_{\text{EECON}}$ (dotted) which are 2100 days and 263 days respectively, and are used to define integration periods in Section 3.4.3.

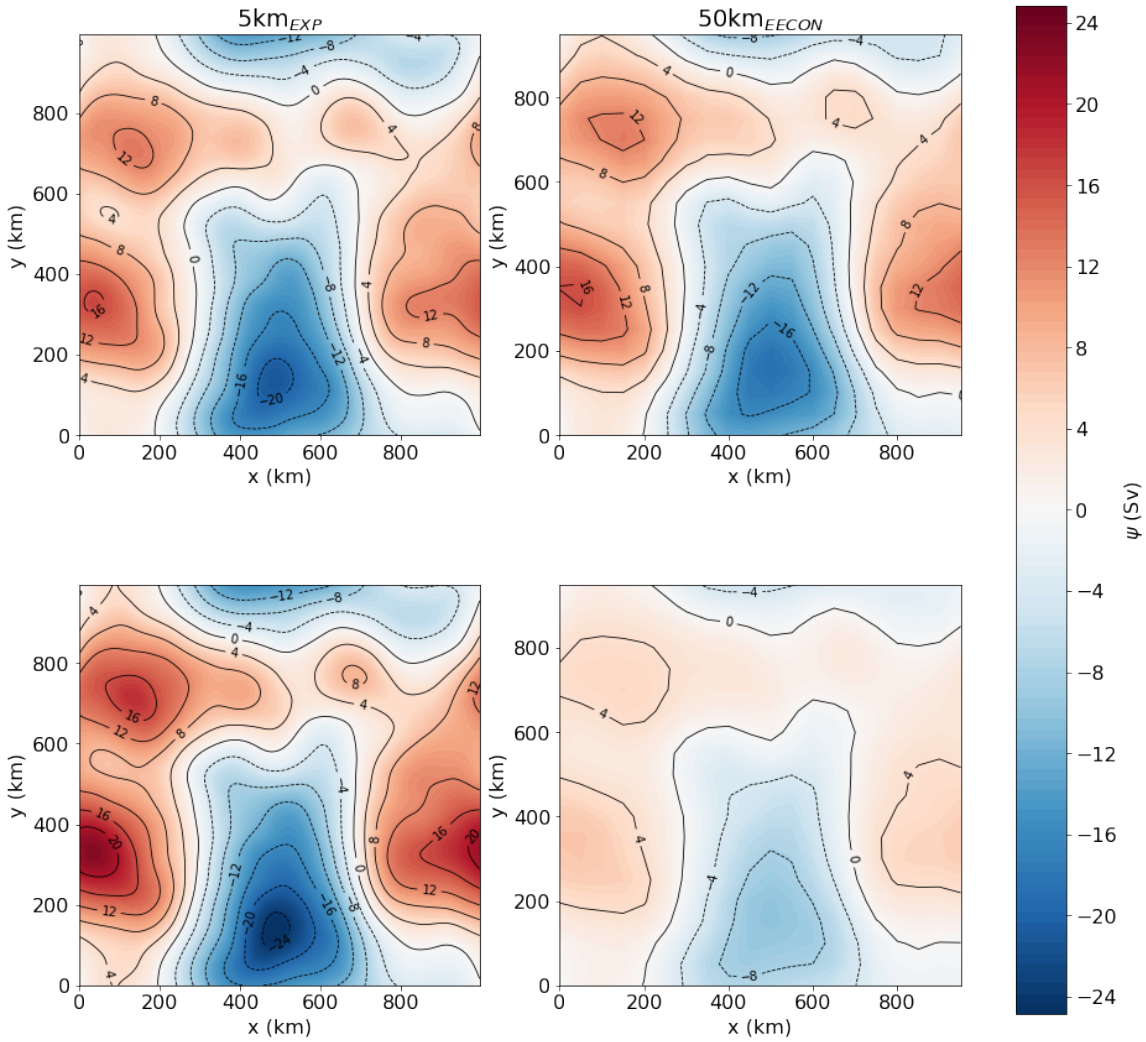

Figure 3.10: Time-mean transport stream function with labelled contours for 5km$_{\mathrm{EXP}}$ (left) and 50km$_{\mathrm{EECON}}$ (right) over the time periods 0 - 1500 days (top) and 1501 - 3000 days (bottom).

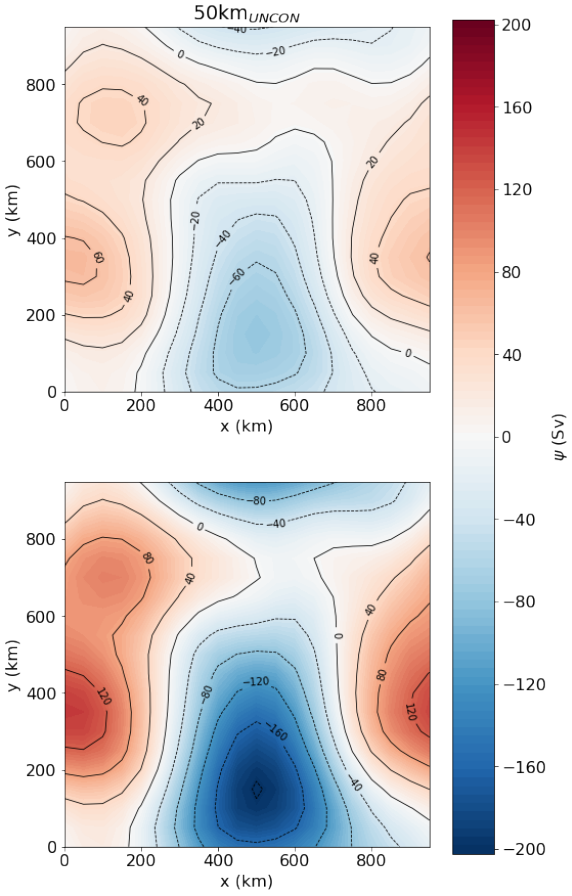

Figure 3.11: Time-mean transport stream function with labelled contours for 50km$_{\mathrm{UNCON}}$ over the time periods 0 - 1500 days (top) and 1501 - 3000 days (bottom).

$50\text{km}_{\text{UNCON}}$ decreases throughout the simulation as PV continues to be mixed. This difference can be seen in the final PV for each simulation (Figure 3.12). 5km_{EXP} and $50\text{km}_{\text{EECON}}$ exhibit similar final PV magnitudes whereas the PV in $50\text{km}_{\text{UNCON}}$ is more mixed and therefore closer to PV homogenization. For clarity, we also include the PV of $50\text{km}_{\text{EECON}}$ at 265 days, when the MPEnstr is at a minimum and hence the time at which PV homogenization is maximised, which is also comparable in magnitude to that of 5km_{EXP}.

Both the eddy-to-mean kinetic energy conversion and mean-to-eddy potential enstrophy conversion in $50\text{km}_{\text{EECON}}$ are of the correct order of magnitude but are initially larger than their counterparts in 5km_{EXP} (Figures 3.9e and 3.9f). This causes the MKE and MPEnstr to initially grow and decay respectively at a faster rate in $50\text{km}_{\text{EECON}}$ than in 5km_{EXP} (Figures 3.9a and 3.9c). It is possible that the input parameters to the parameterization affect the timescale for growth of MKE and decay of MPEnstr, and therefore that tuning of the parameters could lead to a growth rate of MKE and decay rate of MPEnstr in $50\text{km}_{\text{EECON}}$ that are more similar to that of 5km_{EXP}. However, here we focus on the functionality of the parameterization, and do not seek to find optimally tuned parameters. We investigate the effect of varying the input parameters on the resolved flow in Section 3.4.4.

One clear difference between 5km_{EXP} and $50\text{km}_{\text{EECON}}$ is that 5km_{EXP} reaches a state of non-zero mean flow, whereas $50\text{km}_{\text{EECON}}$ returns to a state close to that of no flow. This behaviour is examined in the following section.

3.4.3 Quantifying the Kinetic Energy and Potential Enstrophy Pathways

In Section 3.2.3, we outlined the components of the volume-integrated MKE, EKE, MPEnstr and EPEnstr budgets and summarised the pathways associated with these components for the eddy-resolving simulation, 5km_{EXP} and the simulation employing the energy- and enstrophy-constrained parameterization, $50\text{km}_{\text{EECON}}$, in Figures 3.2 and 3.3 respectively. Here, we quantify and compare the kinetic energy and potential enstrophy transfers associated with these pathways for 5km_{EXP}, and $50\text{km}_{\text{EECON}}$.

value corresponding to no mean flow. Thus, biharmonic diffusion inputs MPEnstr.

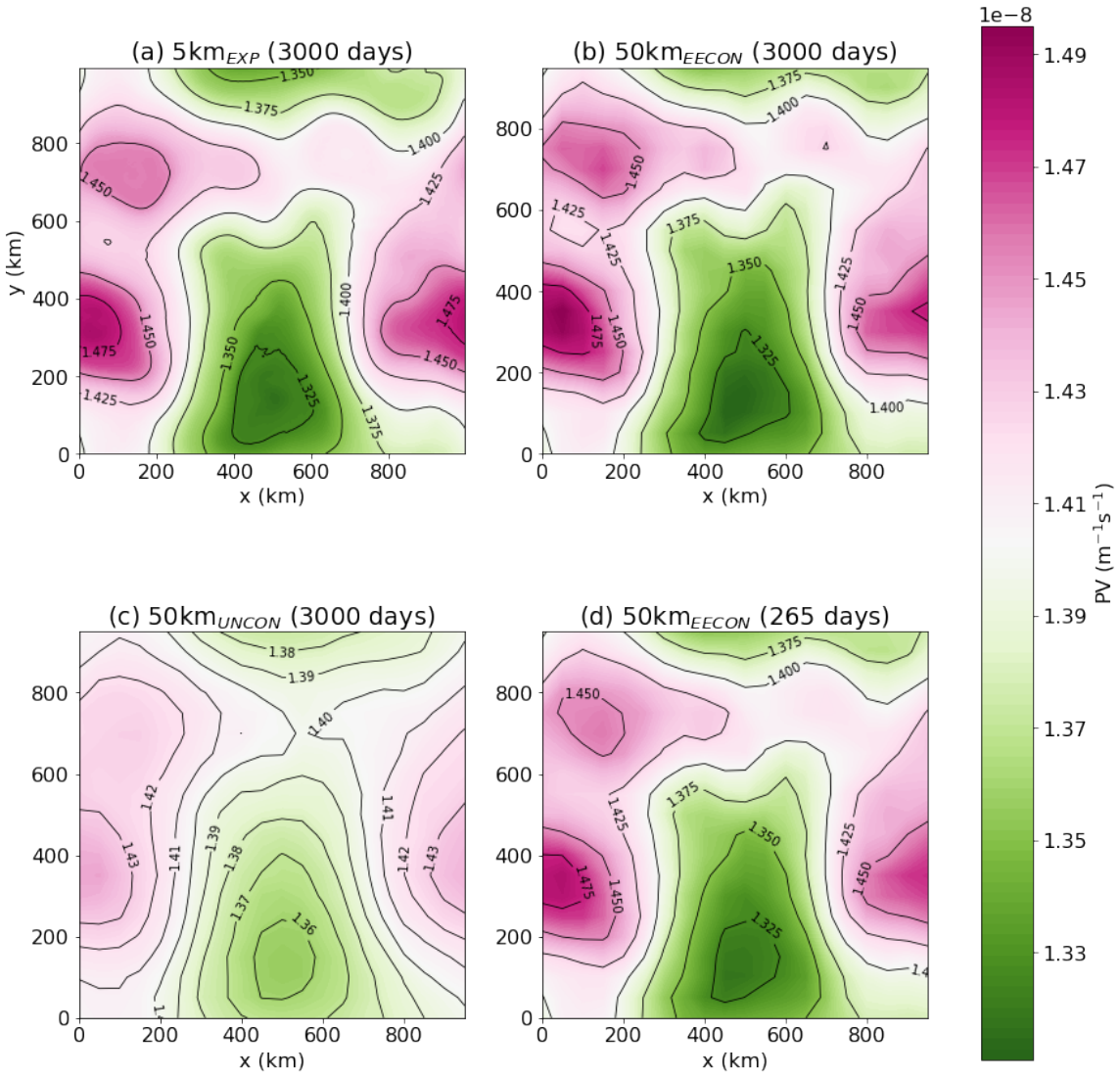

Figure 3.12: PV with labelled contours at 3000 days for (a) 5km$_{\mathrm{EXP}}$; (b) 50km$_{\mathrm{EECON}}$; (c) 50km$_{\mathrm{UNCON}}$; and (d) PV for 50km$_{\mathrm{EECON}}$ at the time of MPEnstr minimum (265 days) representing the point of maximum PV homogenization.

To do this, it is helpful to divide the simulations into a growth period and a quasi-steady period or a decay period. We distinguish these periods in both 5km_{EXP} and $50\text{km}_{\text{EECON}}$ by the peak value in the MKE time series, shown by the solid and dotted vertical lines respectively in Figure 3.9, and occurring at days 2100 and 263 respectively. Therefore, 5km_{EXP} is divided into an initial period of growth (0 - 2100 days) and a later quasi-steady period (2100 - 3000 days) and $50\text{km}_{\text{EECON}}$ is divided into an initial period of growth (0 - 263 days) and a later period of decay (263 - 3000 days). The kinetic energy and potential enstrophy pathways for these periods are illustrated and quantified in Figures 3.13 and 3.14 for 5km_{EXP} and $50\text{km}_{\text{EECON}}$ respectively.

During the growth period in 5km_{EXP} (Figure 3.13) the eddy-to-mean kinetic energy conversion rate is order 10^6 W, while MKE and EKE are extracted at a rate of order 10^5 W. This results in an overall growth of MKE and decay of EKE. There is an input of MPEnstr at a rate of order 10^{-15} m s^{-3}, while both mean-to-eddy potential enstrophy conversion and EPEnstr extraction occur at a rate of order 10^{-13} m s^{-3}. This results in an overall decay of both MPEnstr and EPEnstr.

During the quasi-steady period, all of the above transfer rates decrease. The eddy-to-mean kinetic energy conversion rate is of the same order of magnitude as the MKE extraction rate ($\mathcal{O}(10^4$ W)) and, thus, there is an approximate balance in sources and sinks of MKE, illustrated by the steady MKE in Figure 3.9a. The inputs and extractions of potential enstrophy are unbalanced with a larger EPEnstr extraction rate ($\mathcal{O}(10^{-15}$ m s^{-3})) than MPEnstr input rate ($\mathcal{O}(10^{-16}$ m s^{-3})) and, hence, there is an overall extraction of potential enstrophy from the system.

During the growth period of $50\text{km}_{\text{EECON}}$ (Figure 3.14), the eddy-to-mean kinetic energy conversion rate is an order of magnitude larger than in 5km_{EXP}. However, since the growth period is shorter, the peak values of volume-integrated MKE in 5km_{EXP} and $50\text{km}_{\text{EECON}}$ are similar, with values 7.71×10^{14} J and 7.68×10^{14} J, respectively (not shown). The MKE extraction rate is an order of magnitude larger in $50\text{km}_{\text{EECON}}$ ($\mathcal{O}(10^7$ W)) than in 5km_{EXP} ($\mathcal{O}(10^6$ W)) during the growth period, due to the larger coefficient of biharmonic diffusion required for numerical stability in $50\text{km}_{\text{EECON}}$. All potential enstrophy pathways (MPEnstr input, mean-to-eddy potential enstrophy conversion, and EPEnstr extraction) during the growth period are at least an order of magnitude larger in $50\text{km}_{\text{EECON}}$ than in 5km_{EXP}. These potential enstrophy transfers are fed by the source of MPEnstr from biharmonic diffusion. Hence,

the larger coefficient of biharmonic diffusion in $50km_{EECON}$ than in $5km_{EXP}$ results in a larger input of MPEnstr ($\mathcal{O}(10^{-13}$ m s^{-3}) and $\mathcal{O}(10^{-15}$ m s^{-3}) respectively) and therefore stronger potential enstrophy transfers. While the magnitudes of the transfer rates differ between the kinetic energy and potential enstrophy pathways during the period of growth in $50km_{EECON}$ and $5km_{EXP}$, the behaviour in $50km_{EECON}$ broadly mimics that of $5km_{EXP}$ with the strongest kinetic energy transfer being eddy-to-mean conversion, and the strongest potential enstrophy transfers being mean-to-eddy conversion and extraction of EPEnstr.

During the decay period in $50km_{EECON}$, the eddy-to-mean kinetic energy conversion rate decreases by three orders of magnitude from it's value during the growth period, and is of the same order as that of $5km_{EXP}$ in the quasi-steady period ($\mathcal{O}(10^4$ W)). However, the MKE extraction rate is relatively unchanged from the growth period ($\mathcal{O}(10^6$ W)) and is therefore two orders of magnitude larger than that of $5km_{EXP}$ in the quasi-steady period ($\mathcal{O}(10^4$ W)). This results in a much larger decrease in volume-integrated MKE in $50km_{EECON}$ than in $5km_{EXP}$ during these periods (Figure 3.9a). The MPEnstr input is of the same order of magnitude as during the growth period ($\mathcal{O}(10^{-13}$ m s^{-3}), meaning it is now three orders of magnitude larger than that of $5km_{EXP}$ in the quasi-steady period ($\mathcal{O}(10^{-16}$ m s^{-3}). However, both the mean-to-eddy potential enstrophy conversion rate and EPEnst extraction have decreased by three and one order of magnitude respectively, resulting in a build up of MPEnstr.

Both the rate of eddy-to-mean kinetic energy conversion and the rate of mean-to-eddy potential enstrophy conversion in $50km_{EECON}$ are decreased during the decay period due to the fact that the parameterized EKE has depleted. As the parameterized eddy PV fluxes are a function of K and Λ (Equation 2.9), this results in effectively "turning off" the parameterized eddy PV fluxes and therefore also the parameterized kinetic energy and potential enstrophy conversion terms. When this happens, the mean-to-eddy potential enstrophy conversion cannot extract MPEnstr at the same rate that it is input by biharmonic diffusion. Similarly, the eddy-to-mean kinetic energy conversion cannot input MKE at the same rate that it is extracted by biharmonic diffusion. This results in an overall extraction of MKE and input of MPEnstr to the system during this period. As a result, the kinetic energy and potential enstrophy transfers in $50km_{EECON}$ during this decay period no longer mimic that of $5km_{EXP}$ in the quasi-steady period, in which there is an overall extraction of both kinetic energy and potential enstrophy at rates small enough such that the MKE and

MPEnstr reach a quasi-steady state (Figures 3.9a and 3.9c respectively).

To rectify this erroneous behaviour in the kinetic energy and potential enstrophy transfers in $50\text{km}_{\text{EECON}}$, a mechanism would be required which ensures that the eddy-to-mean kinetic energy conversion and the mean-to-eddy potential enstrophy conversion are sustained throughout the simulation. One way to achieve this, would be to ensure that both the parameterized EKE and parameterized EPEnstr are not sufficiently depleted such that the conversion terms are effectively turned off. We hypothesise that it is in fact sufficient to ensure that the parameterized EKE is not sufficiently depleted since, as long as the parameterized conversion terms are not effectively turned off, the parameterized EPEnstr will be fed by the source of MPEnstr by biharmonic diffusion. In Chapter 4, we outline and test a method for addressing this issue in the kinetic energy and potential enstrophy transfers in the parameterized simulation.

3.4.4 Sensitivity to Input Parameters

We now test the sensitivity of the parameterization performance to the input parameters (specifically, the eddy PV flux efficiency parameter, γ_q; the parameterized EPEnstr damping parameter, r_Λ; and the parameterized EKE and EPEnstr diffusivity, μ) and the initial values of parameterized EKE (K_0) and parameterized EPEnstr (Λ_0) by running a set of simulations in which we systematically vary these parameters. We compare the total amount of eddy-to-mean kinetic energy conversion throughout the simulation, the total amount of mean-to-eddy potential enstrophy conversion throughout the simulation, and the time taken for 90% of the initial parameterized EKE to be depleted as these parameters vary. Since the growth of large-scale kinetic energy is due to the eddy-to-mean kinetic energy conversion, we use the timescale for depletion of parameterized EKE as a proxy for the timescale of the growth of large-scale kinetic energy.

The total amount of eddy-to-mean kinetic energy conversion (Figure 3.15) is predominantly determined by the initial amount of parameterized EKE, K_0, shown by the large variations in panels (a) - (d) compared with the relatively small variations in panels (e) - (j). Panels (e) - (j) show a slightly larger total amount of kinetic energy converted than is available in the initial state (1.8×10^{-4} m^{2}s^{-2}), which likely

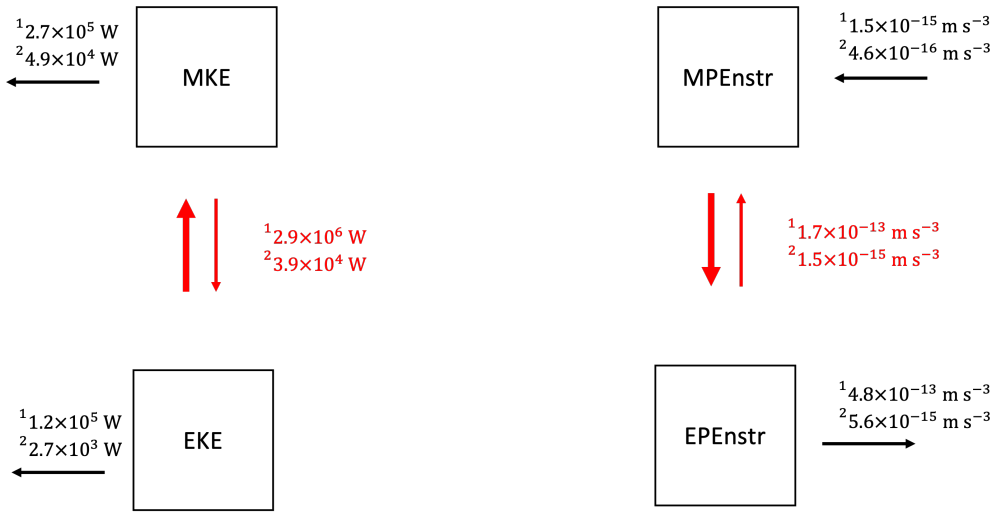

Figure 3.13: Kinetic energy and potential enstrophy transfers associated with the eddy-resolving simulation, 5km_{EXP}. Labels indicate the total (volume- and time-integrated) rates of kinetic energy/potential enstrophy transfer for the growth period (up to the solid vertical line in Figure 3.9, denoted by superscript 1) and the quasi-steady period (after the solid vertical line in Figure 3.9, denoted by superscript 2). Black arrows and numbers represent kinetic energy and potential enstrophy pathways resulting from biharmonic diffusion. Red arrows and numbers represent kinetic energy and potential enstrophy pathways associated with the explicit barotropic eddies. In the case where there are two arrows, the dominant direction of transfer (and therefore the direction of the net transfer rate quantified in the label) is indicated by the bold arrow. Transfer rates associated with the explicit barotropic eddies are calculated from the moving-window time means illustrated in Figure 3.9. Transfer rates associated with biharmonic diffusion are calculated as residuals.

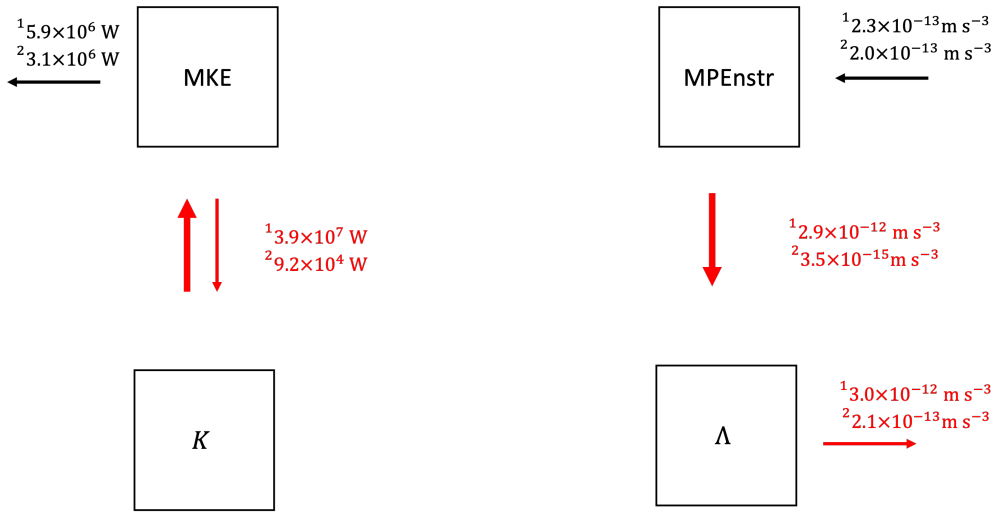

Figure 3.14: Kinetic energy and potential enstrophy transfers associated with the parameterized simulation, $50\text{km}_{\text{EECON}}$. Labels indicate the total (volume- and time-integrated) rates of kinetic energy/potential enstrophy transfers for the growth period (up to the dotted vertical line in Figure 3.9, denoted by superscript 1) and the decay period (after the dotted vertical line in Figure 3.9, denoted by superscript 2). Black arrows and numbers represent kinetic energy and potential enstrophy pathways resulting from biharmonic diffusion. Red arrows and numbers represent kinetic energy and potential enstrophy pathways associated with the parameterized barotropic eddies. In the case where there are two arrows, the dominant direction of transfer (and therefore the direction of the net transfer rate quantified in the label) is indicated by the bold arrow. Transfer rates associated with the parameterized barotropic eddies are calculated from the parameterized values illustrated in Figure 3.9. Transfer rates associated with biharmonic diffusion are calculated as residuals.

comes from numerical effects. However, the flow is still well-constrained in these simulations determined by the maximum MKE compared to that of 5km_{EXP} (not shown).

The total amount of mean-to-eddy potential enstrophy conversion (Figure 3.16) is also predominantly determined by K_0. This aligns with the result of Adcock and Marshall (2000) that eddies mix PV (i.e. convert potential enstrophy from mean to eddy) by an amount set by the energy of the initial state. The total amount of mean-to-eddy potential enstrophy conversion is largely unaffected by μ and, rather counter-intuitively, increases with increasing r_Λ and decreasing γ_q. This can be explained by the variation in timescale for growth of large-scale kinetic energy, or, more precisely, the timescale for the depletion of EKE (Figure 3.17). This timescale increases with decreasing γ_q. A decrease in γ_q decreases the magnitude of the eddy PV fluxes through Equation 2.9. This decrease in fluxes decreases the magnitude of the kinetic energy conversion term in the EKE budget, resulting in a slower depletion of parameterized EKE and a slower growth of large-scale kinetic energy. The effect of varying r_Λ on the timescale for growth is mostly seen for smaller values of γ_q, with an increase in r_Λ resulting in an increase to the timescale for growth. Increasing r_Λ decreases the parameterized EPEnstr which decreases the magnitude of the eddy PV fluxes, leading to a slower growth rate of large-scale kinetic energy as described above, and, correspondingly, a larger timescale for growth. Physically, increasing r_Λ and decreasing γ_q means that the parameterized eddies persist for a longer period of time. The longer the parameterized eddies are present, the more they mix PV and therefore the more mean-to-eddy potential enstrophy conversion occurs.

3.5 Summary and Discussion

In this chapter, we presented the results of experiments designed to test the functionality of the parameterization developed in Chapter 2. We analysed numerical simulations of barotropic freely decaying turbulence over variable bottom topography in a doubly periodic domain. This setup ensures that the main physical process driving the large-scale flow is the eddies, therefore allowing us to compare the effect of the explicit eddies and parameterized eddies on the large-scale flow. We compared the results of an eddy-resolving simulation (5km_{EXP}), a coarse-resolution simulation with no eddy parameterization ($50\text{km}_{\text{NOPAR}}$), a coarse-resolution simulation with parameterized eddies using the parameterization outlined in Chapter 2 ($50\text{km}_{\text{EECON}}$), and

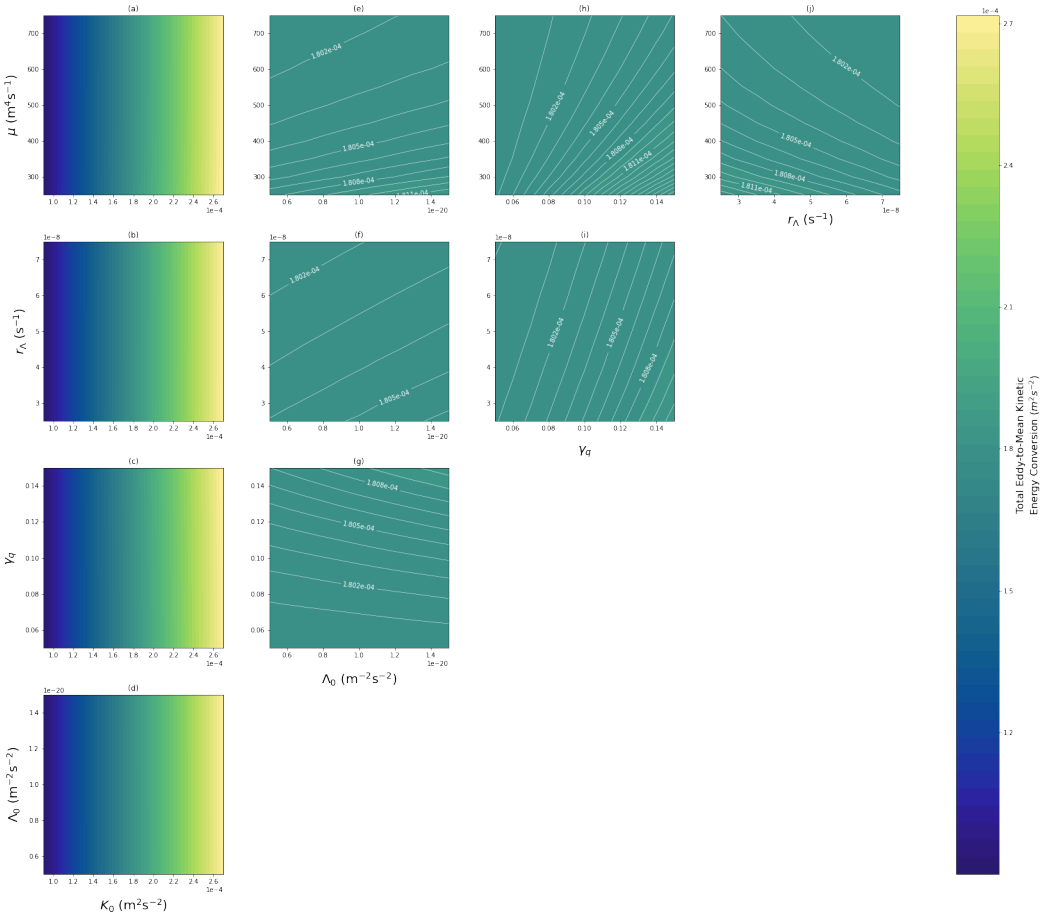

Figure 3.15: Total (time-integrated) volume-averaged eddy-to-mean kinetic energy conversion (contours) for a set of simulations with the same setup as $50\text{km}_{\text{EECON}}$ where the values of the eddy PV flux efficiency parameter, γ_q, the parameterized EPEnstr damping parameter, r_Λ, the parameterized EKE and EPEnstr eddy diffusivity, μ, the initial parameterized EKE, K_0, and the initial parameterized EPEnstr, Λ_0 are varied by 50% of their value in $50\text{km}_{\text{EECON}}$. The variation in values in panels e - j is much smaller than the variation in values in panels a - d so, for clarity, additional contours are drawn and labelled in panels e - j.

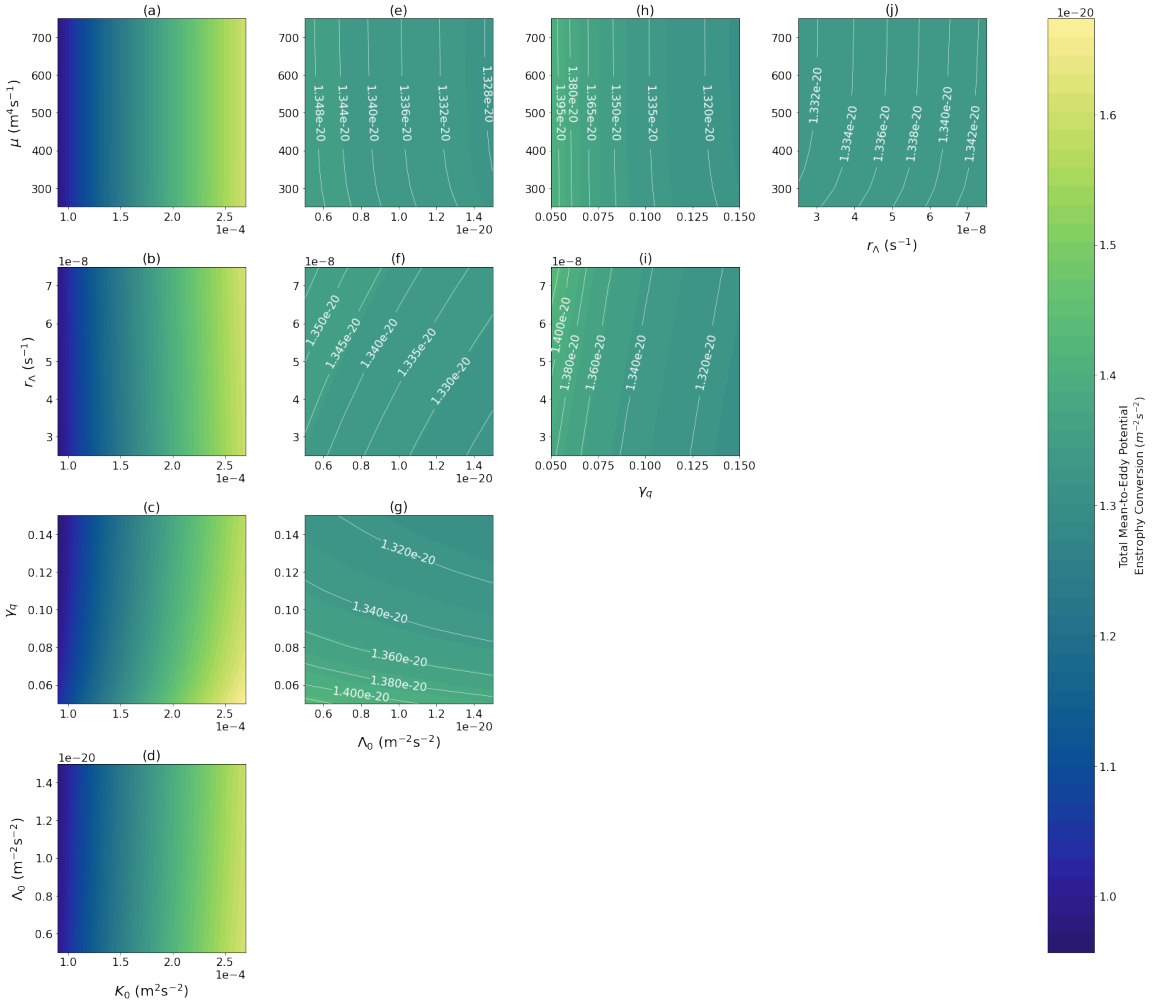

Figure 3.16: Total (time-integrated) volume-averaged mean-to-eddy potential enstrophy conversion (contours) for a set of simulations with the same setup as $50\text{km}_{\text{EECON}}$ where the values of the eddy PV flux efficiency parameter, γ_q, the parameterized EPEnstr damping parameter, r_Λ, the parameterized EKE and EPEnstr diffusivity, μ, the initial parameterized EKE, K_0, and the initial parameterized EPEnstr, Λ_0 are varied by 50% of their value in $50\text{km}_{\text{EECON}}$. The variation in values in panels e - j is much smaller than the variation in values in panels a - d so, for clarity, additional contours are drawn and labelled in panels e - j.

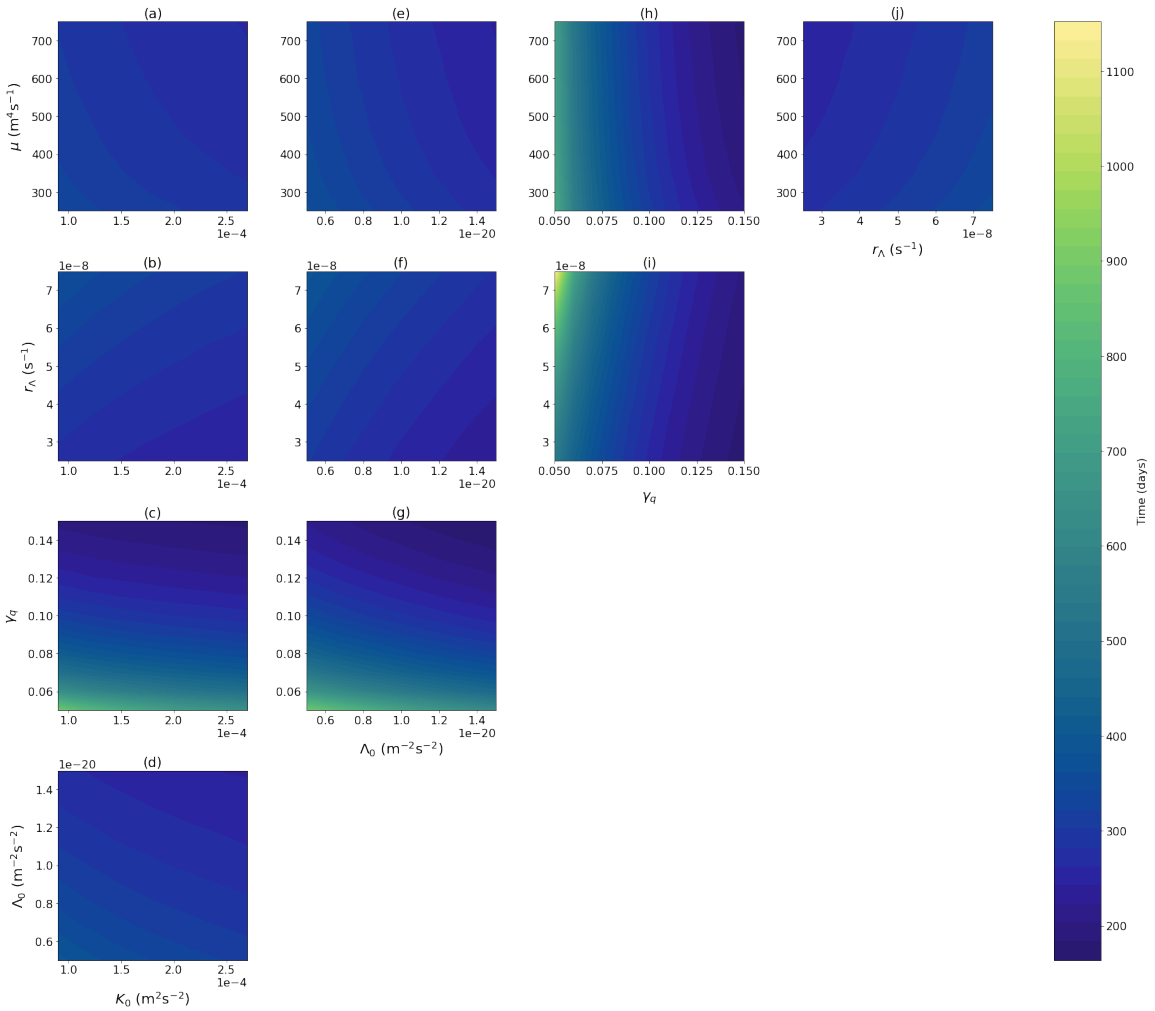

Figure 3.17: Time taken for 90% of the initial parameterized EKE to be depleted (contours) for a set of simulations with the same setup as $50\text{km}_{\text{EECON}}$ where the values of the eddy PV flux efficiency parameter, γ_q, the parameterized EPEnstr damping parameter, r_Λ, the parameterized EKE and EPEnstr diffusivity, μ, the initial parameterized EKE, K_0, and the initial parameterized EPEnstr, Λ_0 are varied by 50% of their value in $50\text{km}_{\text{EECON}}$.

a coarse-resolution simulation employing an unconstrained down-gradient PV mixing parameterization ($50\text{km}_{\text{UNCON}}$).

We first compared the results of 5km_{EXP} and $50\text{km}_{\text{NOPAR}}$ in order to identify the unresolved eddy effect on the large-scale flow in $50\text{km}_{\text{NOPAR}}$. This effect should be present in the parameterized simulations via the parameterized eddies and therefore determines what we require of the parameterization in this setup. We found that the magnitudes of both the eddy-to-mean kinetic energy conversion and the mean-to-eddy potential enstrophy conversion in $50\text{km}_{\text{NOPAR}}$ were small in comparison to 5km_{EXP}, resulting in a negligible MKE and an increase in MPEnstr. Thus, we required the parameterization to increase both the eddy-to-mean kinetic energy conversion and the mean-to-eddy potential enstrophy conversion. In other words, we required the parameterization to mimic a cascade of kinetic energy from small to large scales, and a cascade of potential enstrophy from large to small scales, as is typical of the barotropic mode of quasigeostrophic turbulence.

Our key-findings from the parameterized simulations are:

1. The parameterization produces an emergent indirect kinetic energy cascade, evidenced by a net conversion of kinetic energy from the parameterized eddies to the large-scale flow, resulting in a large-scale topography-following flow.

2. The energetics and enstrophetics exhibit similar behaviour to that of an eddy-resolving simulation. In particular, both the eddy-to-mean kinetic conversion and the mean-to-eddy potential enstrophy conversion increase in magnitude due to the parameterized eddies. This results in an improvement to the MKE and MPEnstr when compared to an unconstrained PV mixing parameterization. These findings suggest that the energy and enstrophy constraints imposed in the parameterization are successful in constraining the kinetic energy and the potential enstrophy of the large-scale flow.

3. During the growth period, the kinetic energy and potential enstrophy transfers in the coarse-resolution simulation employing the parameterization mimic that of the eddy-resolving simulation, specifically, by producing a growth of MKE and an overall extraction of potential enstrophy. During the decay period in the parameterized simulation, the kinetic energy and potential enstrophy transfers no longer resemble that of the eddy-resolving simulation in the quasi-steady

period. Specifically, in the parameterized simulation, there is an overall input of MPEnstr not present in the eddy-resolving simulation, caused by biharmonic diffusion. To rectify this erroneous behaviour in the kinetic energy and potential enstrophy transfers in the later part of the simulation, we hypothesise that a mechanism would be required which ensures that the parameterized EKE is not sufficiently depleted such as to effectively turn off the parameterized conversion terms. We explore a method for rectifying this erroneous behaviour in Chapter 4.

4. The total amount of eddy-to-mean kinetic energy conversion and mean-to-eddy potential enstrophy conversion are both predominantly determined by the amount of parameterized EKE in the initial state. The amount of mean-to-eddy potential enstrophy conversion increases as the timescale for growth of MKE increases. The timescale for growth of MKE is most sensitive to changes in the eddy PV flux efficiency parameter, γ_q, and somewhat sensitive to changes in the parameterized EPEnstr damping parameter, r_Λ, with a decrease in γ_q or an increase in r_Λ resulting in a longer timescale for growth. The parameterized EKE and EPEnstr diffusivity, μ, and the initial values of parameterized EKE and EPEnstr have a relatively small effect on the timescale for growth of MKE.

The experiments presented in this chapter are highly idealised in order to isolate and compare the effect of the explicit and parameterized eddies. An important topic for further investigation is assessing the performance of the parameterization in more realistic setups. One change to the setup which affects the results both quantitatively and qualitatively is introducing land boundaries. Figure 3.18 shows the results of simulations $5\text{km}^*_{\text{EXP}}$ and $50\text{km}^*_{\text{EECON}}$, which are identical to 5km_{EXP} and $50\text{km}_{\text{EECON}}$ respectively, but in a closed domain. That is, these simulations use the topography described in Figure 3.4, the initial stream function described in Figure 3.5 (for 5km_{EXP} only), the parameters specified in Section 3.3.2 for $50\text{km}_{\text{EECON}}$ (except for the initial parameterized EKE, K_0, which is calculated using the kinetic energy of the initial stream function of 5km_{EXP} in a closed domain), and no flux boundary conditions with $\psi = 0$ and $\xi = 0$ on the boundary.

In this setup, the MKE and eddy-to-mean kinetic energy conversion in both $5\text{km}^*_{\text{EXP}}$ and $50\text{km}^*_{\text{EECON}}$ are an order of magnitude smaller than those of 5km_{EXP} and $50\text{km}_{\text{EECON}}$ (Figure 3.9), that is, their counterparts in a doubly periodic domain. In addition, the

mean-to-eddy potential enstrophy conversion in $5\text{km}^*_{\text{EXP}}$ and $50\text{km}^*_{\text{EECON}}$ is an order of magnitude smaller than that of 5km_{EXP} and $50\text{km}_{\text{EECON}}$, and an enstrophetic inconsistency is introduced. Specifically, there is an increase in MPEnstr in both $5\text{km}^*_{\text{EXP}}$ and $50\text{km}^*_{\text{EECON}}$, indicating a source of MPEnstr present in these simulations. It is a known problem that rough model coastlines exert a form drag on the fluid (Adcroft and Marshall, 1998). This drag is the likely cause of the decrease in MKE when land boundaries are introduced and may also be the cause of the source of MPEnstr. Elimination of this source of MPEsntr may be possible by formulating the biharmonic diffusion term such that it is a net sink of MPEnstr when integrated over the domain.

In addition to land boundaries, there are many other more realistic setups in which the parameterization should be tested. For example, an understanding of how the parameterization performs when forcing and friction are introduced is currently lacking. Furthermore, how the parameterization should be implemented in a baroclinic setup remains to be determined. We address these topics later in this thesis, in which we outline one method for implementing the parameterization in a baroclinic model (Chapter 5), and assess the performance of the parameterization in a fully baroclinic model (Chapter 6).

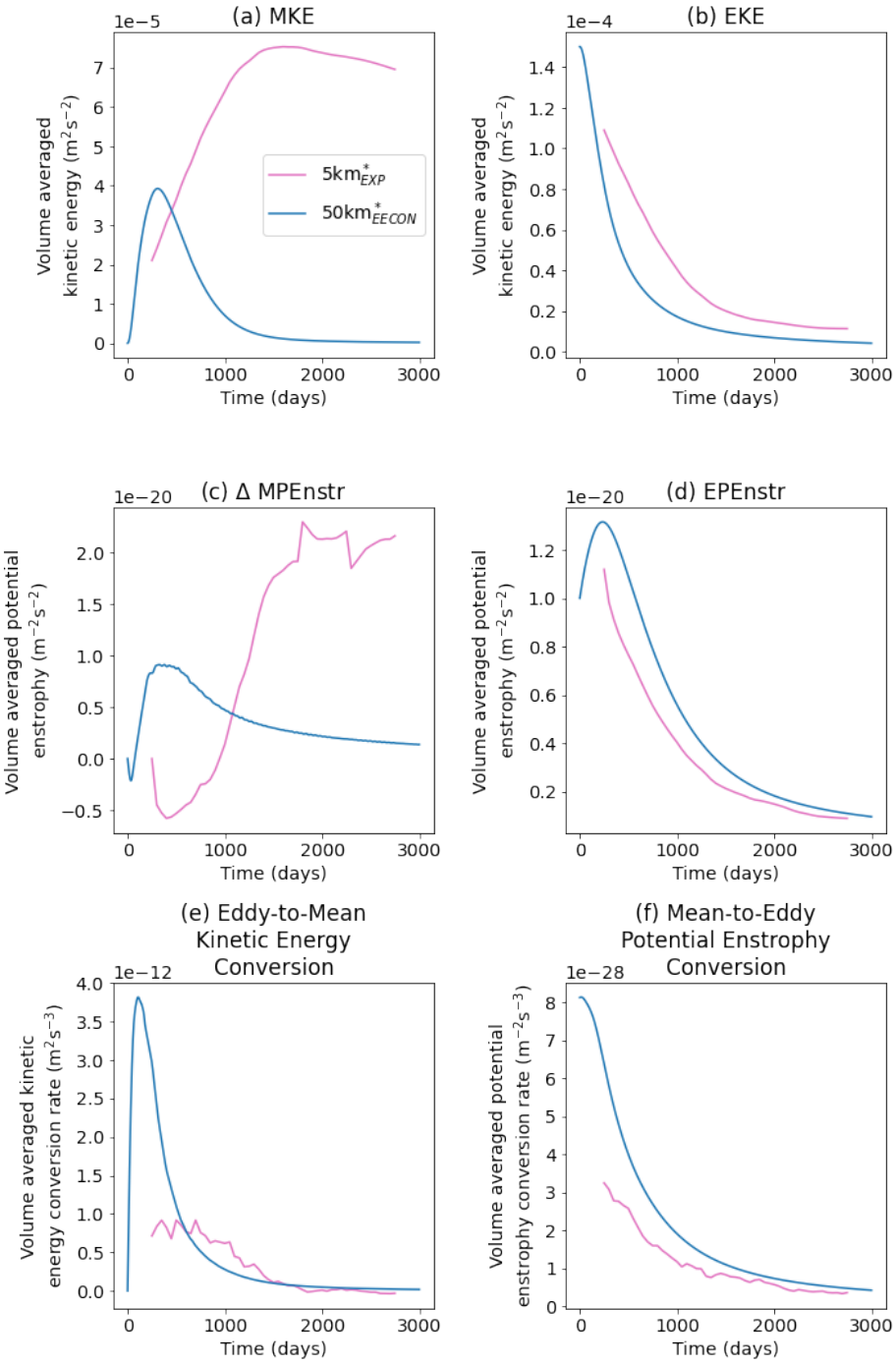

Figure 3.18: Volume-averaged (a) MKE; (b) EKE; (c) change in MPEnstr from initial value; (d) EPEnstr; (e) eddy-to-mean kinetic energy conversion, $-\overline{q'\mathbf{u}'} \cdot \nabla\psi$; and (f) mean-to-eddy potential enstrophy conversion, $-\overline{q'\mathbf{u}'} \cdot \nabla\overline{q}$, for simulations in a closed domain with a setup analogous to 5km_{EXP} (pink, labelled $5\text{km}^*_{\text{EXP}}$) and $50\text{km}_{\text{EECON}}$ (blue, labelled $50\text{km}^*_{\text{EECON}}$). For $5\text{km}^*_{\text{EXP}}$, values shown are moving-window time-means calculated every 50 days over a 500-day period. For $50\text{km}^*_{\text{EECON}}$, values shown are instantaneous values.

Chapter 4

The Kinetic Energy Supercharger

4.1 Introduction

We have seen in Chapter 3 that the depletion of parameterized EKE in the coarse-resolution simulation employing the energy- and enstrophy-constrained parameterization effectively turns off the parameterized eddy-to-mean kinetic energy conversion and the parameterized mean-to-eddy potential enstrophy conversion as designed. However, as a result of biharmonic diffusion, which extracts MKE and inputs MPEnstr, this leads to kinetic energy and potential enstrophy transfers in the parameterized simulation which no longer resemble those of the eddy-resolving simulation. Specifically, in the parameterized simulation, there is an overall extraction of MKE and an overall input of MPEnstr later in the simulation. In contrast, in the eddy-resolving simulation, there is an overall extraction of both MKE and MPEnstr at rates sufficiently small such that the MKE and MPEnstr reach a quasi-steady state. We hypothesised that, to produce kinetic energy and potential enstrophy transfers in the parameterized simulation which more closely resemble those of the eddy-resolving simulation, a mechanism would be required which ensures that the parameterized EKE is not sufficiently depleted such as to effectively turn off the parameterized conversion terms. In this chapter, we outline and test such a method, which we refer to as the kinetic energy supercharger, and which aims to improve the kinetic energy and potential enstrophy transfers in parameterized simulations.

The over-extraction of large-scale kinetic energy from modelled flows by biharmonic diffusion is a documented issue (Jansen and Held, 2014). It has been proposed that

a source of kinetic energy should be introduced to counteract this sink of energy (e.g. Jansen and Held, 2014; Jansen et al., 2015, 2019; Yankovsky et al., 2024), a mechanism typically referred to as backscatter. This is often achieved in eddy-permitting models by reinjecting the kinetic energy at the scale of the resolved eddies, thus re-energising the resolved eddies, which can then cascade this reinjected kinetic energy to large scales. Typically, this source of kinetic energy is introduced into the governing equations as a negative Laplacian of the resolved velocity (e.g. Jansen and Held, 2014; Jansen et al., 2015, 2019; Yankovsky et al., 2024). Jansen et al. (2019) extended this work for use in both non-eddying and eddy-permitting models by employing a backscatter mechanism alongside a subgrid EKE budget, thus re-energising the resolved eddies as well as the parameterized eddies. In doing so, they effectively created a pool of parameterized EKE, which feeds the source of large-scale kinetic energy reinjection. One issue with the mechanism of backscatter described above is that, as the velocity increases in magnitude, it is possible for the reinjection of kinetic energy via a negative Laplacian to occur at a rate faster than it is being extracted by biharmonic diffusion. For this reason, an extra constraint is usually required on the backscatter mechanism to ensure stability when employing a negative Laplacian to reinject kinetic energy.

In this chapter, we incorporate a mechanism into the energetically and enstrophetically constrained parameterization outlined in Chapter 2 which reinjects the kinetic energy extracted by biharmonic diffusion into the parameterized EKE budget. This mechanism differs from the backscatter mechanisms described above for two reasons: 1. we re-energise the parameterized eddies whereas most of the methods described re-energise the explicitly resolved eddies thus facilitating an explicit inverse cascade of kinetic energy; and 2. we do not include a source of kinetic energy in the governing equations in the form of a negative Laplacian, instead letting the pre-existing kinetic energy conversion mechanism within the parameterization convert this reinjected kinetic energy from the parameterized eddies to the large-scale flow based on the dynamics. For these reasons we do not refer to this mechanism as backscatter. We choose to refer to this mechanism as the kinetic energy supercharger[1].

In Section 4.2, we describe the implementation of the kinetic energy supercharger

[1]This terminology comes from an analogy between eddy parameterizations and car engines during a conversation with Dr. Chris Wilson, who assures us that the mechanism is analogous to a supercharger engine.

mechanism into the energetically and enstrophetically constrained parameterization described in Chapter 2, and outline the kinetic energy and potential enstrophy pathways associated with this new setup. In Section 4.3, we analyse the results of a coarse-resolution simulation employing the parameterization with the additional supercharger mechanism, comparing this to a coarse resolution simulation employing the parameterization as described in Chapter 3 (specifically, the simulation $50\text{km}_{\text{EECON}}$ from Chapter 3), to understand the effect of the supercharger mechanism on the resolved flow. We look specifically at the energetics and enstrophetics of the system, finding that including the supercharger mechanism leads to a quasi-steady solution in which the transfers of kinetic energy and potential enstrophy more closely resemble those of the eddy-resolving simulation analysed in Chapter 3 (specifically, the simulation 5km_{EXP}). We analyse the kinetic energy and potential enstrophy transfers associated with the parameterized simulation with the additional supercharger mechanism to determine how the steady state is reached. We then perform sensitivity tests, similar to those described in Section 3.4.4, to understand the effect of varying the input parameters of the parameterization on the quasi-steady solution.

4.2 The Kinetic Energy Supercharger

In the experiments conducted in this chapter, we employ the same barotropic model utilised in Chapter 3 and described in Section 3.2. We modify the parameterization described in Chapter 2 by incorporating the kinetic energy supercharger mechanism into the EKE budget. In the sections that follow, we outline how this mechanism is implemented.

4.2.1 Formulating The Kinetic Energy Supercharger Mechanism

We now formulate the kinetic energy supercharger mechanism. Ideally, this mechanism would function such that MKE extracted by biharmonic diffusion is reinjected locally into the parameterized EKE budget. However, the form of biharmonic diffusion employed in the model (Equations 3.1 and 3.2) is not necessarily a sink of MKE. Locally, this biharmonic diffusion term can act as a sink *or* a source of MKE. The overall effect of the biharmonic diffusion, i.e. the volume-integrated effect, is a net sink of MKE. In order to perform local reinjection of kinetic energy, the biharmonic

diffusion term should extract MKE everywhere to avoid negative reinjections of kinetic energy. To avoid this issue, we instead choose to calculate the volume-integrated MKE extracted by biharmonic diffusion, and reinject the volume average of this value into the parameterized EKE budget at every point in the domain. That is, we redistribute the total amount of kinetic energy extracted by biharmonic diffusion across the whole domain. In this way, we avoid negative reinjections of kinetic energy into the parameterized EKE budget. We discuss the requirements for a local supercharger mechanism in Section 4.4.

In Section 3.2.3.1, we derived the volume-integrated MKE budget (Equation 3.5), and, in doing so, calculated the volume-integrated MKE extracted by biharmonic diffusion. It remains to add this kinetic energy as a source term in the parameterized EKE budget. We reinject the volume-average of the extracted MKE into the parameterized EKE budget at every point in the domain. Therefore, the depth-averaged EKE budget with the reinjected kinetic energy source term is

$$\frac{\partial K}{\partial t} = \overline{q'\mathbf{u}'} \cdot \nabla\overline{\psi} - \frac{1}{\mathrm{H}}\nabla \cdot (K\mathrm{H}\overline{\mathbf{u}}) - r_K K + \frac{\mu}{\mathrm{H}}\nabla^2 \mathrm{H} K + K_{\mathrm{SUPER}}, \tag{4.1}$$

where

$$K_{\mathrm{SUPER}} = -\frac{\int\int_A \mu_\xi \overline{\psi}\nabla^4 \mathrm{H}\overline{q}\ dA}{(\text{domain volume})} \tag{4.2}$$

represents the kinetic energy supercharger mechanism, i.e., the kinetic energy extracted from the mean component by biharmonic diffusion and reinjected into the parameterized EKE budget.

4.2.2 Volume-Integrated EKE Budget With the Kinetic Energy Supercharger Mechanism

By including the supercharger mechanism in the parameterization, we have changed the parameterized EKE budget and hence the associated volume-integrated parameterized EKE budget will change. Here we derive this new budget.

Integrating Equation 4.1 over the domain volume, noting that divergence terms integrate to zero since we are in a doubly periodic domain, we obtain the volume-

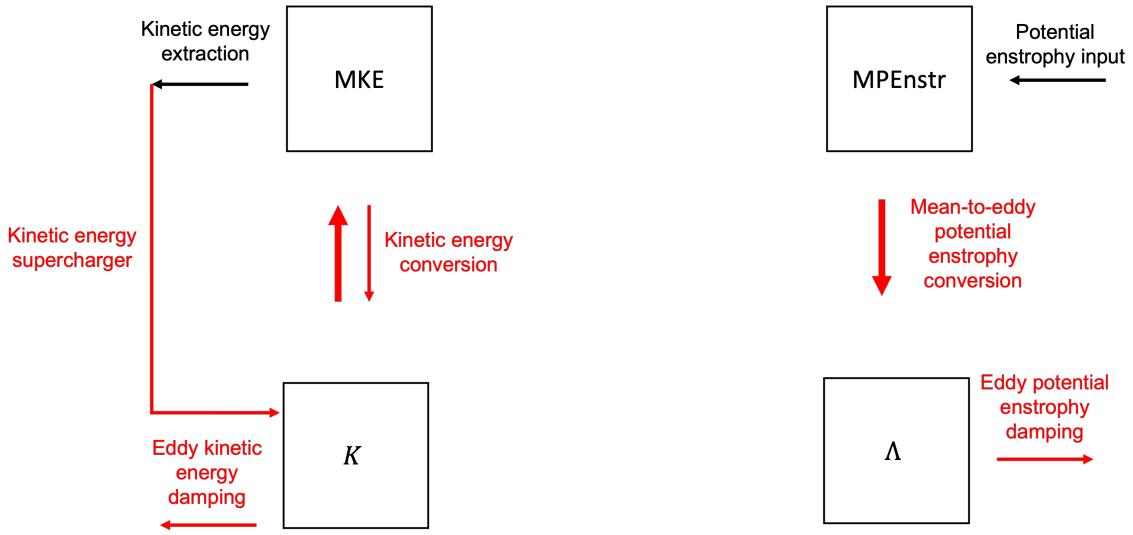

Figure 4.1: Kinetic energy and potential enstrophy pathways for parameterized simulations with the additional kinetic energy supercharger mechanism. Black arrows and labels indicate kinetic energy and potential enstrophy pathways associated with biharmonic diffusion. Red arrows and labels indicate kinetic energy and potential enstrophy pathways associated with the parameterized barotropic eddies (including the supercharger mechanism). In the case where there are two arrows, the dominant direction of transfer is indicated by the bold arrow.

integrated parameterized EKE budget with the kinetic energy supercharger mechanism,

$$\frac{d}{dt}\int\int_A K\ dA = \underbrace{\int\int_A \mathrm{H}\overline{q'\mathbf{u}'}\cdot\nabla\overline{\psi}\ dA}_{\substack{\text{kinetic energy}\\ \text{conversion}}} - \underbrace{\int\int_A \mathrm{H}r_K K\ dA}_{\substack{\text{parameterized}\\ \text{EKE damping}}} + \underbrace{\int\int_A \mathrm{H}K_{\mathrm{SUPER}}\ dA}_{\substack{\text{kinetic energy}\\ \text{supercharger}}}. \tag{4.3}$$

The first term on the right hand side of Equation 4.3 represents kinetic energy conversion between the mean and eddy components of the flow. The second term represents the damping of parameterized EKE. The third term is the kinetic energy supercharger mechanism, representing a source of parameterized EKE. The kinetic energy and potential enstrophy pathways associated with this setup are illustrated in Figure 4.1. Note that this mechanism is implemented entirely in the parameterized EKE budget. No change to the parameterized EPEnstr budget is made. Thus, the parameterized EPEnstr budget in this setup is described by Equation 2.14, and the volume-integrated potential enstrophy budgets associated with this setup are described in Section 3.2.3.2.

4.2.3 Experimental Setup

In Section 4.3 we analyse the results of a coarse-resolution simulation in which we employ the parameterization with the additional kinetic energy supercharger mechanism described in Equations 4.1 and 4.2. We refer to this simulation as $50\text{km}_{\text{SUPER}}$. The remainder of the model setup of $50\text{km}_{\text{SUPER}}$ is identical to that of $50\text{km}_{\text{EECON}}$, described in Chapter 3. That is, the governing equation is Equation 3.2, the model topography is illustrated in Figure 3.4, and the simulation starts from initial conditions which are at rest everywhere. Additionally, the parameters used in $50\text{km}_{\text{SUPER}}$ (i.e. μ_ξ, γ_q, r_Λ, r_K and μ) and the initial values of parameterized EKE and EPEnstr (K_0 and Λ_0 respectively) are the same as those of $50\text{km}_{\text{EECON}}$ (shown in Table 3.1). We compare the results of $50\text{km}_{\text{SUPER}}$ to $50\text{km}_{\text{EECON}}$ to understand the effect of including the kinetic energy supercharger mechanism on the large-scale flow.

4.3 Supercharged Parameterized Eddy Simulations

In this section, we analyse the results of a coarse-resolution simulation employing the parameterization with the additional kinetic energy supercharger mechanism described in Section 4.2.1, which we refer to as $50\text{km}_{\text{SUPER}}$. We compare $50\text{km}_{\text{SUPER}}$ with the parameterized simulation without the kinetic energy supercharger mechanism, $50\text{km}_{\text{EECON}}$, and the eddy-resolving simulation, 5km_{EXP}, both described and analysed in Chapter 3. We aim to understand the effect of including the kinetic energy supercharger mechanism on the large-scale flow.

4.3.1 Time Series of Kinetic Energy and Potential Enstrophy

The time series of kinetic energy and potential enstrophy for the simulations 5km_{EXP}, $50\text{km}_{\text{EECON}}$ and $50\text{km}_{\text{SUPER}}$ are plotted in Figure 4.2. $50\text{km}_{\text{SUPER}}$ reaches a quasi-steady state in which the MKE is increased and the MPEnstr is decreased in comparison to $50\text{km}_{\text{EECON}}$. This quasi-steady-state behaviour in $50\text{km}_{\text{SUPER}}$ is more similar to that of 5km_{EXP} than $50\text{km}_{\text{EECON}}$. Thus, including the kinetic energy supercharger mechanism in the parameterization appears to improve the simulated flow. The quasi-steady solution in $50\text{km}_{\text{SUPER}}$ has non-zero parameterized EKE, EPEnstr, mean-to-eddy potential enstrophy conversion, and eddy-to-mean kinetic energy conversion. In other words, the parameterized eddies persist throughout the simulation. We will see that the parameterized eddies in fact act to maintain the quasi-steady flow.

As a result of the improved energetics and enstrophetics, the time-mean streamfunction for $50\text{km}_{\text{SUPER}}$ (Figure 4.3) more closely resembles that of 5km_{EXP} (Figure 3.10). Specifically, the topography-following flow is maintained at a similar strength over the period 1501 - 3000 days (bottom panel in Figure 4.3) as that of the period 0 - 1500 days (top panel in Figure 4.3). The strength of this topography-following flow is also comparable in magnitude to that of 5km_{EXP}, with a maximum value of 27.4 Sv.

4.3.2 Quantifying the Kinetic Energy and Potential Enstrophy Pathways

We saw in Section 3.4.3 that biharmonic diffusion leads to disparities between the kinetic energy and potential enstrophy transfers in 5km_{EXP} and in $50\text{km}_{\text{EECON}}$ later in the simulation. Specifically, biharmonic diffusion in $50\text{km}_{\text{EECON}}$ leads to a net extraction of MKE and a net input of MPEnstr, causing a decay of the resolved flow and a return to a state of rest. In contrast, in 5km_{EXP} during the later part of the simulation, there is a net extraction of both MKE and MPEnstr, and the extractions rates are sufficiently small such that the flow reaches a quasi-steady state. Here, we compare the kinetic energy and potential enstrophy transfers associated with 5km_{EXP}, $50\text{km}_{\text{EECON}}$ and $50\text{km}_{\text{SUPER}}$, to understand if including the kinetic energy supercharger mechanism in the parameterization improves the representation of the kinetic energy and potential enstrophy transfers.

To understand the effect of the kinetic energy supercharger mechanism on the kinetic energy and potential enstrophy transfers, we divide $50\text{km}_{\text{SUPER}}$ into a growth period and a quasi-steady period, indicated by the vertical lines in Figure 4.2. We define the quasi-steady period as the period in which the volume-averaged MKE does not vary by more than 0.1% of the final value, corresponding to days 1691 - 3000 of the simulation. Hence, the growth period corresponds to days 0 - 1690 of the simulation. The kinetic energy and potential enstrophy transfers in $50\text{km}_{\text{SUPER}}$ for these two periods are illustrated and quantified in Figure 4.4.

During the growth period in $50\text{km}_{\text{SUPER}}$, eddy-to-mean kinetic energy conversion and MKE extraction occur at rates of the same order of magnitude as $50\text{km}_{\text{EECON}}$ (10^7

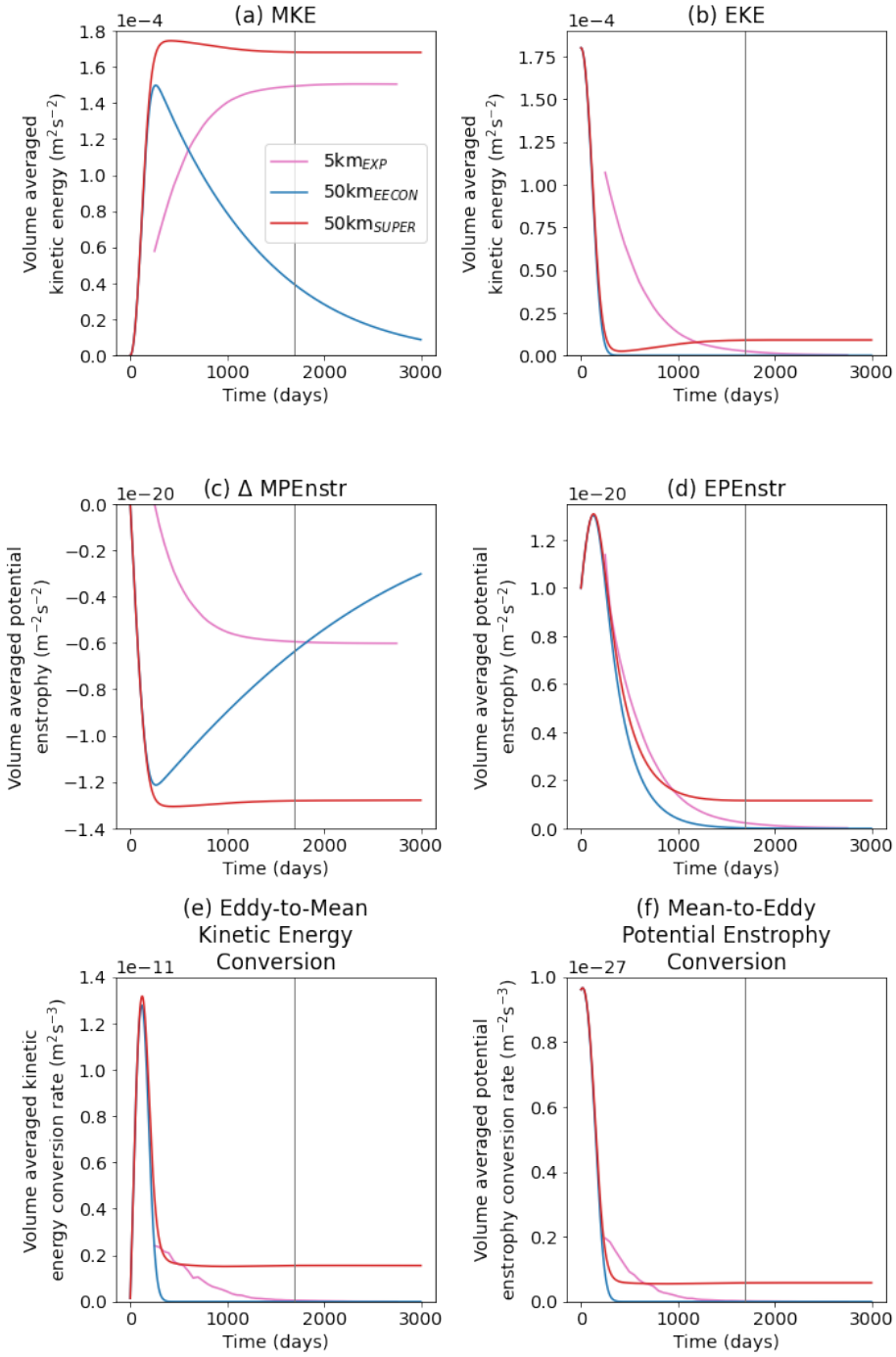

Figure 4.2: Volume-averaged (a) MKE; (b) EKE; (c) change in MPEnstr from initial value; (d) EPEnstr; (e) eddy-to-mean kinetic energy conversion, $-\overline{q'\mathbf{u}'} \cdot \nabla\psi$; and (f) mean-to-eddy potential enstrophy conversion, $-\overline{q'\mathbf{u}'} \cdot \nabla\overline{q}$, for 5km_{EXP} (pink), $50\text{km}_{\text{EECON}}$ (blue) and $50\text{km}_{\text{SUPER}}$ (red). For 5km_{EXP}, values shown are moving-window time-means calculated every 50 days over a 500-day period. For $50\text{km}_{\text{EECON}}$ and $50\text{km}_{\text{SUPER}}$, values shown are instantaneous values. Vertical lines indicate day 1691 of the simulation, used to distinguish between the period of growth (before the vertical line) and the quasi-steady period (after the vertical line) in $50\text{km}_{\text{SUPER}}$.

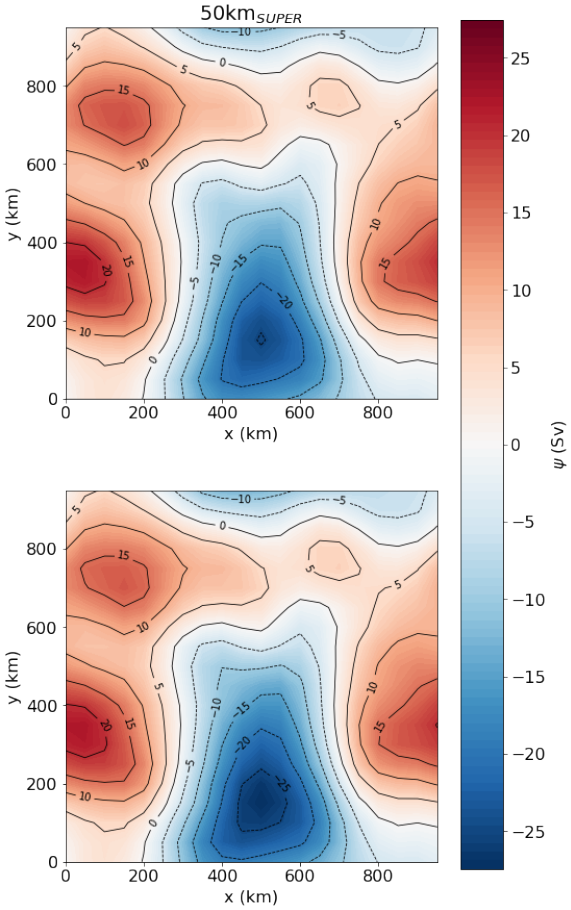

Figure 4.3: Time-mean transport stream function with labelled contours for 50km$_{\mathrm{SUPER}}$ over the time periods 0 - 1500 days (top) and 1501 - 3000 days (bottom).

W and 10^6 W, respectively). This leads to the growth of MKE seen in $50\text{km}_{\text{SUPER}}$ over this period (Figure 4.2). However, by including the kinetic energy supercharger mechanism, there is now an input of parameterized EKE which occurs at a rate of 10^6 W. Overall, these kinetic energy transfers lead to a growth of MKE and a depletion of EKE, similar to the behaviour of $50\text{km}_{\text{EECON}}$ during the growth period.

The EPEnstr extraction during the growth period is an order of magnitude larger than both the MPEnstr input by biharmonic diffusion, and the parameterized mean-to-eddy potential enstrophy conversion ($\mathcal{O}(10^{-12}$ m s^{-3}), $\mathcal{O}(10^{-13}$ m s^{-3}) and $\mathcal{O}(10^{-13}$ m s^{-3}), respectively). This leads to an overall extraction of potential enstrophy from the system during this period, also similar to the behaviour of $50\text{km}_{\text{EECON}}$. One difference is that the mean-to-eddy potential enstrophy conversion is an order of magnitude larger than that of $50\text{km}_{\text{EECON}}$ as a result of including the kinetic energy supercharger mechanism, but the extraction of potential enstrophy remains unchanged.

During the quasi-steady period in $50\text{km}_{\text{SUPER}}$, MKE is extracted by biharmonic diffusion, input to the parameterized EKE by the kinetic energy supercharger mechanism, and converted from parameterized EKE to MKE at approximately the same rates ($\mathcal{O}(10^6$ W)). That is, the system reaches a quasi-steady state in which these three processes are balanced. By design, the MKE extracted by biharmonic diffusion and input to the parameterized EKE by the kinetic energy supercharger mechanism will always balance. The quasi-steady state is reached when these two processes balance the parameterized eddy-to-mean kinetic energy conversion. Since the parameterized kinetic energy conversion depends linearly on γ_q, the value of γ_q may be important in setting the quasi-steady solution when the kinetic energy supercharger mechanism is employed. We investigate this hypothesis in Section 4.3.3.

During the quasi-steady period, MPEnstr input by biharmonic diffusion, parameterized mean-to-eddy potential enstrophy conversion, and extraction of parameterized EPEnstr all occur with approximately the same rates ($\mathcal{O}(10^{-13}$ m s^{-3})). That is, the system reaches a quasi-steady state in which these three processes are balanced. This suggests that r_Λ, which sets the parameterized EPEnstr damping and thus the extraction of parameterized EPEnstr, may be important in setting the steady-state flow field. We investigate this hypothesis in Section 4.3.3.

In summary, we find that during the quasi-steady period in $50\text{km}_{\text{SUPER}}$, both the

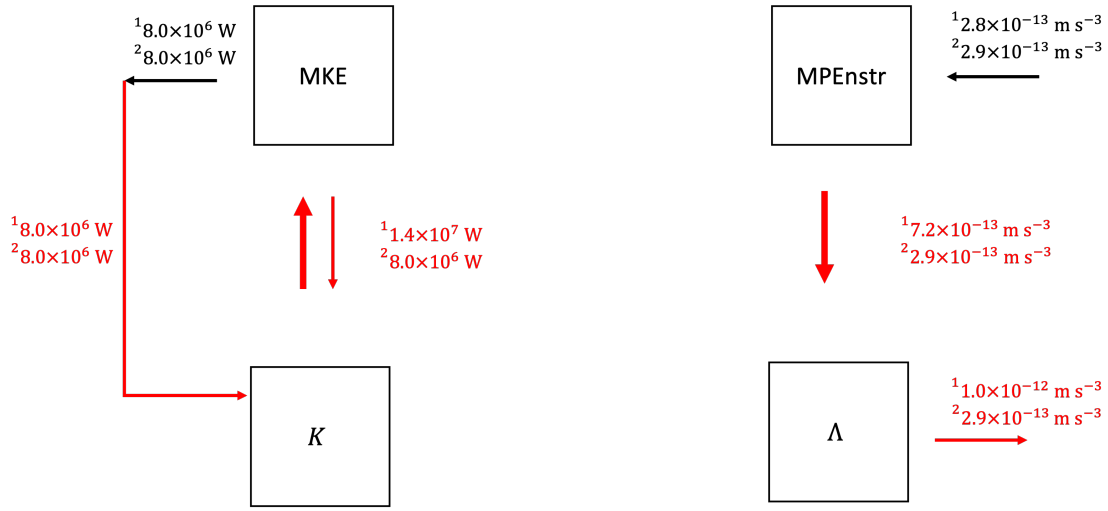

Figure 4.4: Kinetic energy and potential enstrophy transfers associated with the coarse-resolution simulation employing the parameterization with the additional kinetic energy supercharger mechanism, 50km$_{\text{SUPER}}$. Labels indicate the total (volume and time integrated) rates of kinetic energy/potential enstrophy transfer for the growth period (up to the solid vertical line in Figure 4.2, denoted by superscript 1) and the quasi-steady period (after the solid vertical line in Figure 4.2, denoted by superscript 2). Black arrows and numbers represent kinetic energy and potential enstrophy pathways resulting from biharmonic diffusion. Red arrows and numbers represent kinetic energy and potential enstrophy pathways associated with the parameterized barotropic eddies. In the case where there are two arrows, the dominant direction of transfer (and therefore the direction of the labelled transfer rate) is indicated by the bold arrow. Transfer rates associated with biharmonic diffusion are calculated as residuals.

kinetic energy and potential enstrophy transfers are approximately balanced. As a result, there is negligible net extraction or input of kinetic energy or potential enstrophy in the system. In contrast, during the quasi-steady period in 5km$_{\text{EXP}}$, there is a net extraction of both kinetic energy and potential enstrophy. However, these extractions are sufficiently small such that their effect on the volume averaged MKE and MPEnstr respectively are small (Figure 3.9). Thus, including the kinetic energy supercharger mechanism in the parameterization leads to a resolved quasi-steady flow that more closely resembles the behaviour of the quasi-steady flow in 5km$_{\text{EXP}}$ than the decaying flow in 50km$_{\text{EECON}}$.

4.3.3 Dependence of Quasi-Steady Solution on γ_q and r_Λ

We have seen that $50\text{km}_{\text{SUPER}}$ reaches a quasi-steady state in which there is negligible net extraction or input of kinetic energy and potential enstrophy in the system. This quasi-steady state is achieved through a balancing of the parameterized eddy-to-mean kinetic energy conversion with the extraction of MKE by biharmonic diffusion and subsequent reinjection of kinetic energy into the parameterized EKE budget by the supercharger mechanism, as well as the balancing of the parameterized mean-to-eddy potential enstrophy conversion with the MPEnstr input by biharmonic diffusion and the extraction of parameterized EPEnstr. We hypothesised that the eddy PV flux efficiency parameter, γ_q, and the parameterized EPEnstr damping parameter, r_Λ, are important in setting the steady-state solution since they exert some control over the parameterized eddy-to-mean kinetic energy conversion and the extraction of parameterized EPEnstr, respectively. Here, we investigate this hypothesis by performing sensitivity tests similar to those conducted in Section 3.4.4.

We first consider the effect of varying γ_q and r_Λ on the energetics of the system (Figure 4.5). The MKE of the quasi-steady state increases with increasing γ_q and decreasing r_Λ (Figure 4.5a). This is counteracted by a decrease in parameterized EKE with increasing γ_q and decreasing r_Λ (Figure 4.5b), such that the total kinetic energy (the sum of MKE and parameterized EKE) remains roughly constant as these parameters are varied (Figure 4.5c).

This variation in the energetics of the system as γ_q and r_Λ are varied can be explained by considering the kinetic energy transfers described in Sections 3.2.3 and 4.2.2 and plotted in Figure 4.6. When γ_q increases, the magnitude of the parameterized eddy-to-mean kinetic energy conversion increases (Figure 4.6a). As outlined in Section 4.3.2, the quasi-steady state is reached when the parameterized eddy-to-mean kinetic energy conversion is balanced by the extraction of MKE by biharmonic diffusion. Thus, increasing γ_q, leading to an increase in the parameterized eddy-to-mean kinetic energy conversion, results in a steady state in which the rate at which the MKE extracted by biharmonic diffusion is increased relative to the case with a smaller value of γ_q (Figure 4.6b). This increased rate of MKE extraction by biharmonic diffusion corresponds to a state of higher MKE (not shown). Physically, when γ_q is increased, the parameterized eddies are more efficient at fluxing PV and thus surrender their kinetic energy more efficiently to the large-scale flow (as shown by the decrease in timescale for depletion of parameterized EKE in Section 3.4.4). This

makes the parameterized eddies more effective at driving a large-scale flow, resulting in a more energetic large-scale flow.

To understand the effects of r_Λ on the energetics of the system, we consider the MPEnstr and parameterized EPEnstr values (Figure 4.7) and the potential enstrophy transfers outlined in Section 3.2.3 (Figure 4.8) associated with the quasi-steady state. We first note that the extraction of parameterized EPEnstr comes from the linear damping term in Equation 2.14, which is proportional to both r_Λ and the parameterized EPEnstr, Λ. We find that an increase in r_Λ leads to a decrease in the steady-state value of Λ (Figure 4.7b). Thus, there is a competing effect on the extraction of parameterized EPEnstr, with the increase in r_Λ acting to increase this extraction, and the subsequent decrease in steady-state Λ acting to decrease this extraction. The net effect is a decrease in the steady-state extraction of parameterized EPEnstr when r_Λ is increased (Figure 4.8c). That is, rather counter-intuitively, an increase in the parameterized EPEnstr damping rate, r_Λ, leads to a quasi-steady state in which the extraction of parameterized EPEnstr is decreased. We have seen in Section 4.3.2, that the quasi-steady state is reached when the MPEnstr input by biharmonic diffusion, the parameterized mean-to-eddy potential enstrophy conversion, and the parameterized EPEnstr extraction are all balanced. Thus, increasing r_Λ, resulting in a decrease in the extraction of parameterized EPEnstr, results in a steady state in which the MPEnstr input by biharmonic diffusion is also decreased (Figure 4.8a and 4.8b, respectively). In this setup, this MPEnstr input increases as the MKE increases (not shown) and hence, the quasi-steady state occurs for a decreased value of MKE.

We next consider the effect of varying γ_q and r_Λ on the enstrophetics of the system (Figures 4.7 and 4.8). The quasi-steady state parameterized EPEnstr is virtually unaffected by γ_q and decreases with increasing r_Λ (Figure 4.7b). The quasi-steady state MPEnstr decreases with increasing γ_q and decreasing r_Λ (Figure 4.7a). The MPEnstr tells us something about the state of PV homogenization of the resolved flow. Specifically, the smaller the MPEnstr, the closer the resolved flow is to PV homogenization. Therefore, increasing γ_q or decreasing r_Λ leads to a quasi-steady state in which the resolved PV is more mixed.

Let us consider why this is the case for γ_q. An increase in γ_q increases the quasi-steady state parameterized mean-to-eddy potential enstrophy conversion (Figure 4.8a). This parameterized mean-to-eddy potential enstrophy conversion is balanced by both the

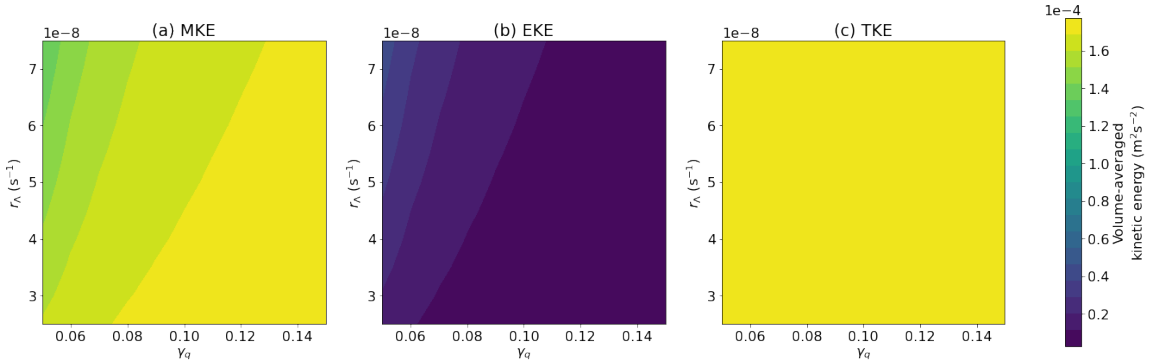

Figure 4.5: Quasi-steady (a) MKE; (b) parameterized EKE; and (c) total (mean + parameterized eddy) kinetic energy (contours) for a set of simulations with the same setup as $50\text{km}_{\text{SUPER}}$ in which r_Λ and γ_q are varied systematically by $\pm 50\%$ of their value in $50\text{km}_{\text{SUPER}}$. The γ_q values used are in the range 0.05 - 0.15 with an increment of 0.01. The r_Λ values used are in the range 2.5×10^{-8} s^{-1} - 7.5×10^{-8} s^{-1} with an increment of 0.5×10^{-8} s^{-1}. There are a total of 121 simulations.

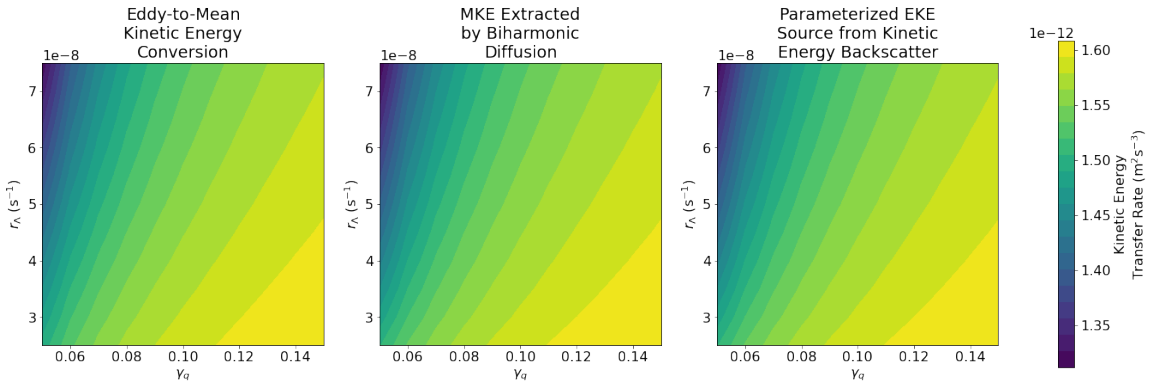

Figure 4.6: Quasi-steady volume-averaged (a) parameterized eddy-to-mean kinetic energy conversion; (b) MKE extraction by biharmonic diffusion; and (c) parameterized EKE source from the kinetic energy supercharger mechanism (contours) for a set of simulations with the same setup as $50\text{km}_{\text{SUPER}}$ in which r_Λ and γ_q are varied systematically by $\pm 50\%$ of their value in $50\text{km}_{\text{SUPER}}$. The γ_q values used are in the range 0.05 - 0.15 with an increment of 0.01. The r_Λ values used are in the range 2.5×10^{-8} s^{-1} - 7.5×10^{-8} s^{-1} with an increment of 0.5×10^{-8} s^{-1}. There are a total of 121 simulations.

MPEnstr input by biharmonic diffusion and the extraction of parameterized EPEnstr for all but small values of r_Λ (Figure 4.8). Thus, increasing γ_q leads to an increase in the quasi-steady state MPEnstr input from biharmonic diffusion relative to the case with a smaller γ_q. In this setup, this source of MPEnstr increases as the MPEnstr decreases (not shown). Thus, a quasi-steady state is reached in which the MPEnstr is decreased, and hence the PV of the resolved flow is more mixed, relative to the case with a smaller value of γ_q. Physically, increasing γ_q increases the efficiency of the parameterized eddies to flux PV down-gradient, i.e. it amplifies the PV mixing by the parameterized eddies.

Now, let us consider the relationship between r_Λ and the state of resolved PV homogenization. An increase in r_Λ decreases the quasi-steady state extraction of parameterized EPEnstr (Figure 4.8c). This extraction of parameterized EPEnstr is balanced by both the parameterized mean-to-eddy potential enstrophy conversion and the MPEnstr input by biharmonic diffusion for all but small values of r_Λ (Figure 4.8). Thus, increasing r_Λ leads to a decrease in the steady-state MPEnstr source from biharmonic diffusion. In this setup, this source of MPEnstr decreases as the MPEnstr increases (not shown). Thus, a steady state is reached in which the MPEnstr is increased, and hence the PV of the resolved flow is less mixed relative to the case with a smaller value of r_Λ.

As seen in Section 2.4, mixing of PV by the parameterized eddies is directly related to the parameterized mean-to-eddy potential enstrophy conversion. Specifically, when the parameterized eddies mix resolved PV in the presence of a background PV gradient, potential enstrophy is converted from the mean component to the parameterized eddy component. This parameterized mean-to-eddy potential enstrophy conversion can therefore be thought of as a direct cascade of potential enstrophy. Thus, the value of r_Λ controls, at least in part, the strength of the parameterized direct potential enstrophy cascade.

The transfers of kinetic energy (Figure 4.6) are approximately balanced for all values of γ_q and r_Λ tested. In contrast, the transfers of potential enstrophy (Figure 4.8) are approximately balanced except for small values of r_Λ. In the case of small r_Λ, the extraction of parameterized EPEnstr is larger than the MPEnstr source from biharmonic diffusion and the parameterized mean-to-eddy potential enstrophy conversion. This would lead to an overall extraction of potential enstrophy in the system, which

is consistent with the transfers of potential enstrophy during the quasi-steady period of the eddy-resolving simulation, 5km_{EXP}.

4.4 Summary and Discussion

In this chapter, we incorporated a kinetic energy supercharger mechanism into the parameterization outlined in Chapter 2. The incorporation of this mechanism was motivated by the kinetic energy and potential enstrophy transfers exhibited by the parameterized simulation in Chapter 3 (i.e. without the kinetic energy supercharger mechanism), $50\text{km}_{\text{EECON}}$. Specifically, $50\text{km}_{\text{EECON}}$ exhibited a net extraction of kinetic energy and a net input of potential enstrophy in the later part of the simulation. The magnitudes of kinetic energy extraction and potential enstrophy input were sufficient to bring the flow to a state of rest. This is in contrast to the eddy-resolving simulation in Chapter 3, 5km_{EXP}, which exhibited a net extraction of both kinetic energy and potential enstrophy. The magnitudes of these extraction rates were sufficiently small such that the flow reached a quasi-steady state.

The kinetic energy extraction and potential enstrophy input exhibited by $50\text{km}_{\text{EECON}}$ in Chapter 3 were caused by the depletion of parameterized EKE, which effectively turned off the parameterized conversion terms. This led us to incorporate the kinetic energy supercharger mechanism into the parameterization, which replenishes the parameterized EKE from the MKE extracted by biharmonic diffusion.

We find that, with the additional kinetic energy supercharger mechanism employed, the simulation reaches a quasi-steady state in which both kinetic energy and potential enstrophy are approximately conserved. This contrasts with the quasi-steady period of 5km_{EXP} in which there is a net extraction of both kinetic energy and potential enstrophy. Nonetheless, the behaviour of the resolved kinetic energy and potential enstrophy in $50\text{km}_{\text{SUPER}}$ more closely resemble that of 5km_{EXP} than those of $50\text{km}_{\text{EECON}}$, i.e. without the supercharger mechanism (Figure 4.2).

In the parameterized setup employing the kinetic energy supercharger mechanism, the values of the eddy PV flux efficiency parameter, γ_q, and the parameterized EPEnstr damping parameter, r_Λ, are important in determining the quasi-steady solution. Increasing γ_q results in an increase to the quasi-steady MKE and a decrease to the

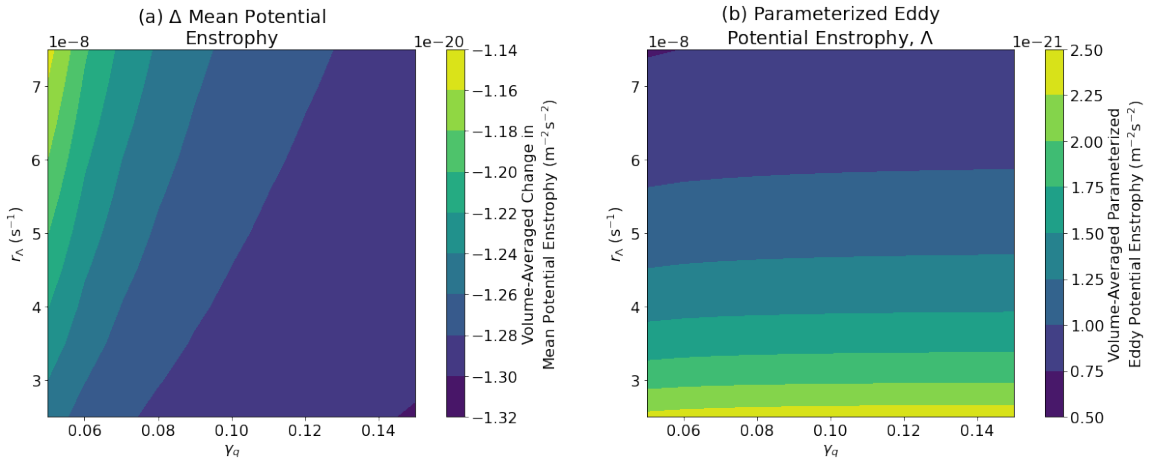

Figure 4.7: Quasi-steady (a) change in MPEnstr from initial conditions; and (b) parameterized EPEnstr, Λ (contours), for a set of simulations with the same setup as $50\text{km}_{\text{SUPER}}$ in which r_Λ and γ_q are varied systematically by $\pm 50\%$ of their value in $50\text{km}_{\text{SUPER}}$. The γ_q values used are in the range 0.05 - 0.15 with an increment of 0.01. The r_Λ values used are in the range 2.5×10^{-8} s^{-1} - 7.5×10^{-8} s^{-1} with an increment of 0.5×10^{-8} s^{-1}. There are a total of 121 simulations.

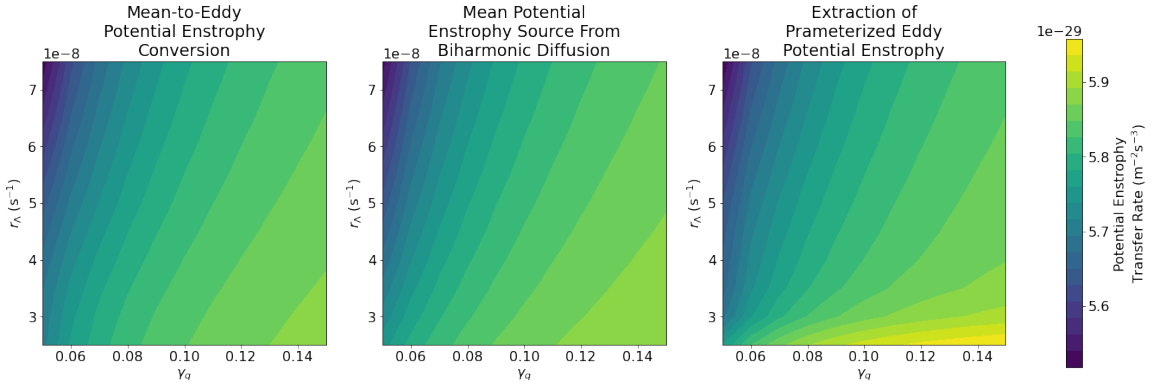

Figure 4.8: Quasi-steady volume-averaged (a) mean-to-eddy potential enstrophy conversion; (b) MPEnstr source from biharmonic diffusion; and (c) extraction of parameterized EPEnstr (contours) for a set of simulations with the same setup as $50\text{km}_{\text{SUPER}}$ in which r_Λ and γ_q are varied systematically by $\pm 50\%$ of their value in $50\text{km}_{\text{SUPER}}$. The γ_q values used are in the range 0.05 - 0.15 with an increment of 0.01. The r_Λ values used are in the range 2.5×10^{-8} s^{-1} - 7.5×10^{-8} s^{-1} with an increment of 0.5×10^{-8} s^{-1}. There are a total of 121 simulations.

quasi-steady MPEnstr, i.e. an increase in resolved PV mixing. Physically, increasing γ_q increases the efficiency of the parameterized eddies to flux PV, resulting in a flow in which the resolved PV is more mixed. It also increases the parameterized eddy-to-mean kinetic energy conversion, resulting in a more energetic resolved flow. Increasing r_Λ results in a decrease to the quasi-steady MKE and an increase in the quasi-steady MPEnstr, i.e. a decrease in resolved PV mixing.

One aspect of the kinetic energy supercharger mechanism which is not optimal is the non-locality of the mechanism. In the implementation of the supercharger mechanism, we effectively redistribute the kinetic energy extracted by biharmonic diffusion across the domain by defining, everywhere, the parameterized EKE source term as the volume-averaged extracted kinetic energy. Ideally, this mechanism would function such that MKE extracted by biharmonic diffusion is reinjected locally into the parameterized EKE budget. Figure 4.9 shows the results of a simulation identical to $50\text{km}_{\text{SUPER}}$ in which the kinetic energy reinjection occurs locally, which we refer to as $50\text{km}^*_{\text{SUPER}}$. That is, in which K_{SUPER} in Equation 5.21 is defined as

$$K_{\text{SUPER}} = -\mu_\xi \overline{\psi} \nabla^4 \text{H} \overline{q}. \tag{4.4}$$

Initially, the behaviour in $50\text{km}^*_{\text{SUPER}}$ (Figure 4.9) is similar to that of $50\text{km}_{\text{SUPER}}$ (Figure 4.2): the eddy-to-mean KE conversion is positive, leading to an increase in MKE and a decrease in parameterized EKE; and the mean-to-eddy potential enstrophy conversion is positive, leading to an increase in parameterized EPEnstr, and a decrease in MPEnstr. However, a quasi-steady state is not reached in $50\text{km}^*_{\text{SUPER}}$. Instead, at around 250 days, there is a continued increase in the parameterized EKE, the MKE and the eddy-to-mean kinetic energy conversion; and a continued decrease in the MPEnstr. It is not obvious from the simulations what causes this change, nor why it would occur when the kinetic energy reinjection occurs locally. It is interesting to note, however, that the final MKE in $50\text{km}^*_{\text{SUPER}}$ is still an order of magnitude smaller than the final MKE in $50\text{km}_{\text{UNCON}}$, the coarse-resolution simulation employing an unconstrained down-gradient PV mixing parameterization, described and analysed in Chapter 3, emphasising how absurd the results of $50\text{km}_{\text{UNCON}}$ are.

Another difficulty with the kinetic energy supercharger mechanism is that it is not easily implemented in a domain with land boundaries. In such a setup, with the biharmonic diffusion term employed here (Equation 3.2), the boundary conditions

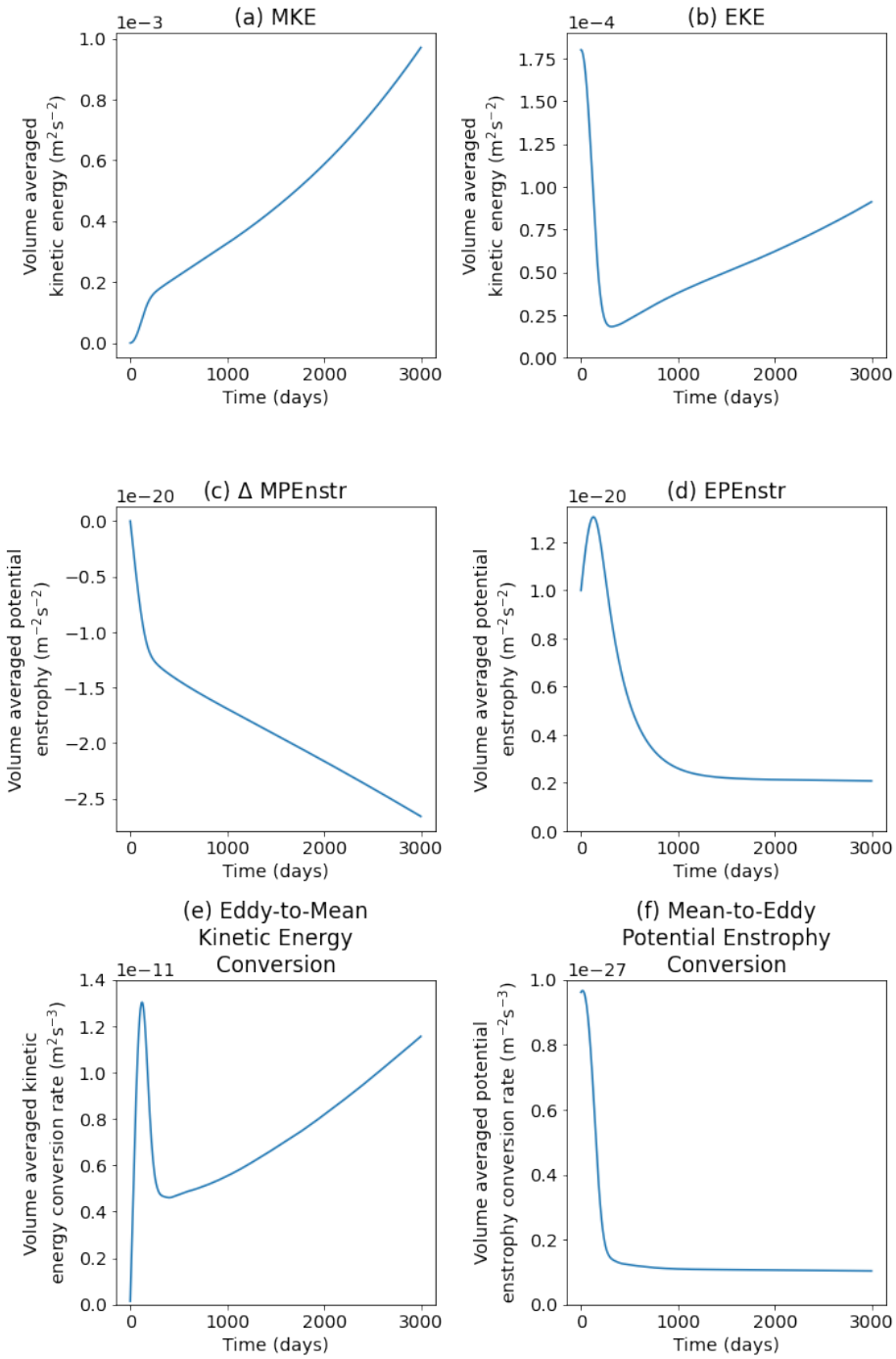

Figure 4.9: Volume-averaged (a) MKE; (b) EKE; (c) change in MPEnstr from initial value; (d) EPEnstr; (e) eddy-to-mean kinetic energy conversion, $-\overline{q'\mathbf{u}'} \cdot \nabla\psi$; and (f) mean-to-eddy potential enstrophy conversion, $-\overline{q'\mathbf{u}'} \cdot \nabla\overline{q}$, for $50\text{km}^*_{\text{SUPER}}$.

required to ensure that biharmonic diffusion acts as a net sink of MKE are: $\overline{\psi} = 0$, $\overline{\xi} = 0$, $\nabla^2\overline{\xi}$, $\nabla\overline{\psi} = 0$, and $\nabla^2\overline{\psi} = 0$. The first three of these conditions are fairly easily implemented, but the final two are rather complicated to implement, particularly in a domain with variable topography.

Despite these shortcomings of the kinetic energy supercharger mechanism, the results of this chapter are promising in that a quasi-steady state is reached which more closely resembles that of the eddy-resolving simulation than the parameterized simulation without the kinetic energy supercharger mechanism. They also highlight how the use of parameterized budgets enables other kinetic energy and/or potential enstrophy pathways to be parameterized by incorporating them into the budget. We utilise this aspect of the budgets in the following chapter to parameterize a specific energy pathway present in a baroclinic setup.

Chapter 5

Implementation in a Baroclinic Setup: GM+PV

5.1 Introduction

Thus far, we have outlined a new energetically and enstrophetically constrained parameterization for barotropic eddy PV fluxes (Chapter 2), and tested it in idealized barotropic simulations (Chapters 3 and 4). Any viable eddy parameterization must be implemented, and function as expected, in a baroclinic setup. In this chapter, we describe one method of implementing the parameterization in a baroclinic setup. For clarity, we refer to the parameterization of barotropic eddy PV fluxes outlined in Chapter 2 as the barotropic parameterization. One way of implementing the barotropic parameterization in a baroclinic setup would be to extend the parameterization to represent the effect of the baroclinic eddy PV fluxes. We instead choose to take inspiration from the GM+E parameterization (Bachman, 2019), in which the mean APE (MAPE) extracted from the system by GM90 is reinjected to resolved scales through the use of a negative Laplacian. Our approach is to reinject a fraction of the MAPE extracted from the system by GM90 into the barotropic EKE budget.

To explain the reasoning behind this approach, let us first revisit the behaviour of quasigeostrophic turbulence illustrated schematically in Figure 1.1. Energy and potential enstrophy are input to the ocean at large scales and cascade to small scales in the baroclinic modes. At scales close to the Rossby radius of deformation, baro-

clinic eddies convert MAPE to eddy energy - which consists of eddy APE (EAPE), barotropic EKE and baroclinic EKE - and convert a fraction of the MPEnstr to barotropic EPEnstr. Barotropic eddies then cascade the barotropic EKE preferentially to large scales and the barotropic EPEnstr to small scales in the barotropic mode. The process of conversion of MAPE to barotropic EKE by baroclinic eddies is known as barotropization.

Given the nature of the barotropic parameterization, we restrict our attention to parameterizing the conversion of MAPE to barotropic EKE, and the subsequent behaviour in the barotropic mode. We do not attempt to parameterize the behaviour of the EAPE nor of the baroclinic EKE. We assume a model setup in which the smallest resolved scale is larger than the Rossby radius of deformation, i.e. a non-eddying model.

We attempt to parameterize this behaviour using all the tools we have available to us. One such tool is the GM90 parameterization of baroclinic eddies. GM90 parameterizes the conversion of MAPE to eddy energy by baroclinic eddies as a flattening of isopycnals, thereby extracting MAPE from the system. This energy is effectively lost in the system, partly due to the fact that GM90 neglects the barotropic mode. By employing the barotropic parameterization alongside GM90, and reinjecting a fraction of the MAPE extracted by GM90 into the barotropic EKE budget, we parameterize the process of barotropization. The pre-existing kinetic energy conversion mechanism within the barotropic parameterization can subsequently transfer this reinjected energy to large scales, as demonstrated in Chapters 3 and 4, mimicking the indirect cascade of kinetic energy in the barotropic mode. The reinjection of extracted MAPE into the barotropic EKE budget is achieved in a similar manner to the kinetic energy supercharger mechanism in Chapter 4, specifically by including a term in the barotropic EKE budget which represents this energy conversion. We refer to this energy conversion mechanism within the barotropic parameterization as the APE-to-EKE conversion mechanism. Inspired by GM+E (Bachman, 2019), we refer to the implementation of the barotropic parameterization with the additional APE-to-EKE conversion mechanism alongside GM90 as GM+PV.

GM+PV (specifically the barotropic parameterization, with the additional APE-to-EKE conversion mechanism) is implemented in the Massachusetts Institute of Technology general circulation model (MITgcm, Marshall et al., 1997b,a). This imple-

mentation of GM+PV is employed and analysed in Chapter 6. In this chapter, we describe GM+PV in more detail, formulating the APE-to-EKE conversion mechanism, and outlining the implementation of GM+PV in MITgcm. We begin in Section 5.2 by considering the baroclinic/depth-varying horizontal momentum equations, and establishing how we will parameterize the eddy vorticity fluxes. In Section 5.3, we briefly explain how the eddy buoyancy fluxes are parameterized using the GM90 parameterization. In Section 5.4, we describe how the barotropic parameterization and GM90 are integrated through the APE-to-EKE conversion mechanism. In Section 5.5, we outline the implementation of the GM+PV into the baroclinic model equations in MITgcm. Finally, in Section 5.6, we summarise and discuss the method of implementation outlined in this chapter.

5.2 Parameterizing the Eddy Momentum Fluxes

The horizontal momentum equation in the hydrostatic primitive equations (modelled in the MITgcm) is

$$\frac{D_h \mathbf{u}_h}{Dt} + f\mathbf{k} \times \mathbf{u}_h + \frac{\nabla_h p}{\rho_0} = \mathbf{F}, \tag{5.1}$$

where D_h/Dt is the horizontal Lagrangian derivative, i.e. $\partial/\partial t + (\mathbf{u}_h \cdot \nabla_h)$, $\mathbf{u}_h$ is the horizontal velocity vector, ∇_h is the horizontal gradient operator, i.e. $(\partial/\partial x, \partial/\partial y)$ and $\mathbf{F}$ represents horizontal momentum forcing. By taking a time average of Equation 5.1, we obtain the time-averaged horizontal momentum equation,

$$\frac{D_h \overline{\mathbf{u}}_h}{Dt} + f\mathbf{k} \times \overline{\mathbf{u}}_h + \frac{\nabla_h \overline{p}}{\rho_0} + \nabla\left(\frac{\overline{\mathbf{u}'_h \cdot \mathbf{u}'_h}}{2}\right) = \overline{\mathbf{F}} - \mathbf{k} \times \overline{\zeta' \mathbf{u}'_h}. \tag{5.2}$$

Thus, the time-mean horizontal eddy vorticity fluxes, $\overline{\zeta' \mathbf{u}'_h}$, influence the time-mean horizontal momentum through the second term on the right hand side of Equation 5.2. This eddy vorticity flux term will have vertical structure in a baroclinic model since both the horizontal velocity perturbation, $\mathbf{u}'_h$ and the relative vorticity perturbation, ζ' will have vertical structure. However, as described above, we do not attempt to parameterize the baroclinic EKE or EAPE. Thus, we consider only the barotropic relative vorticity fluxes and parameterize this term as a barotropic, i.e. a depth-independent, forcing using the barotropic parameterization described in Chapter 2.

5.3 Parameterizing the Eddy Buoyancy Fluxes

We choose to parameterize the eddy buoyancy fluxes using the GM90 parameterization of baroclinic eddies. This can be derived in a general framework, but is most easily described in a quasigeostrophic framework following Gent et al. (1995). In this framework, the quasigeostrophic buoyancy equation is

$$\frac{D_h b}{Dt} + wN^2 = 0, \tag{5.3}$$

where b is the buoyancy, w is the ageostrophic vertical velocity, and N^2 is the buoyancy frequency which is a function of z only under quasigeostrophic assumptions and which is defined as $N^2 = \partial\overline{b}/\partial z$. By taking a time average of Equation 5.3, we obtain the time-mean buoyancy equation,

$$\frac{\partial \overline{b}}{\partial t} + \nabla_h \cdot \overline{\mathbf{u}}_h \overline{b} + \overline{w} N^2 = -\nabla_h \cdot \overline{\mathbf{u}_h' b'}, \tag{5.4}$$

where $\mathbf{u}_h$ is the geostrophic velocity and is therefore non-divergent. Thus, the horizontal eddy buoyancy fluxes, $\overline{\mathbf{u}_h' b'}$, influence the time-mean buoyancy through their divergence on the right hand side of Equation 5.4. GM90 defines w^*, the so-called eddy bolus velocity, as

$$w^* = \nabla_h \cdot \left(\frac{\overline{\mathbf{u}_h' b'}}{N^2} \right), \tag{5.5}$$

such that Equation 5.4 may be written as

$$\frac{D_h \overline{b}}{Dt} + (\overline{w} + w^*) N^2 = 0, \tag{5.6}$$

and parameterizes $\overline{\mathbf{u}_h' b'}$ as

$$\overline{\mathbf{u}_h' b'} = -\kappa_{\mathrm{GM}} \nabla_h \overline{b}. \tag{5.7}$$

GM90 steps forward the modified version of the time-mean buoyancy equation (Equation 5.6) with the eddy bolus velocity parameterized using the Equation 5.7. In the more general framework of the hydrostatic primitive equations employed in MITgcm, and which we utilise in Chapter 6, the horizontal gradient of isoneutral density, σ, is used in Equation 5.7 in place of the horizontal buoyancy gradient.

5.4 Integrating the Barotropic and Baroclinic Parameterizations

We have established that we will parameterize the barotropic eddy vorticity fluxes as a purely barotropic forcing by employing the energy- and enstrophy-constrained parameterization described in Chapter 2, and that we will parameterize the eddy buoyancy fluxes using the GM90 parameterization. In practice, GM90 acts to adiabatically flatten neutral density surfaces by extracting APE from the resolved flow, and thus acts as a mean energy sink. In reality, baroclinic eddies are not directly a sink of total system energy. Instead, they convert APE to eddy energy, a portion of which becomes barotropic EKE through the process of barotropization (Salmon, 1998). We proceed to integrate the barotropic parameterization with GM90 by incorporating a mechanism through which APE extracted by GM90 can be converted to barotropic EKE. Practically, this APE-to-EKE conversion mechanism is achieved by calculating the APE extracted from the system by GM90, and redirecting a fraction of this energy into the barotropic EKE budget of the barotropic parameterization as a source term.

To formulate the APE-to-EKE conversion mechanism, we consider a quasigeostrophic framework to simplify the problem. We begin by calculating the APE extracted from the system by GM90. The resolved potential energy (PE) is given by

$$\mathrm{PE} = \int \overline{\rho} g z \, dz \tag{5.8}$$

$$= -\rho_0 \int \overline{b} z \, dz + \text{constant}, \tag{5.9}$$

where g is the gravity. We consider the change in PE due to the baroclinic eddies. We find that,

$$\frac{D^* \mathrm{PE}}{Dt} = -\rho_0 \int \frac{D^* \overline{b} z}{Dt} \, dz \tag{5.10}$$

$$= -\rho_0 \int \overline{b} \frac{D^* z}{Dt} + z \frac{D^* \overline{b}}{Dt} \, dz, \tag{5.11}$$

where D^*/Dt is the rate of change following the baroclinic eddies only.

We now consider the case in which we employ GM90 to parameterize the baroclinic eddies, that is, we consider Equation 5.11 in which D^*/Dt is the rate of change following the GM90-parameterized baroclinic eddies. In this case, $D^*\overline{b}/Dt$ is zero because GM90 is designed such that the buoyancy following the parameterized baroclinic eddying flow remains constant[1]. Thus, we are left with the first term on the right hand side of Equation 5.11. Since $D^*z/Dt = w^*$, where w^* is the GM90-parameterized bolus velocity, we find that

$$\frac{D^*\mathrm{PE}}{Dt} = -\rho_0 \int \overline{b} w^* \, dz. \tag{5.12}$$

Thus, it remains to evaluate $\overline{b}w^*$. In the quasigeostrophic framework, this can be calculated making use of Equations 5.5 and 5.7. We find that

$$w^* = \nabla_h \cdot \left(\frac{-\kappa_{\mathrm{GM}} \nabla_h \overline{b}}{N^2} \right) \tag{5.13}$$

$$= -\kappa_{\mathrm{GM}} \nabla_h^2 \left(\frac{\overline{b}}{N^2} \right), \tag{5.14}$$

where we have assumed κ_{GM} is constant in the horizontal, and we have used the fact that N is a function of z only under quasigeostrophic assumptions. Multiplying by $\overline{b}$, we obtain the following

$$\overline{b}w^* = -\overline{b}\kappa_{\mathrm{GM}} \nabla_h^2 \left(\frac{\overline{b}}{N^2} \right) \tag{5.15}$$

$$= -\kappa_{\mathrm{GM}} \nabla_h \cdot \left(\overline{b} \nabla_h \left(\frac{\overline{b}}{N^2} \right) \right) + \kappa_{\mathrm{GM}} \nabla_h \left(\frac{\overline{b}}{N^2} \right) \cdot \nabla_h \overline{b} \tag{5.16}$$

$$= -\kappa_{\mathrm{GM}} \nabla_h \cdot \left(\overline{b} \nabla_h \left(\frac{\overline{b}}{N^2} \right) \right) + \kappa_{\mathrm{GM}} \frac{\left(\nabla_h \overline{b} \right)^2}{N^2}. \tag{5.17}$$

[1] More precisely, it is designed such that the density following the parameterized baroclinic eddying flow remains constant.

When we integrate Equation 5.17 over the domain volume, we find that

$$\int_V \overline{b}w^* \, dV = \int_V \kappa_{\mathrm{GM}} \frac{\left(\nabla_h \overline{b}\right)^2}{N^2} \, dV, \tag{5.18}$$

as the first term on the right hand side of Equation 5.17 integrates to zero since $\nabla_h \overline{b} = 0$ on lateral boundaries. Combining Equations 5.12 and 5.18 yields the following

$$\frac{D^*}{Dt} \int_A \mathrm{PE} \, dA = -\rho_0 \int_V \kappa_{\mathrm{GM}} \frac{\left(\nabla_h \overline{b}\right)^2}{N^2} \, dV. \tag{5.19}$$

Equation 5.19 quantifies the total amount of (available) PE extracted from the system by GM90. In reality, this extracted APE is converted to eddy energy, a portion of which becomes barotropic EKE. We propose to reinject a fraction of this extracted APE into the parameterized barotropic EKE budget, thus mimicking the APE-to-EKE conversion which occurs due to baroclinic instability.

It should be noted that the conversion of energy from APE to barotropic EKE does not necessarily occur locally. Indeed, Equation 5.19 indicates that the amount of APE extracted from the system by GM90 can be calculated from the horizontal gradients of buoyancy only in the domain integral. Internal fluxes will redistribute the energy concurrently as it is converted from APE to barotropic EKE by the baroclinic eddies. However, this conversion of energy is commonly assumed to be local in various eddy parameterization methods (e.g. Eden and Greatbatch, 2008; Mak et al., 2017, 2018) and we make this same assumption here. That is, we assume that

$$\frac{D^*\mathrm{PE}}{Dt} = -\rho_0 \kappa_{\mathrm{GM}} \frac{\left(\nabla_h \overline{b}\right)^2}{N^2}. \tag{5.20}$$

We then reinject a portion of this extracted APE into the parameterized barotropic EKE budget[2]. Since this EKE budget is a barotropic (i.e. depth-averaged) budget, we include the depth-average of the right hand side of Equation 5.20 as a source term in the parameterized barotropic EKE budget. Thus, the parameterized barotropic EKE budget with the additional APE-to-EKE conversion mechanism is

$$\frac{\partial K}{\partial t} = \overline{q'\mathbf{u}'} \cdot \nabla \overline{\psi} - \frac{1}{\mathrm{H}} \nabla \cdot (K \mathrm{H} \overline{\mathbf{u}}) + \frac{\mu}{\mathrm{H}} \nabla^2 \mathrm{H} K - r_K K + \lambda K_{\mathrm{APE}}, \tag{5.21}$$

[2]We remove the factor of ρ_0 in Equation 5.20 when adding this value to the parameterized EKE budget because the EKE in the parameterized eddy PV fluxes (Equation 2.9) is the specific EKE (Equation 2.7) and hence we employ a specific EKE budget.

where λ is a constant which represents the fraction of the extracted APE which is converted to barotropic EKE and K_{APE} is the depth-averaged APE extracted by GM90, defined as

$$K_{\mathrm{APE}} = \frac{1}{\mathrm{H}} \int_{\mathrm{H}} \kappa_{\mathrm{GM}} \frac{\left(\nabla_h \bar{b}\right)^2}{N^2} \, dz. \tag{5.22}$$

In this integration, we make no changes to the parameterized barotropic EPEnstr budget and thus we employ the budget as described in Chapter 2 (Equation 2.14). The combination of GM90 and the barotropic parameterization with the additional APE-to-EKE conversion mechanism described above constitutes the GM+PV parameterization.

5.5 GM+PV Implementation in MITgcm

Thus far in this chapter, we have described the GM+PV parameterization by outlining a parameterization for the barotropic eddy vorticity fluxes and the baroclinic eddy buoyancy fluxes, and have adapted the barotropic parameterization to include the APE-to-EKE conversion mechanism. This mechanism effectively integrates GM90 with the barotropic parameterization by parameterizing the energy pathway in which MAPE extracted by baroclinic eddies is converted to barotropic EKE. We now proceed to describe the numerical implementation of GM+PV in MITgcm.

We first make the assumption that the relative vorticity (ξ) is much smaller than the planetary vorticity (f) and that the PV (q) is therefore well approximated by f/H. In the simulations analysed in Chapter 6, we find this assumption to be true (not shown). For simplicity, the parameterization is implemented in MITgcm with $q = f/\mathrm{H}$.

Both the parameterized barotropic EKE budget with the additional APE-to-EKE conversion mechanism (Equation 5.21) and the parameterized barotropic EPEnstr budget (Equation 2.14) are implemented and stepped forward in time in MITgcm using the third-order Adams-Bashforth method (Durran, 1991), for which there exists a pre-existing function within the MITgcm code which we utilise. Advective and diffusive terms in both the EKE and EPEnstr budgets are calculated using the flux form with no flux lateral boundary conditions at land boundaries. The kinetic conversion

and potential enstrophy conversion terms in the parameterized barotropic EKE and EPEnstr budgets, respectively, are implemented as outlined in Section 3.2.2.2.

We now outline the numerical implementation of the APE-to-EKE conversion term described in Equation 5.22. We begin by noting that the formulation described in Section 5.4 assumes a quasigeostrophic framework, whereas, in MITgcm, the hydrostatic primitive equation framework is utilised. In such a framework, GM90 acts on horizontal gradients of isoneutral density, σ, rather than horizontal gradients of buoyancy, b (specifically, in Equation 5.7). Thus, the K_{APE} term in the parameterized barotropic EKE budget (Equation 5.21) depends on the horizontal gradients of σ in place of the horizontal buoyancy gradients. Specifically, in the MITgcm implementation of GM+PV, we have

$$K_{\mathrm{APE}} = \frac{1}{\mathrm{H}} \int_{\mathrm{H}} \kappa_{\mathrm{GM}} \frac{(\nabla_h \overline{\sigma})^2}{N^2} \, dz. \tag{5.23}$$

Expanding the right hand side in Equation 5.23 yields

$$K_{\mathrm{APE}} = \underbrace{\frac{1}{\mathrm{H}} \int_{\mathrm{H}} \kappa_{\mathrm{GM}} \frac{(\partial_x \overline{\sigma})^2}{N^2} \, dz}_{K^x_{\mathrm{APE}}} + \underbrace{\frac{1}{\mathrm{H}} \int_{\mathrm{H}} \kappa_{\mathrm{GM}} \frac{(\partial_y \overline{\sigma})^2}{N^2} \, dz}_{K^y_{\mathrm{APE}}}. \tag{5.24}$$

We calculate the two terms in Equation 5.24 (K^x_{APE} and K^y_{APE}) separately. Figure 5.1 illustrates a single model grid box with labelled points to help visualise the numerical implementation of K_{APE}. We utilise the horizontal gradients of isoneutral density, σ, which are calculated in the pre-exisiting `gmredi` MITgcm package. Note, $\partial\sigma/\partial x$ is located at A points, $\partial\sigma/\partial y$ is located at B points, and $\partial\sigma/\partial z$ has two values located at C points and D points (Figure 5.1a). The integrands of K^x_{APE} and K^y_{APE} are calculated at C and D points by linearly interpolating $\partial\overline{\sigma}/\partial x$ and $\partial\overline{\sigma}/\partial y$ to C and D points respectively. The depth averages are then calculated from these points, giving K^x_{APE} and K^y_{APE} at $\mathrm{C_{2D}}$ and $\mathrm{D_{2D}}$ points. These depth-averaged values are linearly interpolated to E points to give K_{APE} at E points, where the parameterized EKE is located.

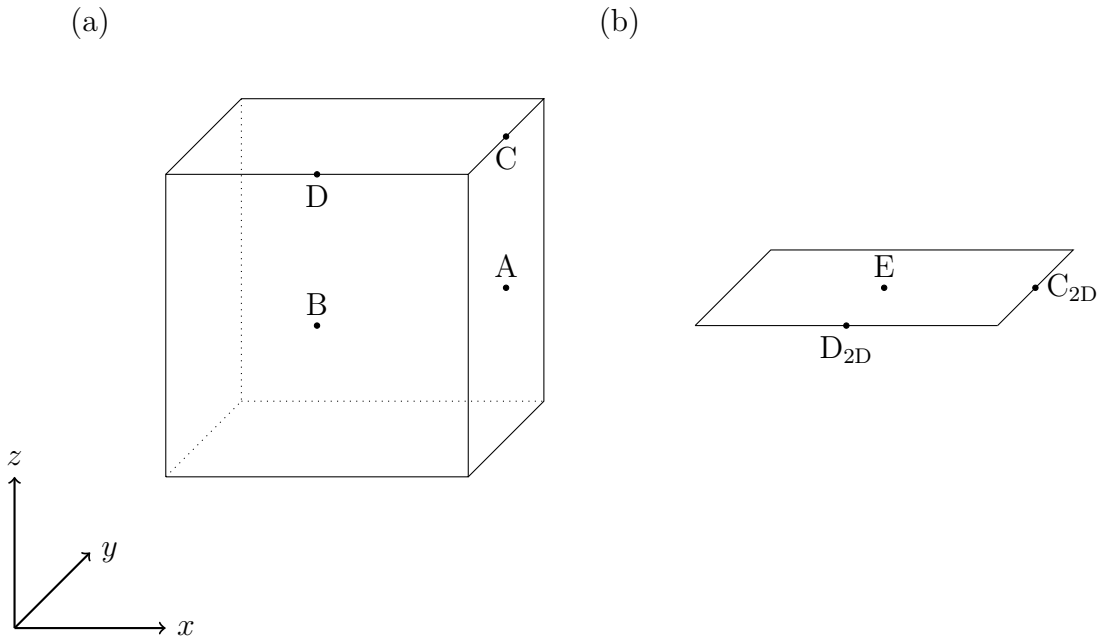

Figure 5.1: (a) A single model grid box with labelled points. Each grid point (and hence A, B, C and D points) are repeated in the x, y and z directions. (b) A two-dimensional model grid box. Each grid point (and hence C_{2D}, D_{2D} and E points) are repeated in the x and y directions.

5.6 Summary and Discussion

In this chapter, we have described one method for extending the parameterization of barotropic eddy PV fluxes described in Chapter 2 for use in a baroclinic setup. We choose to employ the barotropic parameterization to parameterize the barotropic eddies, employing budgets for the parameterized barotropic EKE and EPEnstr, alongside, and integrated with, the GM90 parameterization of baroclinic eddies. The two parameterizations are integrated by including an additional mechanism in the barotropic parameterization through which MAPE extracted from the system by GM90 is reinjected into the barotropic EKE budget. This mechanism mimics the conversion of APE to barotropic EKE which occurs in the barotropization process by baroclinic eddies. Inspired by GM+E (Bachman, 2019), we refer to this implementation of the barotropic parameterization with the additional APE-to-EKE conversion mechanism alongside GM90 as GM+PV.

The method of implementing the barotropic parameterization in a baroclinic setup described here constitutes just one approach to achieving this. As mentioned previously, another option would be to extend the parameterization described in Chapter 2 to represent the effect of the baroclinic eddy PV fluxes. This may be possible through a similar method to Gent et al. (1995), i.e. by first deriving the parameterized EKE and EPEnstr budgets, and the parameterized eddy PV fluxes in an isopycnal coordinate system, and then applying a transformation to height coordinates. This would be a much more complicated method than the GM+PV approach, and we opted not to take this route to prioritise ease of implementation, given that this is a preliminary test of the parameterization in a baroclinic setup.

Chapter 6

GM+PV in an Arctic Ocean Setup

6.1 Introduction

In Chapter 5, we outlined one method for implementing the parameterization in a baroclinic setup, which we refer to as GM+PV. Specifically, we parameterize the effect of barotropic eddy vorticity fluxes using the barotropic parameterization described in Chapter 2, and parameterize the effect of eddy buoyancy fluxes using the GM90 parameterization of baroclinic instability. We integrate these parameterizations by incorporating an APE-to-EKE conversion mechanism. Through this mechanism, APE extracted by GM90 is reinjected into the barotropic EKE budget, thus parameterizing the energy pathway in which APE is converted to barotropic EKE by baroclinic eddies in the process of barotropization. In this chapter, we test GM+PV in a semi-realistic model of the Arctic Ocean. We choose to test the parameterization in this setting since topography-following flows are prevalent in this region (Orvik and Niiler, 2002). There are many unique features of the Arctic Ocean which make it both a physically interesting region and a difficult region to accurately model. We begin by providing a brief summary of the geography and dynamics of the Arctic Ocean, and summarising some of the challenges in modelling the Arctic Ocean accurately.

The geography of the Arctic region is illustrated in Figure 6.1. The Amerasian Basin and the Eurasian Basin are divided by the Lomonosov Ridge. The Amerasian Basin is further subdivided into the Canada and Makarov Basins by the Mendeleev Ridge, and the Eurasian Basin is subdivided into the Amundsen and Nansen Basins by the Nansen-Gakkel Ridge. We refer to the region comprised of the Amerasian Basin, the

Eurasian Basin and the Lomonosov Ridge as the Arctic Basin. The Arctic Basin is connected to the Nordic Seas by Fram Strait and the Barents Sea. The Arctic Ocean is connected to the North Atlantic Ocean through the Greenland-Scotland Ridge and the Canadian Arctic Archipelago, and is connected to the Pacific Ocean through Bering Strait.

There are several aspects of the Arctic Ocean which make it's dynamics unique. One such feature is that, at the latitudes of the Arctic Ocean, the gradient of planetary vorticity, β, is negligible and Sverdrup balance is not a good approximation (Nøst and Isachsen, 2003). Instead, observational studies show that the surface flow follows the topographic features (Orvik and Niiler, 2002) with near-bottom currents which are comparable in strength to those in the rest of the water column (Woodgate et al., 2001). The precise mechanism through which the flow-field is driven to a topography-following state is unclear. Eddy-topography interactions, which we have parameterized in this thesis, may contribute (Nazarenko et al., 1998; Polyakov, 2001). Nøst and Isachsen (2003) propose another theory, in which the bottom geostrophic flow is forced by the portion of Ekman pumping at the surface which is not balanced by flow in the upper layers. This leads to a bottom geostrophic flow which is approximately parallel to topography contours. Despite the lack of consensus over what drives topography-following flows in the Arctic Ocean, the prevalence of such flows makes this setting a useful test site for the implementation of GM+PV in a semi-realistic configuration.

The dominant features of the flow field within the Arctic Basin consist of the Beaufort Gyre and the Arctic Circumpolar Boundary Current. The Beaufort Gyre is an anticyclonic gyre circulation located within the Canada Basin and is driven by the overlying anticyclonic winds. The Arctic Circumpolar Boundary Current is a cyclonic flow which propagates along the boundary of the Arctic Basin. Briefly, observations show that, Atlantic Water which is warm and salty relative to other water masses in the Arctic Ocean, enters the Arctic Basin on the eastern side of Fram Strait in the Fram Strait Branch (Beszczynska-Möller et al., 2012), and via the Barents Sea, where it is transformed to Barents Seawater (Pfirman et al., 1994), entering the Arctic Basin at St. Anna Trough in the Barents Seawater Branch (Rudels et al., 2004). Both branches propagate cyclonically around the perimeter of the Arctic Basin in the Arctic Circumpolar Boundary Current (Rudels et al., 2000). At the Lomonosov Ridge, modelling studies suggest that the boundary current splits, with some flow

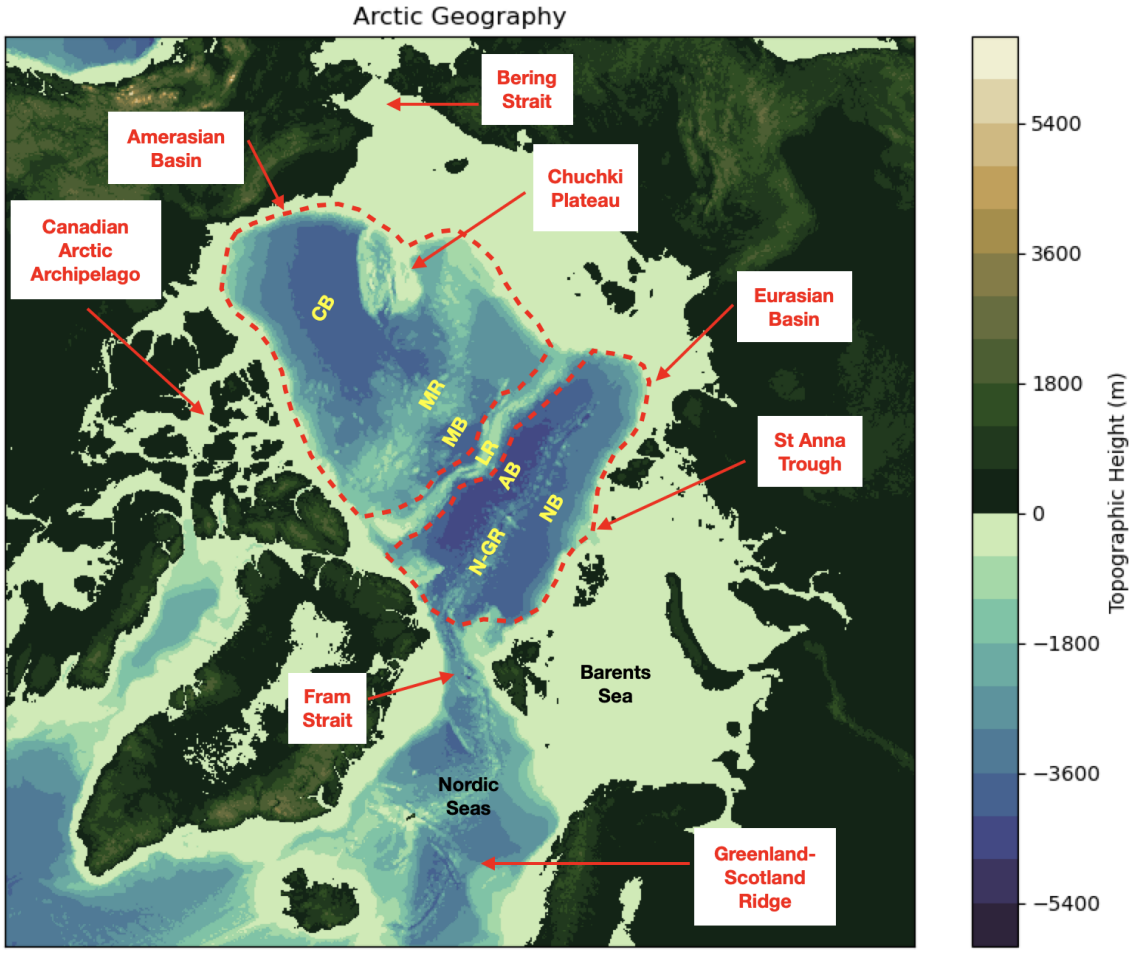

Figure 6.1: Topographic depth (filled contours) in the Arctic Ocean from the International Bathymetric Chart of the Arctic Ocean (IBCAO) version 4.2 (Martin et al., 2020) at 200m horizontal resolution. The Amerasian Basin and the Eurasian Basin (roughly indicated by red dashed lines) are divided by the Lomonosov Ridge (LR). In the Amerasian Basin, the Canada Basin (CB) and Makarov Basin (MB) are separated by the Mendeleev Ridge (MR). In the Eurasian Basin, the Amundsen Basin (AB) and the Nansen Basin (NB) are separated by the Nansen-Gakkel Ridge (N-GR). We refer to the region comprised of the Amerasian Basin, the Eurasian Basin and the Lomonosov Ridge as the Arctic Basin. The Arctic Basin is connected to the Nordic Seas through Fram Strait and the Barents Sea. The Arctic Ocean is connected to the North Atlantic Ocean by the Greenland-Scotland Ridge and the Canadian Arctic Archipelago, and is connected to the Pacific Ocean by Bering Strait.

returning towards Fram Strait along the Lomonosov Ridge, and some flow continuing on it's cyclonic path (Aksenov et al., 2011). Towards the end of this continued cyclonic propagation, water exits the Arctic Basin either through the Canadian Arctic Archipelago (Dickson et al., 2007) or through Fram Strait via the East Greenland Current (Beszczynska-Möller et al., 2012; Richter et al., 2018).

Another distinction between the Arctic Ocean and other lower latitude oceans, and an important feature driving unique Arctic Ocean dynamics, is that it is salinity stratified, with a vertical temperature profile which is more complex than decreasing monotonically with depth. In most of the Arctic Ocean, cold fresh waters reside in the upper layer, with Atlantic Ocean-derived warm salty waters at intermediate levels, and cold salty water in the abyssal regions (Timmermans and Marshall, 2020). The main sources of cold and fresh upper layer water are river discharge, precipitation, and relatively fresh Pacific Water which enters the Arctic Ocean through Bering Strait (Woodgate and Aagaard, 2005; Serreze et al., 2006; Haine et al., 2015).

The Arctic Ocean stratification profile is reinforced by the prevailing wind patterns in the region, which consist of the anticyclonic Beaufort High sitting above the Canada Basin (Serreze and Barrett, 2011) and the cyclonic Icelandic Low sitting above the Nordic Seas (Serreze et al., 1997). The Beaufort High induces an anticyclonic flow in the interior of the Canada Basin, known as the Beaufort Gyre (Proshutinsky et al., 2009). This anticyclonic flow leads to an accumulation of freshwater in the centre of the gyre, as well as downwelling. The latter causes a steepening of the isopycnals in this region. This behaviour, coupled with the stratification profile in which cold, fresh water sits above warm, salty water, inhibits the warm water below from reaching the surface, thus maintaining the halocline stratification and enabling the growth of sea ice by inhibiting fluxes of heat to the surface (Rudels et al., 1996). Baroclinic eddies are generated via baroclinic instability due to the inclined isopycnals in the Beaufort Gyre. These eddies act to flatten the isopycnals and balance the effect of the wind-driven circulation (Manucharyan and Spall, 2016). The presence of sea ice also acts to modulate the wind forcing, equilibrating the gyre and playing a crucial role in setting the gyre depth, freshwater content, and strength (Meneghello et al., 2018).

The unique features described above require extra consideration when modelling this system numerically. In particular, the propagation of Atlantic Water in the Arctic

Circumpolar Boundary Current is a feature which has proved difficult to accurately simulate in modelling studies of the Arctic Ocean: the strength, pattern, and even direction, of the propagation of Atlantic Water in the Arctic Ocean has been shown to vary by model setup. For example, Golubeva and Platov (2007) demonstrate that the inflow of Atlantic Water, as well as its subsequent circulation pattern within the Arctic Ocean, change as the model horizontal diffusion and viscosity are decreased. The prescription of strong horizontal diffusion and viscosity leads to anticyclonic propagation of Atlantic Water, while cyclonic propagation is produced for weaker values of prescribed horizontal diffusion and viscosity. However, this cyclonic propagation becomes unstable and separates into a cyclonic circulation in the Amerasian Basin and an anticyclonic circulation in the Eurasian Basin. Yang (2005) found that the flux of PV into the Arctic Ocean from the surrounding oceans can also change the direction of circulation. Specifically, a net positive flux of PV into the Arctic Basin typically leads to cyclonic circulation, while a net negative PV flux typically leads to anticyclonic circulation within the Arctic Basin.

Adding to the difficulty in modelling the propagation of Atlantic Water in the Arctic Circumpolar Boundary Current, is the uncertainty regarding the underlying mechanism responsible for driving said current. The flow is consistent with the theory of Nøst and Isachsen (2003), in which the flow field is obtained by integrating the wind-stress curl over closed topography contours. However, Aksenov et al. (2011) analysed both climate model data and observational data and concluded that the main mechanism responsible for driving the cyclonic Arctic Circumpolar Boundary Current is the inflow of PV into the Eurasian Basin through St. Anna Trough and into the Canada Basin through Bering Strait. Another theory is that the interaction of eddies with the seafloor, leading to rectified eddy-driven topography-following flows (Bretherton and Haidvogel, 1976), drives the Arctic Circumpolar Boundary Current (Nazarenko et al., 1998; Polyakov, 2001). This latter theory suggests that it is possible that the difficulty in simulating the Arctic Circumpolar Boundary Current, and thus the propagation of Atlantic Water in the Arctic Ocean, is due to the inadequate representation of the effects of mesoscale eddies in the model.

Representing mesoscale eddies in models of the Arctic Ocean is particularly difficult due to the small Rossby radius of deformation at high latitudes. Estimates from climatological data give a Rossby radius of deformation which varies from around $\mathcal{O}(1\text{ km})$ - $\mathcal{O}(10\text{ km})$ in the deep basins, and is $\mathcal{O}(1\text{ km})$ in the shelf regions and

across continental slopes (Nurser and Bacon, 2014; Timmermans and Marshall, 2020). Observations of halocline eddies in the Canada and Eurasian Basins support these estimates (Zhao et al., 2014). Accurate representation of these scales in models would require a horizontal resolution on the order of 1 km. In fact, by comparing simulations of the Arctic Ocean at different resolutions, Wang et al. (2020) argue that horizontal resolutions of *at least* 1 km are necessary to resolve mesoscale eddies in the Arctic Ocean. Such high resolutions are difficult to achieve, especially in global ocean models due to computational limits and consequently, mesoscale eddies in the Arctic Ocean are not typically well represented.

The idea that an improved representation of eddies in Arctic Ocean models may facilitate more accurate simulation of the Arctic Circumpolar Boundary Current is further supported by the results of the Neptune parameterization of mesoscale eddies (Holloway, 1992) in Arctic Ocean simulations. Neptune is based on the idea that eddies drive the flow towards a state of maximum entropy. In practice, and by design, Neptune drives the flow towards a topography-following state. In Arctic Ocean simulations, the inclusion of Neptune led to a consistent cyclonic flow at depth, which was not exhibited in simulations without Neptune (Nazarenko et al., 1998; Golubeva and Platov, 2007; Holloway and Wang, 2009). Nazarenko et al. (1998) also found that Neptune led to a more complicated flow structure in the Barents Sea, and an improved representation of the East Greenland Current. These results suggest that improving the representation of eddies, particularly eddy-topography interactions, may be important in modelling the Arctic Ocean.

In this chapter, we test GM+PV, described in Chapter 5, in a semi-realistic model of the Arctic Basin. We seek to answer the following three questions:

1. What effect does GM+PV have on the simulated flow field in the Arctic Basin?
2. How is the propagation of Atlantic Water in the Arctic Basin affected by employing GM+PV?
3. What is the behaviour of the energetics and enstrophetics when employing GM+PV in this baroclinic setup?

In Section 6.2 we describe the model setup employed. In Section 6.3, we analyse the results of these experiments. In Section 6.4, we summarise and discuss the results.

6.2 Model Setup

We employ the MITgcm to run semi-realistic simulations of the Arctic Basin. We use a semi-realistic Arctic setup consisting of a basin connected to a channel, similar to that used for example in Spall (2013) and Lique et al. (2015). The setup employed here is adapted from that of Lique et al. (2015) with the addition of realistic bathymetry. The setup is non-eddying, hence, all eddy effects are parameterized. In this section, we outline the model setup (Sections 6.2.1 - 6.2.7). Next, we outline the energy pathways associated with the simulations (Section 6.2.8). Finally, we briefly check the spinup of the simulations (Section 6.2.9).

6.2.1 Model Grid

The simulations are run on a cartesian grid using an Arakawa C-grid formation[1]. The domain has horizontal resolution of 50 km and 30 vertical levels ranging from 10 m depth at the surface to 500 m depth at the bottom of the domain. The bathymetry employed is shown in Figure 6.2 and is derived from the International Bathymetric Chart of the Arctic Ocean (IBCAO) version 4.2 (Martin et al., 2020) at 200 m horizontal resolution regridded using an area average to 50 km horizontal resolution. Depth values smaller than 600 m are set to 0 m to remove shelf regions. To create the channel region, an idealised representation of Fram Strait, the bathymetry in the region of Fram Strait is extended in the negative y direction and contours are closed on the southern boundary of the domain. This channel region contains restorative forcing regions (detailed below) which aim to represent the inflow and outflow of water to the Arctic Basin via Fram Strait. The entire bathymetry is then smoothed using `scipy.ndimage.median_filter`.

6.2.2 Model Parameters

The simulations use no slip boundary conditions for the bottom and lateral boundary conditions. Linear bottom drag is employed with a drag coefficient of 2×10^{-4} m s^{-1}. Horizontal and vertical Laplacian viscosity is used with coefficients of 5000 m^2 s^{-1} and 10^{-5} m^2 s^{-1}, respectively. Horizontal and vertical Laplacian diffusivities are set

[1]Of the spurious forces identified by Styles et al. (2022), the present configuration may exhibit forces due to cell thicknesses and model level steps. Spurious forces caused by variations in the planetary vorticity will not be present since we use the f-plane approximation.

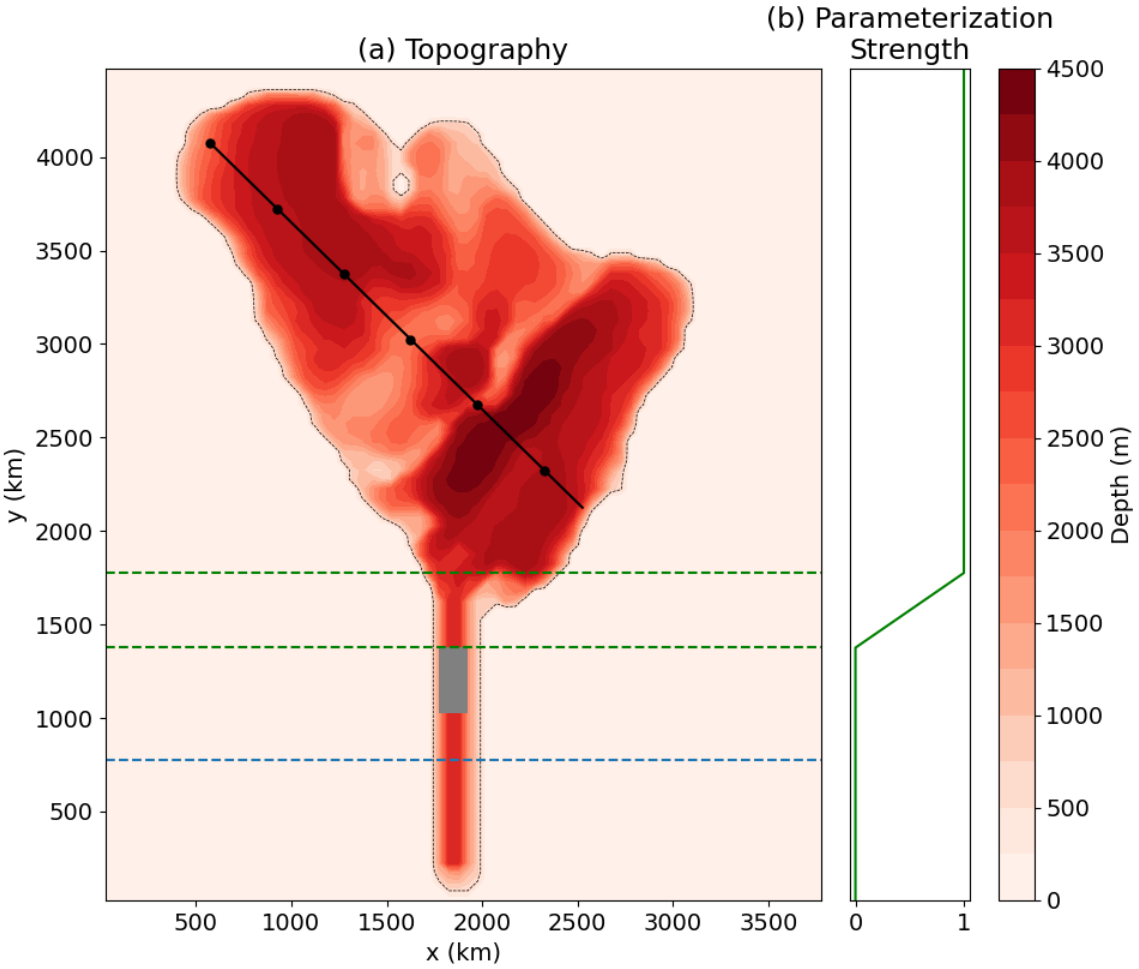

Figure 6.2: (a) Realistic bathymetry (m) shown by red filled contours. The black dashed line indicates land boundaries. The black solid line represents a transect along which values are plotted in Figures 6.10 and 6.14. Black markers along this line indicate distances along the transect in 500 km increments, starting from 0 km at the leftmost marker. The grey rectangle indicates the forcing region in which meridional velocity and temperature are restored on a timescale of one day, aiming to force an inflow and outflow of water at depth through Fram Strait. The region south of the horizontal blue dashed line is the sponge region in which temperature and salinity are restored to their initial profiles and zonal and meridional velocities are restored to zero. The barotropic parameterization is not applied in the channel region to ensure numerical stability. This is achieved by multiplying all barotropic parameterization terms by a parameterization strength, shown in panel (b). This constant is zero in the channel region, and increases linearly across a meridional length of 350 km to a value of 1, north of which it is 1 everywhere. The horizontal green dashed lines in panel (a) signify the limits of the linear increase in the parameterization strength.

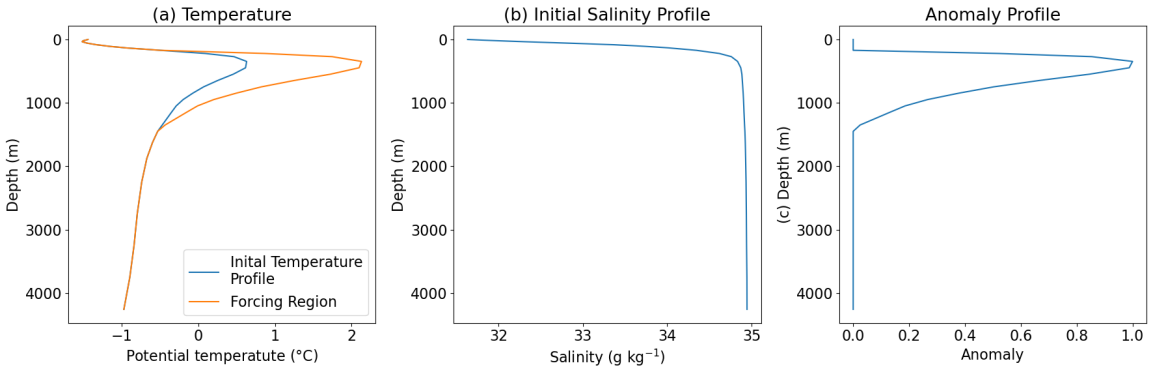

Figure 6.3: (a) Initial vertical potential temperature profile (blue line) which is used at the start of the simulation throughout the domain and the vertical potential temperature profile which temperature is relaxed to in the forcing region on a one day timescale (orange line). (b) Initial salinity profile. (c) Anomaly profile which is used to generate the potential temperature and meridional velocity profiles towards which potential temperature and meridional velocity are relaxed to within the forcing region.

to 500 m^2 s^{-1} and 10^{-5} m^2 s^{-1}, respectively, for both temperature and salinity. These settings are taken from Lique et al. (2015) and scaled for a horizontal resolution of 50 km. We employ the TEOS10 equation of state (IOC et al., 2010).

6.2.3 Initial Conditions

All simulations are initialised with temperature and salinity profiles given by the horizontal average above 75° of the Polar Hydrograhic Climatology (PHC) version 3 dataset (Steele et al., 2001). Temperature is converted to potential temperature using the TEOS-10 standards (specifically using the Gibbs Seawater Oceanographic Toolbox (McDougall and Barker, 2011)). The initial potential temperature and salinity profiles are show in Figure 6.3. The simulations are initialised from zero velocity.

6.2.4 Model Forcing

An anticyclonic wind forcing is applied to the domain, centred over the Canada Basin (Figure 6.4). The centre of the wind forcing is indicated by the blue dot in Figure 6.4, we refer to this point as the wind centre-point. Following Lique et al. (2015), the surface wind-stress is described by

$$\tau^x(\theta, R) = \sin(\theta) \left[\frac{1}{r} \int_0^R r \cos^2(r)\ dr \right], \tag{6.1}$$

and

$$\tau^y(\theta, R) = -cos(\theta) \left[\frac{1}{r} \int_0^R r \cos^2(r)\ dr \right] [2], \tag{6.2}$$

where $\tau^x(\theta, r)$ and $\tau^y(\theta, r)$ are the x- and y-components of the wind-stress respectively, r is the radial length from the wind centre-point, and θ is the angle between the line connecting each grid point to the wind centre-point and the positive x-axis. τ^x and τ^y are then normalized between 0 and 1 and the normalized fields are multiplied by a constant, A, which we set to $A = 0.04$ N m^{-2}. This wind stress pattern produces an anticyclonic wind pattern centred at the wind centre-point, illustrated in Figure 6.4.

We force an inflow and outflow of water through the Fram Strait region by relaxing the meridional velocity to a specified profile (Figure 6.5) within a specified forcing region (grey box in Figure 6.2a) using a relaxation timescale of one day (accomplished using the `rbcs` MITgcm package). This meridional velocity profile forces a flow of water into the Arctic Ocean on the eastern side of Fram Strait and out of the Arctic Ocean on the western side of Fram Strait. To simulate relatively warm Atlantic Water entering the domain, we also relax potential temperature within the forcing region to a specified profile (Figure 6.3a) using a relaxation timescale of one day. Both the meridional velocity profile and potential temperature profile used within the forcing region are generated using a similar method to that of Lique et al. (2015). Specifically, an anomaly profile is created from the potential temperature profile by selecting the values which roughly correspond to the depths of the intermediate layer (200m - 1500m), and setting all other values to zero. These values are then normalized between zero and one to give the anomaly profile (Figure 6.3c). The potential temperature profile within the forcing region is created by multiplying the anomaly profile by 1.5° C and adding this to the initial potential temperature profile. The meridional velocity profile is calculated by multiplying the anomaly profile by 0.25 m s^{-1} and using a cosine function in the zonal direction to obtain northward velocities on the eastern side of the forcing region and southward velocities on the westward side of the forcing region.

[2] Note that r should be non-dimensionalized for use in the cosine function. Here we have used r with units of metres in the calculation.

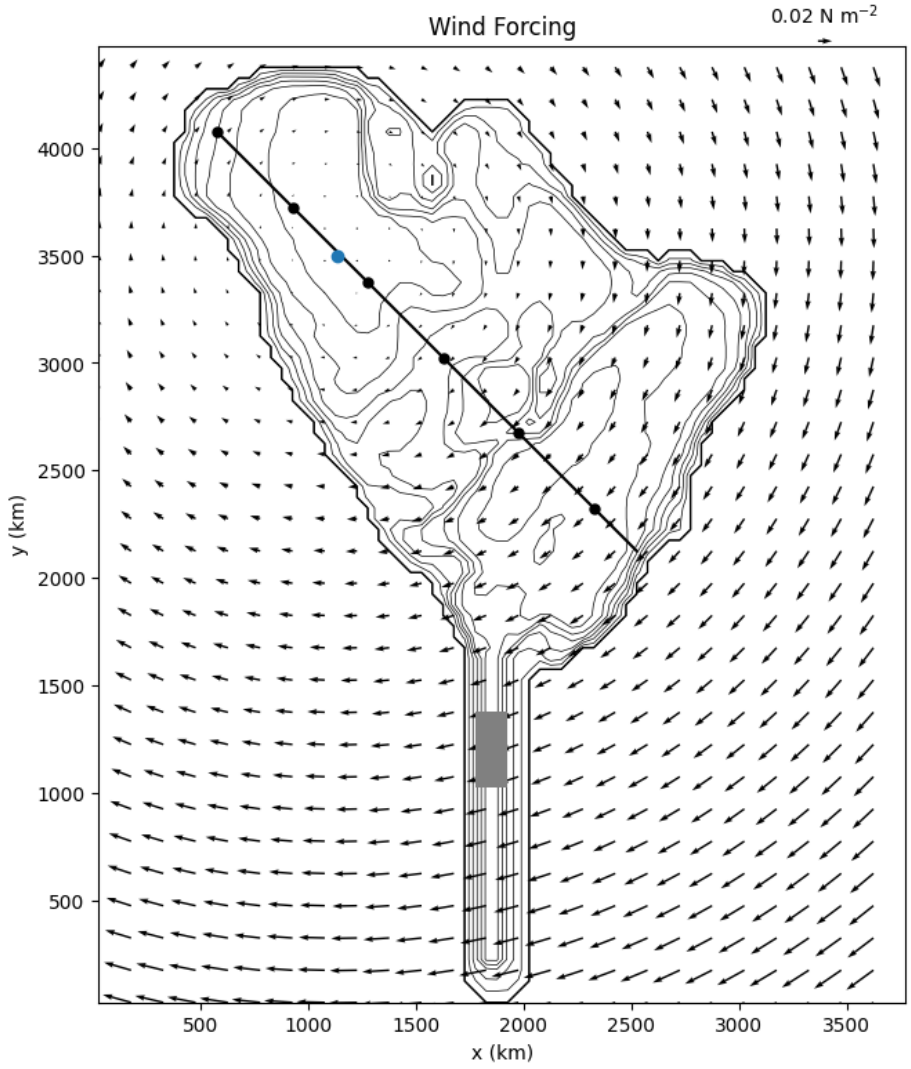

Figure 6.4: Pattern of anticyclonic wind stress employed in all simulations. The blue dot indicates the location of the wind centre-point. Black contours indicate topography contours illustrated in more detail in Figure 6.2. The black solid line represents a transect along which values are plotted in Figures 6.10 and 6.14. Other annotations are as in Figure 6.2.

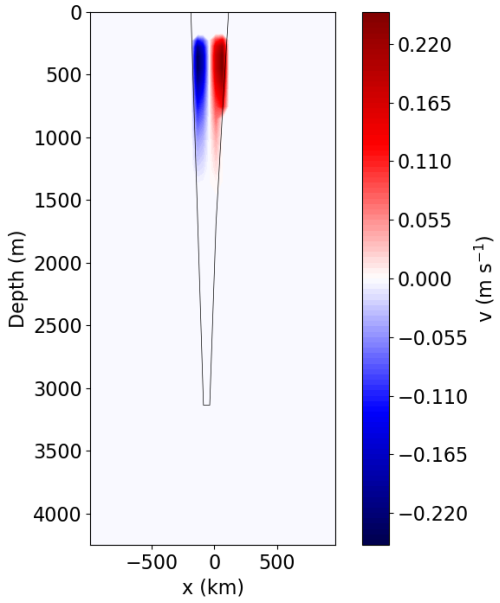

Figure 6.5: Meridional velocity towards which the meridional velocity of the flow is relaxed on a timescale of one day within the forcing region.

6.2.5 Restoration

A sponge region is implemented at the bottom of the channel region (below the blue dashed line in Figure 6.2a) in which potential temperature and salinity are relaxed to their initial profiles and zonal and meridional velocity are relaxed to values of zero (also accomplished using the `rbcs` MITgcm package). The strength of this restorative forcing increases in the negative y-direction, from no restorative forcing at the top of the sponge region to restorative forcing with a timescale of 30 days at the southern boundary.

It has been previously documented that surface salinity restoring is helpful when modelling the Arctic Ocean (e.g. Golubeva and Platov, 2007). Without surface salinity restoring, it is common for the modelled salinity values in the upper ocean to become much larger than observed salinity values in the upper Arctic Ocean. This destabilizes the stratification between the upper and middle layers, leading to convection, and an erosion of the upper cold fresh layer. To avoid this problem, we implement salinity restoring at the surface of the domain, restoring to the surface value of the initial salinity profile everywhere. Following Golubeva and Platov (2007), we use a timescale of 30 days for this surface salinity restoring.

6.2.6 Model Idealisations

The setup outlined here is highly idealised and there are many features and processes which are not included. For clarity, we outline the key features and processes which are not included in the model setup here.

We do not include shelf regions in the model domain (Figure 6.2). The model setup also does not include sea ice, which affects the input of energy into the ocean by atmospheric winds and which provides a source of salinity through brine rejection during sea ice formation and a source of freshwater at the surface during sea ice melt. We further do not include an input of freshwater from surrounding river runoff, precipitation, or the inflow of relatively fresh Pacific Water into the Arctic Basin through Bering Strait. Instead, the surface fresh layer is maintained by surface salinity restoring, described in Section 6.2.5. We do not include an inflow of Barents Seawater into the Arctic Basin at St. Anna Trough. We focus, instead, on the propagation of Atlantic Water in the Arctic Basin by simulating an inflow and outflow of relatively warm water through Fram Strait, described in Section 6.2.4. There is no outflow of water through the Canadian Arctic Archipelago.

6.2.7 Experimental Setup

We compare the results of the following simulations, outlined in Table 6.1:

1. NO PAR does not employ any eddy parameterization. Thus, the effects of unresolved eddies are not present in this simulation.

2. GM100 and GM600 employ GM90 to parameterize the baroclinic eddies, with constant κ_{GM} set to 100 $\mathrm{m}^2\ \mathrm{s}^{-1}$ and 600 $\mathrm{m}^2\ \mathrm{s}^{-1}$, respectively. These simulations do not employ the barotropic parameterization. Thus, only the baroclinic eddy effects are included in these simulations, which are parameterized via GM90 as an extraction of APE.

3. GM+PV100 and GM+PV600 employ the GM+PV parameterization as described in Chapter 5. Thus, both the effect of baroclinic eddies on the APE and the barotropic eddy PV fluxes are parameterized and are coupled via the APE-to-EKE conversion mechanism. A constant value of κ_{GM} is used and is set to 100 $\mathrm{m}^2\ \mathrm{s}^{-1}$ in GM+PV100 and 600 $\mathrm{m}^2\ \mathrm{s}^{-1}$ in GM+PV600. Thus, GM+PV100 can be compared to GM100, where GM+PV100 includes the effect of the barotropic

Configuration	κ_{GM} ($\mathrm{m^2\ s^{-1}}$)	λ	γ_q	r_K ($\mathrm{s^{-1}}$)	r_Λ ($\mathrm{s^{-1}}$)	μ ($\mathrm{m^2 s^{-1}}$)
NO PAR	-	-	-	-	-	-
GM100	100	-	-	-	-	-
GM600	600	-	-	-	-	-
GM+PV100	100	0.3	0.1	10^{-7}	5×10^{-8}	500
GM+PV600	600	0.3	0.1	10^{-7}	5×10^{-8}	500

Table 6.1: Parameters used in the simulations analysed in Section 6.3.

eddy PV fluxes and GM100 does not. The same comparison can be made between GM+PV600 and GM600.

The values of $\kappa_{\mathrm{GM}} = 100\ \mathrm{m^2\ s^{-1}}$ and $\kappa_{\mathrm{GM}} = 600\ \mathrm{m^2\ s^{-1}}$ are chosen based on observations in the Beaufort Gyre, which estimate the inferred lateral eddy buoyancy diffusivity to be within this range (Meneghello et al., 2017).

For simulations that employ the GM+PV parameterization, there are five extra parameters which must be specified: the fraction of GM90-extracted APE reinjected into the parameterized barotropic EKE budget, λ; the PV flux efficiency parameter, γ_q; the parameterized barotropic EKE damping coefficient, r_K; the parameterized barotropic EPEnstr damping coefficient, r_Λ; and the parameterized EKE and EPEnstr diffusivity, μ. We use the same values of γ_q, r_Λ and μ employed in Chapters 3 and 4, specifically, 0.1, $5 \times 10^{-8}\ \mathrm{m^{-2}\ s^{-3}}$, and $500\ \mathrm{m^2\ s^{-1}}$, respectively. Mak et al. (2022a) estimated the zonally averaged eddy energy dissipation timescale from a high-resolution global ocean simulation, finding the timescale to be on the order of months, with longer timescale at high latitudes. As a first attempt, we set $r_K = 10^{-7}\ \mathrm{s^{-1}}$, which corresponds to a dissipation timescale of 3 - 4 months. The fraction of MAPE converted to barotropic EKE is not well established. Aiki et al. (2011) found that, in a 0.1° semi-global ocean model, around 50% or more of the MKE exists in the barotropic component at latitudes higher than around 50°. However, this estimate tells us nothing about the EKE. Zhao et al. (2018) used data from mooring measurements in the Beaufort Gyre to quantify the vertical modes of EKE, estimating that 22.1% of the EKE exists in the barotropic component, but the amount of MAPE converted to barotropic EKE cannot be directly inferred from this estimate. As a first estimate, and lacking any concrete evidence, we set $\lambda = 0.3$ and test other values of λ in the sensitivity experiment in Section 6.23. These parameter values are summarised in Table 6.1.

6.2.8 Energy Pathways

Before we discuss the results of the simulations above, it is helpful to describe and compare the energy pathways associated with these different simulations. The energy components and energy pathways are illustrated as boxes and arrows, respectively, in Figure 6.6. In the baroclinic setup, the mean energy field is composed of both a MAPE component and a MKE component. The eddy energy field consists of only the parameterized EKE component, K, which is employed in GM+PV100 and GM+PV600 only. There is no EAPE component, as this is not tracked in either GM or GM+PV simulations. Black arrows represent energy pathways which are independent of any eddy parameterization, orange arrows represent energy pathways associated with GM90, and red arrows represent energy pathways associated with the barotropic eddy parameterization.

NO PAR includes only the energy pathways represented by black arrows in Figure 6.6. In this simulation, energy is input into the MKE and MAPE component by wind forcing, surface salinity restoring and exchanges between the basin and forcing region. Energy is also exchanged between the MKE and MAPE components via the resolved dynamics. Energy is extracted from the MKE component by bottom drag and explicit diffusion and viscosity.

GM100 and GM600 include energy pathways represented by both black and orange arrows in Figure 6.6 since they employ GM90. In these simulations, energy is input into the mean energy components and is exchanged between the MKE and MAPE components as in the NO PAR simulation. Energy is also extracted from the MKE component by bottom drag and explicit diffusion and viscosity as in the NO PAR simulation. In addition, energy is now also extracted from the MAPE component by the GM90 parameterization.

In GM+PV100 and GM+PV600, all energy pathways illustrated in Figure 6.6 are included. In these simulations, energy is input into the mean energy components and is exchanged between the MKE and MAPE components as in NO PAR, GM100 and GM600. MAPE is also extracted from the system by the GM90 parameterization. In addition, a fraction of the extracted MAPE is reinjected into the parameterized barotropic EKE budget. The remainder of the extracted MAPE represents a loss of energy in the system. Kinetic energy can be converted between the MKE and parameterized EKE components via the kinetic energy conversion mechanism in the

barotropic parameterization. The dominant direction of this transfer of kinetic energy is from the parameterized EKE component to the MKE component. Energy is extracted from the parameterized EKE component by the linear damping term in the parameterized EKE budget, and from the MKE component by bottom drag and explicit diffusion and viscosity.

6.2.9 Spinup

All simulations are run for 99 years[3]. The evolution of the MKE and mean convective energy, which provides a measure of the mean potential energy in the system[4], is plotted for all simulations to understand the spin-up times and if the simulations are reaching a quasi-steady state (Figure 6.7). Over the final 10 years, the convective energy changes by less than 1% in all simulations, and the MKE changes by less than 1% in GM600, GM+PV100 and GM+PV600, and by less than 2% in NO PAR and GM100. Based on these metrics, we consider all simulations to be quasi-steady over the final 10 years of the simulation and we analyse the results over this time period.

6.3 Arctic Basin Simulations

Having described the model setup, we now proceed to analyse the quasi-steady state of the simulations, focusing on addressing the three questions specified in Section 6.1. We begin by investigating the effect of GM+PV on the simulated flow field in the Arctic Basin (Section 6.3.1). In Section 6.3.2, we briefly examine the propagation of Atlantic Water in the Arctic Basin. In Sections 6.3.3 and 6.3.4, we look at the parameterized energetics and enstrophetics, respectively, associated with the GM+PV simulations to describe how the GM+PV parameterization functions in this baroclinic setup. In Section 6.3.5, we investigate the effect of varying the input parameters to GM+PV on the energetics of the system.

[3]The implementation of GM+PV in MITgcm does not allow for the use of tiles. Tiles decompose the domain into components, allowing computations to be performed in parallel thus decreasing the run time of the model. Because GM+PV simulations cannot use the tile feature, these simulations take much longer to run than NO PAR, GM100 and GM600. The time length of all simulations is therefore constrained by the maximum achievable time length of GM+PV100 and GM+PV600, which is 99 years.

[4]More precisely, it quantifies the amount of energy required to homogenize the density stratification of the water column.

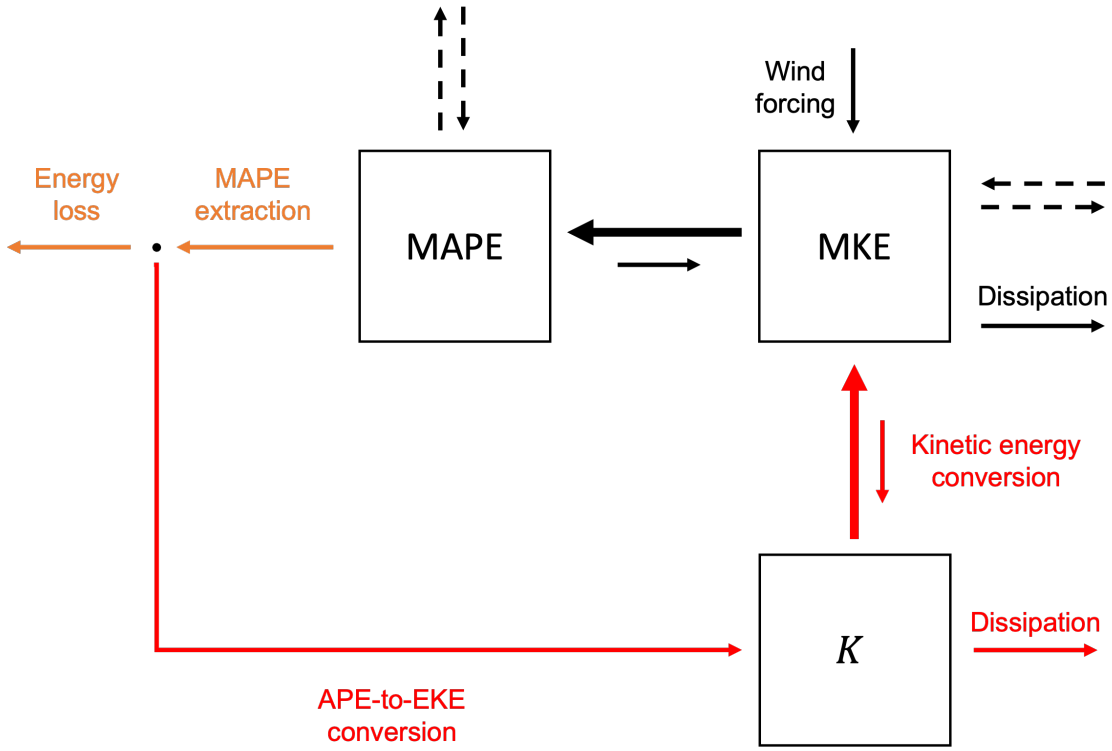

Figure 6.6: Energy components (boxes) and pathways (arrows) associated with the Arctic Basin (excluding the channel region) in simulations described in Section 6.2 and analysed in Section 6.3. The mean energy is composed of the MKE and MAPE. The only eddy energy field is the parameterized barotropic EKE, K, associated with the barotropic eddy parameterization. No EAPE component is present as neither GM90 nor the barotropic parameterization tracks the EAPE. Black arrows indicate energy pathways which are independent of any eddy parameterization. Dashed black arrows indicate energy fluxes between the basin and the channel region, as well as energy fluxes associated with the surface salinity restoring. Orange arrows represent energy pathways associated with GM90. Red arrows represent energy pathways associated with the barotropic eddy parameterization. In the case where there are two arrows, the dominant direction of transfer is indicated by the bold arrow. NO PAR includes only energy pathways represented by black arrows, since it does not employ GM90 or the barotropic eddy parameterization. GM100 and GM600 include energy pathways represented by both black and orange arrows. GM+PV100 and GM+PV600 include all illustrated energy pathways.

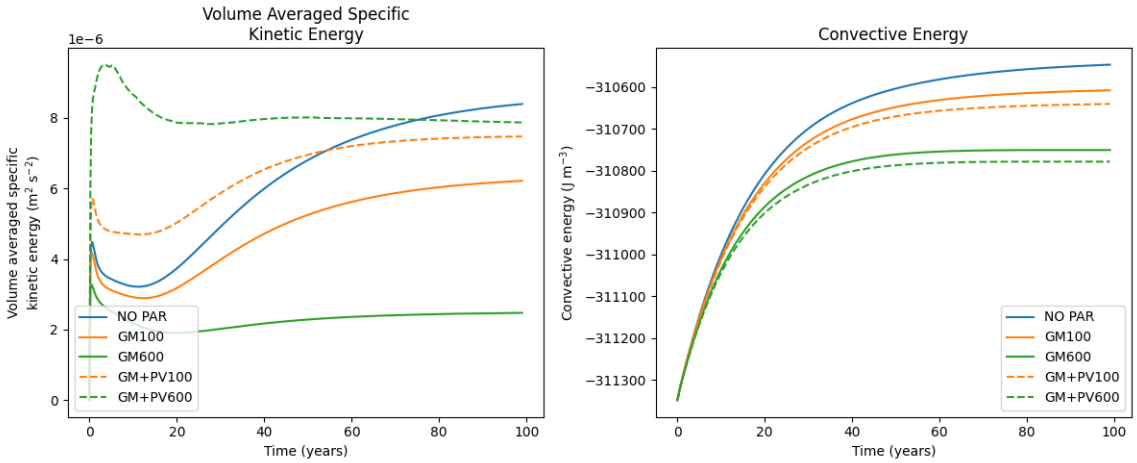

Figure 6.7: Time series of MKE (left) and change in mean convective energy (right) for NO PAR (blue), GM100 (orange, solid), GM600 (green, solid), GM+PV100 (orange, dashed), and GM+PV600 (green, dashed) for the full 99 year run time.

6.3.1 Flow Fields

We begin by considering the time-mean near-surface (62.5 m depth) flow fields of the quasi-steady state (Figure 6.8). All simulations exhibit near-surface anticyclonic motion, consistent with the overlying anticyclonic wind pattern. The speed of this anticyclonic flow decreases as the value of κ_{GM} increases. Employing GM+PV leads to a small decrease in speed and some changes to the flow field such as the introduction of a flow along the Lomonosov Ridge in GM+PV600. Overall, the near-surface flow fields exhibit similar spatial patterns across all simulations with some changes in magnitude. Observations estimate the mean geostrophic surface current to be $\mathcal{O}(1$ cm $\mathrm{s}^{-1})$ (Armitage et al., 2017). Thus, the simulated near-surface velocities are of the correct order of magnitude, but potentially small in GM600 and GM+PV600.

The time-mean flow field at 550 m depth (close to the depth of the maximum in the meridional velocity and temperature forcing profiles, thus representing a level at which Atlantic Water forcing into the basin is strong) is plotted in Figure 6.9. At this depth, NO PAR, GM100 and GM600 all exhibit anticyclonic flow, but with decreased speed compared to the near-surface flow. In contrast, both GM+PV100 and GM+PV600 exhibit a clear topography-following flow. The flow around the perimeter of the Arctic Basin is cyclonic, largely resembling that of the Arctic Circumpolar Boundary Current, and a return flow along the Lomonosov Ridge is present. The flow speed is larger than that of NO PAR, GM100 and GM600. Increasing κ_{GM} decreases the flow

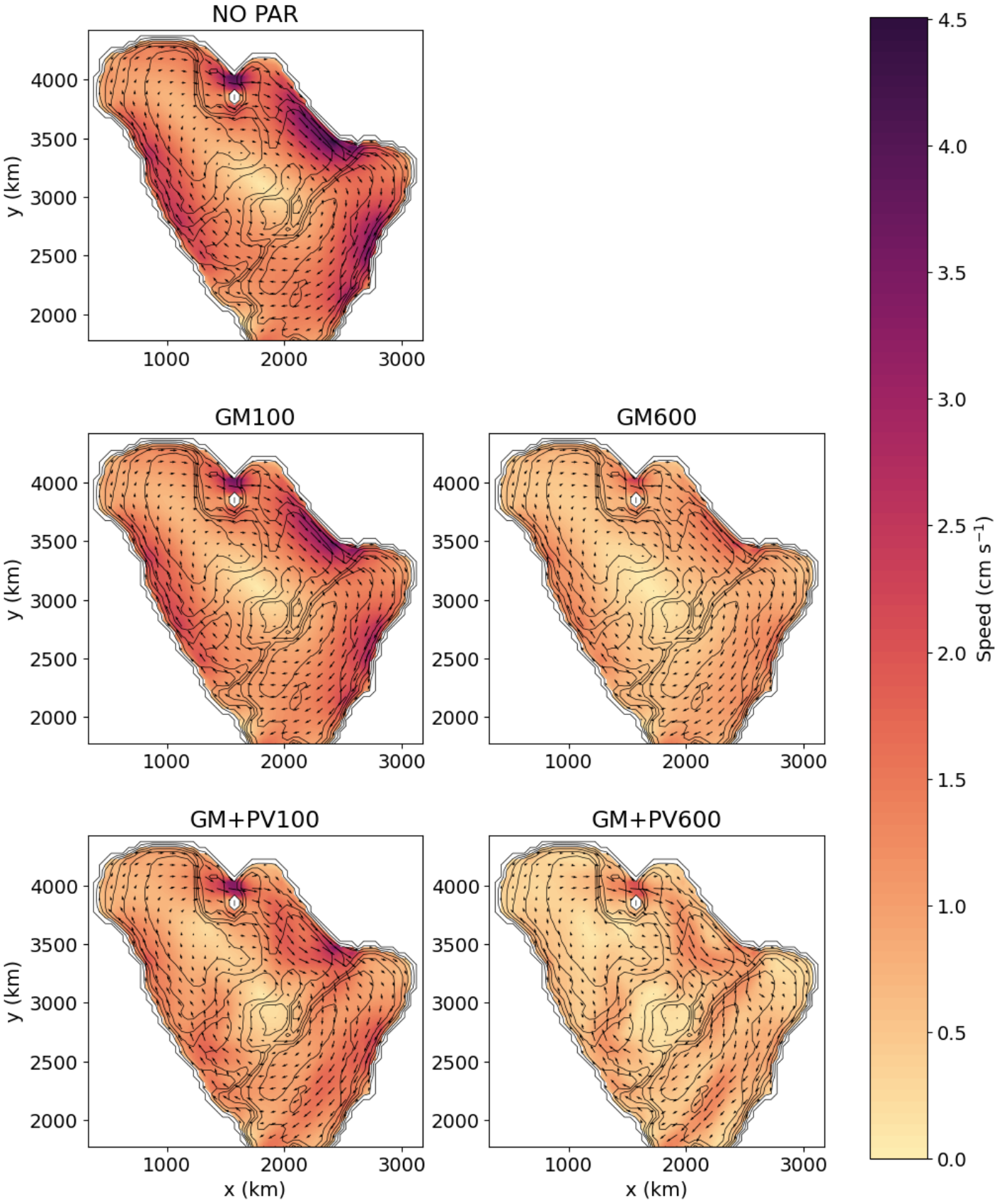

Figure 6.8: Time-mean velocity (vectors) and speed (colour) over years 90 - 99 at a depth of 62.5 m for NO PAR (top left), GM100 (middle left), GM600 (middle right), GM+PV100 (bottom left), and GM+PV600 (bottom right). Black contours indicate the topography.

speed for GM simulations and increases the flow speed for GM+PV simulations.

To gain insight into the vertical structure of the velocity field, the vertical profile of velocity perpendicular to the transect indicated in Figure 6.2 is plotted in Figure 6.10. NO PAR, GM100 and GM600 all exhibit anticyclonic motion at the surface and around the basin boundary at all depths, with the strength of the flow decreasing with depth. Away from the basin boundary at depth, the topography influences the flow and anticyclonic recirculations are seen within the sub-basins. In GM+PV100 and GM+PV600, the near-surface flow is anticyclonic, while the flow at depth is cyclonic around the basin boundary, broadly consistent with the behaviour of the Arctic Circumpolar Boundary Current. The flow at depth is largely barotropic with bottom velocities which are comparable to those in the rest of the water column. Cyclonic recirculations are seen at depth within the sub-basins, consistent with the theory of Bretherton and Haidvogel (1976) that eddies drive cyclonic topography-following flows over topographic troughs. The existence of these cyclonic recirculations in simulations employing GM+PV demonstrates that including the effect of the barotropic eddies can produce an emergent topography-following flow.

We further explore the time-mean flow by considering the depth-integrated streamfunction (Figure 6.11). For NO PAR, GM100 and GM600, this is anticyclonic everywhere in the basin. This suggests that the dominant factor affecting the direction of the circulation in these simulations is the overlying anticyclonic wind. For GM+PV100 and GM+PV600, the depth-integrated flow is cyclonic in the Eurasian and Canada Basins and anticyclonic in the Makarov Basin. The streamlines largely follow the topography contours indicating that the depth-integrated flow follows the topography. This behaviour, coupled with the small variation in the sub-surface horizontal velocity with depth exhibited in Figure 6.10, resembles the phenomenon of Taylor columns in which vertical variations in velocity are suppressed due to rotation, leading to closed recirculations over topography (Taylor, 1917; Proudman, 1916). This suggests that, below the wind-driven surface layer, the barotropic parameterization acts to drive a large-scale topography-following flow resembling Taylor columns.

The strength of the cyclonic flow exhibited in the Makarov Basin increases as κ_{GM} increases, while the strength of the anticyclonic flow decreases as κ_{GM} increases. This indicates that there is a competing effect between the cyclonic flow driven by the parameterized barotropic eddies and the anticyclonic flow driven by the wind. As κ_{GM}

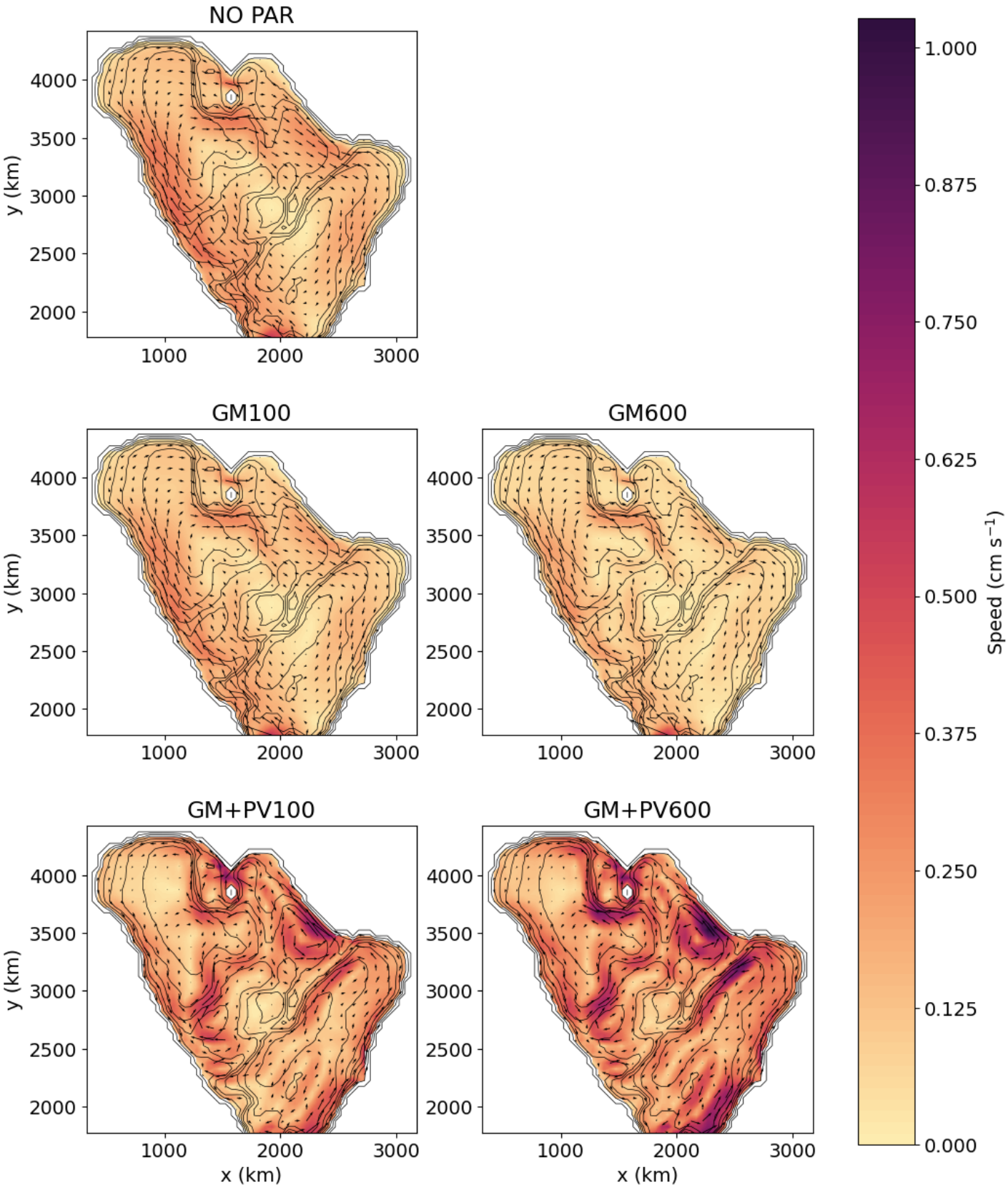

Figure 6.9: Time-mean velocity (vectors) and speed (colour) over years 90 - 99 at a depth of 550 m for NO PAR (top left), GM100 (middle left), GM600 (middle right), GM+PV100 (bottom left), and GM+PV600 (bottom right). Black contours indicate the topography.

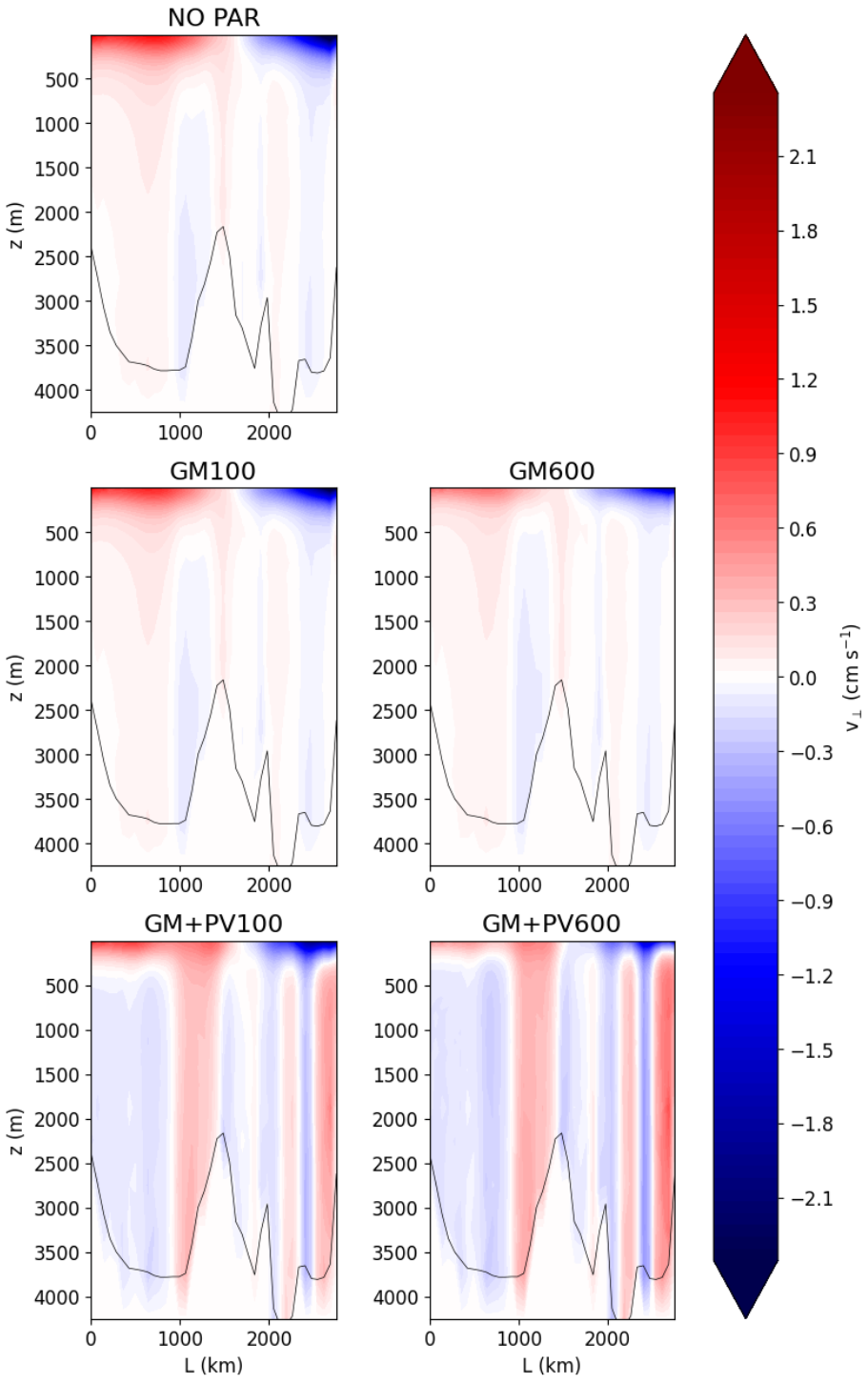

Figure 6.10: Vertical profile of time-mean velocity perpendicular to the transect illustrated in Figure 6.2, $v_\perp$ (colour), over years 90 - 99 for NO PAR (top left), GM100 (middle left), GM600 (middle right), GM+PV100 (bottom left), and GM+PV600 (bottom right). The black line is the depth of the domain along the transect. Some contours are plotted below the depth of the domain due to the use of partial cells.

increases, the parameterized barotropic eddy-driven flow begins to dominate over the wind-driven flow.

While the transition to a largely cyclonic flow field in GM+PV100 and GM+PV600 is an improvement, theory predicts that the flow is cyclonic everywhere in the Arctic Basin *except* in the centre of the Canada Basin where the anticyclonic Beaufort Gyre is situated (Nøst and Isachsen, 2003; Timmermans and Marshall, 2020). This behaviour is demonstrated with observations of the Arctic Circumpolar Boundary Current (Rudels et al., 2000; Aksenov et al., 2011) and the Beaufort Gyre (Proshutinsky et al., 2009). No such anticyclonic circulation is present within the Canada Basin in GM+PV100 and GM+PV600. Instead, anticyclonic motion occurs in the region of the Mendeleev Ridge and the Alpha Ridge in GM+PV simulations, and extends to the Lomonosov Ridge in GM+PV100, that is, it occurs over topographic mounts. It is possible that this anticyclonic motion is at least partly driven by the barotropic parameterized eddies, which will drive anticyclonic motion over topographic mounts. However, the decrease in strength of the anticyclonic motion as κ_{GM} increases leads us to believe that this anticyclonic motion is largely wind-driven. Thus, improving the representation of the anticyclonic motion, i.e. moving it to the centre of the Canada Basin such that it agrees with theory and observations, may be possible by employing more realistic patterns of wind forcing.

Finally, we consider the depth-integrated MKE (Figure 6.12). In NO PAR, this is large in specific areas close to the boundary of the Arctic Basin and small elsewhere. A similar spatial pattern is seen in GM100 and GM600, with the magnitude of MKE decreasing as κ_{GM} is increased, consistent with the decrease in volume-averaged MKE with increasing κ_{GM} (Figure 6.7). In GM+PV100 and GM+PV600, the spatial pattern of the depth-integrated MKE is different, with large values observed where the topographic slope is large, such as along the Lomonosov Ridge and around the Chuchki Plateau. There is a clear increase in MKE magnitude between GM600 and GM+PV600, consistent with the increase in volume-averaged MKE between these two simulations (Figure 6.7). The magnitude of the depth-integrated MKE is comparable between NO PAR, GM+PV100 and GM+PV600, consistent with the similarity of volume-averaged MKE between these simulations (Figure 6.7). This suggests that GM+PV acts largely to redistribute the MKE throughout the domain.

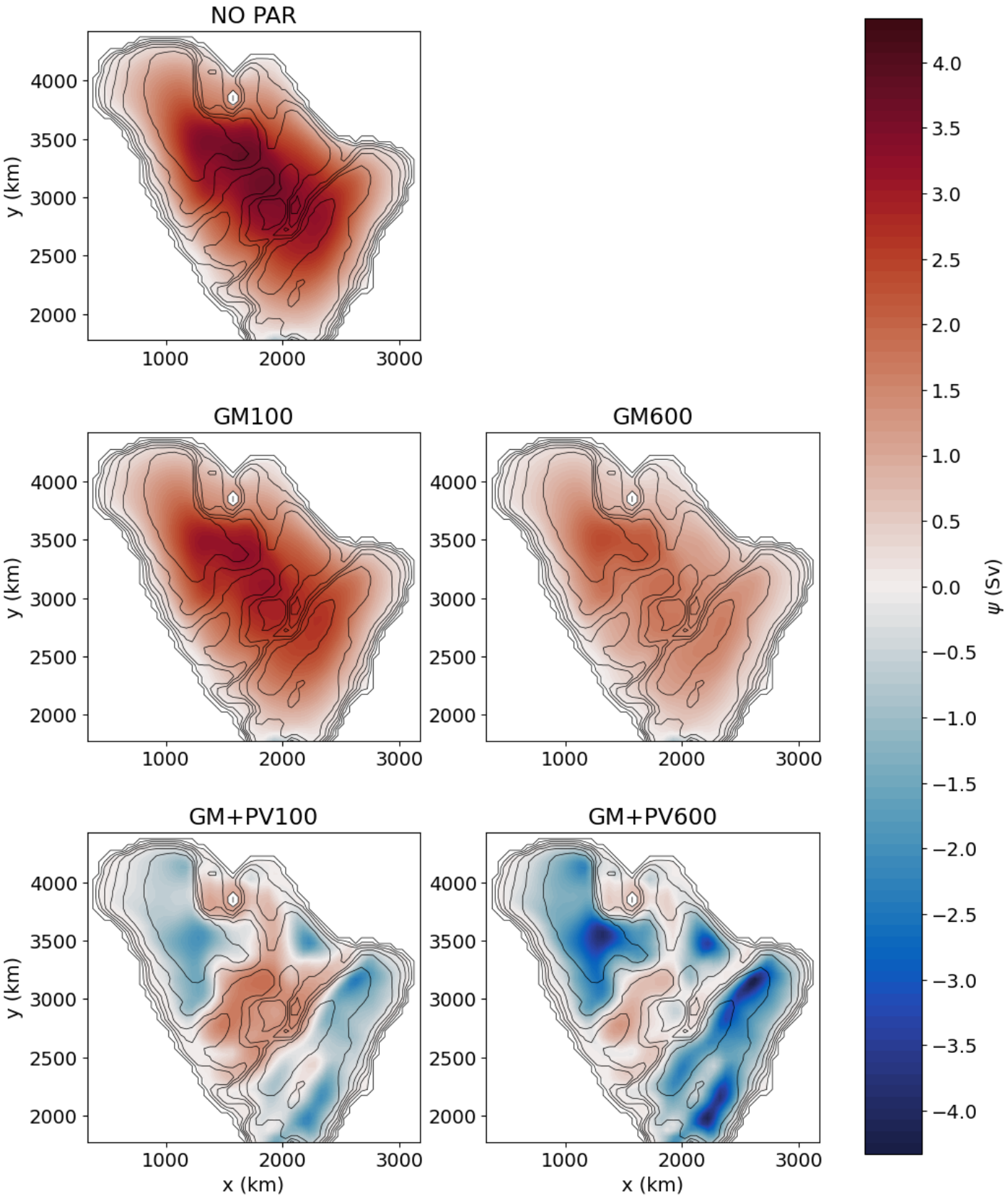

Figure 6.11: Time-mean depth-integrated streamfunction (colours) over years 90 - 99 for NO PAR (top left), GM100 (middle left), GM600 (middle right), GM+PV100 (bottom left), and GM+PV600 (bottom right). Black contours indicate the topography.

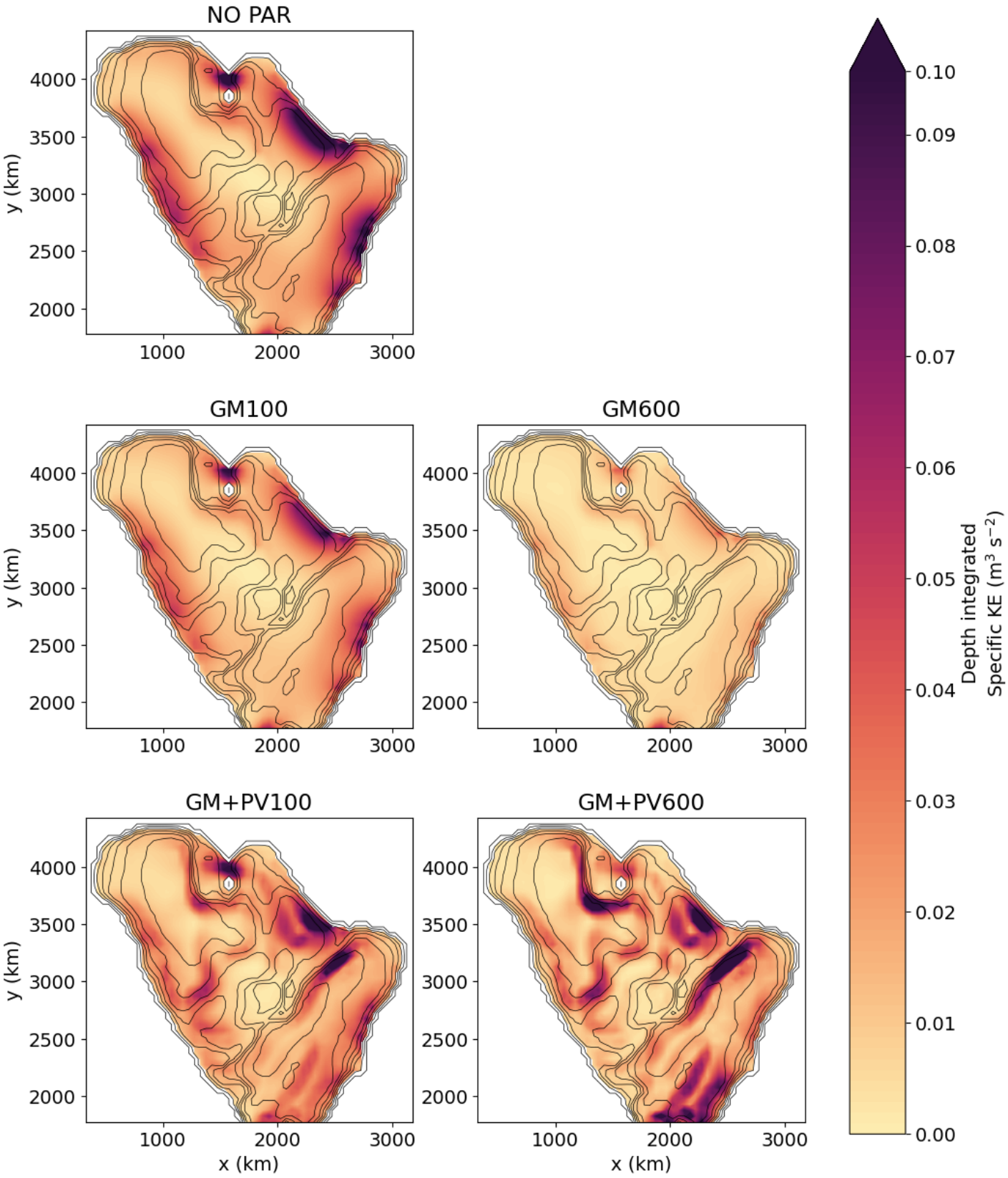

Figure 6.12: Time-mean depth-integrated MKE (colours) over years 90 - 99 for NO PAR (top left), GM100 (middle left), GM600 (middle right), GM+PV100 (bottom left), and GM+PV600 (bottom right). Black contours indicate the topography.

To summarise, in NO PAR, GM100 and GM600, the flow is anticyclonic throughout the Arctic Basin (Figures 6.8, 6.9 and 6.11) and decreases in strength with depth (Figure 6.10). This suggests that the anticyclonic wind forcing is dominant in setting the flow field in these simulations. The strength of the flow decreases as κ_{GM} increases, but the spatial structure of the flow field remains largely unchanged (Figures 6.8, 6.9 and 6.11). In GM+PV100 and GM+PV600, a surface anticyclonic flow is present (Figure 6.8), resembling that of NO PAR, GM100 and GM600, but the flow field at depth changes drastically (Figures 6.9 and 6.10). At depth, a largely barotropic topography-following flow is present in which the direction of the flow around the boundary of the Arctic Basin is reversed, with a cyclonic flow present along the boundary, broadly resembling that of the Arctic Circumpolar Boundary Current (Figures 6.9 and 6.10). This change in circulation from anticyclonic at the surface to cyclonic at depth agrees qualitatively with the simulations employing the Neptune parameterization in the Arctic Ocean (Nazarenko et al., 1998). Below the near-surface wind-driven flow, the strength of the flow is increased relative to NO PAR, GM100 and GM600 (Figure 6.10).

6.3.2 Propagation of Atlantic Water

We now examine how Atlantic Water propagates within the Arctic Basin in the simulations. In this model setup, the inflow of Atlantic Water into the Arctic Basin is simulated by restoring meridional velocity and temperature within the forcing region (grey box in Figure 6.2). The meridional velocity is restored to positive values on the eastern side of the forcing region, thus forcing a flow into the Arctic Basin, and to negative values on the western side of the forcing region, forcing a flow out of the Arctic Basin (Figure 6.5). The potential temperature is also restored in the forcing region such that the water is warm compared to the initial conditions, in which the maximum water temperature is approximately 0.6° (Figure 6.3a). We use potential temperature values $\geq 0.6°$ C as a crude way of identifying Atlantic Water.

We investigate the propagation of Atlantic Water into the Arctic Basin by examining the meridional velocity at $y = 2000$ km (Figure 6.13). This location is close to the boundary between the Arctic Basin and the channel region containing the forcing region, while also being within the region in which the parameterization is employed at full strength (above the uppermost green dotted line in Figure 6.2). NO PAR, GM100 and GM600 exhibit positive meridional velocity (into the Arctic Basin) in

the western half of the domain, with negative meridional velocity (out of the Arctic Basin) in the eastern half of the domain and a small region of weak northward flow close to the eastern boundary. This pattern arises despite the meridional velocity forcing which is positive on the eastern side of the forcing region and negative on the western side of the forcing region (Figure 6.5). The meridional velocity in these simulations indicates that the surface wind forcing is dominating over the forced inflow and outflow of water in the forcing of the circulation, except in a very narrow region on the eastern edge of the domain where there is a northward inflow as a result of the forcing. In contrast, in GM+PV100 and GM+PV600, the near-surface flow follows the wind, while at depth, a strong positive meridional velocity is present on the eastern side of the domain and a negative meridional velocity is present on the western side of the domain (Figure 6.13). This pattern of meridional velocity at $y = 2000$ km is largely consistent, qualitatively, with the inflow of water into the Arctic Basin via the West Spitsbergen Current (Cokelet et al., 2008; Beszczynska-Möller et al., 2012) and the outflow of water via the East Greenland Current (Beszczynska-Möller et al., 2012; Richter et al., 2018) although these observational studies indicate that both of these currents extend to the surface.

The volume transport at $y = 2000$ km in the positive and negative y direction, representing flow into and out of the Arctic Basin respectively, is calculated and summarised in Table 6.2. Comparing NO PAR, GM100 and GM600, the volume transport across $y = 2000$ km decreases in both the positive and negative y directions with the addition of the GM90 parameterization and as κ_{GM} increases. In contrast, in GM+PV100 and GM+PV600, the transport increases significantly, relative to the simulations without the barotropic parameterization, and further as κ_{GM} increases. Beszczynska-Möller et al. (2012) estimate the transport into the Arctic Basin in the West Spitsbergen Current as 6.6 ± 0.4 Sv. Hence, all simulations underestimate the transport of water into the Arctic Basin but employing GM+PV leads to an improved representation of this transport. Note all simulations exhibit a volume transport within the forcing region (grey box in Figure 6.2) of 9.7 Sv in the positive y direction and 7.7 Sv in the negative y direction (not shown). The reduced volume transports into the Arctic Basin in all simulations suggest that a significant portion of this is recirculating within the channel region before entering the Arctic Basin.

The vertical potential temperature profiles along the transect indicated in Figure 6.2 (black line) are plotted in Figure 6.14 as well as the initial potential temperature

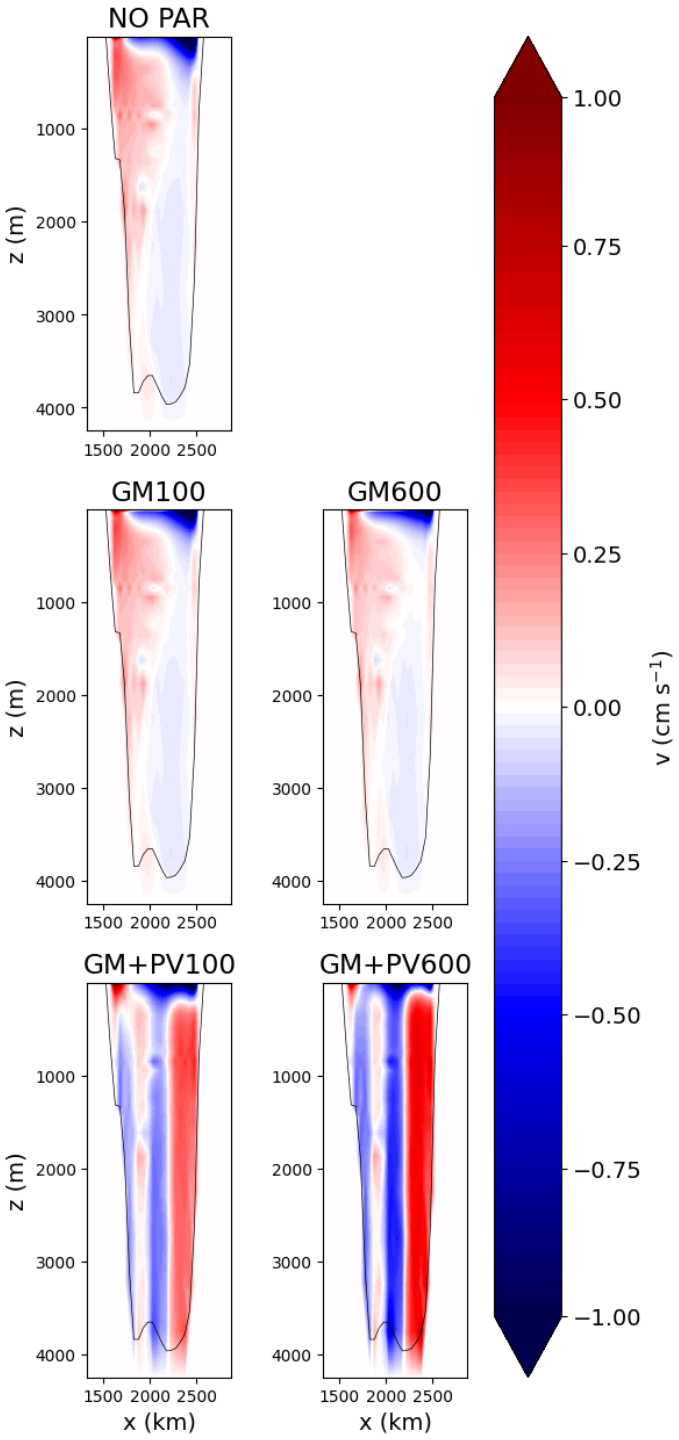

Figure 6.13: Time-mean meridional velocity over years 90 - 99 at $y = 2000$ km for NO PAR (top left), GM100 (middle left), GM600 (middle right), GM+PV100 (bottom left), and GM+PV600 (bottom right). The black line is the depth of the domain. Some contours are plotted below the depth of the domain due to the use of partial cells.

Configuration	Transport in +ve y (Sv)	Transport in -ve y (Sv)
NO PAR	1.9	2.5
GM100	1.7	2.2
GM600	1.3	1.6
GM+PV100	4.0	4.0
GM+PV600	5.8	5.5

Table 6.2: Time-mean volume transport over the years 90 - 99 in the positive and negative y-direction at $y = 2000$ km, representing flow into and out of the Arctic Basin respectively.

profile used in all simulations. All simulations exhibit an increase in potential temperature in the warm layer from the initial potential temperature profile and an increase in the depth of the warm layer, indicating that the warm Atlantic Water is propagating into the domain in all simulations. The maximum temperature in the Atlantic Water layer in NO PAR, GM100, GM600, GM+PV100 and GM+PV600 is 1.19 °C, 1.31 °C, 1.47 °C, 1.60 °C and 1.62 °C, respectively. The higher temperature in the Atlantic Water layer in GM+PV100 and GM+PV600 than in NO PAR, GM100 and GM600 suggests that the warm Atlantic Water entering the Arctic Basin from the channel region is more effective at penetrating into the Arctic Basin in simulations employing the barotropic parameterization than those which do not.

We speculate, based on the meridional velocity at $y = 2000$ km (Figure 6.13), the flow field at depth (Figure 6.9), and the depth-integrated streamfunction (Figure 6.11), that Atlantic Water is propagating anticyclonically within the Arctic Basin in NO PAR, GM100 and GM600, and cyclonically in GM+PV100 and GM+PV600. However, further analysis would be required to confirm this. The suspected cyclonic propagation of Atlantic Water seen in GM+PV100 and GM+PV600 is broadly consistent with the observed behaviour of Atlantic Water circulating around the Arctic Basin in the Arctic Circumpolar Boundary Current (Aksenov et al., 2011).

6.3.3 Energetics

Having described the change in flow structure when GM+PV is employed, we next investigate the basin-averaged (i.e. the volume average over the Arctic Basin) parameterized EKE, K, and the terms in the parameterized EKE budget (Equation 5.21) in GM+PV100 and GM+PV600 to understand how the parameterization functions with respect to the transfers of energy, and how the quasi-steady state is reached.

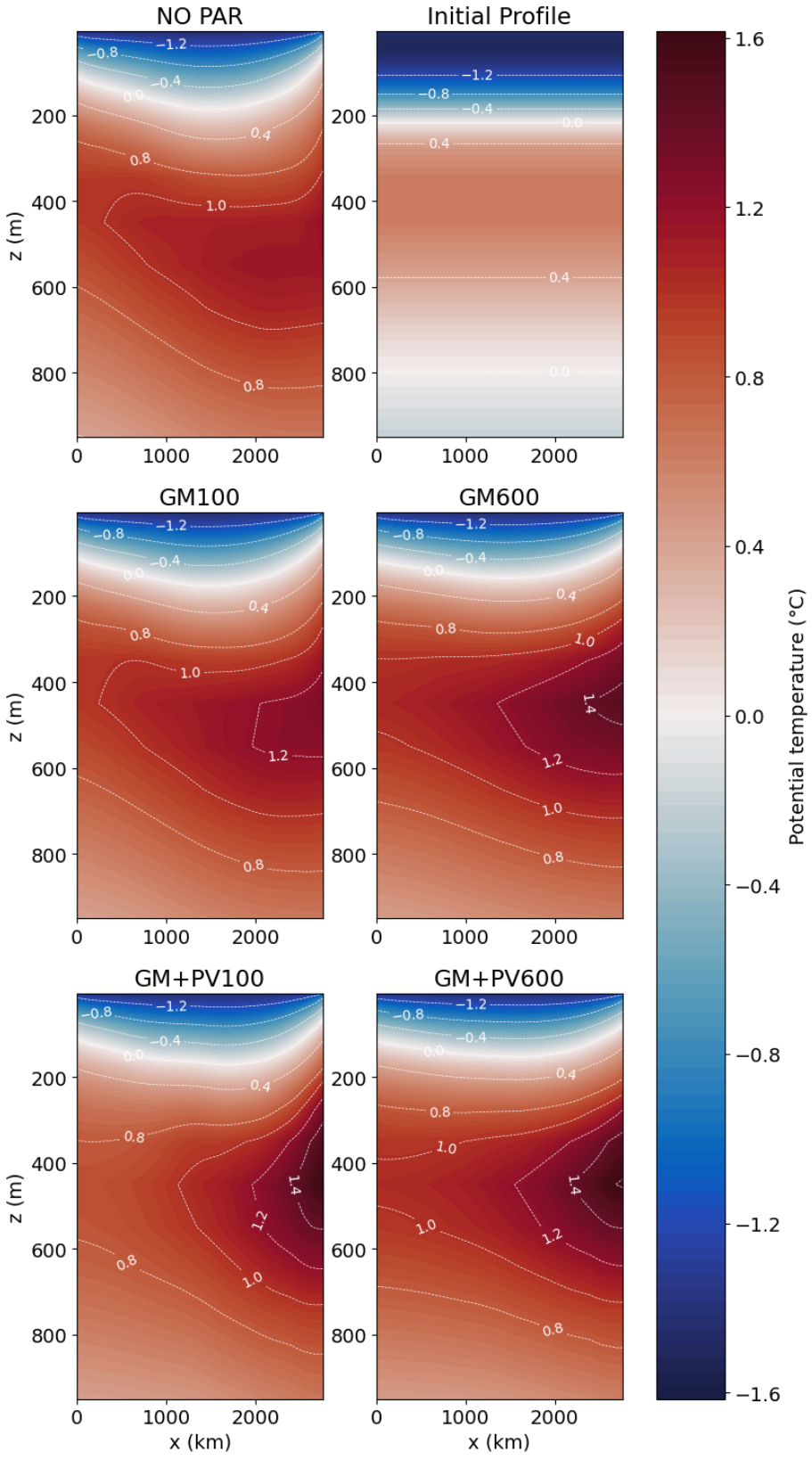

Figure 6.14: Time-mean potential temperature over years 90 - 99 along a transect crossing the Arctic Basin (black line in Figure 3.4) for NO PAR (top left), GM100 (middle left), GM600 (middle right), GM+PV100 (bottom left) and GM+PV600 (bottom right). The initial vertical potential temperature distribution used for all simulations is shown in the top right.

The basin-averaged K (Figure 6.15a) increases throughout the simulation for both GM+PV100 and GM+PV600. The magnitudes of basin averaged K, the APE-to-EKE conversion and the eddy-to-mean kinetic energy conversion increase in magnitude as κ_{GM} increases. In the parameterized EKE budget, the source of K from the APE-to-EKE conversion is largely balanced by the parameterized eddy-to-mean kinetic energy conversion. The APE-to-EKE conversion depends linearly on λ, the APE-to-EKE conversion fraction, and the eddy-to-mean kinetic energy conversion depends linearly on γ_q, the eddy PV flux efficiency parameter. Thus, the balance between APE-to-EKE conversion and eddy-to-mean kinetic energy conversion in the quasi-steady state suggests that both λ and γ_q are important in determining the quasi-steady state. We investigate this hypothesis in sensitivity tests in Section 6.3.5. Note that the advection and diffusion terms in the budget are not shown as they are both of order $\mathcal{O}(10^{-13})$ m^2 s^{-3}, and, hence, these terms do not significantly affect the volume-averaged values of K.

The time-mean spatial pattern of K over years 90 - 99 is plotted in Figure 6.16. Large values of K are seen very close to the Arctic Basin boundary, with values one or two orders of magnitude smaller a short distance away from the boundary. Relatively large values of K are also seen within the centre of the Canada Basin, with values an order of magnitude smaller around the perimeter of the Canada Basin. Relatively small values of K are seen along the Lomonosov Ridge and the Mendeleev Ridge.

The spatial patterns of time-mean APE-to-EKE conversion (Figure 6.17), and kinetic energy conversion between the mean and eddy components (Figure 6.18) over years 90 - 99 are plotted for both GM+PV100 and GM+PV600. In Figure 6.18, negative values (blue contours) indicate eddy-to-mean kinetic energy conversion and positive values (red contours) indicate mean-to-eddy kinetic energy conversion. In both simulations, APE-to-EKE conversion and eddy-to-mean kinetic energy conversion are both largest around the boundary of the Arctic Basin and decrease in magnitude towards the centre of the basin. This pattern of APE-to-EKE conversion is consistent with the expectation that the anticyclonic wind forcing results in downwelling in the centre of the basin, which leads to sloping isopycnals around the boundary of the basin. GM90 acts to flatten these isopycnals and APE is therefore expected to primarily be extracted in the region of the sloping isopycnals. This extracted APE is redirected into the parameterized barotropic EKE budget via the APE-to-EKE conversion mechanism. The pattern of eddy-to-mean kinetic energy conversions indicates

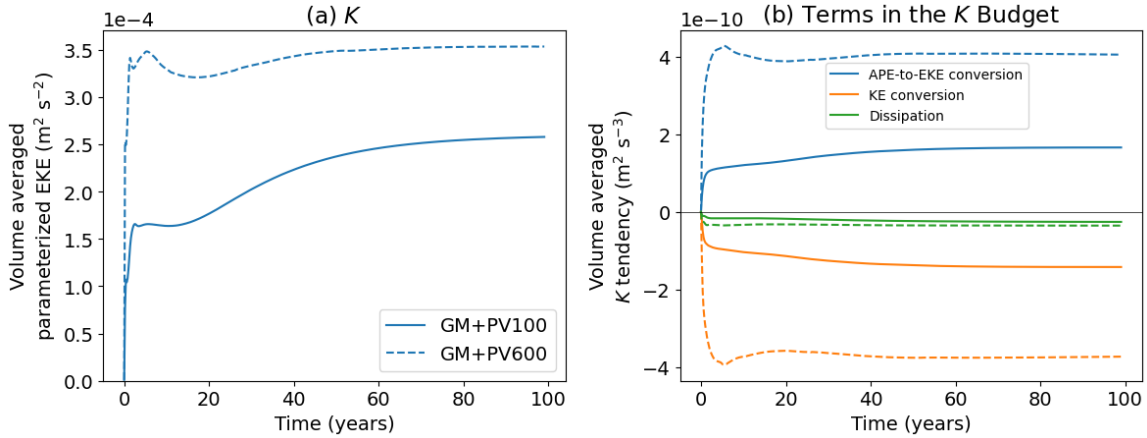

Figure 6.15: Time series of (a) volume-averaged parameterized EKE, K; (b) terms in the parameterized EKE budget, specifically, the APE-to-EKE conversion (blue), KE conversion between the eddy and mean fields (orange) where negative values indicate a conversion from eddy to mean, and dissipation of K (green) for GM+PV100 (solid lines) and GM+PV600 (dashed lines).

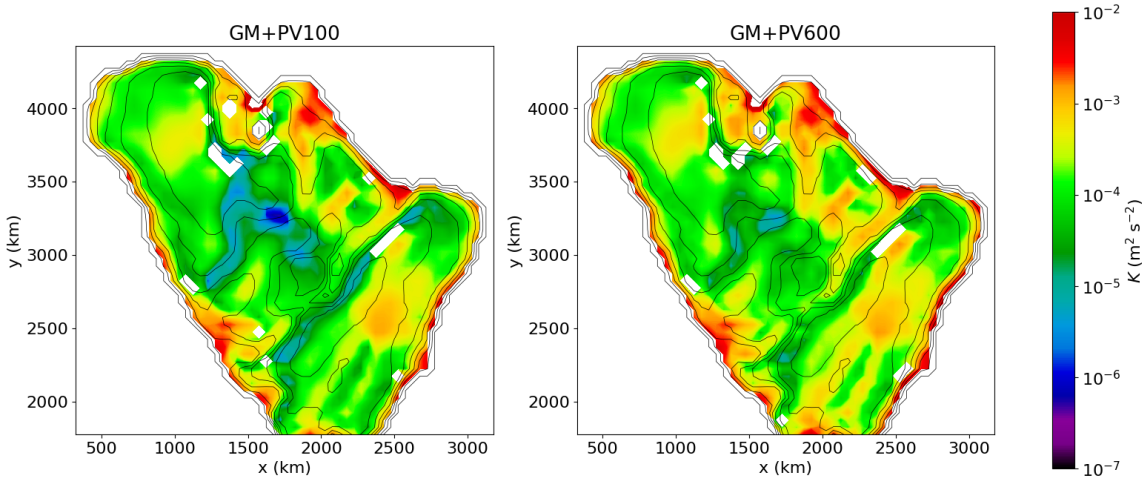

Figure 6.16: Time-mean parameterized EKE, K, (colours) over years 90 - 99 for GM+PV100 (left) and GM+PV600 (right) plotted on a log scale. Black contours indicate the topography. The colour scale is not perceptually uniform, but is used to highlight the large values of K close to the boundary. An accessible version of this plot, with a perceptually uniform colour scale, is shown in Appendix E.

that this reinjected energy is subsequently converted from parameterized barotropic EKE to MKE (Figure 6.9), ultimately forcing a mean boundary current.

Other small-scale features in the parameterized kinetic energy conversion also contribute to the pattern of parameterized EKE, K (Figure 6.16). For example, there is a small area close to the domain boundary in which the magnitude of the eddy-to-mean kinetic energy conversion decreases and, in some areas, changes sign to become mean-to-eddy kinetic energy conversion. No such rapid change in APE-to-EKE conversion is observed close to the domain edge (Figure 6.17). Thus, the source of K from the APE-to-EKE conversion mechanism does not change very close to the domain edge, but the sink of K from the parameterized kinetic energy conversion decreases very close to the domain edge. This results in the larger values of K seen close to the domain edge (Figure 6.16). Additionally, we see areas of mean-to-eddy kinetic energy conversion align with areas of relatively large values of K, such as in the centre of the Canada Basin and the Eurasian Basin. This suggests that mean-to-eddy kinetic energy conversion is the cause of the relatively large values of K in these areas in the parameterized simulations here.

We compare the spatial patterns of K and APE-to-EKE conversion with that of Wang et al. (2020), in which they employed an unstructured-mesh model to run global simulations with a 1 km horizontal resolution in the Arctic Ocean. They describe large values of EKE around the Arctic Basin boundary, with values one or two orders of magnitude smaller a small distance from the boundary, largely verified in observations (von Appen et al., 2022), and consistent with the spatial pattern of K in the GM+PV simulations (Figure 6.16). However, other aspects of the distribution of K do not agree with that of the modelled EKE in this case. Specifically, Wang et al. (2020) describe relatively large values of EKE along the Lomonosov Ridge in the high-resolution model, while both the GM+PV100 and GM+PV600 simulations exhibit relatively small values of K in this region. There is also an area of relatively large K in the centre of the Eurasian Basin in both the GM+PV100 and GM+PV600 simulations which is not seen in the modelled EKE of Wang et al. (2020). It should be noted that Wang et al. (2020) describe upper ocean EKE whereas we describe the barotropic (i.e. depth-averaged) EKE which are not exactly comparable.

The pattern of large APE-to-EKE conversion around the boundary of the Arctic Basin is also largely consistent with that of Wang et al. (2020). However, they

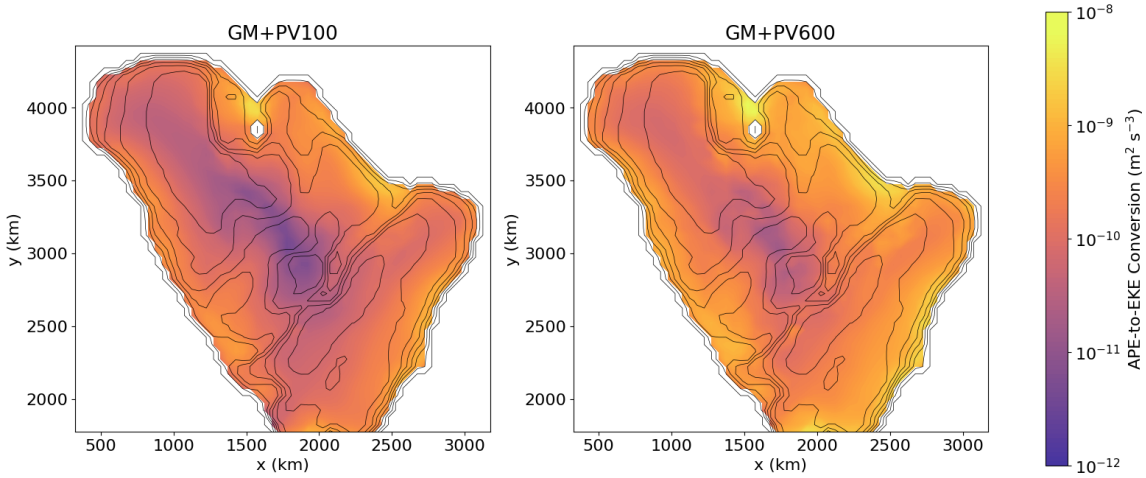

Figure 6.17: Time-mean APE-to-EKE conversion (colours) over the years 90 - 99 for GM+PV100 (left) and GM+PV600 (right) plotted on a log scale. Black contours indicate the topography.

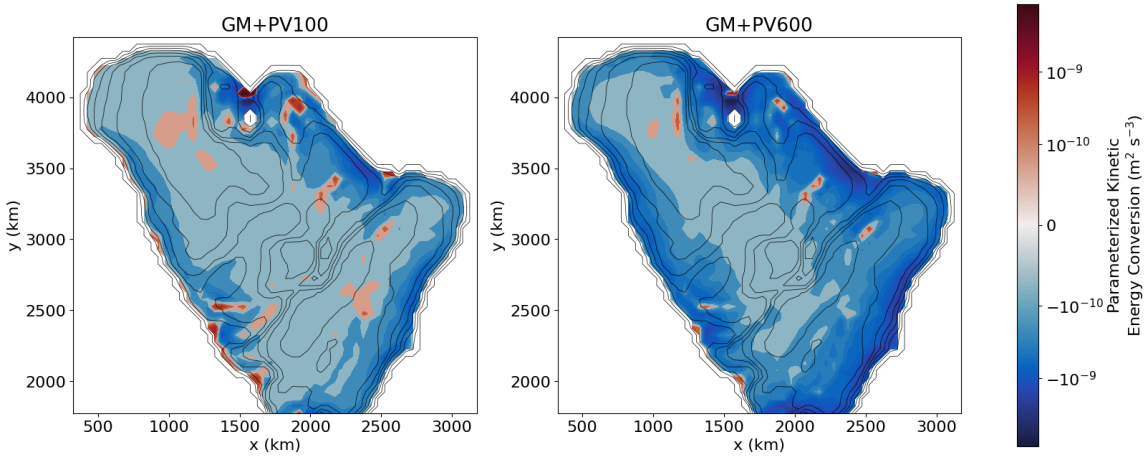

Figure 6.18: Time-mean kinetic energy conversion between the mean and parameterized eddy components (colours), where negative values indicate a conversion from eddy to mean, over the years 90 - 99 for GM+PV100 (left) and GM+PV600 (right). Black contours indicate the topography.

find relatively large values of APE-to-EKE conversion in the centre of the Beaufort Gyre and along the Lomonosov Ridge, which is not present in either GM+PV100 or GM+PV600. In particular, Wang et al. (2020) find that the large APE-to-EKE conversion in the Beaufort Gyre leads to relatively large values of EKE in this region. In contrast, the results described above suggest that large values of mean-to-eddy kinetic energy conversion are the cause of the relatively large values of K seen in the Canada Basin. This difference in behaviour likely comes from the fact that the APE-to-EKE conversion in Wang et al. (2020) comes from the resolved eddies, whereas the pattern of APE-to-EKE conversion in the GM+PV simulations comes from the GM90 parameterization. Since we have employed GM90 with constant κ_{GM}, it is possible that the pattern of APE-to-EKE conversion may change qualitatively by employing a more sophisticated version of GM90.

6.3.4 Enstrophetics

The time series of volume-averaged parameterized barotropic EPEnstr, Λ, and the terms in the Λ budget (Equation 2.14) are plotted in Figure 6.19. The source of Λ from mean-to-eddy potential enstrophy conversion is largely balanced by the dissipation of Λ (Figure 6.19). Since the dissipation of Λ depends linearly on the parameterized EPEnstr damping coefficient, r_Λ, this suggests that r_Λ is important in determining the quasi-steady state. Note that the advection and diffusion terms in the budget are not shown as they are of order $\mathcal{O}(10^{-26})$ m^{-2} s^{-3} and $\mathcal{O}(10^{-30})$ m^{-2} s^{-3} respectively and, hence, these terms do not significantly affect the volume-averaged values of Λ.

The spatial patterns of time-mean parameterized EPEnstr (Figure 6.20) and mean-to-eddy potential enstrophy conversion (Figure 6.21) over years 90 - 99 are plotted for both GM+PV100 and GM+PV600. Potential enstrophy is converted from the mean component to the parameterized eddy component around the boundary of the Arctic Basin, resulting in a spatial pattern of Λ which is relatively large around the boundary of the basin.

The large parameterized mean-to-eddy potential enstrophy conversion seen around the boundary of the Arctic Basin is not seen in other regions with a similarly large topographic slope such as along the Lomonosov Ridge. We determined in Section 2.4 that both strong parameterized eddy PV fluxes (i.e. large eddy PV flux magnitude,

$|\overline{q'\mathbf{u}'}|$) and large background PV gradients can enhance the parameterized mean-to-eddy potential enstrophy conversion, and that $|\overline{q'\mathbf{u}'}|$ is not directly affected by the topographic slope. Figure 6.22 shows the spatial patterns of time-mean parameterized $|\overline{q'\mathbf{u}'}|$ over years 90 - 99 for both GM+PV100 and GM+PV600. The parameterized eddy PV fluxes are indeed large around the boundary of the Arctic Basin where the parameterized mean-to-eddy potential enstrophy conversion is large. However, $|\overline{q'\mathbf{u}'}|$ is 2 - 3 orders of magnitude smaller over the Lomonosov Ridge which likely leads to the smaller parameterized mean-to-eddy potential enstrophy conversion in this region when compared to the Arctic Basin boundary.

The eddy PV diffusivity, κ_{PV}, can be inferred from the parameterized mean-to-eddy potential enstrophy conversion (Figure 6.21) and/or the magnitude of the parameterized eddy PV fluxes (Figure 6.22) in combination with the value of $|\nabla\overline{q}|$ (not shown). This gives a value κ_{PV} of $\mathcal{O}(10^3)$ m^2 s^{-1} around the Arctic Basin boundary and $\mathcal{O}(10^4)$ m^2 s^{-1} in the interior of the Canada and Eurasian Basins. Thus, κ_{PV} is suppressed around the boundary of the Arctic Basin due to the large topographic slope.

6.3.5 Sensitivity of Energetics to Input Parameters

Finally, we investigate the sensitivity of the quasi-steady state kinetic energy components (MKE and parameterized EKE, K) and the transfers associated with the kinetic energy pathways (APE-to-EKE conversion and eddy-to-mean kinetic energy conversion) of GM+PV simulations to some of the input parameters to GM+PV. Specifically, we analyse the results of changes to the eddy PV flux efficiency parameter, γ_q; the fraction of MAPE converted to barotropic EKE, λ; the parameterized EPEnstr damping coefficient, r_Λ; and the parameterized EKE damping coefficient, r_K. We run eight simulations of GM+PV600 in which we systematically increase or decrease one of the parameters listed above. The time-mean basin-averaged values of MKE, K, APE-to-EKE conversion and eddy-to-mean kinetic energy conversion over the years 90 - 99 normalized by their value in GM+PV600 are plotted in Figure 6.23. In all panels, GM+PV600 (without any parameter changes) is the middle value plotted, hence the normalised values are always one.

We first note that the APE-to-EKE conversion undergoes a relatively large change by varying λ and relatively small changes by varying γ_q, r_Λ and r_K. The value of

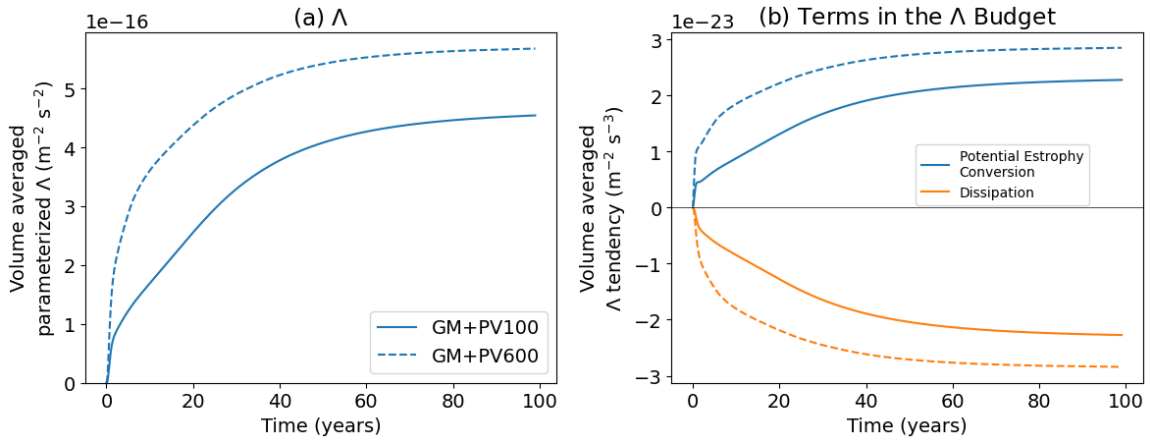

Figure 6.19: Time series of basin-averaged (a) parameterized EPEnstr, Λ; and (b) terms in the parameterized EPEnstr budget, specifically, mean-to-eddy potential enstrophy conversion (blue), and dissipation of Λ (orange) for GM+PV100 (solid lines) and GM+PV600 (dashed lines).

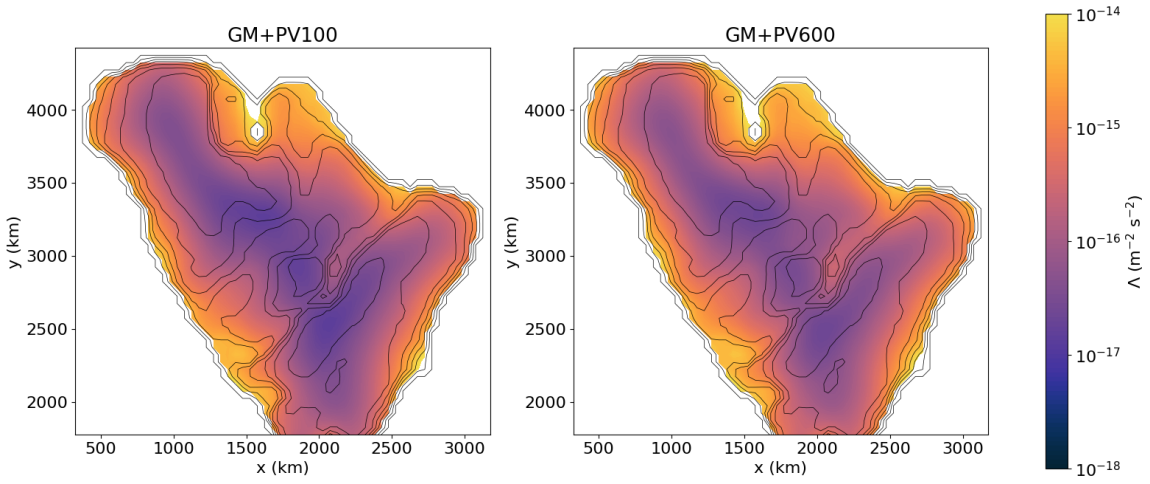

Figure 6.20: Time-mean parameterized EPEnstr, Λ (colours), over the years 90 - 99 for GM+PV100 (left) and GM+PV600 (right) plotted on a log scale. Black contours indicate the topography.

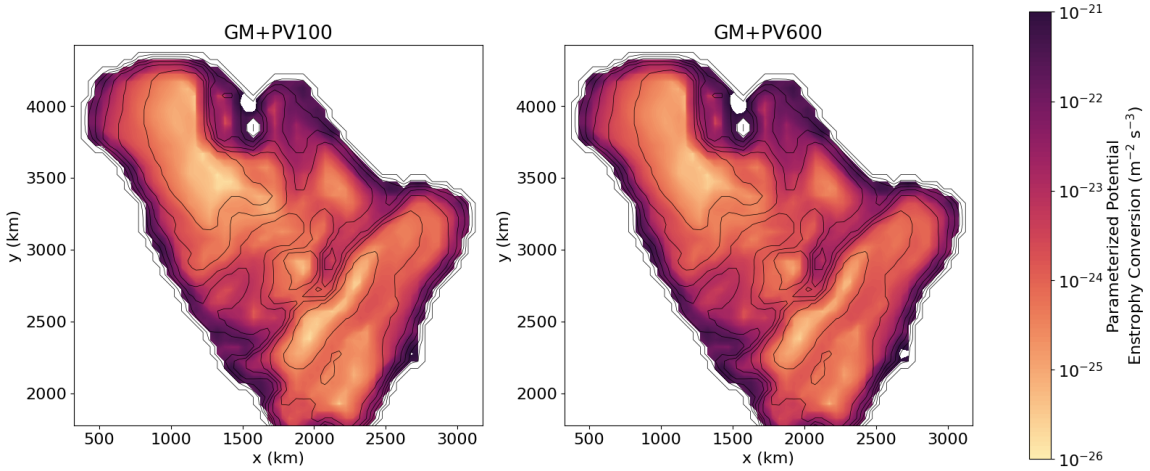

Figure 6.21: Time-mean mean-to-eddy potential enstrophy conversion (colours) over the years 90 - 99 for GM+PV100 (left) and GM+PV600 (right) plotted on a log scale. Black contours indicate the topography.

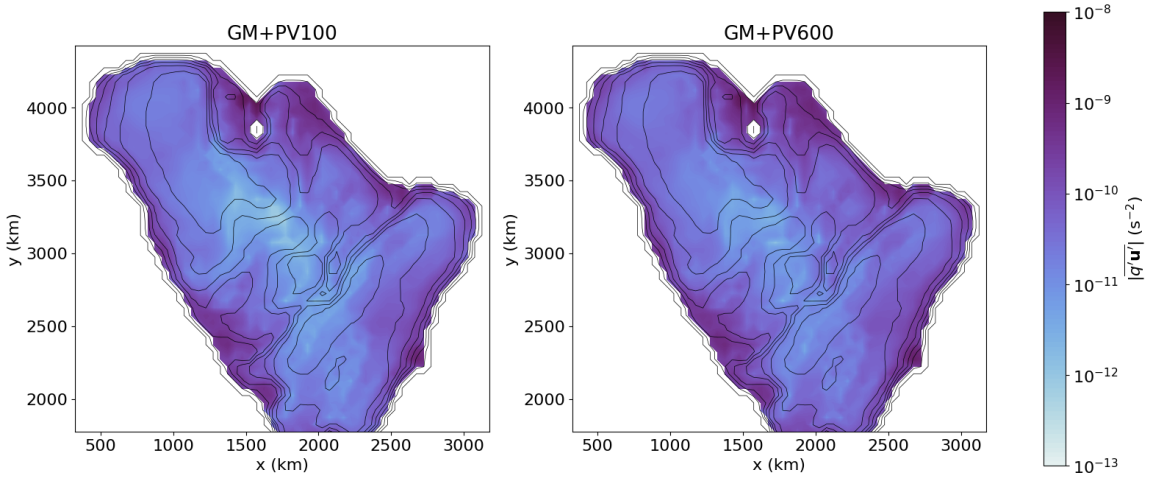

Figure 6.22: Time-mean parameterized eddy PV fluxes (colours) over the years 90 - 99 for GM+PV100 (left) and GM+PV600 (right) plotted on a log scale. Black contours indicate the topography.

the APE-to-EKE conversion is directly affected by λ and there is a linear dependence of the former on the latter (Equation 5.21). This linear dependence is seen when λ is varied and is also observed for the MKE, K and the eddy-to-mean kinetic energy conversion (Figure 6.23b). The MKE is most sensitive to changes in λ (Figure 6.23b) and relatively small changes in the MKE are seen when other parameters are varied. K appears to absorb much of the effect of varying both γ_q (Figure 6.23a) and r_Λ (Figure 6.23c) such that the effect on the MKE is relatively small in comparison. Varying the value of r_K (Figure 6.23d) has the smallest effect on the kinetic energy components and pathways. The relatively small effect of γ_q, r_Λ and r_K on the MKE, as well as the observed approximate linear relationship between the value of λ and the kinetic energy components and pathways indicates that λ may be of use in tuning the GM+PV parameterization.

6.4 Summary and Discussion

In this chapter, we have tested the GM+PV parameterization, as described in Chapter 5, in a semi-realistic Arctic Ocean setup. We compare simulations employing no eddy parameterization (NO PAR); GM90 only using constant κ_{GM} with values 100 $\mathrm{m^2\ s^{-1}}$ and 600 $\mathrm{m^2\ s^{-1}}$ (GM100 and GM600 respectively); and GM+PV using constant κ_{GM} with values 100 $\mathrm{m^2\ s^{-1}}$ and 600 $\mathrm{m^2\ s^{-1}}$ (GM+PV100 and GM+PV600 respectively). Thus, GM+PV100 can be compared to GM100, where GM+PV100 includes the parameterized effects of barotropic eddy PV fluxes and GM100 does not. The same comparison can be made between GM+PV600 and GM600.

We find that in NO PAR, GM100 and GM600, the flow is wind-driven and anticyclonic everywhere in the Arctic Basin, with a strength that decreases with depth. Thus, the dominant process affecting the flow in these simulations appears to be the wind forcing. In contrast, in both GM+PV100 and GM+PV600, the near-surface flow is wind-driven and anticyclonic, while at depth there is a cyclonic flow around the boundary of the Arctic Basin, broadly resembling the Arctic Circumpolar Boundary Current. This current structure is reflected in the transport streamfunction which is anticyclonic everywhere in the Arctic Basin for NO PAR, GM100 and GM600, and cyclonic in much of the basin in GM+PV100 and GM+PV600. The results suggest that, when GM+PV is employed, there is a competing effect between the effect of the wind and the effect of the parameterized eddies in driving the large-scale flow.

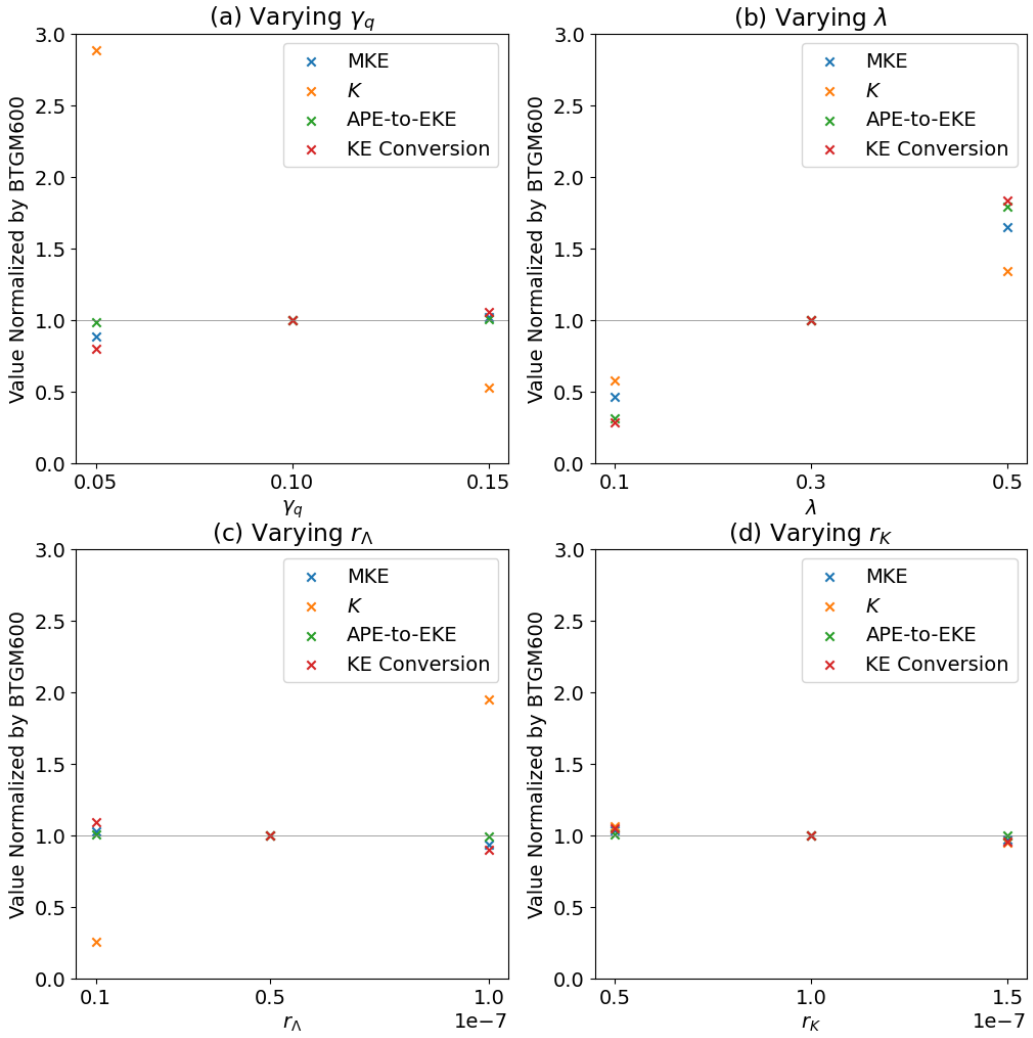

Figure 6.23: Basin-averaged time-mean values of MKE (blue), parameterized EKE, K, (orange), APE-to-EKE conversion (green) and eddy-to-mean kinetic energy conversion (red) over the years 90 - 99 normalized by their value in GM+PV600. Each set of values corresponds to a simulation identical to GM+PV600 except for a change in one of the parameterization input parameters. The input parameters which are varied are (a) the eddy PV flux efficiency parameter, γ_q; (b) the fraction of MAPE converted to barotropic EKE, λ; (c) the parameterized EPEnstr damping coefficient, r_Λ; and (d) the parameterized EKE damping coefficient, r_K. In all panels, the middle value plotted is the GM+PV600 simulation (without any changes to parameter values) and thus the normalised values are always one.

As κ_{GM} is increased, the effect of the parameterized eddies dominates over the wind forcing, indicated by the increase in cyclonic flow and decrease in anticyclonic flow. The spatial distribution of depth-integrated MKE is largely unchanged between NO PAR, GM100 and GM600, although the magnitude decreases as κ_{GM} increases. Employing GM+PV leads to a redistribution of MKE, with large MKE values exhibited in areas of large topographic slope, such as along the Lomonosov Ridge and around the Chuchki Plateau.

Employing GM+PV leads to an improved representation of the flow of water into the Arctic Basin close to Fram Strait. In NO PAR, GM100 and GM600, the anticyclonic circulation forced by the wind dominates over the cyclonic circulation forced by the inflow and outflow of water to the Arctic Basin at Fram Strait. This leads to an outflow of water across most of the eastern side of Fram Strait and an inflow of water across the western side of Fram Strait and in a very small region close to the boundary on the eastern side of the strait. In GM+PV100 and GM+PV600, there is an inflow of water at depth on the eastern side and an outflow of water at depth on the western side of Fram Strait, broadly consistent, qualitatively, with the inflow of water into the Arctic Basin via the West Spitsbergen Current (Cokelet et al., 2008; Beszczynska-Möller et al., 2012) and the outflow of water via the East Greenland Current (Beszczynska-Möller et al., 2012; Richter et al., 2018). Additionally, the transport of water into and out of the Arctic Basin close to Fram Strait is increased when GM+PV is employed, which leads to volume transport values which are closer to observed values.

The energetics and enstrophetics of the simulations employing GM+PV show that the quasi-steady state is achieved by a near balancing of the APE-to-EKE conversion with the eddy-to-mean kinetic energy conversion, and a balancing of the parameterized EPEnstr dissipation with the mean-to-eddy potential enstrophy conversion. The majority of APE-to-EKE conversion occurs around the boundary of the Arctic Basin, and this kinetic energy is largely converted from the parameterized barotropic EKE to MKE via the barotropic parameterization. Areas of mean-to-eddy kinetic energy conversion also occur in the Canada and Eurasian Basins, which contribute to areas of large parameterized EKE. Mean-to-eddy potential enstrophy conversion largely occurs around the boundary of the Arctic Basin, indicating that the parameterized eddies are mixing PV more strongly in this region.

The effects of the GM+PV parameterization on the modelled flow field presented here are promising, particularly the emergent cyclonic propagation around the boundary at depth, broadly resembling the Arctic Circumpolar Boundary Current. However, the model setup employed here is highly idealised and further tests of the parameterization should include additional processes which are missing in this setup. This could involve including the Barents Sea in the model domain, employing a sea ice component which modulates the transfer of momentum from the atmospheric winds to the ocean, and/or including the effect of freshwater sources and air-sea fluxes. Additionally, we have speculated that Atlantic Water is propagating anticyclonically around the Arctic Basin in simulations which do not employ GM+PV, and cyclonically in simulations which do employ GM+PV, but further analysis would be required to confirm this. A more robust understanding of the movement of Atlantic Water in the Arctic Basin may be possible by utilising Lagrangian particle tracking methods (van Sebille et al., 2017).

In their study of the energetics in the Arctic Ocean using a model with 1 km resolution in this region, Wang et al. (2020) find the resolved EKE has significant vertical structure. By design, the parameterized barotropic EKE is independent of depth in GM+PV. One way of introducing vertical structure to the parameterized EKE would be to use the method of Yankovsky et al. (2024) in which they use a structure function, formulated from the equivalent barotropic mode, to impose vertical structure onto the two-dimensional backscatter component. Observations of the vertical structure of kinetic energy in the ocean are largely consistent with the equivalent barotropic mode (de La Lama et al., 2016) justifying the use of such a structure function. A similar structure function could be applied to the parameterized EKE to introduce vertical structure in this field. It may also be important to introduce vertical structure in the parameterized EPEnstr field, however, it is not obvious if the equivalent barotropic mode is appropriate for adding vertical structure to the EPEnstr.

Chapter 7

Conclusions

7.1 Summary

In this thesis, we have presented a new parameterization of barotropic eddy PV fluxes for use in non-eddying models which is both energetically and enstrophetically constrained. The parameterization represents the eddy PV fluxes as down-gradient PV mixing and exploits a mathematical bound on the magnitude of the eddy PV fluxes to incorporate the constraints. Employing constraints in a down-gradient PV mixing parameterization is necessary since, if left unconstrained, the parameterized eddies will always act to bring the flow to a PV-homogenized state. This contradicts modelling experiments of freely decaying barotropic turbulence which indicate that the initial energy of the system determines the amount of PV mixing which occurs (Siegelman and Young, 2023). Specifically, if the initial energy of the system is lower than that of a PV homogenized state, the modelled flow should not reach PV homogenization without a source of energy. Eddies parameterized as unconstrained PV mixing will always act to drive the flow towards a state of PV homogenization, regardless of the initial energy of the system. Thus, when parameterized in this way, the eddies can act as a spurious source of energy in the system. In this new parameterization, we aim to remove this spurious source of energy by imposing physically motivated constraints in the parameterization.

In Chapter 2, we formulated the parameterization of barotropic eddy PV fluxes. We showed how the eddy PV fluxes can be related to both the EKE and the EPEnstr.

Then, by introducing the eddy PV flux efficiency parameter, we formulated a down-gradient PV mixing parameterization which is constrained by both the EKE and the EPEnstr. We constructed a parameterized EKE budget and a parameterized EPEnstr budget to constrain the parameterized eddy PV fluxes. This work builds from the success of previous studies which incorporate an energetic constraint into the GM90 parameterization of baroclinic instability (e.g. Cessi, 2008; Eden and Greatbatch, 2008; Marshall et al., 2012; Mak et al., 2017, 2018; Jansen et al., 2019; Yankovsky et al., 2024) and a down-gradient PV mixing parameterization (Marshall and Adcroft, 2010) through the use of an energy budget. To the author's knowledge, this is the first mesoscale ocean eddy parameterization which incorporates an additional potential enstrophy constraint through the use of an EPEnstr budget. Through these budgets, the parameterization can convert kinetic energy bidirectionally between the parameterized eddies and the large-scale flow and potential enstrophy from the large-scale flow to the parameterized eddies.

In Chapter 3, we performed the first tests of this parameterization, comparing the results of a non-eddying simulation employing the parameterization to that of an eddy-resolving simulation. We used a highly idealised setup to isolate the effects of the explicit/parameterized eddies. The parameterization was tested in a model of freely decaying barotropic turbulence in a doubly periodic domain over variable topography on an f-plane. We find that the constraints imposed in the parameterization are successful in constraining the kinetic energy and potential enstrophy of the large-scale flow when compared to a simulation employing an unconstrained PV mixing parameterization. As a result, the parameterization produces a topography-following flow of a realistic magnitude as determined by the eddy-resolving simulation. The kinetic energy and potential enstrophy transfers in the parameterized simulation initially resemble those of the eddy-resolving simulation, in which there is a net transfer of kinetic energy from the parameterized eddies to the large-scale flow, and a net extraction of potential enstrophy from the system. Later in the simulation, the kinetic energy and potential enstrophy transfers of the parameterized and eddy-resolving simulations diverge. The eddy-resolving simulation reaches a quasi-steady state in which there is a net extraction of both kinetic energy and potential enstrophy. The magnitudes of these extractions are sufficiently small such that the MKE and MPEnstr reach a quasi-steady state. In contrast, the parameterized simulation exhibits a net extraction of kinetic energy, much larger in magnitude than that of the eddy-resolving simulation, and a net input of potential enstrophy. These transfers act to damp the

resolved flow, bringing the flow towards a state of rest. This behaviour is caused by the depletion of parameterized EKE, which effectively turns off the parameterized conversions of kinetic energy and potential enstrophy.

In Chapter 4, we implemented a kinetic energy supercharger mechanism into the parameterization, motivated by the results of the previous chapter. This mechanism replenishes the parameterized EKE in order to ensure that it does not get sufficiently depleted so as to effectively turn off the parameterized conversions of kinetic energy and potential enstrophy. The aim was to produce sustained kinetic energy and potential enstrophy transfers in the parameterized simulation which more closely resemble those of the eddy-resolving simulation. The kinetic energy supercharger mechanism reinjects the kinetic energy extracted from the large-scale flow by biharmonic diffusion into the parameterized EKE budget. Such a mechanism has previously been tested in an eddy parameterization employing an eddy energy budget in combination with a negative Laplacian of the resolved velocity in the governing equations to transfer this kinetic energy to resolved scales (Jansen et al., 2019). In the implementation of this parameterization, we did not employ a negative Laplacian in the governing equations, instead relying on the pre-existing kinetic energy conversion mechanism within the parameterization to transfer this kinetic energy to the large-scale flow. When the kinetic energy supercharger mechanism is employed, the parameterized simulation reaches a quasi-steady state in which both kinetic energy and potential enstrophy are approximately conserved. This leads to a quasi-steady state in which there is an emergent topography-following flow which more closely resembles that of the eddy-resolving simulation.

In Chapter 5, we outlined one method of implementing the parameterization of barotropic eddy PV fluxes in a baroclinic setup. We did not extend the parameterization to represent the baroclinic eddy PV fluxes. Instead, we chose to employ the parameterization of barotropic eddy PV fluxes, alongside and integrated with, the GM90 parameterization of baroclinic instability. These parameterizations were integrated by incorporating the APE-to-EKE conversion mechanism, through which a fraction of the APE extracted from the large-scale flow by GM90 is reinjected into the parameterized barotropic EKE budget. This APE-to-EKE conversion mechanism mimics the process of barotropization, in which APE is converted to eddy energy, a fraction of which becomes barotropic EKE. Inspired by the GM+E parameterization (Bachman, 2019), we refer to this implementation of the barotropic parameterization

alongside and integrated with GM90 as GM+PV. We described how the GM+PV parameterization was implemented in the MITgcm.

In Chapter 6, we tested the GM+PV parameterization, outlined in the previous chapter, in a semi-realistic Arctic Ocean configuration in MITgcm. We chose this setup since topography following-flows are prevalent in this region (Orvik and Niiler, 2002). We ran simulations with no eddy parameterization; with GM90 only; and with GM+PV. We find that, in simulations with no eddy parameterization and with GM90 only, the flow is wind-driven and anticyclonic everywhere in the basin, and the strength of the flow decreases with depth. In simulations employing GM+PV, there is a wind-driven anticyclonic flow near the surface and a reversal of the flow at depth. In particular, a cyclonic boundary current is present at depth, largely resembling that of the Arctic Circumpolar Boundary Current, which is not present in simulations which do not employ GM+PV. The quasi-steady state in the simulations employing GM+PV is achieved through a near balancing of the parameterized APE-to-EKE conversion with the parameterized eddy-to-mean kinetic energy conversion, and a balancing of the parameterized mean-to-eddy potential enstrophy conversion with the dissipation of parameterized EPEnstr.

7.2 Discussion

Through the parameterization formulation presented in Chapter 2, we have essentially transferred the problem from parameterizing the eddy PV fluxes directly, to parameterizing the EKE and EPEnstr. Thus, an obvious question is: how should the EKE and EPEnstr be parameterized? We constructed parameterized budgets in Chapter 2, making choices about the processes we included in these budgets and the method of representing them. One benefit of this approach is that specific energy and/or potential enstrophy pathways can be included in the parameterization by incorporating them into the budgets, as demonstrated in Chapters 4 and 5. However, the choices we make about the processes included in the parameterized budgets and the method for representing them will affect the results of the parameterized simulations.

Many of the choices we have made in the construction of the parameterized budgets have been oversimplifications, justified by the fact that these are preliminary

tests of a new concept. For example, we represent the dissipation of parameterized EKE as linear damping with a dissipation timescale which is constant in time and space. The dissipation of mesoscale EKE includes a number of processes, for example, bottom drag (Sen et al., 2008), the generation of lee waves over rough topography (Naveira Garabato et al., 2013), and loss of balance (Chouksey et al., 2018). Representing the combination of these processes as linear drag is a crude approximation. Additionally, it has been shown that, when eddy energy dissipation is represented as linear damping in the GEOMETRIC implementation of GM90, modest changes in the dissipation timescale lead to significant changes in the ocean circulation transport and global ocean heat content over long timescales (Mak et al., 2022b). Thus, a more accurate representation of EKE dissipation is an area for improvement in the parameterization in its current form.

Similarly, an understanding of the dissipation routes of potential enstrophy in the ocean is lacking, and it is certainly possible that representing dissipation of EPEnstr as linear damping is also an oversimplification. Since the dissipation of parameterized EPEnstr is found to be important in setting the quasi-steady solution, an understanding of this process is important. Furthermore, we neglect the eddy advection of EPEnstr in the formulation of the parameterized EPEnstr budget, but numerical experiments have demonstrated that this term can dominate the redistribution of EPEnstr (Wilson and Williams, 2004). In fact, during the statistically-steady state solution in numerical models of a wind-driven ocean in a basin with flat topography, the direction of the eddy PV flux with respect to the large-scale PV gradient is linked to the advection of EPEnstr, which is dominated by the eddy advection component (Wilson and Williams, 2004). Thus, a better understanding of the dynamics of EPEnstr may help in improving the formulation of the parameterized EPEnstr budget, and may even prove useful in extending the parameterization to include up-gradient fluxes of PV.

Refining the formulations of the budgets of both EKE and EPEnstr would require a better understanding of the processes which affect these quantities in the ocean. While there has been a significant effort applied to gaining an understanding of the energy pathways in the ocean (e.g. Ferrari and Wunsch, 2009; Aiki et al., 2011), the same focus has not been applied as thoroughly to understanding the potential enstrophy pathways in the ocean. The work presented in this thesis suggests that furthering our understanding of the dynamics of potential enstrophy in the ocean may be useful in

parameterizing mesoscale ocean eddies. This may be possible through a combination of high-resolution idealised numerical modelling studies and observational studies.

One challenge to observing potential enstrophy in the ocean is that derivatives of the velocity are required to calculate the PV. Yu et al. (2021) used OSMOSIS (Ocean Surface Mixing, Ocean Submesoscale Interaction Study) data to calculate PV, from which it is possible to calculate the potential enstrophy. Additionally, the SWOT (Surface Water and Ocean Topography) Mission (Durand et al., 2010) provides the opportunity to calculate gradients of geostrophic velocity anomalies from sea surface height measurements using swath altimetry. Either of these methods could be utilised to provide a measure of potential enstrophy in the ocean which can be analysed to investigate the pathways of potential enstrophy. However, both methods provide surface measurements and therefore do not directly tell us anything about the behaviour of potential enstrophy below the surface. Measurements of the deeper ocean are sparse and, at present, calculating derivatives of velocity on small scales in the deep ocean would be challenging.

In addition to the EKE and EPEnstr, a more thorough investigation into the eddy PV flux efficiency parameter, γ_q, is also an important next step. We may want to know if the magnitude of γ_q varies across different flow regimes, if γ_q varies in time and in space and, if so, which conditions strongly affect the magnitude of γ_q. Here, we have used a constant value of γ_q everywhere and at all times. One method of refining the parameterization could include a more complex prescription of γ_q. This could be achieved by imposing physics-based constraints on γ_q and/or providing some element of variability to γ_q, for example, through the use of stochastic forcing. All of the above statements also apply to the fraction of MAPE converted to barotropic EKE, λ, in the GM+PV parameterization.

In analysing the performance of the parameterization, we have made simplifications, and restricted our attention to specific model configurations as a first step in testing the parameterization. Avenues for future work could address some of these gaps by testing and/or adapting the parameterization to work in other configurations. For example, here we have restricted our attention to testing the parameterization on an f-plane over topography, hence only the topography affects the background PV. In more realistic model setups, the β-effect also affects the background PV. Thus, one clear topic for investigation is analysing the performance of the parameterization on

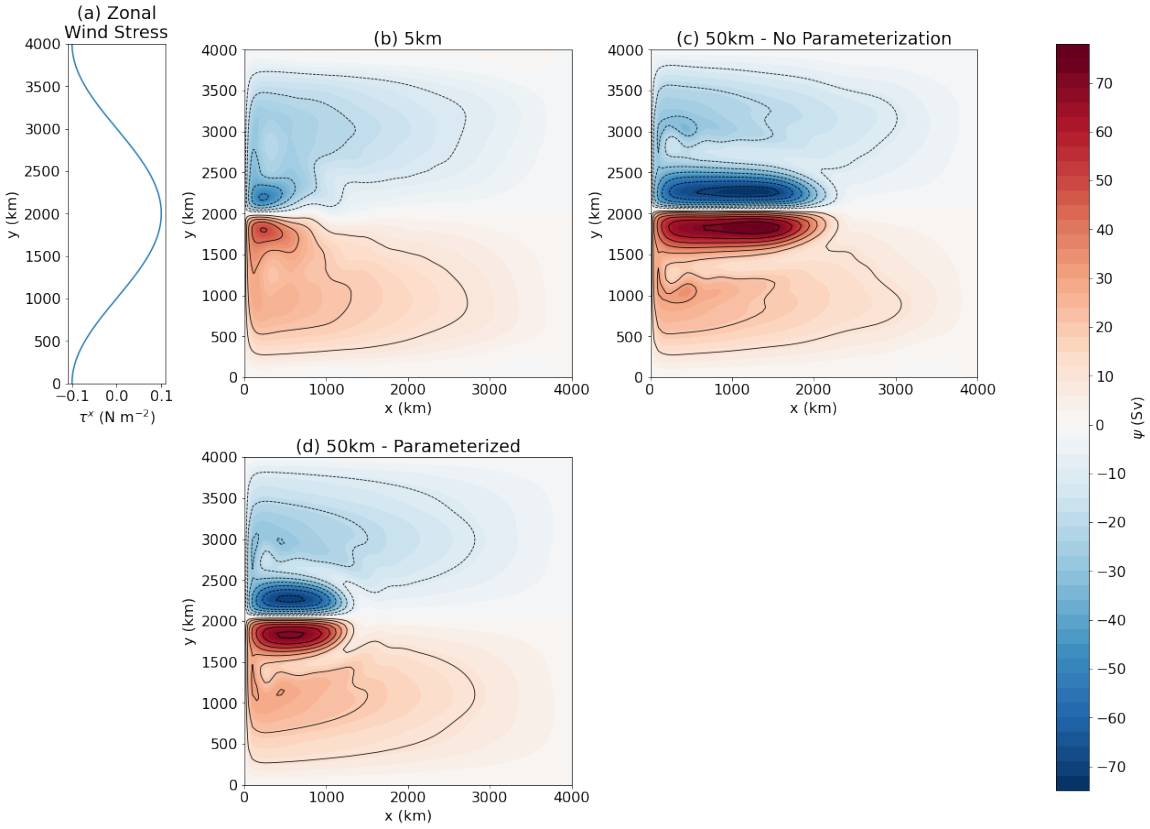

Figure 7.1: (a) Zonal wind stress. Time-mean streamfunction (filled contours) during the quasi-steady period of barotropic wind-driven simulations on a β-plane with flat topography for (b) an eddy-resolving simulation at 5km horizontal resolution; (c) a coarse-resolution simulation at 50km horizontal resolution without any eddy parameterization; and (d) a coarse-resolution simulation at 50km horizontal resolution employing the parameterization of barotropic eddy PV fluxes outlined in Chapter 2. Black contours are plotted every 10 Sv for positive values (solid lines) and negative values (dashed lines).

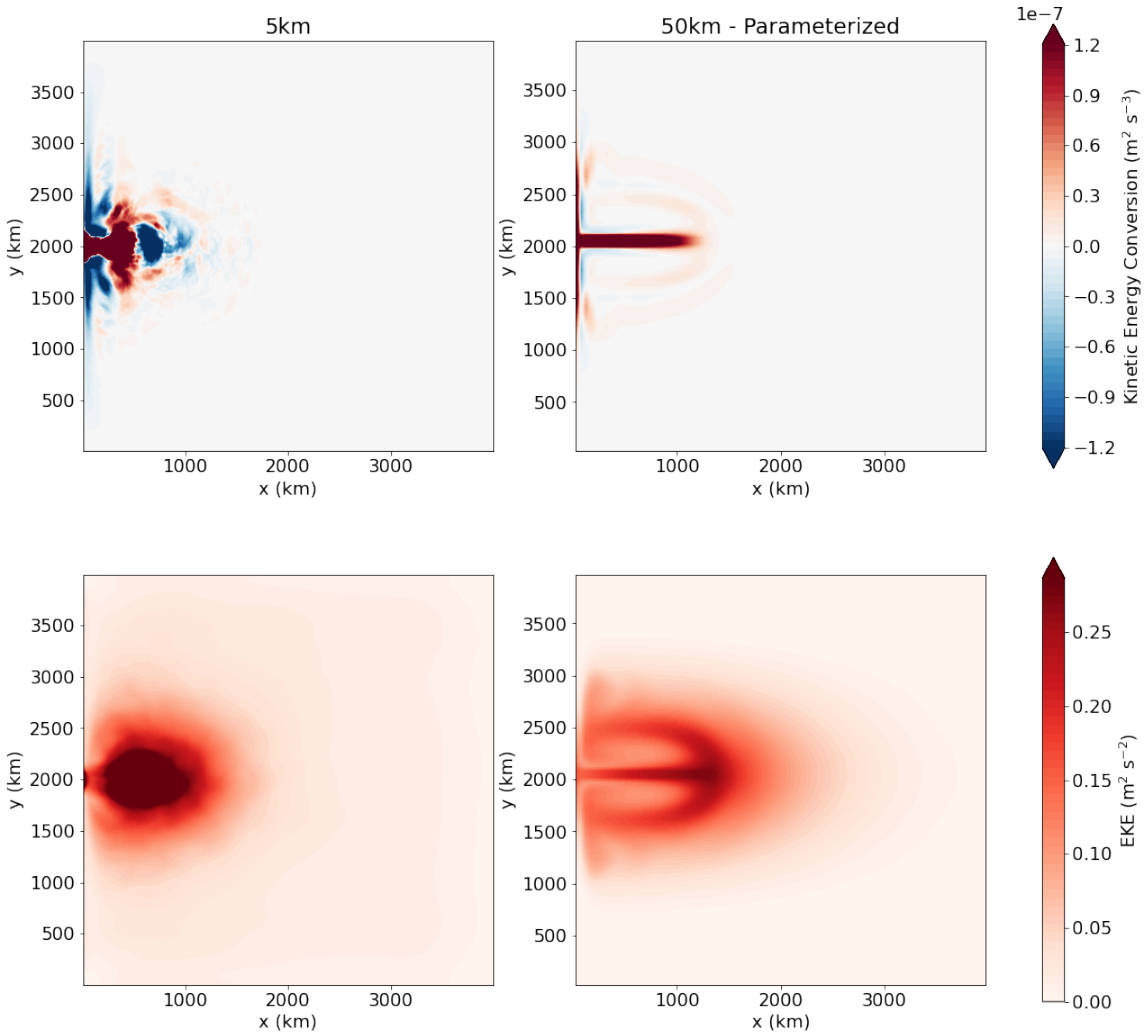

Figure 7.2: Time-mean kinetic energy conversion, $\overline{q'\mathbf{u}'} \cdot \nabla\overline{\psi}$ (top), and EKE (bottom) during the quasi-steady period of barotropic wind-driven simulations on a β-plane with flat topography for an eddy-resolving simulation at 5km horizontal resolution (left) and a coarse-resolution simulation at 50km horizontal resolution employing the parameterization of barotropic eddy PV fluxes outlined in Chapter 2 (right). The explicit EKE and kinetic energy conversion are plotted for the eddy-resolving simulation and the parameterized values are plotted for the parameterized simulation. Positive kinetic energy conversion values indicate mean-to-eddy conversion and negative values indicate eddy-to-mean conversion.

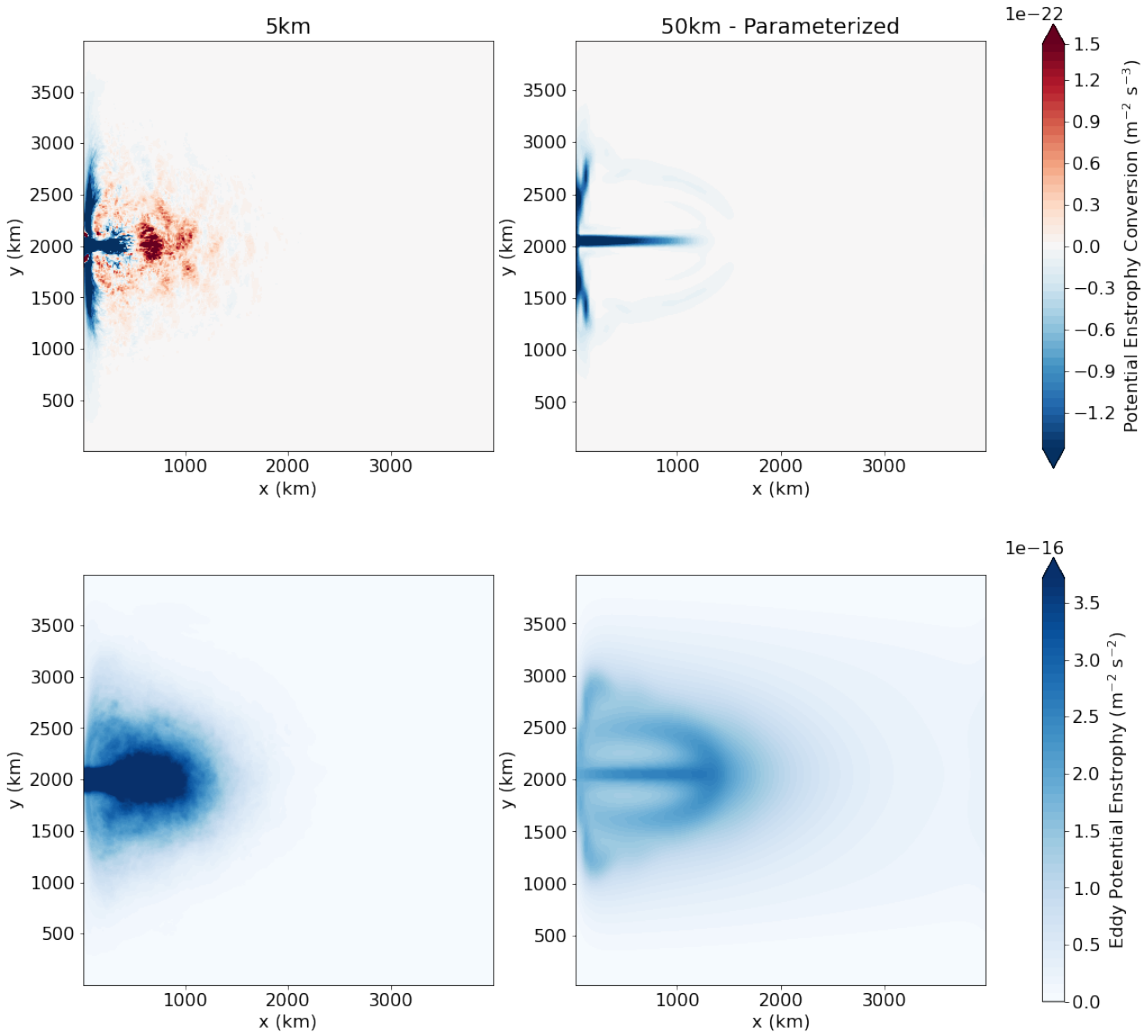

Figure 7.3: Time-mean potential enstrophy conversion, $\overline{q'\mathbf{u}'} \cdot \nabla\overline{q}$ (top), and EPEnstr (bottom) during the quasi-steady period of barotropic wind-driven simulations on a β-plane with flat topography for an eddy-resolving simulation at 5km horizontal resolution (left) and a coarse-resolution simulation at 50km horizontal resolution employing the parameterization of barotropic eddy PV fluxes outlined in Chapter 2 (right). The explicit EPEnstr and potental enstrophy conversion are plotted for the eddy-resolving simulation and the parameterized values are plotted for the parameterized simulation. Positive potential enstrophy conversion values indicate mean-to-eddy conversion and negative values indicate eddy-to-mean conversion.

a β-plane. We performed some preliminary tests of the parameterization as described in Chapter 2 (i.e. in a barotropic setup without the kinetic energy supercharger mechanism) in a wind-driven barotropic model on a β-plane (with $f_0 = 0.7 \times 10^{-4}$ s^{-1} and $\beta = 2 \times 10^{-11}$ m^{-1} s^{-1}) with flat topography and free-slip lateral boundary conditions. The wind forcing was purely zonal with wind-stress, τ^x, shown in Figure 7.1a. We employed linear bottom drag with coefficient 0.5×10^{-7} s^{-1}. Comparing the time-mean streamfunction of an eddy-resolving simulation (Figure 7.1b) with a coarse-resolution simulation without any eddy parameterization (Figure 7.1c), we find that the coarse-resolution simulation leads to a jet which is increased in strength and in horizontal extent relative to the jet in the eddy-resolving simulation. In the eddy-resolving simulation, a combination of mean-to-eddy kinetic energy conversion within the jet and eddy-to-mean kinetic energy conversion on the flanks of the jet act to stabilise the jet close to the western boundary (Figure 7.2). Mean-to-eddy kinetic energy conversion destabilises the jet, which decreases the strength and horizontal extent of the jet, and leads to an EKE bullet (Waterman and Jayne, 2012) (Figure 7.2). In the parameterized simulation, parameterized mean-to-eddy kinetic energy conversion occurs in the region of the jet, with eddy-to-mean kinetic energy conversion on the flanks close to the western boundary, mimicking some of the kinetic energy conversion structure seen in the eddy-resolving simulation (Figure 7.2). This leads to a decrease in the horizontal extent of the jet (Figure 7.1d), an improvement from the coarse-resolution simulation with no eddy parameterization (Figure 7.1c), and an area of large EKE in the region of the jet (Figure 7.2). In the eddy-resolving simulation, mean-to-eddy potential enstrophy conversion occurs in the region of the jet core and in the flanks on the western boundary, with eddy-to-mean conversion occurring downstream of the jet core, leading to a localised area of maximum EPEnstr within the jet (Figure 7.3). In the parameterized simulation, only mean-to-eddy potential enstrophy conversion occurs by construction, a consequence of the imposed down-gradient PV mixing. The pattern of this mean-to-eddy potential enstrophy conversion largely resembles that of the mean-to-eddy potential enstrophy conversion in the eddy-resolving simulation, and an area of large EPEnstr is seen within the jet (Figure 7.3). The patterns of parameterized kinetic energy and potential enstrophy conversion and the improvements to the large-scale flow in the parameterized simulation are promising, although a more thorough investigation into the parameterization performance in this setup is needed.

In the formulation of the parameterization, we have also restricted our attention to

the use of non-eddying models. The increase in computational abilities in recent years has led to the development of scale aware parameterizations which can be employed in both non-eddying and eddy-permitting regimes. Thus, another route for future work is to test the parameterization in an eddy-permitting model, and potentially adapt the parameterization formulation for use in such setups. For example, it is possible that an unconstrained down-gradient PV mixing parameterization employed in an eddy-permitting model could mix any resolved PV anomalies. Thus, explicitly resolved eddies may be suppressed in a similar manner to that which occurs when GM90 is employed in eddy-permitting models. However, the use of parameterized EKE and EPEnstr budgets in the parameterization can act to control the amount of PV mixing which occurs. Thus, it is not obvious if such suppression of resolved PV anomalies will necessarily occur if the parameterization were employed in an eddy-permitting model. Nonetheless, it is likely that adaptations will need to be made to employ the parameterization in eddy-permitting models. Recently, Mak et al. (2023) proposed employing a "splitting" procedure in the GEOMETRIC implementation of GM90. In this procedure, the resolved flow is split into a large-scale component and a resolved eddy component. The parameterized eddy-induced velocity is computed from, and acts only on, the large-scale component of the resolved flow. This method may potentially be of use in implementing the parameterization presented in this thesis in eddy-permitting models.

Finally, in the formulation of GM+PV, in which we implement the barotropic parameterization alongside and integrated with GM90 in a baroclinic setup, we employ GM90 with a constant value of κ_{GM}. Thus, in the form of GM+PV tested in this thesis, there is no feedback of the unresolved eddy energy on the parameterized baroclinic eddies and therefore only the parameterized barotropic eddies are energetically constrained. Thus, an avenue for improvement of GM+PV would be to employ an energetically constrained version of GM90, for example, the GEOMETRIC implementation of GM90 (Marshall et al., 2012; Mak et al., 2017, 2018). However, the barotropic parameterization described in Chapter 2 and the GEOMETRIC implementation of GM90 are not immediately integrable. Specifically, the GEOMETRIC implementation of GM90 employs an eddy energy budget, in contrast to the barotropic EKE budget employed in the barotropic parameterization. Ideally, one energy budget would be employed which informs both the barotropic and baroclinic parameterizations. These energy budgets should therefore be unified, although how this could be achieved remains unclear. Nonetheless, integrating the GEOMETRIC

implementation of GM90 into the GM+PV framework is an interesting and exciting area for future research.

7.3 Concluding Remarks

The work presented in this thesis builds from the existing literature on energetically constrained mesoscale eddy parameterizations while also introducing a novel concept through which an additional enstrophetic constraint can be employed. As a result of these constraints, combined with the use of down-gradient PV mixing, a topography-following flow emerges which is of realistic magnitude in barotropic simulations, and which improves the representation of the large-scale flow in baroclinic Arctic Ocean simulations. I hope that the work presented here encourages more studies on incorporating eddy-seafloor interactions into models, as well as the use of budget-based parameterizations which, we have demonstrated, enable the incorporation of specific processes. This work also motivates further study into the fundamental behaviour of kinetic energy and potential enstrophy in the ocean, which may be accomplished through a combination of numerical experiments and observational analysis.

Appendix A

Derivation of the eddy kinetic energy equation

Here we derive the time-mean depth-integrated eddy kinetic energy (EKE) equation for a barotropic fluid with depth H on a doubly periodic domain. We begin with the vector invariant form of the momentum equation,

$$\frac{\partial \mathbf{u}}{\partial t} + \mathbf{k} \times \mathrm{H} q\mathbf{u} + \nabla B = \mathbf{F}, \tag{A.1}$$

where B is the Bernoulli potential defined as

$$B = \frac{\mathbf{u} \cdot \mathbf{u}}{2} + \frac{p}{\rho_0}, \tag{A.2}$$

where p is the pressure and ρ_0 is a reference density, and $\mathbf{F}$ represents external forces on a fluid parcel.

Taking the time-mean of Equation A.1, we obtain the time-mean momentum equation,

$$\frac{\partial \overline{\mathbf{u}}}{\partial t} + \mathbf{k} \times \mathrm{H}\overline{q}\ \overline{\mathbf{u}} + \mathbf{k} \times \mathrm{H}\overline{q'\mathbf{u}'} + \nabla \overline{B} = \mathbf{F}, \tag{A.3}$$

where we have made use of the relation $\overline{q\mathbf{u}} = \overline{q}\ \overline{\mathbf{u}} + \overline{q'\mathbf{u}'}$. Taking Equation A.3 from Equation A.1 we obtain the eddy momentum equation,

$$\frac{\partial \mathbf{u}'}{\partial t} + \mathbf{k} \times (\mathrm{H}\overline{q}\mathbf{u}' + \mathrm{H}q'\overline{\mathbf{u}} + \mathrm{H}q'\mathbf{u}' - \mathrm{H}\overline{q'\mathbf{u}'}) + \nabla B' = \mathbf{F}'. \tag{A.4}$$

Dotting $\mathbf{u}'$ with Equation A.4 gives the EKE equation,

$$\frac{\partial}{\partial t}\left(\frac{\mathbf{u}' \cdot \mathbf{u}'}{2}\right) + \mathbf{u}' \cdot \mathbf{k} \times (\mathrm{H}\overline{q}\mathbf{u}' + \mathrm{H}q'\overline{\mathbf{u}} + \mathrm{H}q'\mathbf{u}' + \mathrm{H}\overline{q'\mathbf{u}'}) + \mathbf{u}' \cdot \nabla B' = \mathbf{u}' \cdot \mathbf{F}'. \tag{A.5}$$

The terms $\mathbf{u}' \cdot \mathbf{k} \times \mathrm{H}\overline{q}\mathbf{u}'$ and $\mathbf{u}' \cdot \mathbf{k} \times \mathrm{H}q'\mathbf{u}'$ are both equal to zero. Multiplying Equation A.5 by H, making use of the continuity equation (Equation 3.3), and dividing by H gives

$$\frac{\partial}{\partial t}\left(\frac{\mathbf{u}' \cdot \mathbf{u}'}{2}\right) + \mathbf{u}' \cdot \mathbf{k} \times \mathrm{H}q'\overline{\mathbf{u}} + \mathbf{u}' \cdot \mathbf{k} \times \mathrm{H}\overline{q'\mathbf{u}'} + \frac{1}{\mathrm{H}}\nabla \cdot \mathrm{H}\mathbf{u}'B' = \mathbf{u}' \cdot \mathbf{F}'. \tag{A.6}$$

The continuity equation (Equation 3.3) allows us to define a streamfunction such that

$$\mathrm{H}u = -\frac{\partial \psi}{\partial y} \text{ and } \mathrm{H}v = \frac{\partial \psi}{\partial x}. \tag{A.7}$$

Thus, we can rewrite the second term on the left hand side of Equation A.6 as follows

$$\mathbf{u}' \cdot \mathbf{k} \times \mathrm{H}q'\overline{\mathbf{u}} = \mathbf{u}' \cdot \mathbf{k} \times q'(\mathbf{k} \times \nabla\overline{\psi}) \tag{A.8}$$

$$= -q'\mathbf{u}' \cdot \nabla\overline{\psi}. \tag{A.9}$$

Making this substitution into Equation A.6, taking the time-average, integrating over depth and rearranging, we obtain the time-averaged, depth-integrated EKE equation,

$$\mathrm{H}\frac{\partial}{\partial t}\left(\frac{\overline{\mathbf{u}' \cdot \mathbf{u}'}}{2}\right) = \mathrm{H}\overline{q'\mathbf{u}'} \cdot \nabla\overline{\psi} - \nabla \cdot \mathrm{H}\overline{\mathbf{u}'B'} + \mathbf{F}_{\mathrm{EKE}}, \tag{A.10}$$

where $\mathbf{F}_{\mathrm{EKE}}$ represents sources and sinks of depth-integrated EKE, and where the third term on the left hand side has disappeared since $\overline{\mathbf{u}'} = 0$.

Appendix B

Derivation of the eddy potential enstrophy equation

Here we drive the time-mean depth-integrated eddy potential enstrophy (EPEnstr) equation for a barotropic fluid with depth H on a doubly periodic domain. We begin with the vorticity equation for a barotropic fluid,

$$\frac{\partial \xi}{\partial t} = -\nabla \cdot \zeta \mathbf{u} + \mathbf{F}_\xi, \tag{B.1}$$

where $\mathbf{F}_\xi$ represents external forcing on the relative vorticity. The time-mean vorticity equation is

$$\frac{\partial \overline{\xi}}{\partial t} = -\nabla \cdot \overline{\zeta}\ \overline{\mathbf{u}} - \nabla \cdot \overline{\zeta' \mathbf{u}'} + \overline{\mathbf{F}}_\xi, \tag{B.2}$$

where we have used the relation $\overline{\zeta \mathbf{u}} = \overline{\zeta}\ \overline{\mathbf{u}} + \overline{\zeta' \mathbf{u}'}$. By taking Equation B.2 from Equation B.1 we obtain the eddy vorticity equation,

$$\frac{\partial \xi'}{\partial t} = -\nabla \cdot \overline{\zeta} \mathbf{u}' - \nabla \cdot \zeta' \overline{\mathbf{u}} - \nabla \cdot \zeta' \mathbf{u}' + \nabla \cdot \overline{\zeta' \mathbf{u}'} + \mathbf{F}'_\xi. \tag{B.3}$$

From the definition of potential vorticity, q, (Equation 2.1) and since f and H do not vary in time, $\xi' = \mathrm{H}q'$, $\overline{\zeta} = \mathrm{H}\overline{q}$ and $\zeta' = \mathrm{H}q'$. Thus, we may rewrite Equation B.3 as follows

$$\mathrm{H}\frac{\partial q'}{\partial t} = -\nabla \cdot \mathrm{H}\overline{q} \mathbf{u}' - \nabla \cdot \mathrm{H}q' \overline{\mathbf{u}} - \nabla \cdot \mathrm{H}q' \mathbf{u}' + \nabla \cdot \mathrm{H}\overline{q' \mathbf{u}'} + \mathbf{F}'_\xi. \tag{B.4}$$

Multiplying Equation B.4 by q' gives

$$\mathrm{H}\frac{\partial}{\partial t}\left(\frac{q'^2}{2}\right) = -q'\nabla\cdot\mathrm{H}\overline{q}\mathbf{u}' - q'\nabla\cdot\mathrm{H}q'\overline{\mathbf{u}} - q'\nabla\cdot\mathrm{H}q'\mathbf{u}' + q'\nabla\cdot\mathrm{H}\overline{q'\mathbf{u}'} + q'\mathbf{F}'_{\xi}. \tag{B.5}$$

We now consider the terms on the right hand side of Equation B.5 separately. The first term can be simplified as follows

$$q'\nabla\cdot\mathrm{H}\overline{q}\mathbf{u}' = \mathrm{H}q'\mathbf{u}'\cdot\nabla\overline{q} + q'\overline{q}\nabla\cdot\mathrm{H}\mathbf{u}' \tag{B.6}$$

$$= \mathrm{H}q'\mathbf{u}'\cdot\nabla\overline{q}, \tag{B.7}$$

where we have used the continuity equation (Equation 3.3).

We now consider the second term on the right hand side of Equation B.5, We may manipulate this term as follows

$$q'\nabla\cdot\mathrm{H}q'\overline{\mathbf{u}} = q'\mathrm{H}\overline{\mathbf{u}}\cdot\nabla q' + q'^2\nabla\cdot\mathrm{H}\overline{\mathbf{u}} \tag{B.8}$$

$$= q'\mathrm{H}\overline{\mathbf{u}}\cdot\nabla q' \tag{B.9}$$

$$= \nabla\cdot q'^2\mathrm{H}\overline{\mathbf{u}} - q'\nabla\cdot\mathrm{H}q'\overline{\mathbf{u}}, \tag{B.10}$$

where we have again used the continuity equation (Equation 3.3). Moving the second term on the right hand side of Equation B.10 to the left hand side yields the following

$$q'\nabla\cdot\mathrm{H}q'\overline{\mathbf{u}} = \frac{1}{2}\nabla\cdot\mathrm{H}q'^2\overline{\mathbf{u}} \tag{B.11}$$

$$= \nabla\cdot\left(\mathrm{H}\frac{q'^2}{2}\overline{\mathbf{u}}\right). \tag{B.12}$$

Similarly, we find for the third term on the right hand side of Equation B.5 that

$$q'\nabla\cdot\mathrm{H}q'\mathbf{u}' = \nabla\cdot\left(\mathrm{H}\frac{q'^2}{2}\mathbf{u}'\right). \tag{B.13}$$

Therefore Equation B.5 becomes

$$\mathrm{H}\frac{\partial}{\partial t}\left(\frac{q'^2}{2}\right) = -\mathrm{H}q'\mathbf{u}'\cdot\nabla\overline{q} - \nabla\cdot\left(\mathrm{H}\frac{q'^2}{2}\overline{\mathbf{u}}\right) - \nabla\cdot\left(\mathrm{H}\frac{q'^2}{2}\mathbf{u}'\right) + q'\nabla\cdot\mathrm{H}\overline{q'\mathbf{u}'} + q'\mathbf{F}'_{\xi}. \quad \text{(B.14)}$$

Finally, we take the time-average of Equation B.14 to obtain the time-averaged, depth-integrated EPEnstr equation,

$$\mathrm{H}\frac{\partial}{\partial t}\left(\frac{\overline{q'^2}}{2}\right) = -\mathrm{H}\overline{q'\mathbf{u}'}\cdot\nabla\overline{q} - \nabla\cdot\left(\frac{\overline{q'^2}}{2}\mathrm{H}\overline{\mathbf{u}}\right) - \nabla\cdot\left(\mathrm{H}\overline{\frac{q'^2}{2}\mathbf{u}'}\right) + \mathbf{F}_{\Lambda}, \quad \text{(B.15)}$$

where $\mathbf{F}_{\Lambda}$ represents external forcing on the depth-integrated EPEnstr, and where the fourth term on the right hand side of Equation B.14 has disappeared since $\overline{q'} = 0$.

Appendix C

Derivation of the mean kinetic energy equation

Here, we derive the volume-integrated time-mean kinetic energy equation for a barotropic fluid with depth H in a double periodic domain on an f-plane. We begin with the vorticity equation for a barotropic fluid,

$$\frac{\partial \xi}{\partial t} = -\nabla \cdot \zeta \mathbf{u} + \mathbf{F}_\xi, \tag{C.1}$$

where $\mathbf{F}_\xi$ represents external forcing on the relative vorticity. In the simulations described and analysed in Chapters 3 and 4, the external forcing on ξ consists of biharmonic diffusion, and thus the vorticity equation employed is

$$\frac{\partial \xi}{\partial t} = -\nabla \cdot \zeta \mathbf{u} - \mu_\xi \nabla^4 \xi. \tag{C.2}$$

Note that Equation C.2 is relevant to both simulations with explicit eddies only and with parameterized eddies. Taking a time-mean of Equation C.2 yields the time-mean vorticity equation,

$$\frac{\partial \overline{\xi}}{\partial t} = -\nabla \cdot \overline{\zeta}\ \overline{\mathbf{u}} - \nabla \cdot \overline{\zeta' \mathbf{u}'} - \mu_\xi \nabla^4 \overline{\xi}, \tag{C.3}$$

where we have used the relation $\overline{\zeta \mathbf{u}} = \overline{\zeta}\ \overline{\mathbf{u}} + \overline{\zeta' \mathbf{u}'}$. Again we note that Equation C.3 is relevant to both simulations with explicit eddies only and with parameterized eddies. For the eddy-resolving simulation (i.e. with explicit eddies only), the flow is decomposed into a large-scale flow and an eddy component of the flow using a Reynolds

averaging procedure. Overbars in Equation C.3 represent the large-scale flow and primes represent the eddy component of the flow. For simulations with parameterized eddies, overbars denote the resolved flow (which is considered the large-scale flow in these simulations) and primes denote the unresolved flow (which is the parameterized eddy component of the flow in these simulations).

We multiply $\partial\overline{\xi}/\partial t$ by $-\overline{\psi}$, and substituting $\overline{\xi}$ for $\overline{\psi}$ using the vorticity-stream function relation (Equation 3.4) to obtain the following:

$$-\overline{\psi}\frac{\partial\overline{\xi}}{\partial t} = -\overline{\psi}\frac{\partial}{\partial t}\left(\nabla\cdot\left(\frac{\nabla\overline{\psi}}{\mathrm{H}}\right)\right) \tag{C.4}$$

$$= -\overline{\psi}\nabla\cdot\left(\frac{\partial}{\partial t}\left(\frac{\nabla\overline{\psi}}{\mathrm{H}}\right)\right) \tag{C.5}$$

$$= -\nabla\cdot\left(\overline{\psi}\,\frac{\partial}{\partial t}\left(\frac{\nabla\overline{\psi}}{\mathrm{H}}\right)\right) + \frac{\partial}{\partial t}\left(\frac{\nabla\overline{\psi}}{\mathrm{H}}\right)\cdot\nabla\overline{\psi} \tag{C.6}$$

$$= -\nabla\cdot\left(\overline{\psi}\,\frac{\partial}{\partial t}\left(\frac{\nabla\overline{\psi}}{\mathrm{H}}\right)\right) + \frac{\partial}{\partial t}\left(\frac{\nabla\overline{\psi}\cdot\nabla\overline{\psi}}{2\mathrm{H}}\right) \tag{C.7}$$

From the continuity equation (Equation 3.3) we can define the time-mean zonal and meridional components of the velocity respectively as

$$\overline{u} = -\frac{1}{\mathrm{H}}\frac{\partial\overline{\psi}}{\partial y}, \text{ and } \overline{v} = \frac{1}{\mathrm{H}}\frac{\partial\overline{\psi}}{\partial x}. \tag{C.8}$$

Then, from the following relationship,

$$\frac{\nabla\overline{\psi}\cdot\nabla\overline{\psi}}{2\mathrm{H}} = \frac{\mathrm{H}^2\overline{u}^2 + \mathrm{H}^2\overline{v}^2}{2\mathrm{H}} \tag{C.9}$$

$$= \frac{\mathrm{H}(\overline{u}^2 + \overline{v}^2)}{2}, \tag{C.10}$$

$$= \mathrm{H}\frac{\overline{\mathbf{u}}\cdot\overline{\mathbf{u}}}{2} \tag{C.11}$$

we see that the second term on the right hand side of Equation C.7 is the rate of change of the depth-integrated MKE. Thus, substituting in the time-mean vorticity equation (Equation C.3) in Equation C.7 and rearranging, we obtain the depth-integrated MKE equation,

$$\mathrm{H}\frac{\partial}{\partial t}\left(\frac{\overline{\mathbf{u}}\cdot\overline{\mathbf{u}}}{2}\right)=\nabla\cdot\left(\overline{\psi}\,\frac{\partial}{\partial t}\left(\frac{\nabla\overline{\psi}}{\mathrm{H}}\right)\right)+\overline{\psi}\nabla\cdot(\overline{\zeta}\;\overline{\mathbf{u}})+\overline{\psi}\nabla\cdot(\overline{\zeta'\mathbf{u}'})+\mu_\xi\overline{\psi}\nabla^4\overline{\xi}. \quad \text{(C.12)}$$

It is helpful to rearrange Equation C.12 when calculating the volume-integral. Consider the second term on the right hand side of Equation C.12:

$$\overline{\psi}\nabla\cdot(\overline{\zeta}\;\overline{\mathbf{u}})=\nabla\cdot(\overline{\psi}\;\overline{\zeta}\;\overline{\mathbf{u}})-\overline{\zeta}\;\overline{\mathbf{u}}\cdot\nabla\overline{\psi} \quad \text{(C.13)}$$

$$=\nabla\cdot(\overline{\psi}\;\overline{\zeta}\;\overline{\mathbf{u}}) \quad \text{(C.14)}$$

since $\overline{\mathbf{u}}\cdot\nabla\overline{\psi}=0$.

Now, consider the third term on the right hand side of Equation C.12:

$$\overline{\psi}\nabla\cdot(\overline{\zeta'\mathbf{u}'})=\nabla\cdot(\overline{\psi}\;\overline{\zeta'\mathbf{u}'})-\overline{\zeta'\mathbf{u}'}\cdot\nabla\overline{\psi} \quad \text{(C.15)}$$

Making these substitutions in Equation C.12 yields

$$\mathrm{H}\frac{\partial}{\partial t}\left(\frac{\overline{\mathbf{u}}\cdot\overline{\mathbf{u}}}{2}\right)=\nabla\cdot\left(\overline{\psi}\,\frac{\partial}{\partial t}\left(\frac{\nabla\overline{\psi}}{\mathrm{H}}\right)\right)+\nabla\cdot(\overline{\psi}\;\overline{\zeta}\;\overline{\mathbf{u}})+\nabla\cdot(\overline{\psi}\;\overline{\zeta'\mathbf{u}'})-\overline{\zeta'\mathbf{u}'}\cdot\nabla\overline{\psi}+\mu_\xi\overline{\psi}\nabla^4\overline{\xi}. \quad \text{(C.16)}$$

From the definition of potential vorticity, q, (Equation 2.1) and since f and H do not vary in time, $\overline{\zeta}=\mathrm{H}\overline{q}$ and $\zeta'=\mathrm{H}q'$. Thus, we may rewrite Equation C.16 in terms of q as follows

$$\mathrm{H}\frac{\partial}{\partial t}\left(\frac{\overline{\mathbf{u}}\cdot\overline{\mathbf{u}}}{2}\right)=\nabla\cdot\left(\overline{\psi}\,\frac{\partial}{\partial t}\left(\frac{\nabla\overline{\psi}}{\mathrm{H}}\right)\right)+\nabla\cdot(\mathrm{H}\overline{\psi}\;\overline{q}\;\overline{\mathbf{u}})+\nabla\cdot(\mathrm{H}\overline{\psi}\;\overline{q'\mathbf{u}'})-\mathrm{H}\overline{q'\mathbf{u}'}\cdot\nabla\overline{\psi}+\mu_\xi\overline{\psi}\nabla^4\mathrm{H}\overline{q}, \quad \text{(C.17)}$$

where we have also used the fact that $\nabla\mathrm{H}\overline{q}=\nabla\overline{\xi}$ since f does not vary in space on an f-plane approximation. Integrating equation C.17 over the domain area, noting that integrals of divergent terms are zero since we are in a doubly periodic domain, we obtain the volume-integrated MKE budget,

$$\frac{d}{dt}\int\int_A \mathrm{H}\frac{\overline{\mathbf{u}}\cdot\overline{\mathbf{u}}}{2}\,dA = -\int\int_A \mathrm{H}\overline{q'\mathbf{u}'}\cdot\nabla\overline{\psi}\,dA + \int\int_A \mu_\xi\overline{\psi}\nabla^4\mathrm{H}\overline{q}\,dA, \tag{C.18}$$

where A is the domain area.

Appendix D

Derivation of the mean potential enstrophy equation

Here, we derive the volume-integrated time-mean potential enstrophy equation for a barotropic fluid with depth H in a doubly periodic domain on an f-plane. We start with the time-mean vorticity equation, derived in Appendix C, which is relevant to both explicit eddy and parameterized eddy simulations,

$$\frac{\partial \overline{\xi}}{\partial t} = -\nabla \cdot \overline{\zeta}\ \overline{\mathbf{u}} - \nabla \cdot \overline{\zeta' \mathbf{u}'} - \mu_\xi \nabla^4 \overline{\xi}. \tag{D.1}$$

Using the definition of potential vorticity, q, (Equation 2.1) and since f and H do not vary in time, $f + \overline{\xi} = \mathrm{H}\overline{q}$, $\overline{\zeta} = \mathrm{H}\overline{q}$ and $\zeta' = \mathrm{H}q'$. Thus, we may rewrite Equation D.1 in terms of q as follows

$$\mathrm{H}\frac{\partial \overline{q}}{\partial t} = -\nabla \cdot \mathrm{H}\overline{q}\ \overline{\mathbf{u}} - \nabla \cdot \mathrm{H}\overline{q' \mathbf{u}'} - \mu_\xi \nabla^4 \mathrm{H}\overline{q}, \tag{D.2}$$

where we have also used the fact that $\nabla \mathrm{H}\overline{q} = \nabla \overline{\xi}$ and $\partial f / \partial t = 0$ since f does not vary in space nor time on an f-plane approximation.

Multiplying by $\overline{q}$ we obtain the depth-integrated mean potential enstrophy equation,

$$\mathrm{H}\frac{\partial}{\partial t}\left(\frac{\overline{q}^2}{2}\right) = -\overline{q}\nabla \cdot \mathrm{H}\overline{q}\ \overline{\mathbf{u}} - \overline{q}\nabla \cdot \mathrm{H}\overline{q' \mathbf{u}'} - \overline{q}\mu_\xi \nabla^4 \mathrm{H}\overline{q}. \tag{D.3}$$

It is helpful, when calculating the volume-integrated mean potential enstrophy budget, to rearrange some of the terms on the right hand side of Equation D.3. Consider the first term on the right hand side of Equation D.3:

$$\overline{q}\nabla \cdot \mathrm{H}\overline{q}\overline{\mathbf{u}} = \overline{q}\mathrm{H}\overline{\mathbf{u}} \cdot \nabla\overline{q} + \overline{q}\ \overline{q}\nabla \cdot \mathrm{H}\overline{\mathbf{u}} \tag{D.4}$$

$$= \overline{q}\mathrm{H}\overline{\mathbf{u}} \cdot \nabla\overline{q} \tag{D.5}$$

$$= \nabla \cdot \overline{q}\ \overline{q}\mathrm{H}\overline{\mathbf{u}} - \overline{q}\nabla \cdot \mathrm{H}\overline{q}\overline{\mathbf{u}}. \tag{D.6}$$

Moving the second term on the right hand side of Equation D.6 to the left hand side yields

$$\overline{q}\nabla \cdot \mathrm{H}\overline{q}\overline{\mathbf{u}} = \frac{1}{2}\nabla \cdot \mathrm{H}\overline{q}\ \overline{q}\overline{\mathbf{u}} \tag{D.7}$$

$$= \nabla \cdot \left(\mathrm{H}\frac{\overline{q}^2}{2}\overline{\mathbf{u}}\right). \tag{D.8}$$

Now, consider the second term on the right hand side of Equation D.3:

$$\overline{q}\nabla \cdot \mathrm{H}\overline{q'\mathbf{u}'} = \nabla \cdot (\overline{q}\mathrm{H}\ \overline{q'\mathbf{u}'}) - \mathrm{H}\overline{q'\mathbf{u}'} \cdot \nabla\overline{q} \tag{D.9}$$

Substituting Equations D.8 and D.9 into Equation D.3 gives the following

$$\mathrm{H}\frac{\partial}{\partial t}\left(\frac{\overline{q}^2}{2}\right) = -\nabla \cdot \left(\mathrm{H}\frac{\overline{q}^2}{2}\overline{\mathbf{u}}\right) - \nabla \cdot (\overline{q}\mathrm{H}\ \overline{q'\mathbf{u}'}) + \mathrm{H}\overline{q'\mathbf{u}'} \cdot \nabla\overline{q} - \overline{q}\mu_\xi\nabla^4\mathrm{H}\overline{q}, \tag{D.10}$$

Integrating equation D.10 over the domain area, noting that integrals of divergent terms are zero since we are in a doubly periodic domain, we obtain the volume-integrated MPEnstr budget,

$$\frac{d}{dt}\int\int_A \mathrm{H}\frac{\overline{q}^2}{2}\ dA = \int\int_A \mathrm{H}\overline{q'\mathbf{u}'} \cdot \nabla\overline{q}\ dA - \int\int_A \overline{q}\mu_\xi\nabla^4\mathrm{H}\overline{q}\ dA, \tag{D.11}$$

where A is the domain area.

Appendix E

Accessible Plots

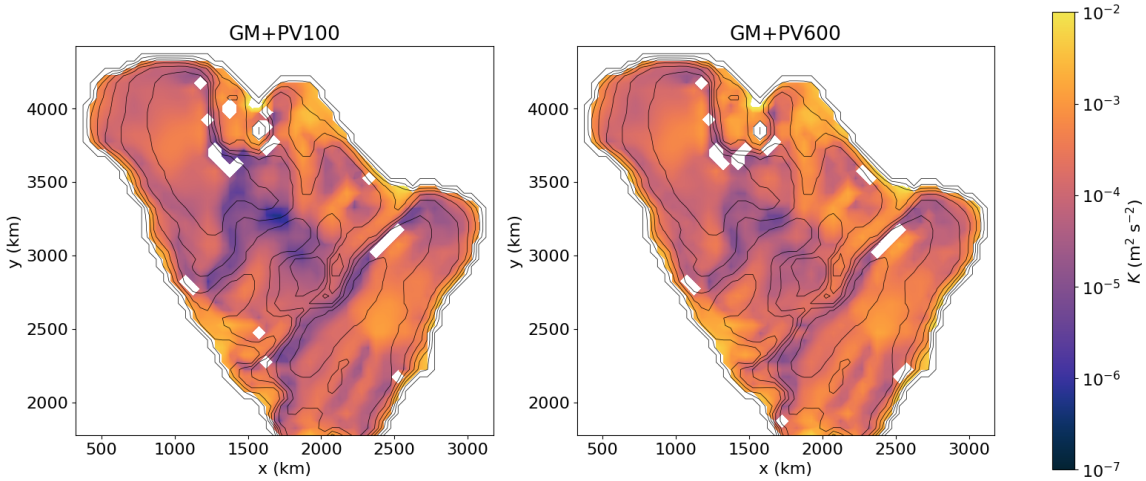

Figure E.1: Time-mean parameterized EKE, K, (contours) over years 90 - 99 for BTGM100 (left) and BTGM600 (right) plotted on a log scale. Black contours indicate the topography.

Bibliography

Abernathey, R., J. Marshall, and D. Ferreira, 2011: The dependence of southern ocean meridional overturning on wind stress. *J. Phys. Oceanogr.*, **41**, 2261–2278, https://doi.org/https://doi.org/10.1175/JPO-D-11-023.1.

Abernathey, R. P., and J. Marshall, 2013: Global surface eddy diffusivities derived from satellite altimetry. 901–916 pp., https://doi.org/10.1002/jgrc.20066.

Adcock, S. T., and D. P. Marshall, 2000: Interactions between geostrophic eddies and the mean circulation over large-scale bottom topography. *J. Phys. Oceanogr.*, **30**, 3223–3238, https://doi.org/10.1175/1520-0485(2000)030⟨3223:ibgeat⟩2.0.co;2.

Adcroft, A., and D. P. Marshall, 1998: How slippery are piecewise-constant coastlines in numerical ocean models? *Tellus*, **50**, 95–108.

Aiki, H., K. J. Richards, and H. Sakuma, 2011: Maintenance of the mean kinetic energy in the global ocean by the barotropic and baroclinic energy routes: the roles of JEBAR and Ekman dynamics. *Ocean Dyn.*, **61 (5)**, 675–700, https://doi.org/10.1007/s10236-011-0382-y.

Aksenov, Y., V. V. Ivanov, A. J. G. Nurser, S. Bacon, I. V. Polyakov, A. C. Coward, A. C. Naveira-Garabato, and A. Beszczynska-Moeller, 2011: The Arctic Circumpolar Boundary Current. *J. Geophys. Res.*, **116**, https://doi.org/10.1029/2010JC006637.

Arakawa, A., 1966: Computational design for long term numerical integration of the equations of fluid motion: two-dimensional incompressible flow. part i. *J. Comput. Phys.*, **1**, 119–143.

Armitage, T. W. K., S. Bacon, A. L. Ridout, A. A. Petty, S. Wolbach, and M. Tsamados, 2017: Arctic Ocean surface geostrophic circulation 2003–2014. **11 (4)**, 1767–1780, https://doi.org/10.5194/tc-11-1767-2017.

Arnold, V. I., 1965: Conditions for nonlinear stability of stationary plane curvilinear flows of an ideal fluid. *Dokl. Akad. Nauk. SSSR.*, **162**, 975–978.

Bachman, S. D., 2019: The GM+E closure: A framework for coupling backscatter with the Gent and McWilliams parameterization. *Ocean Modell.*, **136**, 85–106, https://doi.org/10.1016/j.ocemod.2019.02.006.

Beszczynska-Möller, A., E. Fahrbach, U. Schauer, and E. Hansen, 2012: Variability in Atlantic water temperature and transport at the entrance to the Arctic Ocean, 1997–2010. *ICES J. Mar. Sci.*, **69 (5)**, 852–863.

Bretherton, F. P., and D. B. Haidvogel, 1976: Two-dimensional turbulence above topography. *J. Fluid Mech.*, **78 (1)**, 129–154, https://doi.org/10.1017/S002211207600236X.

Cessi, P., 2008: An energy-constrained parameterization of eddy buoyancy flux. *J. Phys. Oceanogr.*, **38**, 1807–1819, https://doi.org/10.1175/2007JPO3812.1.

Chen, R., G. R. Flierl, and C. Wunsch, 2014: A description of local and nonlocal eddy-mean flow interaction in a global eddy-permitting state estimate. *J. Phys. Oceanogr.*, **44 (9)**, 2336–2352, https://doi.org/10.1175/JPO-D-14-0009.1.

Chouksey, M., C. Eden, and N. Brüggemann, 2018: Internal gravity wave emission in different dynamical regimes. *J. Phys. Oceanogr.*, **48 (8)**, 1709–1730, https://doi.org/10.1175/JPO-D-17-0158.1.

Cokelet, E. D., N. Tervalon, and J. G. Bellingham, 2008: Hydrography of the West Spitsbergen Current, Svalbard Branch: Autumn 2001. *J. Geophys. Res.*, **113 (C1)**, C01 006, https://doi.org/10.1029/2007JC004150.

Danabasoglu, G., J. C. McWilliams, and P. R. Gent, 1994: The role of mesoscale tracer transports in the global ocean circulation. *Science*, **264**, 1123–1126.

de La Lama, M. S., J. H. LaCasce, and H. K. Fuhr, 2016: The vertical structure of ocean eddies. *Dyn. Stat. Clim. Syst.*, dzw001, https://doi.org/10.1093/climsys/dzw001.

Dickson, R., B. Rudels, S. Dye, M. Karcher, J. Meincke, and I. Yashayaev, 2007: Current estimates of freshwater flux through Arctic and subarctic seas. *Prog. Oceanogr.*, **73 (3)**, 210–230, https://doi.org/https://doi.org/10.1016/j.pocean.2006.12.003.

Donohue, K. A., K. L. Tracey, D. R. Watts, M. P. Chidichimo, and T. K. Chereskin, 2016: Mean Antarctic Circumpolar Current transport measured in Drake Passage. *Geophys. Res. Lett.*, **43 (22)**, 11,760–11,767, https://doi.org/10.1002/2016GL070319.

Durand, M., L.-L. Fu, D. P. Lettenmaier, D. E. Alsdorf, E. Rodriguez, and D. Esteban-Fernandez, 2010: The Surface Water and Ocean Topography mission: Observing terrestrial surface water and oceanic submesoscale eddies. *Proc. IEEE*, **98 (5)**, 766–779, https://doi.org/10.1109/JPROC.2010.2043031.

Durran, D. R., 1991: The third-order Adams-Bashforth method: an attractive alternative to leapfrog time differencing. *Mon. Weather Rev.*, **119 (3)**, 702–720, https://doi.org/10.1175/1520-0493(1991)119⟨0702:TTOABM⟩2.0.CO;2.

Eby, M., and G. Holloway, 1994: Sensitivity of a large-scale ocean model to a parameterization of topographic stress. *J. Phys. Oceanogr.*, **24**, 2577–2588.

Eden, C., 2009: Parameterising meso-scale eddy momentum fluxes based on potential vorticity mixing and a gauge term. *Ocean Modell.*, **32**, 58–71, https://doi.org/https://doi.org/10.1016/j.ocemod.2009.10.008.

Eden, C., and R. J. Greatbatch, 2008: Towards a mesoscale eddy closure. *Ocean Modell.*, **20**, 223–239, https://doi.org/10.1016/j.ocemod.2007.09.002.

Eyring, V., S. Bony, G. A. Meehl, C. A. Senior, B. Stevens, R. J. Stouffer, and K. E. Taylor, 2016: Overview of the Coupled Model Intercomparison Project Phase 6 (CMIP6) experimental design and organization. *Geosci. Model Dev.*, **9**, 1937–1958, https://doi.org/10.5194/gmd-9-1937-2016.

Ferrari, R., and M. Nikurashin, 2010: Suppression of eddy diffusivity across jets in the Southern Ocean. *J. Phys. Oceanogr.*, **40 (7)**, 1501–1519, https://doi.org/10.1175/2010jpo4278.1.

Ferrari, R., and C. Wunsch, 2009: Ocean circulation kinetic energy: Reservoirs, sources, and sinks. *Annu. Rev. Fluid Mech.*, **41 (1)**, 253–282, https://doi.org/10.1146/annurev.fluid.40.111406.102139.

Ferreira, D., J. Marshall, and P. Heimbach, 2005: Estimating eddy stresses by fitting dynamics to observations using a residual-mean ocean circulation model and its adjoint. *J. Phys. Oceanogr.*, **35 (10)**, 1891–1910, https://doi.org/10.1175/JPO2785.1.

Gallet, B., 2024: Two-dimensional turbulence above topography: condensation transition and selection of minimum enstrophy solutions. *arXiv.org*.

Gent, P. R., and J. C. McWilliams, 1990: Isopycnal mixing in ocean circulation models. *J. Phys. Oceanogr.*, **20**, 150–155.

Gent, P. R., J. Willebrand, T. J. McDougall, and J. C. McWilliams, 1995: Parameterizing eddy-induced tracer transports in ocean circulation models. *J. Phys. Oceanogr.*, **25 (4)**, 463–474, https://doi.org/10.1175/1520-0485(1995)025⟨0463:peitti⟩2.0.co;2.

Golubeva, E. N., and G. A. Platov, 2007: On improving the simulation of Atlantic Water circulation in the Arctic Ocean. *J. Geophys. Res.*, **112 (C4)**, https://doi.org/10.1029/2006JC003734.

Gregory, J. M., and Coauthors, 2016: The Flux-Anomaly-Forced Model Intercomparison Project (FAFMIP) contribution to CMIP6: Investigation of sea-level and ocean climate change in response to CO2 forcing. *Geosci. Model Dev.*, **9**, 3993–4017, https://doi.org/10.5194/gmd-9-3993-2016.

Griffies, S. M., and Coauthors, 2009: Coordinated Ocean-Ice Reference Experiments (COREs). *Ocean Modell.*, **26**, 1–46, https://doi.org/10.1016/j.ocemod.2008.08.007.

Griffies, S. M., and Coauthors, 2016: OMIP contribution to CMIP6: experimental and diagnostic protocol for the physical component of the Ocean Model Intercomparison Project. *Geosci. Model Dev.*, **9**, 3231–3296, https://doi.org/10.5194/gmd-9-3231-2016.

Haine, T. W. N., and Coauthors, 2015: Arctic freshwater export: Status, mechanisms, and prospects. *Global Planet. Change*, **125 (C)**, 13–35, https://doi.org/10.1016/j.gloplacha.2014.11.013.

Hallberg, R., and A. Gnanadesikan, 2006: The role of eddies in determining the structure and response of the wind-driven southern hemisphere overturning: Results from the modeling eddies in the southern ocean (meso) project. *J. Phys. Oceanogr.*, **36 (12)**, 2232–2252, https://doi.org/10.1175/JPO2980.1.

He, J., and Y. Wang, 2024: Multiple states of two-dimensional turbulence above topography. *J. Fluid Mech.*, **994**, https://doi.org/10.1017/jfm.2024.633.

Holloway, G., 1992: Representing topographic stress for large-scale ocean models. *J. Phys. Oceanogr.*, **22 (9)**, 1033–1046, https://doi.org/10.1175/1520-0485(1992)022⟨1033:RTSFLS⟩2.0.CO;2.

Holloway, G., and Z. Wang, 2009: Representing eddy stress in an Arctic Ocean model. *J. Geophys. Res.*, **114 (C6)**, C06 020, https://doi.org/10.1029/2008JC005169.

IOC, SCOR, and IAPSO, 2010: *The international thermodynamic equation of seawater 2010 (TEOS-10): Calculation and use of thermodynamic properties*. Intergovernmental Oceanographic Commission, Manuals and Guides 56, UNESCO (English).

Jansen, M. F., A. J. Adcroft, S. Khani, and H. Kong, 2019: Toward an energetically consistent, resolution aware parameterization of ocean mesoscale eddies. *J. Adv. Model. Earth Syst.*, **11**, 2844–2860, https://doi.org/10.1029/2019MS001750.

Jansen, M. F., and I. M. Held, 2014: Parameterizing sub-grid scale eddy effects using energetically consistent backscatter. *Ocean Modell.*, **80**, 36–48, https://doi.org/10.1016/j.ocemod.2014.06.002.

Jansen, M. F., I. M. Held, A. Adcroft, and R. Hallberg, 2015: Energy budget-based backscatter in an eddy permitting primitive equation model. *Ocean Modell.*, **94**, 15–26.

Jones, C. D., and Coauthors, 2016: C4MIP-The Coupled Climate-Carbon Cycle Model Intercomparison Project: Experimental protocol for CMIP6. *Geosci. Model Dev.*, **9**, 2853–2880, https://doi.org/10.5194/gmd-9-2853-2016.

Juricke, S., S. Danilov, N. Koldunov, M. Oliver, and D. Sidorenko, 2020: Ocean kinetic energy backscatter parametrization on unstructured grids: Impact on global eddy-permitting simulations. *J. Adv. Model. Earth Syst.*, **12**, https://doi.org/10.1029/2019MS001855.

Juricke, S., S. Danilov, A. Kutsenko, and M. Oliver, 2019: Ocean kinetic energy backscatter parametrizations on unstructured grids: Impact on mesoscale turbulence in a channel. *Ocean Modell.*, **138**, 51–67, https://doi.org/10.1016/j.ocemod.2019.03.009.

Karsten, R., H. Jones, and J. Marshall, 2003: The role of eddy transfer in setting the stratification and transport of a circumpolar current. *J. Phys. Oceanogr.*, **34**, 2341–2354, https://doi.org/10.1175/1520-0485(2002)032⟨0039:TROETI⟩2.0.CO;2.

Köhl, A., 2007: Generation and stability of a quasi-permanent vortex in the Lofoten Basin. *J. Phys. Oceanogr.*, **37 (11)**, 2637–2651, https://doi.org/10.1175/2007JPO3694.1.

Lique, C., H. L. Johnson, and P. E. D. Davis, 2015: On the interplay between the circulation in the surface and the intermediate layers of the Arctic Ocean. *J. Phys. Oceanogr.*, **45 (5)**, 1393–1409.

Mak, J., A. Avdis, T. David, H. S. Lee, Y. Na, Y. Wang, and F. E. Yan, 2022a: On constraining the mesoscale eddy energy dissipation time-scale. *J. Adv. Model. Earth Syst.*, **14 (11)**, https://doi.org/10.1029/2022MS003223.

Mak, J., J. R. Maddison, D. P. Marshall, and D. R. Munday, 2018: Implementation of a geometrically informed and energetically constrained mesoscale eddy parameterization in an ocean circulation model. *J. Phys. Oceanogr.*, **48**, 2363–2382, https://doi.org/10.1175/JPO-D-18-0017.1.

Mak, J., J. R. Maddison, D. P. Marshall, X. Ruan, Y. Wang, and L. Yeow, 2023: Scale-awareness in an eddy energy constrained mesoscale eddy parameterization. *J. Adv. Model. Earth Syst.*, **15 (12)**, https://doi.org/10.1029/2023MS003886.

Mak, J., D. P. Marshall, J. R. Maddison, and S. D. Bachman, 2017: Emergent eddy saturation from an energy constrained parameterisation. *Ocean Modell.*, **112**, 125–138, https://doi.org/10.1016/j.ocemod.2017.02.007.

Mak, J., D. P. Marshall, G. Madec, and J. R. Maddison, 2022b: Acute sensitivity of global ocean circulation and heat content to eddy energy dissipation timescale. *Geophys. Res. Lett.*, **49**, https://doi.org/10.1029/2021GL097259.

Manucharyan, G. E., and M. A. Spall, 2016: Wind-driven freshwater buildup and release in the Beaufort Gyre constrained by mesoscale eddies. *Geophys. Res. Lett.*, **43**, 273–282, https://doi.org/10.1002/2015GL065957.

Marshall, D. P., and A. J. Adcroft, 2010: Parameterization of ocean eddies: Potential vorticity mixing, energetics and Arnold's first stability theorem. *Ocean Modell.*, **32**, 188–204, https://doi.org/10.1016/j.ocemod.2010.02.001.

Marshall, D. P., J. R. Maddison, and P. S. Berloff, 2012: A framework for parameterizing eddy potential vorticity fluxes. *J. Phys. Oceanogr.*, **42**, 539–557, https://doi.org/10.1175/JPO-D-11-048.1.

Marshall, D. P., R. G. Williams, and M.-M. Lee, 1999: The relation between eddy induced transport and isopycnic gradients of potential vorticity. *J. Phys. Oceanogr.*, **29**, 1571–1578, https://doi.org/10.1175/1520-0485(1999)029⟨1571:TRBEIT⟩2.0.CO;2.

Marshall, J., A. Adcroft, C. Hill, L. Perelman, and C. Heisey, 1997a: A finite-volume, incompressible Navier Stokes model for studies of the ocean on parallel computers. *J. Geophys. Res.*, **102 (C3)**, 5753–5766, https://doi.org/10.1029/96JC02775.

Marshall, J., C. Hill, L. Perelman, and A. Adcroft, 1997b: Hydrostatic, quasi-hydrostatic, and nonhydrostatic ocean modeling. *J. Geophys. Res.*, **102 (C3)**, 5733–5752, https://doi.org/10.1029/96JC02776.

Marshall, J., E. Shuckburgh, H. Jones, and C. Hill, 2006: Estimates and implications of surface eddy diffusivity in the Southern Ocean derived from tracer transport. *J. Phys. Oceanogr.*, **36 (9)**, 1806–1821, https://doi.org/10.1175/JPO2949.1.

Marshall, J. C., 1981: On the parameterization of geostrophic eddies in the ocean. *J. Phys. Oceanogr.*, **11**, 257–271.

Martin, J., and Coauthors, 2020: The International Bathymetric Chart of the Arctic Ocean version 4.0. *Sci. Data*, **7 (1)**, 176–176, https://doi.org/10.1038/s41597-020-0520-9.

McDougall, T. J., and P. M. Barker, 2011: Getting started with TEOS-10 and the Gibbs Seawater (gsw) oceanographic toolbox.

Meneghello, G., J. Marshall, J.-M. Campin, E. Doddridge, and M.-L. Timmermans, 2018: The ice-ocean governor: Ice-ocean stress feedback limits Beaufort Gyre spin-up. 11,293–11,299 pp., https://doi.org/10.1029/2018GL080171.

Meneghello, G., J. Marshall, S. T. Cole, and M.-L. Timmermans, 2017: Observational inferences of lateral eddy diffusivity in the halocline of the Beaufort Gyre. *Geophys. Res. Lett.*, **44 (24)**, 12,331–12,338, https://doi.org/10.1002/2017GL075126.

Munday, D. R., H. L. Johnson, and D. P. Marshall, 2013: Eddy saturation of equilibrated circumpolar currents. *J. Phys. Oceanogr.*, **43**, 507–532, https://doi.org/10.1175/JPO-D-12-095.1.

Naveira Garabato, A. C., R. Ferrari, and K. L. Polzin, 2011: Eddy stirring in the Southern Ocean. *J. Geophys. Res.*, **116 (C9)**, https://doi.org/10.1029/2010JC006818.

Naveira Garabato, A. C., A. J. G. Nurser, R. B. Scott, and J. A. Goff, 2013: The impact of small-scale topography on the dynamical balance of the ocean. *J. Phys. Oceanogr.*, **43 (3)**, 647–668, https://doi.org/10.1175/JPO-D-12-056.1.

Nazarenko, L., G. Holloway, and N. Tausnev, 1998: Dynamics of transport of "Atlantic signature" in the Arctic Ocean. *J. Geophys. Res.*, **103**, 31 003–31 015, https://doi.org/10.1029/1998JC900017.

Nøst, O. A., and P. E. Isachsen, 2003: The large-scale time-mean ocean circulation in the nordic seas and arctic ocean estimated from simplified dynamics. *J. Mar. Res.*, **61**, 175–210.

Nurser, A. J. G., and S. Bacon, 2014: The Rossby radius in the Arctic Ocean. *Ocean Sci.*, **10 (6)**, 967–975, https://doi.org/10.5194/os-10-967-2014.

Orvik, K. A., and P. Niiler, 2002: Major pathways of Atlantic Water in the northern North Atlantic and Nordic Seas toward Arctic. *Geophys. Res. Lett.*, **29 (19)**, 2–1–2–4, https://doi.org/10.1029/2002GL015002.

Pfirman, S. L., D. Bauch, and T. Gammelsrød, 1994: *The Northern Barents Sea: Water Mass Distribution and Modification*, 77–94. American Geophysical Union (AGU), https://doi.org/https://doi.org/10.1029/GM085p0077, URL https://agupubs.onlinelibrary.wiley.com/doi/abs/10.1029/GM085p0077.

Polyakov, I., 2001: An eddy parameterization based on maximum entropy production with application to modeling of the Arctic Ocean circulation. *J. Phys. Oceanogr.*, **31 (8)**, 2255–2270, https://doi.org/10.1175/1520-0485(2001)031⟨2255:AEPBOM⟩2.0.CO;2.

Proshutinsky, A., and Coauthors, 2009: Beaufort Gyre freshwater reservoir: State and variability from observations. *J. Geophys. Res.*, **114 (C1)**, C00A10, https://doi.org/10.1029/2008JC005104.

Proudman, J., 1916: On the motion of solids in a liquid possessing vorticity. *Proc. R. Soc. London, Ser. A*, **92 (642)**, 408–424, https://doi.org/10.1098/rspa.1916.0026.

Redi, M. H., 1982: Oceanic isopycnal mixing by coordinate rotation. *J. Phys. Oceanogr.*, **12 (10)**, 1154–1158.

Rhines, P. B., and W. R. Young, 1982: Homogenization of potential vorticity in planetary gyres. *J. Fluid Mech.*, **122**, 347–367, https://doi.org/10.1017/S0022112082002250.

Richter, M. E., W.-J. von Appen, and C. Wekerle, 2018: Does the East Greenland Current exist in the northern Fram Strait? *Ocean Sci.*, **14 (5)**, 1147–1165, https://doi.org/10.5194/os-14-1147-2018.

Rudels, B., L. G. Anderson, and E. P. Jones, 1996: Formation and evolution of the surface mixed layer and halocline of the Arctic Ocean. *J. Geophys. Res.*, **101 (C4)**, 8807–8821, https://doi.org/10.1029/96JC00143.

Rudels, B., E. P. Jones, U. Schauer, and P. Eriksson, 2004: Atlantic sources of the Arctic Ocean surface and halocline waters. *Polar Res.*, **23 (2)**, 181–208, https://doi.org/10.1111/j.1751-8369.2004.tb00007.x.

Rudels, B., R. D. Muench, J. Gunn, U. Schauer, and H. J. Friedrich, 2000: Evolution of the Arctic Ocean boundary current north of the Siberian shelves. *J. Mar. Syst.*, **25 (1)**, 77–99, https://doi.org/10.1016/S0924-7963(00)00009-9.

Salmon, R., 1998: *Lectures on geophysical fluid dynamics*. 1st ed., Oxford scholarship online, Oxford University Press, New York, 393 pp.

Sen, A., R. B. Scott, and B. K. Arbic, 2008: Global energy dissipation rate of deep-ocean low-frequency flows by quadratic bottom boundary layer drag: Computations from current-meter data. *Geophys. Res. Lett.*, **35 (9)**, L09 606, https://doi.org/10.1029/2008GL033407.

Serreze, M. C., and A. P. Barrett, 2011: Characteristics of the Beaufort Sea high. *J. Climate*, **24 (1)**, 159–182, https://doi.org/10.1175/2010jcli3636.1.

Serreze, M. C., F. Carse, R. G. Barry, and J. C. Rogers, 1997: Icelandic Low cyclone activity: Climatological features, linkages with the NAO, and relationships with recent changes in the northern hemisphere circulation. *J. Climate*, **10 (3)**, 453–464, https://doi.org/10.1175/1520-0442(1997)010⟨0453:ILCACF⟩2.0.CO;2.

Serreze, M. C., and Coauthors, 2006: The large-scale freshwater cycle of the Arctic. *J. Geophys. Res.*, **111 (C11)**, C11 010, https://doi.org/10.1029/2005JC003424.

Siegelman, L., and W. R. Young, 2023: Two-dimensional turbulence above topography: Vortices and potential vorticity homogenization. *Proc. Natl. Acad. Sci. (USA)*, **120 (44)**, 1–e2308018 120.

Søiland, H., and T. Rossby, 2013: On the structure of the Lofoten Basin Eddy. *J. Geophys. Res.*, **118 (9)**, 4201–4212, https://doi.org/10.1002/jgrc.20301.

Solodoch, A., A. L. Stewart, and J. C. McWilliams, 2021: Formation of anticyclones above topographic depressions. *J. Phys. Oceanogr.*, **51 (1)**, 207–228, https://doi.org/10.1175/JPO-D-20-0150.1.

Spall, M. A., 2013: On the circulation of Atlantic Water in the Arctic Ocean. *J. Phys. Oceanogr.*, **43 (11)**, 2352–2371.

Steele, M., R. Morley, and W. Ermold, 2001: Phc: A global ocean hydrography with a high-quality Arctic Ocean. *J. Climate*, **14 (9)**, 2079–2087, https://doi.org/10.1175/1520-0442(2001)014⟨2079:PAGOHW⟩2.0.CO;2.

Sterl, M. F., J. H. LaCasce, S. Groeskamp, A. Nummelin, P. E. Isachsen, and M. L. J. Baatsen, 2024: Suppression of mesoscale eddy mixing by topographic pv gradients. *J. Phys. Oceanogr.*, **54 (5)**, 1089–1103, https://doi.org/10.1175/JPO-D-23-0142.1.

Styles, A. F., M. J. Bell, D. P. Marshall, and D. Storkey, 2022: Spurious forces can dominate the vorticity budget of ocean gyres on the C-grid. *J. Adv. Model. Earth Syst.*, https://doi.org/10.1029/2021MS002884.

Tamarin, T., J. R. Maddison, E. Heifetz, and D. P. Marshall, 2016: A geometric interpretation of eddy Reynolds stresses in barotropic ocean jets. *J. Phys. Oceanogr.*, **46**, 2285–2307, https://doi.org/10.1175/JPO-D-15-0139.1.

Taylor, G. I., 1917: Motion of solids in fluids when the flow is not irrotational. *Proc. R. Soc. London, Ser. A*, **93 (648)**, 99–113, https://doi.org/10.1098/rspa.1917.0007.

Timmermans, M.-L., and J. Marshall, 2020: Understanding Arctic Ocean circulation: A review of ocean dynamics in a changing climate. *J. of Geophys. Res.: Oceans*, **125 (4)**.

Treguier, A. M., I. M. Held, and V. D. Larichev, 1997: Parameterization of quasigeostrophic eddies in primitive equation models. *J. Phys. Oceanogr.*, **27**, 567–580, https://doi.org/10.1175/1520-0485(1997)027⟨0567:POQEIP⟩2.0.CO;2.

van Sebille, E., and Coauthors, 2017: Lagrangian ocean analysis: fundamentals and practices. *Ocean Modell.*, **121**, 49–75, https://doi.org/10.1016/j.ocemod.2017.11.008.

Visbeck, M., J. Marshall, and T. Haine, 1997: Specification of eddy transfer coefficients in coarse-resolution ocean circulation models. *J. Phys. Oceanogr.*, **27**, 381–402, https://doi.org/10.1175/1520-0485(1997)027⟨0381:SOETCI⟩2.0.CO;2.

von Appen, W.-J., T. M. Baumann, M. Janout, N. Koldunov, Y.-D. Lenn, R. S. Pickart, R. B. Scott, and Q. Wang, 2022: Eddies and the distribution of eddy kinetic energy in the Arctic Ocean. *Oceanography*, **35 (3/4)**, 42–51, https://doi.org/10.5670/oceanog.2022.122.

Wang, Q., N. V. Koldunov, S. Danilov, D. Sidorenko, C. Wekerle, P. Scholz, I. L. Bashmachnikov, and T. Jung, 2020: Eddy kinetic energy in the Arctic Ocean from a global simulation with a 1-km Arctic. *Geophys. Res. Lett.*, **47 (14)**, https://doi.org/10.1029/2020GL088550.

Wardle, R., and J. Marshall, 2000: Representation of eddies in primitive equation models by a PV flux. *J. Phys. Oceanogr.*, **30 (10)**, 2481–2503, https://doi.org/10.1175/1520-0485(2000)030⟨2481:ROEIPE⟩2.0.CO;2.

Waterman, S., N. G. Hogg, and S. R. Jayne, 2011: Eddy—Mean flow interaction in the kuroshio extension region. *J. Phys. Oceanogr.*, **41 (6)**, 1182–1208, https://doi.org/10.1175/2010jpo4564.1.

Waterman, S., and S. R. Jayne, 2012: Eddy-driven recirculations from a localized transient forcing. *J. Phys. Oceanogr.*, **42 (3)**, 430–447.

Waterman, S., and J. M. Lilly, 2015: Geometric decomposition of eddy feedbacks in barotropic systems. *J. Phys. Oceanogr.*, **45**, 1009–1024, https://doi.org/10.1175/JPO-D-14-0177.1.

Wilson, C., and R. G. Williams, 2004: Why are eddy fluxes of potential vorticity difficult to parameterize? *J. Phys. Oceanogr.*, **34 (1)**, 142–155, https://doi.org/10.1175/1520-0485(2004)034⟨0142:WAEFOP⟩2.0.CO;2.

Woodgate, R. A., and K. Aagaard, 2005: Revising the Bering Strait freshwater flux into the Arctic Ocean. *Geophys. Res. Lett.*, **32 (2)**, L02 602, https://doi.org/10.1029/2004GL021747.

Woodgate, R. A., K. Aagaard, R. D. Muench, J. Gunn, G. Björk, B. Rudels, A. T. Roach, and U. Schauer, 2001: The Arctic Ocean Boundary Current along the Eurasian slope and the adjacent Lomonosov Ridge: Water mass properties, transports and transformations from moored instruments. *Deep Sea Res., Part I*, **48 (8)**, 1757–1792, https://doi.org/10.1016/S0967-0637(00)00091-1.

Yang, J., 2005: The Arctic and Subarctic ocean flux of potential vorticity and the Arctic Ocean circulation. *J. Phys. Oceanogr.*, **35 (12)**, 2387–2407, https://doi.org/10.1175/JPO2819.1.

Yankovsky, E., S. Bachman, K. S. Smith, and L. Zanna, 2024: Vertical structure and energetic constraints for a backscatter parameterization of ocean mesoscale eddies. *J. Adv. Model. Earth Syst.*, **16 (7)**, https://doi.org/10.1029/2023MS004093.

Yu, X., A. C. N. Garabato, A. P. Martin, and D. P. Marshall, 2021: The annual cycle of upper-ocean potential vorticity and its relationship to submesoscale instabilities. *J. Phys. Oceanogr.*, **5**, 385–402, https://doi.org/10.1175/JPO-D-20-0099.1.

Zhao, M., M. Timmermans, R. Krishfield, and G. Manucharyan, 2018: Partitioning of kinetic energy in the Arctic Ocean's Beaufort Gyre. *J. Geophys. Res.*, **123**, 4806–4819, https://doi.org/10.1029/2018JC014037.

Zhao, M., M.-L. Timmermans, S. Cole, R. Krishfield, A. Proshutinsky, and J. Toole, 2014: Characterizing the eddy field in the Arctic Ocean halocline. *J. Geophys. Res.*, **119 (12)**, 8800–8817, https://doi.org/10.1002/2014JC010488.